



6-2013

Global Skin Friction Diagnostics: The Glof Technique and Measurements of Complex Separated Flows

Sudesh A. Woodiga

Western Michigan University, sudeshwoodiga@gmail.com

Follow this and additional works at: <https://scholarworks.wmich.edu/dissertations>



Part of the Aerodynamics and Fluid Mechanics Commons, and the Structures and Materials Commons

Recommended Citation

Woodiga, Sudesh A., "Global Skin Friction Diagnostics: The Glof Technique and Measurements of Complex Separated Flows" (2013). *Dissertations*. 173.

<https://scholarworks.wmich.edu/dissertations/173>

This Dissertation-Open Access is brought to you for free and open access by the Graduate College at ScholarWorks at WMU. It has been accepted for inclusion in Dissertations by an authorized administrator of ScholarWorks at WMU. For more information, please contact wmu-scholarworks@wmich.edu.



GLOBAL SKIN FRICTION DIAGNOSTICS: THE GLOF TECHNIQUE AND
MEASUREMENTS OF COMPLEX SEPARATED FLOWS

by

Sudesh A. Woodiga

A dissertation submitted to the Graduate College
in partial fulfillment of the requirements
for the degree of Doctor of Philosophy
Mechanical and Aeronautical Engineering
Western Michigan University
June 2013

Doctoral Committee:

Tianshu Liu, Ph.D., Chair
Parviz Merati, Ph.D.
Javier Martin Montefort-Sanchez, Ph.D.
Phuriwat Anusonti-Inthra, Ph.D.

GLOBAL SKIN FRICTION DIAGNOSTICS: THE GLOF TECHNIQUE AND MEASUREMENTS OF COMPLEX SEPARATED FLOWS

Sudesh A. Woodiga, Ph.D.

Western Michigan University, 2013

This work describes the application of the global luminescent oil film skin friction meter to quantitative global skin friction diagnostics of complex separated flows. The development of this technique is based on the relationship between the oil film thickness and luminescent intensity of a luminescent oil film. The projected thin oil film equation is given to relate the normalized luminescent intensity with skin friction. The variational formulation with a smoothness constraint on skin friction is proposed to obtain a snap shot solution from two consecutive images for a relative skin friction field. A complete skin friction field is reconstructed through superposition of a sequence of snap shot solutions.

A refinement is implemented for this technique focused on data reduction simplification and robustness, luminescent oil formulation, UV excitation and oil film application. This is complemented by a systematic study with emphasis on parametric analysis of data reduction variables such as spatial resolution, time step, Lagrange multiplier, image file format and image filtering.

A number of separated flows were also investigated – a low aspect ratio NACA0012 rectangular wing at different angles of attack, wing-body junction flow and delta wings at different angles of attack, yaw and roll. Detailed analysis of the complex

skin friction topology of each test case was carried out along with topological constraint analysis using the Poincare-Bendixson index formula. The conservation law given by the Poincare-Bendixson index formula for the number of isolated singular points and boundary switch points in a region enclosed by a penetrable boundary is utilized as a general approach in analyzing the topological features of the skin friction fields.

A systematic approach was developed to map skin friction vectors from the two dimensional image plane to a three dimensional model surface in the object space. Combined surface pressure and global skin friction measurements were also conducted for junction flows and the Ahmed body to provide a unique perspective of studying these separated flows. Finally, the feasibility of heat transfer and mass transfer approaches for global skin friction diagnostics were also investigated.

© 2013 Sudesh A. Woodiga

ACKNOWLEDGEMENTS

The completion of this work would not have been possible without the contributions of numerous groups and individuals. I would like to start by thanking my mentor and dissertation committee chair, Dr. Tianshu Liu for all of his guidance and patience in mentoring me to arrive at this point in my life. Also to Dr. Parviz Merati, Dr. Javier Martin Montefort-Sanchez and Dr. Phuriwat Anusonti-Inthra, my dissertation committee members, I would like to express my sincerest gratitude for all their support, feedback and encouragement in making this work a success. Dr. Koorosh Naghshineh has also played an important role as the departmental graduate advisor in ensuring that my pursuit of this doctoral degree has been productive and trouble free and for this I would like to recognize and thank him. Mr. Peter Thannhauser is also acknowledged for his vast contributions in terms of advice and expertise to instrumentation hardware and software setup for wind tunnel testing.

I would also like to thank Dr. Ramakrishna Guda from the Department of Chemistry at Western Michigan University for his assistance in characterization of the luminescent dyes and excitation sources used in this work. Mr. Vewen Ramasamy and Mr. Sai Kumar Kode, both research assistants in the group have been instrumental in assisting with experiments and preparation of materials for this work and are duly recognized and thanked with my greatest appreciation. Another important group that has contributed in the preparation of wind tunnel models and test fixtures are part of the

Acknowledgements -- Continued

machine shop team from the Department of Industrial and Manufacturing Engineering at Western Michigan University, Mr. Glenn Hall, Mr. Mike Konkel and Mr. John Jager, and I would like to thank them for all their hard work, unwavering commitment and excellent machining output that has been an important part in producing the high quality experimental results in this work.

A number of institutions and researchers have also contributed in research collaborations in this work. I would like to recognize Professor Keisuke Asai and the GCOE Program at Tohoku University which enabled my visit to Tohoku University in Japan to perform collaborative research detailed in Chapter 9 of this work. Professor Jian Ming Wang and Dr. Zhong Hongjie from Shenyang Aerospace University are also recognized for inviting me to Shenyang Aerospace University in China for collaborative research work as detailed in Chapter 8 of this work. F. Bouvier from ONERA, M. Carbonaro from the Von Karman Institute and Dr. Jim Gregory from Ohio State University are also duly recognized for providing their experimental data used in Chapter 11 of this work.

Last but not least, I would like to recognize my family – my mother, father and sister for always being there for me and providing encouragement and support even when times were trying, I owe my success today to you and I thank you for all that you have done.

Sudesh A. Woodiga

TABLE OF CONTENTS

| | |
|---|----|
| ACKNOWLEDGEMENTS | ii |
| LIST OF TABLES | x |
| LIST OF FIGURES | xi |
| CHAPTER | |
| 1. INTRODUCTION | 1 |
| 1.1 Skin Friction Measurement Techniques | 3 |
| 1.1.1 Point Techniques | 3 |
| 1.1.2 Global Techniques | 8 |
| 2. GLOBAL LUMINESCENT OIL FILM SKIN FRICTION METER | 10 |
| 2.1 Theory..... | 11 |
| 2.2 Uncertainty Analysis | 14 |
| 2.3 Effect of Thin Oil Film on Flow Characteristics | 16 |
| 2.4 Measurement System | 19 |
| 3. SKIN FRICTION TOPOLOGY | 22 |
| 3.1 Historical Perspective..... | 22 |
| 3.2 Modern Developments | 27 |
| 3.2.1 Foss' Collapsed Sphere Method..... | 29 |
| 3.2.2 Poincare-Bendixson Index Formula | 30 |
| 3.3 Summary..... | 35 |
| 4. GLOF TECHNIQUE REFINEMENT | 36 |

Table of Contents -- Continued

| | | |
|---------|--|----|
| CHAPTER | | |
| 4.1 | Data Reduction..... | 36 |
| 4.2 | Luminescent Oil..... | 39 |
| 4.3 | UV Excitation | 44 |
| 4.4 | Oil Film Application | 48 |
| 4.5 | Summary..... | 50 |
| 5. | PARAMETRIC ANALYSIS OF DATA REDUCTION VARIABLES | 52 |
| 5.1 | Spatial Resolution | 53 |
| 5.2 | Time Step..... | 56 |
| 5.3 | Lagrange Multiplier..... | 60 |
| 5.4 | Image Filtering..... | 61 |
| 5.5 | Image File Format | 62 |
| 5.6 | Summary..... | 63 |
| 6. | LOW ASPECT RATIO NACA 0012 WING | 64 |
| 6.1 | Experimental Setup | 65 |
| 6.2 | Evolution of Skin Friction Field Topology by Varying Angle of Attack..... | 68 |
| 6.3 | Skin Friction Topology Constraint Analysis | 74 |
| 6.3.1 | Wing Upper Surface at 18° AoA..... | 74 |
| 6.3.2 | Wing Side Surface at 18° AoA..... | 77 |
| 6.3.3 | Wing Upper Surface with Leading Edge Roughness Strip at 18° AoA..... | 79 |

Table of Contents -- Continued

| | | |
|---|---|-----|
| CHAPTER | | |
| | 6.3.4 Wing Upper Surface at 0°, 5°, 12°, 13.5°, 14° and 16° AoA..... | 82 |
| | 6.4 Summary..... | 83 |
| 7. DELTA WINGS | | 85 |
| | 7.1 Experimental Setup | 89 |
| | 7.2 65° Delta Wing | 92 |
| | 7.3 76/40° Double Delta Wing | 95 |
| | 7.3.1 76/40° Double Delta Wing – Baseline..... | 95 |
| | 7.3.2 76/40° Double Delta Wing – Diamond Fillet | 98 |
| | 7.3.3 76/40° Double Delta Wing – Parabolic Fillet | 101 |
| | 7.4 Skin Friction Topology Constraint Analysis | 104 |
| | 7.5 Summary..... | 107 |
| 8. WING-BODY JUNCTION FLOW AND MAPPING OF SKIN FRICTION VECTORS FROM THE IMAGE PLANE TO A 3D MODEL IN THE OBJECT SPACE..... | | 109 |
| | 8.1 Mapping Skin Friction Vectors from the Image Plane to the Object Space | 112 |
| | 8.2 Experimental Setup | 115 |
| | 8.3 Skin Friction Fields Mapped onto a 3D Model Surface..... | 119 |
| | 8.4 Evolution of Skin Friction Field Topology by Varying Angle of Attack | 124 |
| | 8.5 Skin Friction Topology Constraint Analysis | 129 |
| | 8.5.1 AoA = 0° | 131 |

Table of Contents -- Continued

| | | |
|---------|--|-----|
| CHAPTER | | |
| | 8.5.2 AoA = 6° | 132 |
| | 8.5.3 AoA = 12° | 135 |
| | 8.6 Summary..... | 135 |
| 9. | COMBINED SURFACE PRESSURE AND GLOBAL SKIN FRICTION MEASUREMENTS | 137 |
| | 9.1 Experimental Setup | 138 |
| | 9.1.1 GLOF..... | 140 |
| | 9.1.2 PSP..... | 141 |
| | 9.2 Junction Flows | 143 |
| | 9.2.1 Square Cylinder Junction Flow | 144 |
| | 9.2.2 Diamond Cylinder Junction Flow | 151 |
| | 9.2.3 Skin Friction Topology Constraint Analysis..... | 154 |
| | 9.3 Ahmed Model | 156 |
| | 9.4 Summary..... | 162 |
| 10. | GLOBAL SKIN FRICTION DIAGNOSTICS BASED ON SURFACE TEMPERATURE MEASUREMENTS | 164 |
| | 10.1 Theory..... | 166 |
| | 10.1.1 Asymptotic Form of the Energy Equation at a Wall | 166 |
| | 10.1.2 Variational Solution for Skin Friction Fields..... | 168 |
| | 10.1.3 Uncertainty Analysis and Intrinsic Limitations..... | 170 |
| | 10.1.4 Model for Time-Averaged Measurements..... | 171 |
| | 10.2 Measurement System | 174 |

Table of Contents -- Continued

| | |
|---------|---|
| CHAPTER | |
| 10.3 | Experimental Setup 175 |
| 10.4 | Measurements of Jet Impingement on a Flat Plate 179 |
| 10.4.1 | Normal Impinging Jets..... 179 |
| 10.4.2 | Oblique Impinging Jets 184 |
| 10.5 | Effects of the Lagrange Multiplier and Gaussian Filter Size 190 |
| 10.6 | Summary..... 192 |
| 11. | GLOBAL SKIN FRICTION DIAGNOSTICS BASED ON SURFACE MASS TRANSFER VISUALIZATIONS 194 |
| 11.1 | Theory..... 195 |
| 11.1.1 | Asymptotic Form of the Mass Transport Equation at a Wall 196 |
| 11.1.2 | Measurements with Pressure Sensitive Paint 198 |
| 11.1.3 | Measurements with Sublimating Coatings 204 |
| 11.1.4 | Variational Solution for Skin Friction Fields..... 207 |
| 11.1.5 | Uncertainty Analysis and Intrinsic Limitations..... 208 |
| 11.2 | Measurements with Pressure Sensitive Paint 210 |
| 11.2.1 | Impinging Nitrogen Jets..... 211 |
| 11.2.2 | Colliding Impinging Nitrogen Jets 218 |
| 11.2.3 | Oscillating Impinging Nitrogen Jet 222 |
| 11.3 | Measurements with Sublimating Coatings 226 |
| 11.3.1 | Delta Wing 226 |
| 11.3.2 | Shock/Boundary-Layer Interaction 229 |

Table of Contents -- Continued

| | |
|-----------------------|-----|
| CHAPTER | |
| 11.4 Summary..... | 231 |
| 12. CONCLUSIONS | 233 |
| 13. FUTURE WORK..... | 238 |
| REFERENCES..... | 239 |

LIST OF TABLES

| | | |
|-----|---|----|
| 4.1 | Summary of strengths and weaknesses of luminescent molecules evaluated | 42 |
| 4.2 | Summary of strengths and weaknesses of excitation sources | 47 |
| 4.3 | Summary of strengths and weaknesses of oil film application methods evaluated | 50 |
| 6.1 | Summary of isolated singular points, boundary switch points and left and right hand side values of P-B Index Formula | 83 |
| 7.1 | Test matrix for wind tunnel testing of the delta wings | 90 |

LIST OF FIGURES

| | | |
|-----|--|----|
| 1.1 | Indirect point measurement methods (from left to right) : Stanton tube, Preston tube, hot film sensor..... | 6 |
| 1.2 | Direct measurement methods (from left to right) : MEMS floating element, oil film interferometry | 8 |
| 2.1 | Surface, object-space and image coordinates..... | 12 |
| 2.2 | Illustration of experimental setup for GLOF measurements..... | 20 |
| 2.3 | Typical (a)raw luminescent oil image, (b)skin friction line plot for a NACA 0012 wing at 18° angle of attack..... | 21 |
| 3.1 | Structures of (a)nodal points, (b)focus and (c)saddle [44]..... | 25 |
| 3.2 | A three dimensional body B_1 and B_2 mounted on a wind tunnel floor..... | 26 |
| 3.3 | A pipe junction representing a double torus [38] | 27 |
| 3.4 | Boundary switch points, (a)negative switch point and (b)positive switch point..... | 31 |
| 3.5 | A sphere with a small hole deformed into a disk..... | 33 |
| 3.6 | A cylinder on a base surface..... | 34 |
| 3.7 | Skin friction line plot of a low aspect ratio NACA 0012 wing at 18° angle of attack with penetrable boundary ABCDA, singular points and switch points highlighted..... | 35 |
| 4.1 | Flowchart of processing steps in the data reduction procedure for the GLOF technique..... | 39 |

List of Figures -- Continued

| | | |
|------|--|----|
| 4.2 | Absorption and emission spectra of Perylene | 42 |
| 4.3 | Absorption spectrum of DFSB K-175 | 43 |
| 4.4 | Emission spectrum of DFSB K-175 with 365 and 400 nm excitation..... | 44 |
| 4.5 | UV excitation sources – UV LED array, blacklight lamp..... | 44 |
| 4.6 | Emission spectrum of UV illumination sources | 45 |
| 4.7 | Emission spectrum of DFSB K-175 with blacklight lamp and UV LED excitation..... | 46 |
| 4.8 | Successive image frames for a delta wing with a luminescent oil film excited by a fluorescent UV lamp source | 47 |
| 4.9 | Successive image frames for a delta wing with a luminescent oil film excited by a UV LED array source..... | 47 |
| 4.10 | Oil application apparatus (from left to right) - paint brush, foam brush, HVLP spray gun | 48 |
| 4.11 | Oil film applied to model by (a)paint brush, (b)spray gun..... | 49 |
| 5.1 | Spatial resolution effect on GLOF measurements..... | 53 |
| 5.2 | GLOF measurements near the leading edge of a square cylinder-floor junction surface for full resolution images, (a)typical raw image, (b)skin friction magnitude plot, (c)skin friction line plot..... | 55 |
| 5.3 | GLOF measurements near the leading edge of a square cylinder-floor junction surface for downsampled images, (a)typical raw image, (b)skin friction magnitude plot, (c)skin friction line plot..... | 56 |
| 5.4 | Time step effect on GLOF measurements - fixed dt, varying ns | 57 |

List of Figures -- Continued

| | | |
|-----|---|----|
| 5.5 | Time step effect on GLOF measurements - fixed ns, varying dt | 58 |
| 5.6 | Time step effect on GLOF measurements - fixed end point, varying dt and ns | 59 |
| 5.7 | Lagrange multiplier effect on GLOF measurements | 60 |
| 5.8 | Gaussian filter effect on GLOF measurements | 61 |
| 5.9 | Image file format effect on GLOF measurements..... | 62 |
| 6.1 | Image of LAR NACA 0012 Wing..... | 66 |
| 6.2 | Illustration of experimental setup for GLOF measurements on a LAR NACA 0012 wing..... | 67 |
| 6.3 | NACA 0012 LAR wing at 18° AoA, (a)typical luminescent oil image, (b)skin friction lines, (c)skin friction vectors and (d)relative skin friction magnitude | 67 |
| 6.4 | Skin friction lines on the upper surface of a LAR NACA 0012 wing at 0° AoA..... | 70 |
| 6.5 | Skin friction lines on the upper surface of a LAR NACA 0012 wing at 5° AoA..... | 70 |
| 6.6 | Skin friction lines on the upper surface of a LAR NACA 0012 wing at 12° AoA..... | 71 |
| 6.7 | Skin friction lines on the upper surface of a LAR NACA 0012 wing at 13.5° AoA..... | 71 |
| 6.8 | Skin friction lines on the upper Surface of a LAR NACA 0012 wing at 14° AoA..... | 72 |

List of Figures -- Continued

| | | |
|------|--|----|
| 6.9 | Skin friction lines on the upper surface of a LAR NACA 0012 wing at 16° AoA..... | 72 |
| 6.10 | Force data vs. angle of attack, (a) C_L vs. AoA (experimental measurements vs. Helmbold approximation) and (b) C_D vs. AoA (experimental measurements vs. induced drag approximation) | 73 |
| 6.11 | Skin friction lines on the upper surface of a LAR NACA 0012 wing at 18° AoA..... | 76 |
| 6.12 | Zoomed-in views near singular points (a) S_1 , (b) N_2 and (c) N_4 on the upper surface of a LAR NACA 0012 wing at 18° AoA | 77 |
| 6.13 | Skin friction lines on the side surface of a LAR NACA 0012 wing at 18° AoA..... | 78 |
| 6.14 | Zoomed-in views near boundary switch points (a) Z_2^+ and Z_3^- and (b) Z_3^+ , Z_4^+ and Z_3^- , Z_4^- , Z_5^- , Z_6^- on the side surface of a LAR NACA 0012 wing at 18° AoA..... | 79 |
| 6.15 | Skin friction lines on the upper surface of a tripped LAR NACA 0012 wing at 18° AoA | 81 |
| 6.16 | Zoomed-in views near singular points (a) N_1 and S_1 , (b) S_2 , Z_1^- , Z_3^- , and Z_1^+ and (c) N_2 , S_4 and Z_5^- on top surface of a tripped LAR NACA 0012 wing at 18° AoA | 82 |
| 7.1 | Images of (a)65° delta wing, (b)baseline 76/40° double delta wing , (c)76/40° double delta wing with a diamond fillet and (d)76/40° double delta wing with a parabolic fillet | 89 |
| 7.2 | Images of (a)yaw and roll adjustment mechanism and (b)76/40° baseline double delta wing mounted on the adjustment mechanism | 90 |

List of Figures -- Continued

| | | |
|------|--|-----|
| 7.3 | 65° delta wing at 10° AoA, (a)typical luminescent oil image, (b)skin friction line plot, (c)skin friction vector plot and (d)skin friction magnitude plot..... | 91 |
| 7.4 | Skin friction line plots for a 65° delta wing at AoA, (a)10° and (b)20° | 94 |
| 7.5 | Skin friction line plots for a 65° delta wing at (AoA, YA), (a)(10°, 10°) and (b)(10°, 15°)..... | 94 |
| 7.6 | Skin friction line plots for a 65° delta wing at (AoA, RA), (a)(20°, 10°) and (b)(20°, 20°)..... | 95 |
| 7.7 | Skin friction line plots for a baseline 76/40° double delta wing at AoA, (a)10° and (b)20° | 97 |
| 7.8 | Skin friction line plots for a baseline 76/40° double delta wing at (AoA, YA), (a)(10°, 10°) and (b)(10°, 15°)..... | 97 |
| 7.9 | Skin friction line plots for a baseline 76/40 double delta wing at (AoA, RA), (a)(20°, 10°) and (b)(20°, 20°)..... | 98 |
| 7.10 | Skin friction line plots for a 76/40° double delta wing with a diamond juncture fillet at AoA, (a)10° and (b)20° | 100 |
| 7.11 | Skin friction line plots for a 76/40° double delta wing with a diamond juncture fillet at (AoA, YA), (a)(10°, 10°) and (10°, 15°) | 100 |
| 7.12 | Skin friction line plots for a 76/40° double delta wing with a diamond juncture fillet at (AoA, RA), (a)(20°, 10°) and (b)(20°, 20°)..... | 101 |
| 7.13 | Skin friction line plots for a 76/40° double delta wing with a parabolic juncture fillet at AoA, (a)10° and (b)20° | 103 |
| 7.14 | Skin friction line plots for a 76/40° double delta wing with a parabolic juncture fillet at (AoA, YA), (a)(10°, 10°) and (b)(10°, 15°)..... | 103 |

List of Figures -- Continued

| | | |
|------|---|-----|
| 7.15 | Skin friction line plots for a 76/40° double delta wing with a diamond juncture fillet at (AoA, RA), (a)(20°, 10°) and (b)(20°, 20°)..... | 104 |
| 7.16 | Skin friction lines on a baseline 76/40° double delta wing at (AoA, YA) (a)(16°,6°) and (b)(24°,6°)..... | 106 |
| 7.17 | Magnified views of singular points on the skin friction fields of a baseline 76/40° double delta wing at (AoA, YA), (a)(16°,6°) and (b)(24°,6°) | 106 |
| 8.1 | Shenyang Aerospace University low speed wind tunnel | 116 |
| 8.2 | Rood wing mounted on an elevated flat plate in the wind tunnel test section..... | 116 |
| 8.3 | Typical GLOF images for the five regions of interest at AoA = 6°, (1)wing suction side base surface, (2)wing pressure side base surface (3)wingtipsurface (4)pressure side wing surface and (5)suction side wing surface | 120 |
| 8.4 | GLOF intensity field mapped on the surface of the wing-body junction flow model (left) and the mesh of the Rood wing model (right) at AoA = 6° | 120 |
| 8.5 | Skin friction lines mapped on the surface of the wing-body junction model viewed from (a)wing suction side and (b)wing pressure side, at AoA of 0°, where the color map indicates the luminescent intensity distribution of the oil film..... | 121 |
| 8.6 | Skin friction lines mapped on the surface of the wing-body junction model viewed from (a)wing suction side and (b)wing pressure side, at AoA of 6°, where the color map indicates the luminescent intensity distribution of the oil film..... | 122 |

List of Figures -- Continued

| | | |
|------|--|-----|
| 8.7 | Skin friction lines mapped on the surface of the wing-body junction model viewed from (a)wing suction side and (b)wing pressure side, at AoA of 12° , where the color map indicates the luminescent intensity distribution of the oil film..... | 123 |
| 8.8 | Illustration of the primary separation line and the line of low streamwise shear on the base surface of the wing-body junction model at AoA of 0° | 124 |
| 8.9 | Skin friction lines extracted from GLOF images taken from five different viewing angles and positions for AoA = 0° on (1)base surface on the suction side of the wing, (2)base surface on the pressure side of the wing, (3)wingtip surface (4)wing surface | 128 |
| 8.10 | Skin friction lines extracted from GLOF images taken from five different viewing angles and positions for AoA = 6° on (1)base surface on the suction side of the wing, (2)base surface on the pressure side of the wing, (3)wingtip surface, (4)pressure surface of the wing and (5)suction surface of the wing | 129 |
| 8.11 | Illustration of a penetrable boundary defined for the base surface of a wing-body junction flow model..... | 130 |
| 8.12 | Magnified views of skin friction lines in selected regions on the wing-body junction model at AoA of 0° as defined in Figure 8.9 for regions, (a)A and (b)B | 132 |
| 8.13 | Magnified views of skin friction lines in selected regions on the wing-body junction model at AoA of 6° as defined in Figure 8.10 for regions, (a)A, (b)B, (c)C and (d)D | 134 |
| 9.1 | Schematic of junction flow setup | 138 |
| 9.2 | Schematic of Ahmed model setup | 139 |
| 9.3 | Image of experimental setup for GLOF measurements | 140 |

List of Figures -- Continued

| | | |
|------|--|-----|
| 9.4 | Square cylinder junction flow, (a)typical luminescent oil image, (b)skin friction line plot, (c)skin friction vector plot and (d)skin friction magnitude plot | 145 |
| 9.5 | Surface pressure coefficient field with overlay of skin friction lines for the base surface of a square cylinder junction flow | 147 |
| 9.6 | High spatial resolution images of square cylinder junction flow, (a)typical luminescent oil image, (b)skin friction line plot, (c) skin friction vector plot and (d)skin friction magnitude plot..... | 148 |
| 9.7 | Conjectured flow topology of a six vortex system upstream of a square cylinder junction flow..... | 149 |
| 9.8 | Downsampled high spatial resolution images of square cylinder junction flow, (a)typical luminescent oil image, (b)skin friction line plot, (c)skin friction vector plot and (d)skin friction magnitude plot | 151 |
| 9.9 | Diamond cylinder junction flow, (a)typical luminescent oil image, (b)skin friction line plot, (c)skin friction vector plot and (d)skin friction magnitude plot | 152 |
| 9.10 | Surface pressure coefficient field with overlay of skin friction lines for the base surface of a diamond cylinder junction flow | 153 |
| 9.11 | Zoomed in views identifying singular points and boundary switch points for the region (a)upstream of the square cylinder junction flow base surface and (b)immediately behind the square cylinder junction flow base surface | 155 |
| 9.12 | Zoomed in view identifying singular points and boundary switch points for the region immediately behind the diamond cylinder junction flow base surface | 156 |

List of Figures -- Continued

| | | |
|------|---|-----|
| 9.13 | Top surface of an Ahmed model at 0° sideslip, (a)typical luminescent oil image, (b)skin friction line plot, (c)skin friction vector plot and (d)skin friction magnitude plot with an overlay of skin friction lines | 158 |
| 9.14 | Surface pressure coefficient (C_p) field of the top surface of an Ahmed model at 0° sideslip | 158 |
| 9.15 | Top surface of an Ahmed model at 20° sideslip, (a)skin friction line plot and (b)skin friction magnitude plot with an overlay of skin friction lines | 159 |
| 9.16 | Surface pressure coefficient (C_p) field of the top surface of an Ahmed model at 20° sideslip | 160 |
| 9.17 | Leeward side surface of an Ahmed model at 0° sideslip, (a)skin friction line plot, and (b)skin friction magnitude plot with an overlay of skin friction lines | 161 |
| 9.18 | Surface pressure coefficient (C_p) field of the leeward side surface of an Ahmed model at 0° sideslip | 161 |
| 9.19 | Leeward side surface of an Ahmed model at 20° sideslip, (a)skin friction line plot, and (b)skin friction magnitude plot with an overlay of skin friction lines | 162 |
| 9.20 | Surface pressure coefficient (C_p) field of the leeward side surface of an Ahmed model at 0° sideslip | 162 |
| 10.1 | Surface, object space and image coordinates | 168 |
| 10.2 | Illustrations of the (a)experimental setup for TSP measurements for an impinging jet and (b)wall jet and impingement regions and the coordinate system for the test setup | 177 |

List of Figures -- Continued

| | | |
|-------|---|-----|
| 10.3 | Plots of (a)the time averaged surface temperature field and (b)normalized skin friction vector and magnitude fields for a normal impinging jet at H/D of 6..... | 180 |
| 10.4 | Skin friction magnitude distribution normalized by the maximum value along the x-axis for a normal impinging jet | 182 |
| 10.5 | Plots of (a)normalized maximum skin friction magnitude and (b)position of the peak skin friction as a function of H/D in a normal impinging jet | 184 |
| 10.6 | Plots of (a)time averaged surface temperature field and (b)normalized skin friction vector and magnitude fields for an oblique impinging jet at an impingement angle of 75° | 185 |
| 10.7 | Skin friction magnitude distribution normalized by the maximum value along the x-axis in an oblique impinging jet at an impingement angle of 75°..... | 186 |
| 10.8 | Plots of (a)time averaged surface temperature field and (b)normalized skin friction vector and magnitude fields for an oblique impinging jet at an impingement angle of 45° | 188 |
| 10.9 | Skin friction magnitude distribution normalized by the maximum value along the x-axis in an oblique impinging jet at an impingement angle of 45°..... | 188 |
| 10.10 | Plots of (a)time averaged surface temperature field and (b)normalized skin friction vector and magnitude fields for an oblique impinging jet at an impingement angle of 30° | 189 |
| 10.11 | Skin friction magnitude distribution normalized by the maximum value along the x-axis in an oblique impinging jet at an impingement angle of 30°..... | 190 |

List of Figures -- Continued

| | | |
|-------|---|-----|
| 10.12 | Plots of the normalized skin friction distributions along the x-axis in the normal impinging jet looking at (a)effect of the Lagrange multiplier for an initial std of 18 pixels for the Gaussian filter and (b)effect of the initial std of the Gaussian filter for α of 0.006..... | 192 |
| 11.1 | Surface, object space and image coordinates | 200 |
| 11.2 | Experimental setup schematic for PSP visualizations for an impinging nitrogen jet..... | 211 |
| 11.3 | Plots of (a)PSP intensity ratio and (b)normalized skin friction vector and magnitude fields for a normal impinging jet | 213 |
| 11.4 | Skin friction magnitude distribution normalized by the maximum value along the x-axis for a normal impinging jet | 214 |
| 11.5 | Effect of the Lagrange multiplier on the extracted skin friction magnitude distribution for a normal impinging jet | 215 |
| 11.6 | Relative difference between the extracted skin friction value and hot-film data as a function of the Lagrange multiplier for a normal impinging jet..... | 215 |
| 11.7 | Plots of (a)PSP intensity ratio and (b)normalized skin friction vector and magnitude fields for an oblique impinging jet at an impingement angle of 75° | 217 |
| 11.8 | Skin friction magnitude distribution normalized by the maximum value along the x-axis in an oblique impinging jet at the impingement angle of 75° | 217 |
| 11.9 | Experimental setup schematic for dual colliding impinging jets (a)side view and (b)top view | 218 |

List of Figures -- Continued

| | | |
|-------|--|-----|
| 11.10 | PSP intensity ratio images for dual colliding impinging jets at offsets of (a)0 mm, (b)4 mm, (c)7.5 mm and (d)11.5 mm | 220 |
| 11.11 | Plots of skin friction vectors and normalized magnitude fields for dual colliding impinging jets at offsets of (a)0 mm, (b)4 mm, (c)7.5 mm and (d)11.5 mm..... | 221 |
| 11.12 | Plots of skin friction lines for dual colliding impinging jets at offsets of (a)0 mm, (b)4 mm, (c)7.5 mm and (d)11.5 mm | 222 |
| 11.13 | Normalized PSP intensity images for a 9.4-kHz oscillating impinging jet from a microfluidic oscillator at (a)0 μ s, (b)20 μ s and (c)40 μ s [159]..... | 224 |
| 11.14 | Solutions for (a) the snapshot field and (b) variation field in a 9.4-kHz oscillating impinging jet from a microfluidic oscillator at 0 μ s. | 225 |
| 11.15 | Plots of extracted skin friction vector and normalized magnitude fields in a 9.4-kHz oscillating impinging jet from a microfluidic oscillator at (a)0 μ s, (b)20 μ s and (c)40 μ s..... | 226 |
| 11.16 | Plots of (a)sublimation image and (b)extracted skin friction vector and magnitude fields on the upper surface of a 75° delta wing at an angle of attack of 32° [152] | 227 |
| 11.17 | Skin friction line plot of the upper surface of a 75° delta wing at an angle of attack of 32° [152] | 228 |
| 11.18 | Plots of (a)sublimation image and (b)extracted skin friction vector and magnitude fields on a flat plate in shock/boundary-layer interaction over a vertically-mounted triangular fin at an angle of attack of 40° at Mach 6 (flow from left to right) [160] | 230 |

List of Figures -- Continued

| | | |
|-------|---|-----|
| 11.19 | Skin friction lines extracted from the sublimation image on a flat plate in shock/boundary-layer interaction over a vertically-mounted triangular fin at an angle of attack of 40° at Mach 6 (flow from left to right) [160] | 230 |
|-------|---|-----|

CHAPTER 1

INTRODUCTION

In the discipline of fluid mechanics, pressure, temperature, velocity and shear stress are important parameters. In flow measurements and visualization, it is desirable to have non-intrusive flow measurement techniques to ensure that the flow is not perturbed by any probe or sensor. Non-intrusive, global measurement systems are readily available for pressure, temperature and velocity but not for wall shear stress i.e. skin friction.

Skin friction is one of the most important surface parameters in the discipline of fluid mechanics and aerodynamics as it characterizes the interaction between the fluid and the surface with which it interacts. It is also the most difficult parameter to measure since it is a function of the velocity gradient as given by Equation 1.1, where τ, μ and $\partial u / \partial y$ represent the shear stress, dynamic viscosity of the fluid and velocity gradient, respectively. When Equation 1.1 is evaluated at the wall boundary ($y=0$), skin friction is obtained.

$$\tau(y) = \mu \frac{\partial u}{\partial y} \quad (1.1)$$

A variety of skin friction measurement techniques have been developed over the years [1-21]. They can be divided into two major approaches; point-based techniques such as the Preston tube, Stanton tube, microbalance systems, optical microelectromechanical systems (MEMS) based gages and oil film interferometry which

measure skin friction at a limited number of points or regions on a surface and recently developed global approaches such as shear sensitive liquid crystals and the surface stress sensitive film technique which are able to measure skin friction fields on a surface.

On the other hand, numerical simulations using Computational Fluid Dynamics (CFD) suffer from accuracy issues as discussed by Anderson [2] in his brief review on the accuracy of numerical simulations in predicting skin friction. Three major factors were noted to affect the capability of simulations in predicting skin friction. The first is the requirement for a very fine mesh sizing near the wall to enable the accurate prediction of the velocity gradient. Next is the uncertainty in the accuracy of the turbulence models in computing turbulent flows and finally, the inability of turbulence models in predicting laminar to turbulent transition. It has been documented that the average accuracy of skin friction predictions from CFD is between 18 to 40 percent depending on the solver and turbulence model utilized [2].

The ability to quantitatively measure skin friction on a global scale (infinite number of points limited by optical resolution) is a highly desirable capability enabling fundamental surface flow characterization. This capability will provide a powerful tool for the characterization of classic separated flows such as junction flows and flow over delta wings. It will also have an enormous impact from a design perspective in the aerospace and automotive industry as it will allow the optimization of air and ground based vehicles by understanding the fundamental surface flow characteristics using a global skin friction measurement approach. This will allow the design refinement of these vehicles in reducing drag, enhancing lift and increasing efficiency.

1.1 Skin Friction Measurement Techniques

As discussed earlier, classical and modern skin friction measurement techniques can be divided into two categories – point and global techniques which measure skin friction at a limited number of discrete points and global fields respectively. These measurement techniques can be further classified into two methods – direct and indirect. Indirect methods utilize an empirical or theoretical correlation to measure skin friction and have a limited range of application due to the assumptions in the correlations used. Some examples of indirect methods are the Preston tube, Stanton tube and thermal sensors. Direct methods on the other hand, do not require any empirical or theoretical correlation as the quantity measured responds directly to skin friction. Liquid crystals, MEMS based direct sensors and oil film techniques are some popular examples of the direct method.

1.1.1 Point Techniques

Point skin friction measurement techniques can be divided into a few categories – velocity based techniques and thermal sensors which are indirect approaches and MEMS based direct sensors and oil film interferometry which are direct and quasi-direct approaches, respectively. The first reported skin friction measurement was by Stanton et al. [1], who attempted to determine the fluid velocity close to a boundary to investigate the slip condition at a wall for a turbulent flow. This was accomplished by a rectangular shaped Pitot tube with the wall as one of its sides. The pressure difference measured by this Pitot tube and the static pressure was then used to determine the velocity at the midpoint of the Pitot tube. In systematic experiments in fully developed laminar flow, Stanton discovered that the relationship between the measured pressure difference and

the velocity was not governed by the equation for a Pitot tube in free flow. A calibration curve was then produced for the effective center point of the instrument referred to as a Stanton tube. Systematic experiments were conducted in a fully developed turbulent flow using the Stanton tube and it was demonstrated that for a turbulent flow, the time averaged velocity variation close to a wall is given by Equation 1.2 which defines skin friction as a function of velocity. Velocity is obtained from the pressure measurement using the Stanton tube with its effective center located close enough to the wall.

$$\bar{U} = \frac{\tau_w}{\mu} y, \quad (1.2)$$

A subsequent development to the Stanton tube is the Preston tube which was developed by Preston. The Preston tube utilized a conventional Pitot tube in contrast to a Stanton tube which is complicated to manufacture. Preston argued that the velocity variation close to the wall for a given fluid does not depend on the geometry or previous history of the system and is solely a function of the local wall shear stress. The theoretical foundation for Preston's approach in utilizing the Preston tube in turbulent flows is the assumption that the velocity variation close to the wall is valid across a larger range than the range of validity for Equation 1.2 which then allows for larger Pitot tubes to measure wall shear stress. This would simplify the process of instrumentation setup compared to the Stanton tube which is complicated to fabricate. The Stanton tube and Preston tube are both illustrated in Figure 1.1.

With the advancements in the field of micro and nano technology, the fabrication of micro and nano sensors, actuators and systems have become mainstream and well established. From the perspective of skin friction measurements, micro or nano scale sensors are desirable when considering sensor spatial and temporal resolution as well as

physical packaging. These devices are able to perform at high frequency responses (kHz range) and are small enough to satisfy spatial resolution requirements as well as being easily integrated to the surface being measured without being intrusive to the flow. MEMS based measurement techniques have been reviewed extensively [1]. The hot film sensor is a MEMS based thermal sensor which operates on the relationship between skin friction and surface heat flux given by the Reynolds analogy as described by Equation 1.3 below

$$\dot{q} \approx \frac{\tau_w c_p (T_w - T_\infty)}{V_\infty} \quad (1.3)$$

where \dot{q} , τ_w , c_p , T_w , T_∞ and V_∞ are surface heat flux, skin friction, heat capacity of the fluid, wall temperature, ambient temperature of the fluid and freestream velocity. The implication of Equation 1.3 is that skin friction can be determined by measuring heat flux. The relationship between local skin friction and surface heat flux from a small heated element has been derived by Lighthill [16], and further heat transfer analysis of a heated element on a wall in a boundary layer is given by Liu et al. [17] and Gelderblom et al. [18]. This relationship also provides a theoretical foundation for the flush-mounted hot-film/hot-wire skin friction sensor developed by Liepmann and Skinner [19]. Currently, hot-film skin friction sensors have become a mature technique for skin friction measurements at discrete locations. The principle of a hot-film sensor is also the basis of MEMS skin friction sensors that are primarily miniaturized versions of hot-film/hot-wire sensors [20]. The Stanton tube, Preston tube and hot film sensor are all indirect skin friction measurement approaches which utilize a correlation based approach to measure skin friction. They are illustrated in Figure 1.1 below.

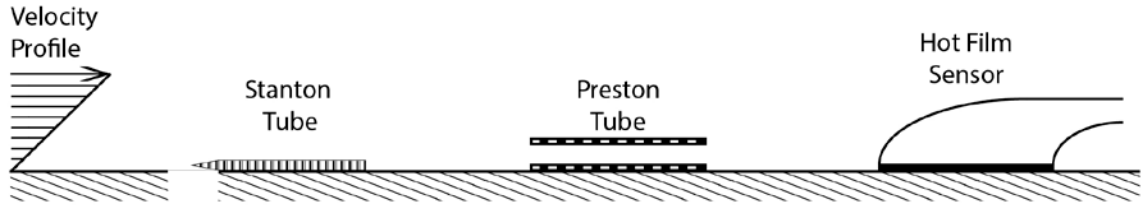


Figure 1.1 Indirect point measurement methods (from left to right) : Stanton tube, Preston tube, hot film sensor

Another MEMS based approach is the direct sensor which reacts directly to skin friction in the form of a displacement in the sensing device. This is a direct technique in which the measured quantity i.e. displacement, responds directly to skin friction. Several different versions of the direct sensor such as the floating element sensor, differential capacitive sensor, axial piezoresistive sensor and the force-feedback electrostatic comb-finger sensor have been successfully demonstrated in measuring skin friction. The major differences in the various direct sensing approaches can be attributed to the different techniques of sensing displacement related to skin friction. Besides the spatial and temporal resolution advantages of MEMS based sensors, direct MEMS sensors have negligible alignment errors as the device is fabricated monolithically using established MEMS fabrication techniques instead of being assembled from individual components. Flow perturbation due to the gap between the sensing element and the wall is also reduced with this sensor. This gap is usually on the order of a few microns which is typically smaller than a few viscous length scales. Errors due to pressure gradients are also favorably small for the direct MEMS sensor, on the order of 0.001% for a typical sensor [20].

The oil film skin friction meter, invented by Tanner and Blows [11], is based on detecting the temporal-spatial evolution of the thickness of a thin oil film to determine skin friction. Laser and image based interferometers [11-15] have been used to measure

the thickness of a thin oil film at a particular location. The governing equation, which describes the response of a thin oil film on a surface $X_3 = S(X_1, X_2)$ to the externally applied three dimensional aerodynamic flow is given in a form of the summation convention [20, 22]

$$\frac{\partial h}{\partial t} + \frac{\partial}{\partial X_i} \left[\frac{\tau_i h^2}{2\mu} - \left(\frac{\partial p}{\partial X_i} - \rho g_i \right) \frac{h^3}{3\mu} \right] = 0, \quad (i = 1, 2) \quad (1.4)$$

where h is the oil film thickness, $\boldsymbol{\tau} = (\tau_1, \tau_2)$ is the skin friction vector, p is the pressure gradient, μ is the oil viscosity, ρ is the oil density, and (g_1, g_2) is the gravity vector. In the simplest case where skin friction is constant and the effects of pressure gradient and gravity are neglected, skin friction along a skin friction line is given by [12, 20]

$$\tau_s = -\frac{\mu}{h} \frac{\partial h}{\partial t} \bigg/ \frac{\partial h}{\partial s}, \quad (1.5)$$

where s is the coordinate along a skin friction line. Equation 1.5 is a self-similar solution that is valid locally when skin friction is approximately constant in a small area. Interferometric oil film meters utilize Equation 1.4 and its equivalent or extended forms to obtain the local skin friction magnitudes from the evolution of oil droplets distributed on a surface, which makes it a quasi-direct, point measurement approach. Brown and Naughton [15] have made attempts to recover a global skin friction field as an inverse problem by solving the thin oil film equation. However, a single equation for the oil film thickness is not sufficient in determining the two unknown components of skin friction; therefore the direction of skin friction is required to solve the equation for the skin friction magnitude. The MEMS mechanical sensor and oil film interferometry are two direct skin friction point measurement techniques illustrated below.

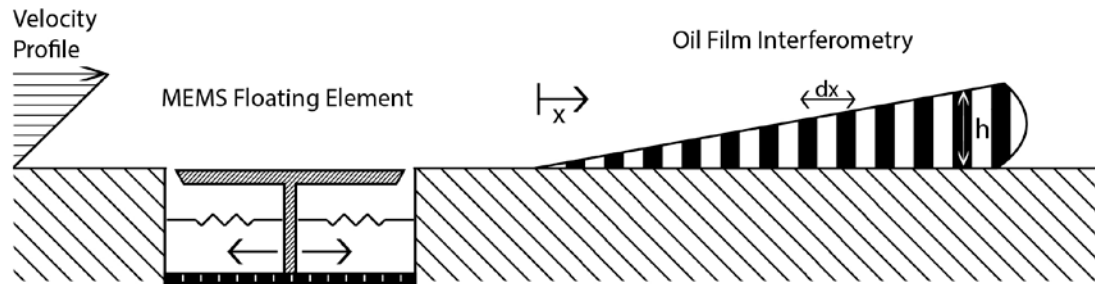


Figure 1.2 Direct measurement methods (from left to right) : MEMS floating element, oil film interferometry

1.1.2 Global Techniques

Candidate techniques for global skin friction measurements are shear-sensitive liquid crystals (SSLC) and surface stress sensitive film (S3F). These techniques are considered direct or semi direct because the quantity detected responds directly to skin friction.

Shear sensitive liquid crystals (SSLC) for quantitative skin friction measurements has been developed extensively by Reda [6-8]. The observed quantities in SSLC are transient color changes that result from the change in the pitch of the helix of the cholesteric structure of SSLC caused by the change in mechanical stress. For fluid mechanics applications, the liquid crystals are mixed with a solvent such as Freon at a ratio of 1 part liquid crystal to 9 parts solvent. The mixture is then sprayed onto the surface being studied which is required to be a smooth, flat black surface for color contrast. Once the solvent evaporates, a uniform thin film of liquid crystals is formed allowing the surface to be studied. Once the shear condition is applied to the surface, the liquid crystal coating causes different color-play response based on magnitude and direction of the shear stress. Data analysis using color as a parameter to measure both magnitude and direction of a skin friction vector is a complex procedure for reliable quantitative measurements. The strong dependency on reflection for the illumination

direction and viewing angle of a camera poses a challenge for universal system calibration. Although SSLC has successfully been used for global skin friction measurements for an impinging jet, the complex calibration procedures prevent SSLC from being used routinely in wind tunnel testing or fluid mechanics experiments.

Surface stress sensitive film (S3F) is a relatively new approach for global skin friction measurements. This technique combines a particle image velocimetry (PIV) based correlation technique and fluorescence for measuring the deformation field of a specific polymeric film in flow [9, 10]. The polymeric film is seeded with tracer particles and doped with luminescent molecules. Skin friction and pressure are simultaneously determined from tangential and normal components of deformation based on a particular system model. A cavity on the model or a flexible layer that can be attached onto the model is required to form a polymeric film with good control of film thickness. This requirement limits the application of S3F in conditions where modification of a model is not permitted. The capability of S3F has been demonstrated in several flows ranging from low-pressure turbine blades to delta wings to measure the complicated topological structures of skin friction fields. Due to the special requirements of adapting S3F to a test model, it remains to be seen if S3F can be used as a convenient technique for wind tunnel testing or fluid mechanics experiments.

These techniques, while fulfilling the role as global skin friction measurement tools are complicated to use, from a calibration or experimental implementation standpoint, therefore it is desirable for a simple, easily implemented global skin friction measurement approach to be developed.

CHAPTER 2

GLOBAL LUMINESCENT OIL FILM SKIN FRICTION METER

Liu and Sullivan [22] originally proposed a luminescent oil film skin friction meter that utilizes luminescence instead of the traditional interferometry approach [15] to measure oil film thickness. A global extension of the luminescent oil film (GLOF) skin friction meter has recently been introduced by Liu et al. [27] which presents two critical steps in the development of the technique – measuring oil film thickness and projecting the thin oil film equation onto the image plane. For a luminescent oil film, luminescent intensity is proportional to the oil film thickness. The measurement of thickness by luminescent intensity is simpler and more robust compared to interferometry measurements. The thin oil film equation is projected onto the image plane to describe the relationship between skin friction and temporal and spatial derivatives of image intensity. To solve the projected thin oil film equation, a variational formulation is introduced with a regularization term for the smoothness of a skin friction field. The corresponding functional is minimized and the resulting Euler-Lagrange equations are solved numerically imposing the Neumann condition for a snapshot solution of a skin friction field. A complete relative skin friction field is reconstructed through fusion of snapshot solutions. Through in-situ calibration, absolute skin friction fields can be obtained using values given by a reliable point based skin friction measurement method at one or several locations.

2.1 Theory

For an optically thin luminescent oil film on a surface, the luminescent emission intensity (radiance, I) under excitation is proportional to the oil film thickness, i.e., [22]

$$I(X_1, X_2) = a I_{ex}(X_1, X_2) h(X_1, X_2), \quad (2.1)$$

where (X_1, X_2) are the spatial coordinates on the surface, $I_{ex}(X_1, X_2)$ is the intensity of the excitation light on the surface, a is the coefficient proportional to the quantum efficiency of the seeded luminescent molecules and dye concentration and h is the oil film thickness. Substituting Equation 2.1 into Equation 1.3 yields

$$\frac{\partial}{\partial t} \left(\frac{I}{I_{ex}} \right) + \frac{\partial}{\partial X_i} \left[\frac{\tau_i}{2\mu a} \left(\frac{I}{I_{ex}} \right)^2 - \left(\frac{\partial p}{\partial X_i} - \rho g_i \right) \frac{I}{3\mu a^2} \left(\frac{I}{I_{ex}} \right)^3 \right] = 0. \quad (i = 1, 2) \quad (2.2)$$

One-to-one mapping exists between the image plane (x_1, x_2) and the surface $X_3 = S(X_1, X_2)$ [20]. When the image plane of a camera is parallel to the flat surface area to be measured, the perspective projection transformation is simple. In this case, $\partial/\partial X_i = \lambda \partial/\partial x_i$, where the scaling factor λ is considered a constant. For a highly curved surface, λ cannot be treated as a constant, requiring an intricate transformation. Figure 2.1 illustrates a special object-space coordinate system $(\bar{X}_1, \bar{X}_2, \bar{X}_3)$, in which the plane (\bar{X}_1, \bar{X}_2) is parallel to the image plane (x_1, x_2) . Therefore, a relation between (\bar{X}_1, \bar{X}_2) and (x_1, x_2) is $\partial/\partial \bar{X}_i = \lambda \partial/\partial x_i$, where λ is a scaling constant. An image on a camera is the scaled projection of the surface onto the plane (\bar{X}_1, \bar{X}_2) . If the transformation between (\bar{X}_1, \bar{X}_2) and (X_1, X_2) is given by $\bar{X}_1 = F_1(X_1, X_2)$ and

$\bar{X}_2 = F_2(X_1, X_2)$, then $\partial/\partial X_i = h_{ji} \partial/\partial \bar{X}_j = \lambda h_{ji} \partial/\partial x_j$, where $h_{ji} = \partial F_j/\partial X_i$ which is dependent on the geometric properties of the surface.

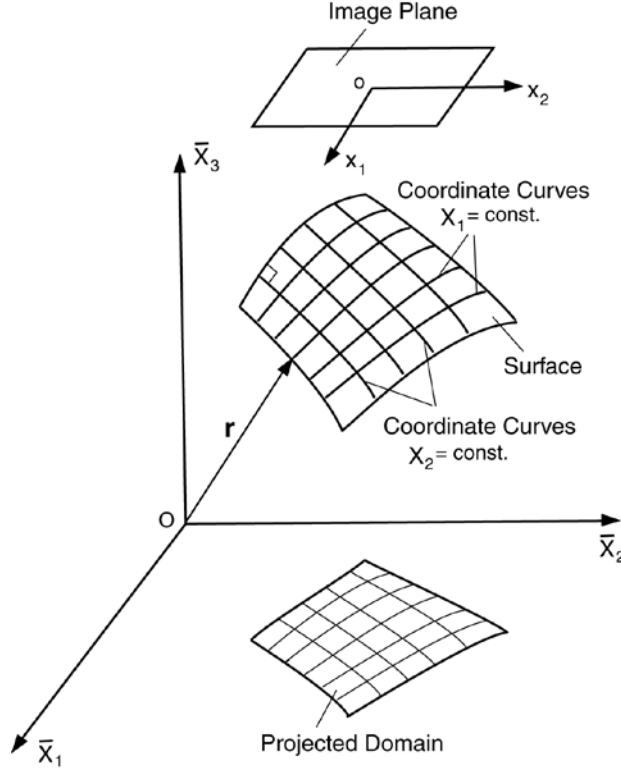


Figure 2.1 Surface, object-space and image coordinates

By introducing the normalized luminescent intensity $g = I/I_{ex}$ and the equivalent skin friction $\bar{\tau} = \tau g (\lambda/2\mu a)$, Equation 2.2 can be expressed in the image coordinates

$$\partial g / \partial t + \nabla \cdot (g \bar{\tau}) = f(x_1, x_2, g) \quad (2.3)$$

where $\nabla = \partial/\partial x_i$ is the gradient operator in the image plane, and the effects of the pressure gradient and gravity are described by

$$f(x_1, x_2, g) = \lambda \frac{\partial}{\partial x_i} \left[\left(\lambda \frac{\partial p}{\partial x_i} - \rho g_i \right) \frac{g^3}{3\mu a^2} \right]. \quad (i = 1, 2) \quad (2.4)$$

where the measured quantity g is mapped onto the image plane. Equation 2.3 is the projected thin oil film equation for a luminescent oil film. When the radiometric response function of a camera is linear, g is the normalized gray level of the image.

To determine the equivalent skin friction field $\bar{\tau} = (\bar{\tau}_1, \bar{\tau}_2)$, a variational formulation is given with a regularization term based on the L^2 norm of the skin friction gradient as proposed by Horn and Schunck [24] for computing optical flow. The smoothness constraint ensures that the equivalent skin friction field is locally continuous in all directions. A functional with the Horn-Schunck regularization term is defined on an image domain

$$J(\bar{\tau}) = \int_{\Omega} (\partial g / \partial t + \nabla \cdot (g \bar{\tau}) - f)^2 dx_1 dx_2 + \alpha \int_{\Omega} (|\nabla \bar{\tau}_1|^2 + |\nabla \bar{\tau}_2|^2) dx_1 dx_2. \quad (2.5)$$

where α is the Lagrange multiplier. The Euler-Lagrange equations for Equation 2.5 are

$$g \frac{\partial}{\partial x_1} \left[\frac{\partial g}{\partial t} + \nabla \cdot (g \bar{\tau}) - f \right] + \alpha \nabla^2 \bar{\tau}_1 = 0, \quad g \frac{\partial}{\partial x_2} \left[\frac{\partial g}{\partial t} + \nabla \cdot (g \bar{\tau}) - f \right] + \alpha \nabla^2 \bar{\tau}_2 = 0 \quad (2.6)$$

where the Neumann condition $\partial \bar{\tau} / \partial n = 0$ is imposed on the domain boundary $\partial \Omega$. The numerical solution to Equation 2.6 is described by Liu et al. [27].

Solving Equation 2.6 for two consecutive images gives a snapshot solution for a skin friction field, for a short time step in a relatively long process of oil film development. In general, the snapshot solutions differ in magnitude and shape depending on the process of oil film development because of the existence of a spectrum of time and spatial scales that characterize the oil film development in different regions on the surface. A snapshot solution captures the prominent skin friction signatures in the regions where the oil film development is most sensitive to the flow at that particular instant. To capture the major skin friction signatures in different regions at different

instances in the process of oil film development, a sequence of snapshot solutions is required. A complete skin friction field is then reconstructed through the fusion of snapshot solutions. Liu et al. [27] have proposed a direct superposition method as well as a wavelet based method for fusing successive snapshot solutions. Both approaches have been shown to be equivalent in reconstructing a complete relative skin friction field.

Without calibration, skin friction fields obtained using this approach are relative or normalized. To determine the proportional constant in the relative skin friction field, in-situ calibration is performed using accurate values of skin friction at one or several locations. This is performed utilizing a reliable point based skin friction measurement technique which subsequently allows for a global, absolute skin friction fields to be obtained. This work presents the relative skin friction field ($\bar{\tau} / g$) or the normalized skin friction field. A detailed description of the GLOF technique is presented by Liu et al. [27]. The technique was validated by applying it to a simulated Oseen vortex pair and uniform flow, an oblique impinging jet compared with hot-film measurements, and a NACA 2412 airfoil compared with CFD simulations.

2.2 Uncertainty Analysis

At this stage, it is essential to evaluate the sensitivity of calculation of skin friction to the elemental errors. The decompositions, $g = g_0 + \delta g$ and $\tilde{\tau} = \tilde{\tau}_0 + \delta \tilde{\tau}$ are introduced, where δg and $\delta \tilde{\tau}$ are errors, and g_0 and $\tilde{\tau}_0$ are the non-perturbed fields satisfying the Euler-Lagrange equations, Equation 2.6. Substituting the above decompositions into Equation 2.6 and neglecting the higher-order smaller terms leads to an error propagation equation, given by

$$(\delta\tilde{\boldsymbol{\tau}} \cdot \nabla g_0) \nabla g_0 - \alpha \nabla^2 \delta\tilde{\boldsymbol{\tau}} = - \left(\frac{\partial}{\partial t} (\delta g) + \tilde{\boldsymbol{\tau}}_0 \cdot \nabla \delta g \right) \nabla g_0, \quad (2.7)$$

where the first δg term contributes to $\delta\tilde{\boldsymbol{\tau}}$ through a time operator while the second δg term contributes to $\delta\tilde{\boldsymbol{\tau}}$ through a gradient operator projected on the skin friction vector.

To simplify the analysis, a local region is considered where ∇g_0 is a constant vector (this is always a reasonable linear approximation locally), and define $\|\nabla g_0\|$ as the magnitude of ∇g_0 . Thus, the unit normal vector to an iso-value line $g_0 = \text{const.}$ is $\mathbf{N}_T = \nabla g_0 / \|\nabla g_0\|$. The error of skin friction projected on \mathbf{N}_T is defined as

$(\delta\hat{\boldsymbol{\tau}})_N = \delta\hat{\boldsymbol{\tau}} \cdot \mathbf{N}_T$. Normalization of Equation 2.7 yields the relative error estimate

$$\frac{(\delta\tilde{\boldsymbol{\tau}})_N}{\|\tilde{\boldsymbol{\tau}}_0\|} = - \frac{\partial \left(\frac{\delta g}{\partial t} \right)}{\|\nabla g_0\| \|\tilde{\boldsymbol{\tau}}_0\|} - \left(\frac{\tilde{\boldsymbol{\tau}}_0}{\|\tilde{\boldsymbol{\tau}}_0\|} \right) \cdot \delta \mathbf{N}_T + \frac{\alpha}{\|\nabla g_0\|^2} \nabla^2 \left[\frac{(\delta\tilde{\boldsymbol{\tau}})_N}{\|\tilde{\boldsymbol{\tau}}_0\|} \right] \quad (2.8)$$

where $\|\tilde{\boldsymbol{\tau}}_0\|$ is a characteristic value of skin friction such as the mean value. In the derivation of Equation 2.8, it is assumed that ∇ and δ can be exchanged. The first term in the right-hand side (RHS) of Equation 2.8 is the contribution from the elemental error in measurement of the time rate of the intensity gradient. The second term is the contribution from the elemental error in measurement of the intensity gradient. The third term is the contribution from the artificial diffusion of the error $(\delta\tilde{\boldsymbol{\tau}})_N$ associated with the Lagrange multiplier. Equation 2.8 can be solved iteratively for $(\delta\tilde{\boldsymbol{\tau}})_N / \|\tilde{\boldsymbol{\tau}}_0\|$. The first two terms in the RHS of Equation 2.8 are used as an initial approximation of $(\delta\tilde{\boldsymbol{\tau}})_N / \|\tilde{\boldsymbol{\tau}}_0\|$, and then it is substituted into the third term to estimate the diffusion term in the first-order approximation. By iterating, successive approximations can be obtained.

The first and third terms in the RHS of Equation 2.8 are inversely proportional to $\|\nabla g_o\|$ and its square, respectively. This indicates that the error $(\delta\tilde{\tau})_N / \|\tilde{\tau}_o\|$ will be very large when $\|\nabla g_o\|$ approaches zero. This imposes an intrinsic limitation on application of this technique in certain local regions where $\|\nabla g_o\|$ is close to zero. The proportional constant in the third term is $\alpha \|\nabla g_o\|^{-2}$. Therefore, the Lagrange multiplier must be sufficiently small to reduce the error $(\delta\tilde{\tau})_N / \|\tilde{\tau}_o\|$ particularly when $\|\nabla g_o\|$ is small.

2.3 Effect of Thin Oil Film on Flow Characteristics

The GLOF technique has proven to be a powerful tool in performing quantitative global skin friction diagnostics in complex three dimensional separated flows such as junction flows, low aspect ratio airfoils and delta wings as highlighted in published literature [27-28, 57]. At this juncture, it is important to understand the effects of a thin oil film on the surface of a model in air flow. The question to pose is whether its presence causes interference to the flow and alters important flow features such as separation and reattachment lines. A study was conducted by Zheng [59] on the reliability of surface oil flow diagnostics for quantitative flow diagnostics. Equation 2.9 is introduced to represent the differential form of the momentum equation for the thin oil film along with a few assumptions 2.9(a) and (b). The assumptions are that on the wall, the oil is at rest and at the air-oil interface, the velocity of the air and oil along with the viscous stresses are equal.

$$\frac{\partial \mathbf{u}_{oil}}{\partial t} + \frac{1}{\rho_{oil}} \frac{\partial P}{\partial x} = \frac{\mu_{oil}}{\rho_{oil}} \left(\frac{\partial^2 \mathbf{u}_{oil}}{\partial x^2} + \frac{\partial^2 \mathbf{u}_{oil}}{\partial y^2} \right) \quad (2.9)$$

Assumptions : At y = h

$$u_{oil} = u_{air}, \tau_{oil} = \tau_{air}, \mu_{oil} \frac{\partial u_{oil}}{\partial y} = \mu_{air} \frac{\partial u_{air}}{\partial y} \quad (2.9 (a))$$

At y = 0

$$u_{oil} = 0 \quad (2.9(b))$$

Equation 2.10 describes the velocity of the oil at the air-oil interface. It is a result of solving Equation 2.9 with the assumptions 2.9(a) and (b).

$$u_{oil(y=h)} = \frac{\mu_{air}}{\mu_{oil}} \left[-\frac{h^2}{2} \left(\frac{1}{\mu_{air}} \frac{\partial P}{\partial x} \right) + h \left(\frac{\partial u_{air}}{\partial y} \right)_{(y=h)} \right] \quad (2.10)$$

The wall streamlines of the flow are defined in Equations 2.11 (a) and (b) which describe the wall streamlines with and without oil, respectively.

$$\left(\frac{\partial x}{\partial z} \right)_{air} = \left(\frac{u_{air}}{w_{air}} \right)_{y=0} = \frac{(\partial u_{air} / \partial y)_{y=0}}{(\partial w_{air} / \partial y)_{y=0}} \quad (2.11(a))$$

$$\left(\frac{\partial x}{\partial z} \right)_{oil} = \frac{(\partial u_{air} / \partial y)_{y=0} + \frac{\partial P}{\partial x} \left(\frac{y}{2} - h \right)}{(\partial w_{air} / \partial y)_{y=0} + \frac{\partial P}{\partial z} \left(\frac{y}{2} - h \right)} \quad (2.11(b))$$

From Equation 2.10 we can deduce that, the velocity of the oil at the air-oil interface ($y=h$), is typically small. This is due to the contribution of a few terms, the viscosity ratio, oil film thickness and streamwise pressure gradient. The viscosity ratio of air to oil is typically in the range of 10^{-2} to 10^{-4} and oil film thickness is on the order of 10^{-3} to 10^{-4} m. The streamwise pressure gradient is typically small except in separation or reattachment regions. In most typical cases, taking into account the three terms discussed, the oil velocity at the air oil interface is small ($u_{oil,h}/u_{\infty} < 1\%$). This implies that the boundary conditions near the wall do not differ drastically compared to when no oil is present which indicates that the oil film will not destabilize the flow.

The largest potential negative effect of the presence of the oil film is from the streamwise pressure gradient, especially close to location of separation as highlighted by Equations 2.10 and 2.11(b). Zheng performed a statistical analysis on pressure gradient measurements. It was found that at subsonic and transonic speeds, the measured pressure gradient was in the range of $10^2 - 10^4$ Pascal/m. Using an oil viscosity of 10 centistokes at a thickness of 100 microns, the velocity of the oil at the oil-air interface is a few orders of magnitude lower than the freestream velocity which implies that the oil film will not destabilize the flow and can be applied reliably as a quantitative flow diagnostic technique.

At higher transonic and supersonic speeds, it was found that the streamwise pressure gradients ranged between $10^6 - 10^9$ Pascal/m. These ranges of pressure gradients will not significantly affect the oil velocity at the air-oil interface but will cause a change of stream line directions near the separation location. These adverse pressure gradients occur within a range of 0.05 to 0.1 chord lengths which leads to a change of separation location from the leading edge of not more than 2% due to the presence of the oil film. Realistically, this level of accuracy is tolerable for quantitative flow diagnostics.

Zheng's work has provided useful insight into the use of a thin oil film for global skin friction diagnostics. The flows of interest in this study are low speed flows with relatively low streamwise pressure gradients. This coupled with a well applied oil film in the range of 20 – 40 microns allows for reliable quantitative global skin friction diagnostics without the thin oil film affecting the inherent flow characteristics.

2.4 Measurement System

The luminescent oil used consists of silicone oil doped with a luminescent dye. Luminescent oil is prepared by mixing a small amount of a petroleum based Ultraviolet (UV) dye, DFSB-K175 manufactured by Risk Reactor with silicone oil manufactured by Clearco Fluids (Dow Corning 200 equivalent). The selection of oil viscosity was based on providing a reasonable rate of oil film development for a specific test case. Oil viscosities of between 50 to 200 centistokes were used. The luminescent oil emits radiation at a longer wavelength due to the Stokes shift when illuminated by an excitation source such as a UV lamp or LED array.

Experiments were conducted at the Applied Aerodynamics Laboratory at Western Michigan University. Measurements for the low aspect ratio ($AR = 1.2$) wing, 65° delta wing and $76/40^\circ$ double delta wing were conducted in the Small Wind Tunnel (SWT) facility which is a low speed wind tunnel with a test section of 0.41 by 0.41 meters with a turbulence intensity of approximately 0.2%. Measurements for the square cylinder junction flow was conducted in the Advanced Design Wind Tunnel (ADWT) facility that is a low speed, closed circuit, continuous flow, single return, and atmospheric pressure tunnel. The ADWT has a test section of 0.813 m height, 1.14 m width and 2.44 m length with a turbulence intensity of 0.1%. Collaborative work was also performed at two facilities, Tohoku University in Japan for the combined skin friction and surface pressure measurements and Shenyang Aerospace University in China for the Rood wing junction flow measurements.

For all test facilities, a glass window at the top of the test section provided optical access. The camera was placed above the top section of the wind tunnel and set to be

parallel to the model surface. The luminescent oil was applied onto the test surface and excited to luminescence by the UV lamps. The UV lamps were arranged to ensure a uniform illumination field in the test area. A 500 nm long-pass filter was used to filter the light captured by the camera allowing only detection of the emission of the luminescent oil centered at approximately 530 nm. The wind tunnel was then run in a dark environment, and images were captured by a Basler Aviator CCD camera. Image acquisition was performed using Streampix 5.0 software by NorPix at up to 100 frames per second. Acquired images were processed using an in-house developed MATLAB data reduction code to obtain skin friction fields. Figure 2.2 is an illustration of a typical experimental setup for GLOF measurements in a wind tunnel.

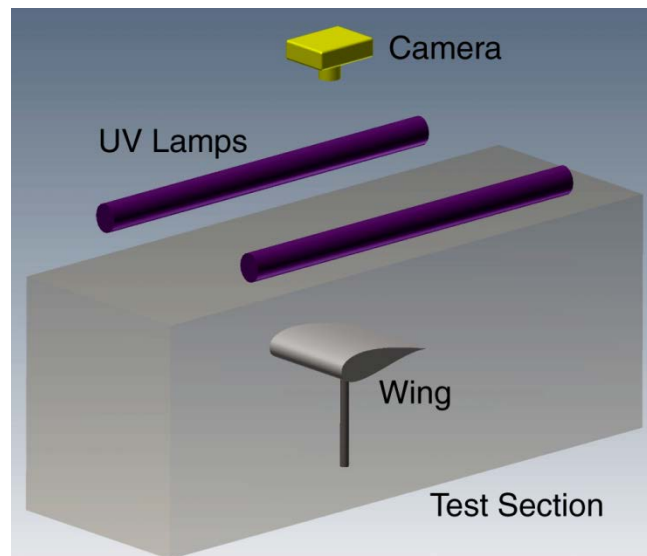


Figure 2.2 Illustration of experimental setup for GLOF measurements

Two potential sources of errors are the effect of non-uniform illumination on the surface of interest and temperature effects. Non-uniform illumination can be eliminated using a homogeneous luminescent reference base coating applied on the surface. In this work, the illumination lights were arranged appropriately such that the illumination field was approximately uniform in the region of interest. This work does not consider

temperature effects as all experiments were carried out at low speed with constant temperature.

Figures 2.3 (a) and (b) show a typical image obtained from experiments and a skin friction line plot obtained using this technique, respectively, for measurements on a low aspect ratio NACA 0012 wing at 18° angle of attack. The flow direction is from the top to bottom of the images. The complicated flow structures associated with the fully separated flow and tip vortex interaction is identifiable. The skin friction lines are observed to converge along the leading edge indicating separation at the leading edge. At $(x/c, y/c) = (0.18, 0)$ it is seen that the flow is partially reattached at the source node (N_1) and secondary separation occurs at the saddle (S_2) at $(x/c, y/c) = (0.3, 0)$. A pair of spiraling nodes (N_2 and N_3) located at $x/c = 0.6$ are clearly visible along with two pairs of saddle structures (S_1 and S_3 and S_4 and S_5) upstream and downstream of the spiraling nodes located at $x/c = 0.28$ and $x/c = 0.95$, respectively. The capability of this technique in resolving global skin friction fields is clearly highlighted in this example of a complex separated flow.

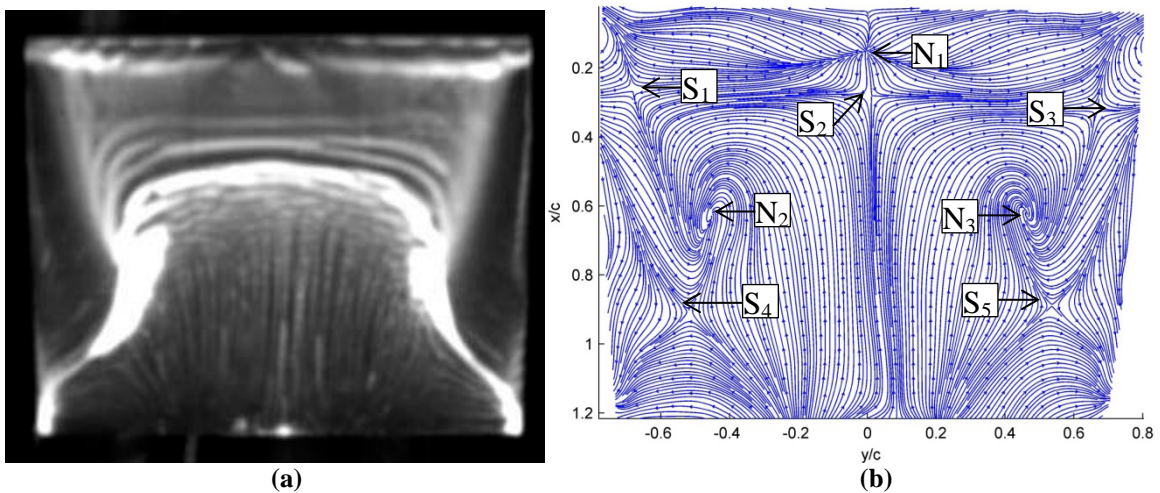


Figure 2.3 Typical (a)raw luminescent oil image, (b)skin friction line plot for a NACA 0012 wing at 18° angle of attack

CHAPTER 3

SKIN FRICTION TOPOLOGY

The phenomenon of flow separation has been studied extensively over the years. Three dimensional flow separation is a common occurrence in most practical flow situations such as flow over aircraft at high angles of attack, wing tips, vortical flows over delta wings and junction flows. Traditionally, three dimensional flow separation has been studied in detail with respect to skin friction topology utilizing oil streak visualization. With the availability of a quantitative global skin friction diagnostic tool [27], high resolution global skin friction fields can be measured. Topological features such as separation lines, reattachment lines and singular points including nodes, foci and saddle points which describe flow features such as flow separation and reattachment as well as standing vortices, can be observed from the measured skin friction fields. The study of skin friction topology can also be extended to the application of topological constraints to the measured skin friction fields to verify its compliance with the topological rules which in turn affirm its accuracy.

3.1 Historical Perspective

The study of topology related to fluid flows can be divided into three major milestones [30-57]. The first is the development of Poincare's Theorem. This idea was then rigorously developed and refined by Legendre resulting concepts such as skin friction lines, critical points and topological rules and constraints pertaining to these

features. Legendre and Werlé [34] performed numerous flow visualization experiments, most notable are visualizations on flows over delta wings, flows over elongated bodies, flows over obstacles, base flows and visualization of helicopter rotor blade tip vortices. Legendre's work can be considered the second milestone in the development of the topology of separated flows. Hunt et al. [38] extended Legendre's idea of topological constraints and defined the topological constraints of a flow around a three-dimensional body making it the third major milestone in the development of the topology of separated flows.

The study of topology originated in the mid to late 1800's in the work of German mathematicians Riemann, Listing, Möbius and Klein. In 1895, Poincaré revolutionized the study of topology by introducing algebraic quantities, known as fundamental groups and homology groups. This major contribution leads to Poincaré being known as the father of algebraic topology. In the study of topology in separated flows, Poincaré's index theorem forms the basis of topological constraints used in interpreting topological structures present in these flows. Poincaré's index theorem is an important theorem in differential topology which simply states that on a closed orientable surface, the sum of indices of a vector field with a finite number of singular points is equal to the Euler characteristic of the surface [31, 49]. The Euler characteristic is an invariant number in topology describing the topological space's shape or structure regardless of the way it is deformed and is defined for various shapes and surfaces. Two examples are a sphere and a torus which have a Euler characteristic of 2 and 0, respectively.

In the early 1950's Robert Legendre introduced the basic concepts of the Critical Point Theory providing a foundation for defining three dimensional flow separation.

Legendre's work on the Critical Point Theory was inspired by earlier work of Poincaré and has been instrumental in the adoption of terms such as skin friction lines, critical points, separation and attachment lines and surfaces and topological rules enabling a consistent study and interpretation of flow fields, specifically three dimensional separated flows. In looking for a description of separation, it is reasonable to consider the characteristic of the flow on the surface of the body being studied. In other words, the focus of the flow on the surface of the body of interest is towards the shear stress on the wall. The shear stress on the wall is a vector field of which the trajectories are called skin friction lines or also sometimes called limiting streamlines because they are the limit of the streamline when the distance to the wall becomes zero [34].

A singular point in a vector field is a point where the magnitude of the vector becomes zero. Singular points can be classified into nodes and saddles. Nodes can be classified into two types, a nodal point and a focus. A nodal point is a common point to an infinite number of skin friction lines. At a nodal point of attachment, all of the skin friction lines are directed outward away from the node, conversely at a nodal point of separation, all of the skin friction lines are directed inward towards the node. The difference between a nodal point and a focus is that the focus possesses no common tangent line and an infinite number of skin friction lines spiral around it. For a focus of attachment, the skin friction lines spiral away from it and conversely, for a focus of separation, the skin friction lines spiral into it. For a saddle, there are only two lines that intersect at the singular point, with each line having its vectors oriented toward or away from the singular point along with asymptotic neighboring lines called separator lines [44]. Figure 3.1 Illustrates structures of a nodal point, focus and saddle.

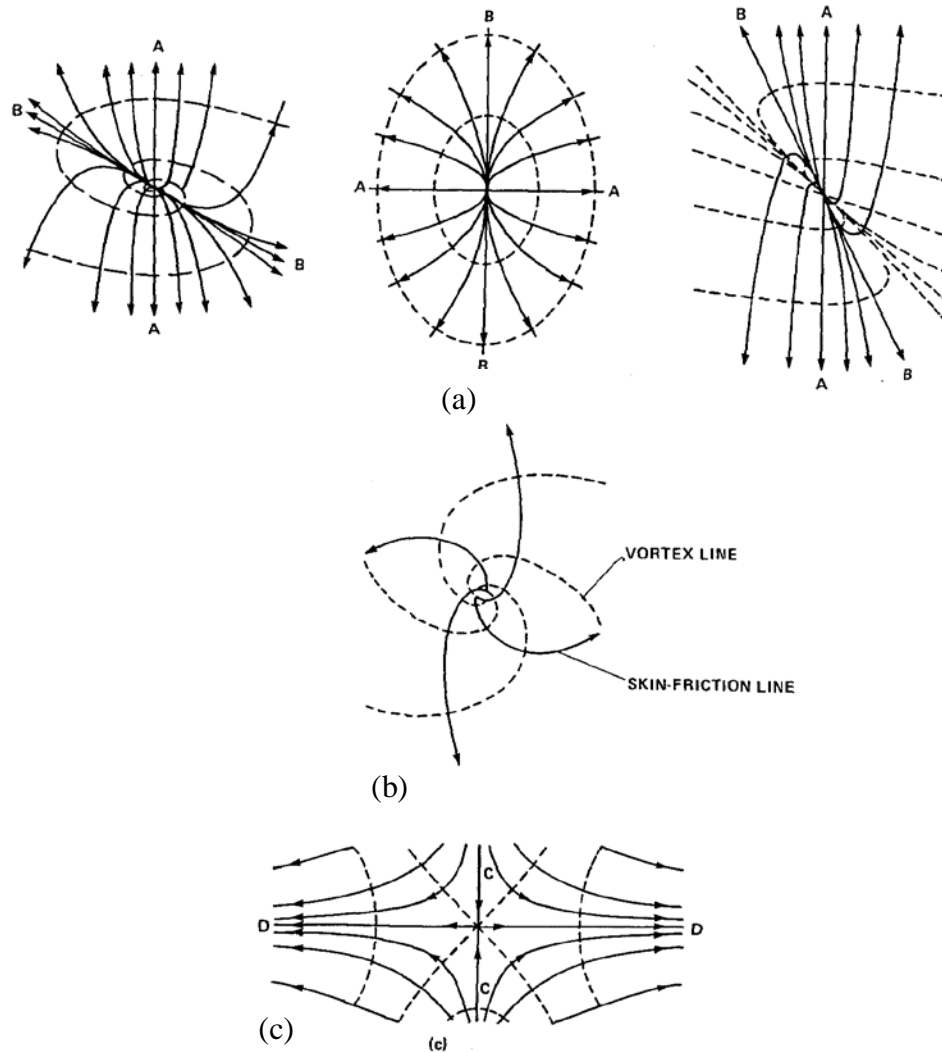


Figure 3.1 Structures of (a)nodal points, (b)focus and (c)saddle [44]

In the late 1970's, Hunt et al. [38] introduced an extension of the topological rules and constraints developed by Poincaré and Legendre. Hunt proposed a summation rule for a three dimensional body mounted on a wind tunnel floor. If the wind tunnel floor and the three dimensional body were considered part of the surface of a torus, the index summation for the system would be zero. This is achieved by taking the sum of nodes minus the sum of saddles in the skin friction field which equals to the Euler characteristic of a torus that is zero i.e. there are an equal number of nodes and saddle points in such a flow. A case was also made for a three dimensional body with a hole mounted on a wind

tunnel floor. In this system, the body and the wind tunnel floor become part of a double torus, making the index summation for the system -2 which equals the Euler characteristic of a double torus that is -2 i.e. there are two more saddle points than nodes in the skin friction field. Illustrations for both cases of a three dimensional body (B_1) and three dimensional body (B_2) with a through hole mounted on a wind tunnel floor can be seen in Figure 3.2.

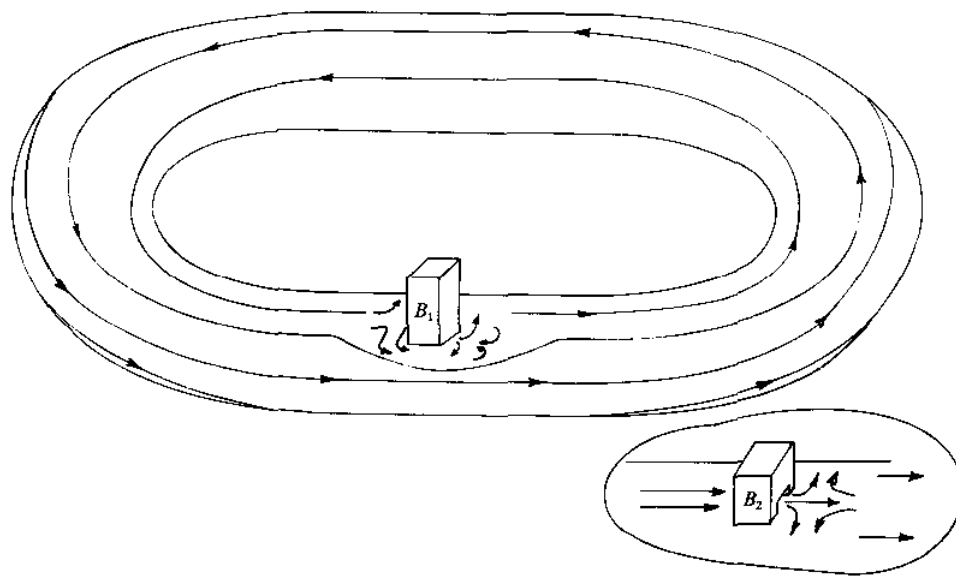


Figure 3.2 A three dimensional body B_1 and B_2 mounted on a wind tunnel floor [38]

Hunt also proposed the index summation for a junction of two pipes. If a mirror image of the pipe junction is considered and joined with the real part, the resulting geometry is a double torus. As seen for the previous case a double torus results in a summation index of -2 . Taking into account only the actual part of the pipe junction, a summation index of -1 is achieved i.e. there is one more saddle point than nodes in the skin friction field. An illustration of this case is shown in Figure 3.3.

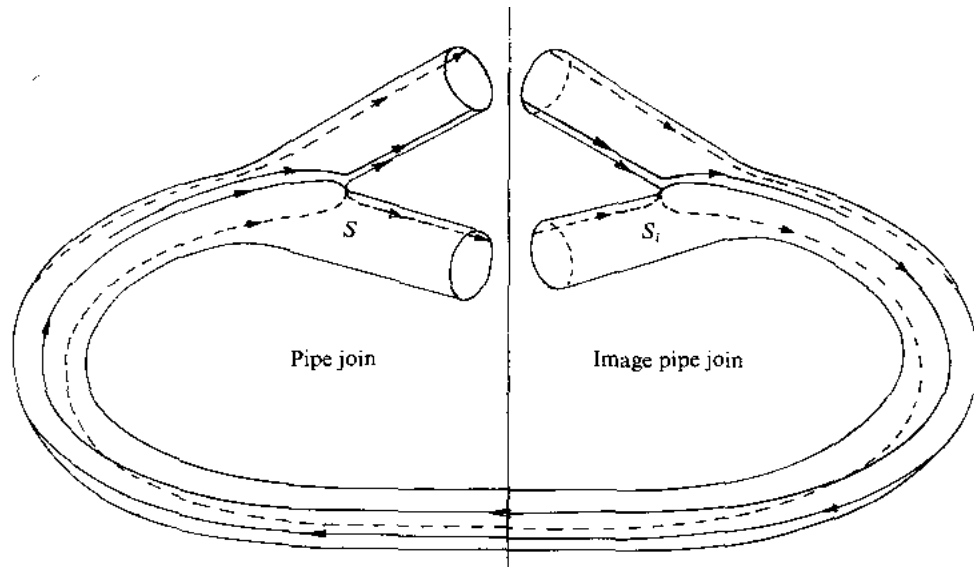


Figure 3.3 A pipe junction representing a double torus [38]

3.2 Modern Developments

Traditionally, skin friction topology has been observed through oil streak visualizations in wind tunnel tests. Skin friction lines were reconstructed by visual inspection of the oil streak patterns on the model surface based on logic and intuition. Unfortunately, this method makes identifying detailed topological features in complex three dimensional separated flows very difficult. Although this method has been extensively utilized to generate a vast amount of data on the topology of skin friction fields, it remains a qualitative and relatively subjective approach. The existence of topological constraints on skin friction fields as a result of Poincare's Theorem and subsequent development and refinement of the theorem has enabled researchers to infer the results obtained from the relatively crude technique of oil streak visualization to fit within certain rules. The assumption is that the topological constraints are mathematically valid; however these rules have not been examined thoroughly from an experimental standpoint due to the lack of high resolution global skin friction diagnostics

as well as computational fluid dynamics (CFD) data of the skin friction field of these complex separated flows.

The development of the global luminescent oil film (GLOF) skin friction meter by Liu et al. [27] has provided a means to conduct high resolution global skin friction diagnostics. The capability of the technique in obtaining high resolution, detailed skin friction fields for complicated three dimensional separated flows such as junction flows, a low aspect ratio NACA 0012 airfoil at high angles of attack and delta wings has been demonstrated in published literature [27, 28]. This tool will be useful in providing not only detailed skin friction fields, but also contribute towards studying and refining the topological rules and constraints for topological studies of skin friction fields

Previous global topological studies with the exception of Foss's work [35, 36], are derived for isolated singular points on a closed surface and a surface with a non-penetrable boundary not considering the inflow and outflow across a boundary. Experimentally, it is challenging if not impossible to obtain a skin friction field on a completely closed surface. Experiments allow the measurement of skin friction fields in a region enclosed by a penetrable boundary with vectors able to move freely inward and outward across this boundary. Some examples include the upper surface of a wing enclosed by a boundary that consists of the leading, side and trailing edges or the surface of a three dimensional aerodynamic body with a boundary defined by the projected surface of the body onto the image plane. A penetrable boundary can be drawn arbitrarily on a surface, although to interpret the skin friction topology in such a region, a general topological rule is required for the relationship between the distribution of the isolated singular points enclosed by a penetrable boundary and the inflow and outflow

across the boundary. It is not sufficient to consider only the isolated singular points in a bounded region without including the relevant boundary inflow and outflow. Chapman and Yates [30] have noted that the difference between the sum of the nodes and saddles remains unchanged if the direction of the vector field does not change as it crosses the boundary. In considering flow through a boundary, Foss [35, 36] utilized holes punched on a collapsed sphere and provided a number of applications where the collapsed sphere method is applied.

Recently, Liu et al. [57] have utilized the Poincare-Bendixson (P-B) index formula in describing the topology of the complex separated flow on the upper surface of a low aspect ratio wing. By utilizing the P-B index formula, the aforementioned restrictions in global topological diagnostics are tackled.

3.2.1 Foss' Collapsed Sphere Method

In the interests of generalizing the topological constraints developed by Hunt et al. [38] for a broader range of applications, Foss [35, 36] developed an approach that relates the topological features of a surface flow to the Euler characteristic of a collapsed sphere. This collapsed sphere can be thought of as a two-sided disk with holes and handles. The edge of the collapsed sphere where there is no hole is called a seam to which vectors are tangential. This allows for seams to represent solid boundaries, streamlines or skin friction lines. To topologically simulate flow in and out through a boundary on a surface, holes are punched on the edge of the collapsed sphere. The Euler characteristic ($\chi_{surface}$) of a sphere with holes and handles is given by $\chi_{surface} = 2 - \#holes - 2\#handles$. The relationship between $\chi_{surface}$ to the number of isolated singular points and half-singular points of a vector field on a surface is defined

by $\chi_{surface} = 2 \#N + \#N' - 2\#S - \#S'$, where $\#N$, $\#N'$, $\#S$, $\#S'$ denote the numbers of the nodes, half-nodes, saddles and half-saddles, respectively. An important consideration in applying the collapsed sphere method to a vector field on a surface is the selection of a suitable boundary that consists of seams and holes. Examples of complex flow fields topologically analyzed by the collapsed sphere method are given by Foss [35, 36]. The application of the collapsed sphere method in more complex flows requires a boundary with seams of finite lengths such as skin friction lines, streamlines and solid boundaries. The P-B formula however, is not applicable for such a boundary with seams since it contains a section of a skin friction line, streamline or a solid wall. To this effect, the approach employed in applying the collapsed sphere method and the P-B formula differ specifically in selecting a boundary, although they are complementary approaches for different applications.

3.2.2 Poincare-Bendixson Index Formula

Typically, global skin friction diagnostics gives a skin friction vector field on a region enclosed by a penetrable boundary on the surface of a three dimensional body. The vectors are able to move freely inwards and outwards across the penetrable boundary. In interpreting the topological structure of a vector field in such a region, the Poincare-Bendixson (P-B) index formula can be used as a constraint, which fundamentally is a conservation law for the number of isolated singular points enclosed by a boundary and the boundary switch points. In simple notation, the P-B formula can be written as

$$\#N - \#S = 1 + (\#Z^+ - \#Z^-) / 2 \quad (3.1)$$

where $\#N$ is the number of the nodes, $\#S$ the number of the saddles, $\#Z^+$ the number of the positive switch points, and $\#Z^-$ the number of the negative switch points. A penetrable boundary contains inflow and outflow segments. If a point Z on the boundary exists such that the neighboring inflow and outflow segments are divided, this point is called a switch point. Two types of switch points are defined. These switch points are identifiable by tracing a skin friction line or streamline. If the vector in a adequately small region of Z moves inward first and then outward across the boundary, the switch point is defined as negative, denoted by Z^- . Conversely, if the vector moves outward first and inward across the boundary in the region of Z , the switch point is defined as positive, denoted by Z^+ . These negative and positive switch points on a boundary are illustrated in Figure 3.4. A switch point is also called the tangent point at which a skin friction line (or a streamline) is tangent to the boundary. When the inflow and outflow across a closed boundary is unchanged, i.e., the difference between positive and negative switch points is fixed, Equation 3.1 indicates that nodes and saddles enclosed by the boundary must appear in pairs.

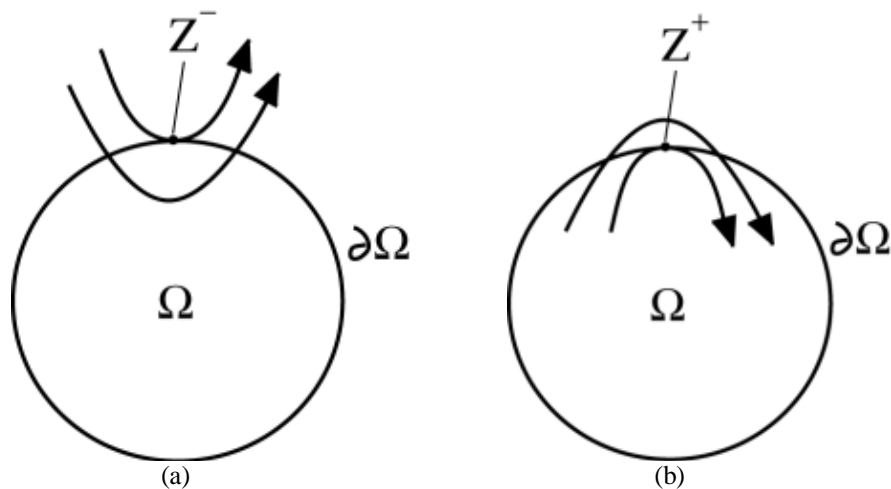


Figure 3.4 Boundary switch points, (a)negative switch point and (b)positive switch point

Liu et al. [57] have also given a practical computational approach for identifying and locating switch points utilizing the normal and tangential components of a skin friction vector. For the outflow segment, the normal skin friction magnitude is positive and conversely, for the inflow segment it is negative. Using this logic, a switch point can be identified as a zero-crossing point of the normal skin friction vector magnitude along the boundary. The tangential skin friction vector is an indicator of the switching direction between two different segments. A negative switch point is identified when switching occurs from the inflow to outflow segment. Conversely, a switch point is positive when switching occurs from the outflow to inflow segment. Equation 3.1 is valid for a finite number of switch points on a boundary which imposes a requirement that the defined boundary not be part of a skin friction line (or a streamline) or an envelope of skin friction lines (or streamlines). If this condition is fulfilled, a boundary can be selected fairly arbitrarily to apply the P-B formula.

Liu et al. [57] have also shown an application of the P-B formula in analyzing classical cases such as the hairy sphere theorem and the topological rule given by Hunt et al. [38] for junction flows. One of the proofs [53] of the hairy sphere theorem describes a sufficiently small circle around an arbitrary nonsingular point drawn on the surface of a sphere for which all the vectors are similarly oriented. Figure 3.5 illustrates the circle denoted by ABCD, in which no singular point is contained. A small hole is then punched on ABCD and the remaining part of the sphere is deformed into a disk. As observed in Figure 3.5, the almost uniform vectors on the small circle ABCD on the sphere transforms to the vectors changing the direction along the circumference of the disk.

Since only two positive switch points Z_1^+ and Z_2^+ are identified on the circumference of the disk, the hairy sphere theorem $\#N - \#S = 2$ is a direct consequence of Equation 3.1.

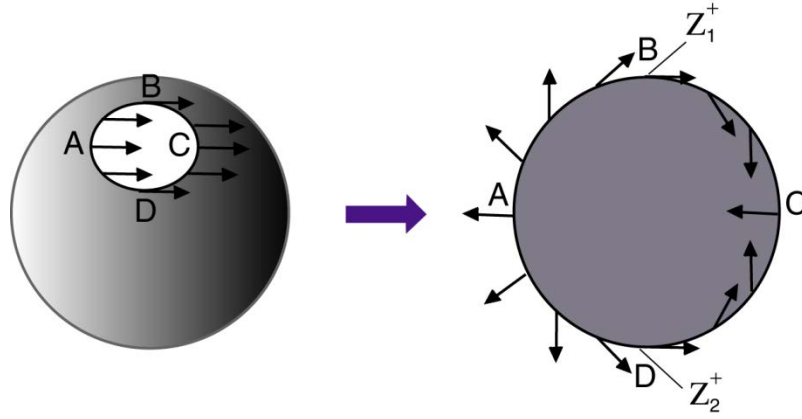


Figure 3.5 A sphere with a small hole deformed into a disk

Hunt et al. [38] derived the topological rule $\#N - \#S = 0$ for the base surface and the surface of a cylinder in junction flow by employing an imaginary body to reconstruct a sphere such that the hairy sphere theorem can be used. This rule can be inferred directly using Equation 3.1. As illustrated by Figure 3.6, a circular boundary is drawn around the cylinder on the base surface to enclose all the singular points, which is sufficiently large such that the skin friction vectors on the front and back sections of the circumference generally go into and out the circle, respectively. As a consequence, only two negative switch points Z_1^- and Z_2^- exist. When applying the P-B formula to this case, the conservation law $\#N - \#S = 0$ holds on the surface enclosed by the circle (the base surface plus the surface of the cylinder) as inferred by Equation 3.1. This rule can be written in a straightforward manner because the inflow and outflow across a sufficiently large boundary is simple and remains unchanged regardless of what occurs around the cylinder.

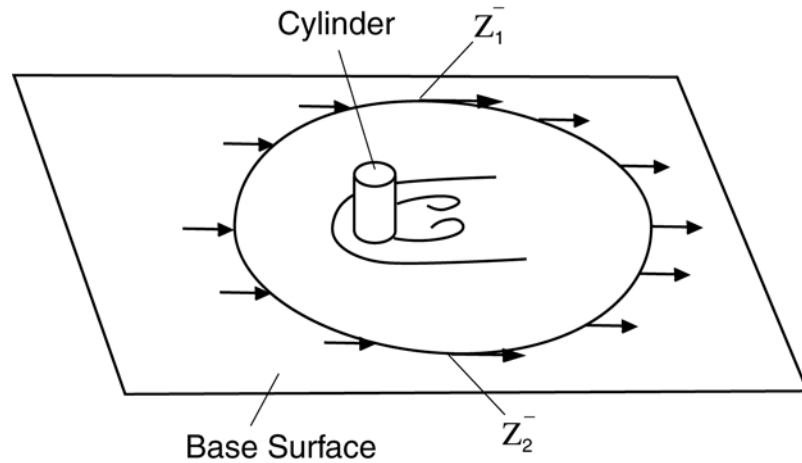


Figure 3.6 A cylinder on a base surface

The P-B index formula is given as a conservation law for the number of isolated singular points and switch points of a vector field in a singly-connected region enclosed by a penetrable boundary on a surface. This conservation law is applicable to the topological analysis of high-resolution skin friction fields as well as 2D velocity fields since a boundary of a singly-connected region on a surface can be arbitrarily selected for the convenience of analysis as long as it does not contain a section of a skin friction line (or a streamline). It has been successfully employed by Liu et al. [57] in analyzing the complex skin friction topology in the complex separated flow on a low-aspect-ratio rectangular wing.

An example of the application of the P-B formula to a skin friction field measured in experiments using the global luminescent oil film skin friction meter is shown in Figure 3.7, which is a skin friction line plot of the low aspect ratio NACA 0012 wing at 18° angle of attack as discussed in Figure 2.3. A penetrable boundary ABCDA is defined and the number of switch points and singular points are identified - $\#N = 3$, $\#S = 5$, $\#Z^+ = 2$ and $\#Z^- = 8$. Applying the P-B formula which states $\#N - \#S = 1 + (\#Z^+ + \#Z^-) / 2$, the left and right side of the formula are equal to -2, therefore the conservation law holds.

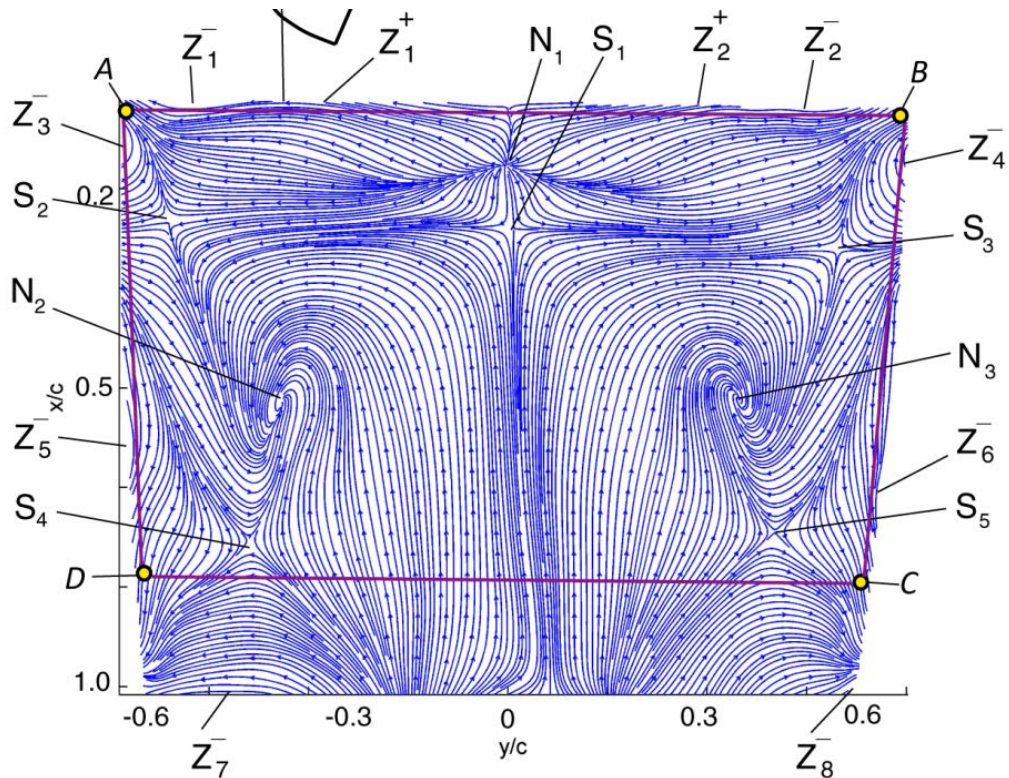


Figure 3.7 Skin friction line plot of a low aspect ratio NACA 0012 wing at 18° angle of attack with penetrable boundary ABCDA, singular points and switch points highlighted

3.3 Summary

This section has discussed the historical sense of the study of topology of a vector field and the application of the Poincare-Bendixson index formula in analyzing the topology of skin friction fields. At this point, the question may be posed on the significance of topological analysis of skin friction fields particularly from a fluid mechanics perspective. There are two answers to the question. First, topological analysis using constraints such as the P-B formula allow for verification of the consistency of measured skin friction fields. Topological analysis also allows for the identification of critical points and features such as separation and reattachment lines which contribute towards the analysis of skin friction fields in complex separated flows. Global skin friction diagnostics and topological analysis are two important tools in studying and understanding the nature of complex separated flows.

CHAPTER 4

GLOF TECHNIQUE REFINEMENT

Prior work in developing the Global Luminescent Oil Film (GLOF) skin friction meter centered on the proof of concept phase of the technique along with various global skin friction measurements in complex separated flows. This phase of the study will focus on the refinement of the technique from the perspective of data reduction and measurement instrumentation setup. For data reduction, MATLAB code was rewritten in a streamlined and modular manner to improve processing performance, robustness and ease of use alongside the addition of various other features such as image manipulation, parallel processing and post processing. Measurement instrumentation improvements encompassed luminescent oil preparation, ultraviolet (UV) excitation selection and oil film application techniques.

4.1 Data Reduction

Data reduction code was written in MATLAB in four separate modules, a preprocessor, processor, post processor and an image manipulation module. Figure 4.1 is a flow chart detailing the steps in the data reduction procedure utilizing the modules detailed. The data reduction procedure starts with the preprocessing stage using the preprocessor module. This module consists of two sub modules, variable input and image sequence display. The variable input sub module receives the data reduction variables such as time step, number of solutions, and image filtering along with region of

interest and masking parameters. A MATLAB '.mat' file containing all variable settings is automatically generated at the end of the variable input sub module that will be subsequently used in the image sequence display sub module and, processor and post processor modules. The image sequence display sub module displays the image sequence to be processed with all data reduction variables applied to the image set which is used for optimized selection of these variables. Typically, the process involves setting a baseline value for the variables followed by viewing the image sequence and making any necessary adjustments to the variables. Adjustments to variables are based on visual observations of the image sequence to ensure that the selected variables display a sufficient rate of oil film development and detailed features are captured. The process of variable adjustment is iterated up to the point where a satisfactory image set is observed from the image sequence viewer. The data reduction procedure then moves on to the processing stage utilizing the processor module.

The processor module performs the function of processing image pairs to obtain skin friction fields based on the parameters defined by the preprocessor module. There are two execution modes of this module, one that takes advantage of multi-core parallel processing capabilities of modern computers and a traditional one that utilizes a single computation core of the computer. Execution mode selection depends on the capabilities of the computer used as well as the availability of the MATLAB parallel processing toolbox. Benchmarks were performed comparing the parallel processing module to the traditional module using a standardized test case. The computation time recorded was 726 seconds and 273 seconds for a single and four core processor respectively. This produces a 266 % or 2.66 times improvement in processing time using four processor

cores. This improvement is a definite advantage in improving throughput for processing large image sets or higher resolution images. At the end of execution, the output produced are two '.dat' files containing skin friction vectors in the streamwise (x) and spanwise (y) directions and skin friction field plots. The resulting data can then be post processed to produce customized plots using the post processor module. There are two versions of the post processor module, a global and zoom module, which produce global or magnified region views of the skin friction field. The function of this module is to generate high quality figures of skin friction line, vector and magnitude plots with customizable labels, axes, size and resolution.

The image manipulation module is an auxiliary module used to perform image manipulation. This module is able to perform 2D spatial transformations, region of interest selection and image downsampling. The 2D spatial transformation is based on a projective plane transformation. Region of interest selection allows the reduction of the image size by removing outside borders of the image not containing areas of the model. Image downsampling is performed based on wavelet decomposition and is able to reduce image size by a factor of $1/(n+1)^2$ ($n = 0,1,2,..$), i.e. 1/4, 1/9 and 1/16. Downsampling is useful to produce smaller images that will reduce processing times with the tradeoff of loss of resolution and details in the skin friction fields obtained. Once the desired parameters are set, the module manipulates the images and outputs it to a new image file which can then be used for data reduction. All four MATLAB data reduction modules are a critical component of this technique and work together in unison to produce global skin friction fields.

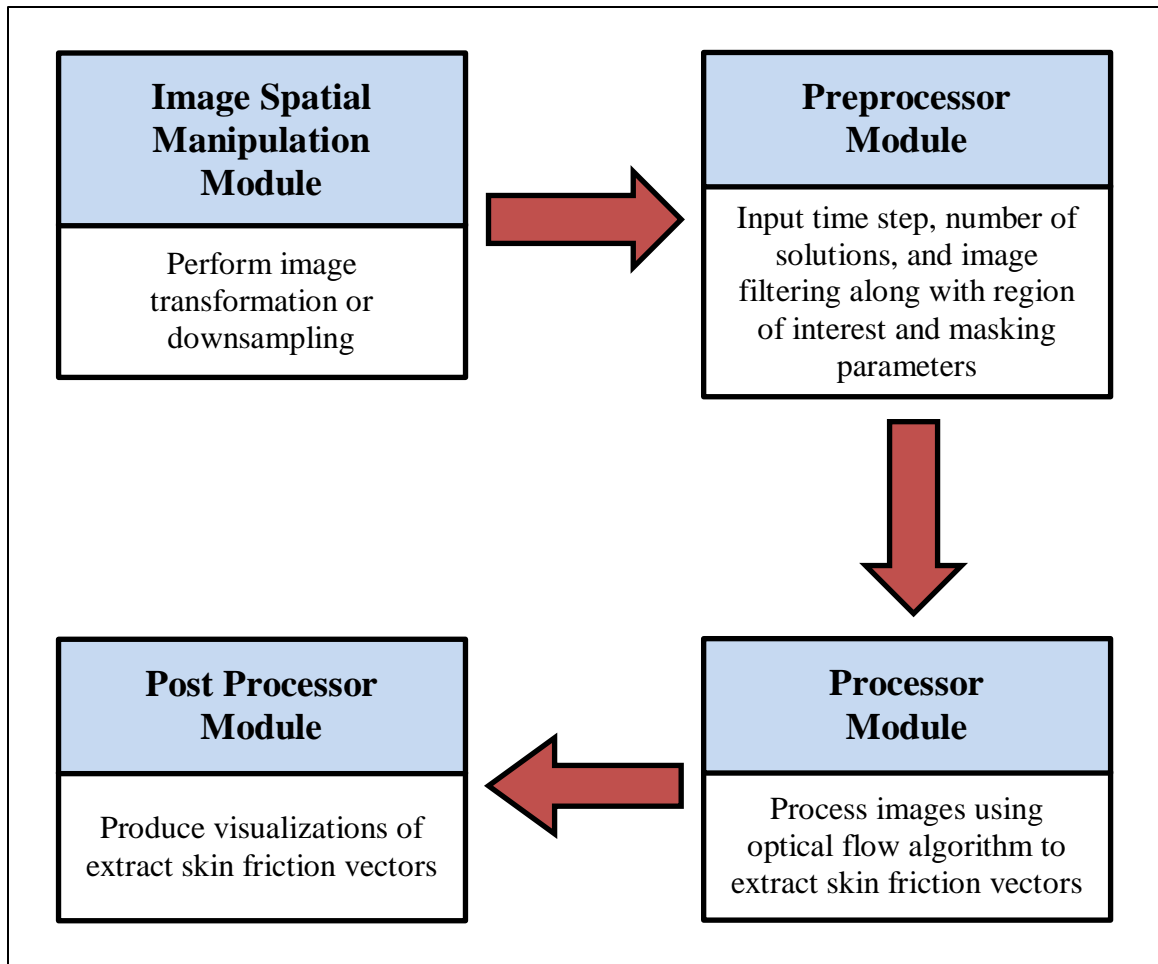


Figure 4.1 Flowchart of processing steps in the data reduction procedure for the GLOF technique

4.2 Luminescent Oil

Luminescent oil is a critical component of the global luminescent oil film (GLOF) skin friction meter. Oil film thickness is a key parameter which is related to the luminescent intensity of the oil. Therefore it is important that the luminescent oil produces the best signal possible to be detected by the image acquisition system. The luminescent oil consists of silicone oil and a UV dye.

The silicone oil used is a Dow Corning 200 equivalent silicone oil produced by Clearco. It is also referred to by its chemical name, Polydimethylsiloxane (PDMS). PDMS is the selected oil for the technique as it possesses a few desirable characteristics.

PDMS is a clear, colorless, odorless and non-toxic fluid which is non-flammable and is stable at high and low temperatures. These traits make it suitable to be used as a component of the luminescent oil for the technique. Although it is stable at high and low temperatures, a constant is defined to characterize the viscosity of the oil for a given temperature range. The viscosity temperature coefficient (VTC) is a measure of the change of viscosity of the oil over the temperature range of 38°C to 99°C and is defined by Equation 4.1 below, where VTC is the viscosity temperature coefficient, ν_{38} and ν_{99} are the viscosities of the oil at 38°C and 99°C respectively.

$$\text{VTC} = 1 - \frac{\nu_{99}}{\nu_{38}} \quad (4.1)$$

Care must be taken in applying the GLOF technique in flow regimes that cause heating of the model surface and subsequently heating of the silicone oil as silicone oil of 200 centistokes (cs) at 38°C will have a viscosity of 80 cs at 99°C. This will certainly affect the oil film development process and subsequently the calculated skin friction fields.

Four luminescent dyes were evaluated in selecting the best candidate for the technique. The first dye evaluated was Europium (III) Thenoytrifluoroacetate (EuTTA). The EuTTA solid was dissolved in Aero Gloss Dope Thinner made by Midwest Products. The resulting solution was then mixed with the silicone oil and stirred to distribute the dye solution evenly. EuTTA was a good dye candidate as it had a bright orange emission centered around approximately 615 nm with UV excitation around 365 nm. Although EuTTA was a suitable candidate since the absorption and emission spectrum are distinctly apart with a strong emission, it had a tendency to adhere to the

surface of the model, causing artificial patterns to appear in the captured images of oil film development.

A UV excited powder based pigment was the second candidate tested. The powder was UVXPBR manufactured by LDP LLC. The powder was mixed directly with silicone oil and agitated with a magnetic stirrer to evenly mix it with the oil. This dye was also a good candidate with similar absorption and emission spectra as EuTTA. As with EuTTA, the major issue with this pigment is its tendency to adhere to the surface of the model.

Perylene was the third candidate UV dye evaluated. Perylene is an aromatic hydrocarbon based molecule which is lipid soluble making it suitable candidate to be mixed in silicone oil. One batch of luminescent oil is produced by mixing Perylene and silicone oil at a ratio of 1 mg to 200 ml respectively. Perylene emits a strong blue emission when excited by UV illumination. Figure 4.2 is a plot of the absorption and emission spectra of Perylene represented by the purple and blue lines respectively. The absorption and emission maxima occur at approximately 400nm and 460nm respectively. The lipid solubility and strong luminescent emission of Perylene make it an excellent candidate to be used as a luminescent dye for this technique, although two major issues disqualify it. The first is the close absorption and emission spectrum at 400 nm and 460 nm, respectively, as observed in Figure 4.2. This makes it difficult to distinguish between the excitation source and the molecule emission spectra. The second issue is the carcinogenic nature of Perylene making it hazardous to those handling it especially since it is dissolved in oil and could cause contamination in the application and wind tunnel operations phases.

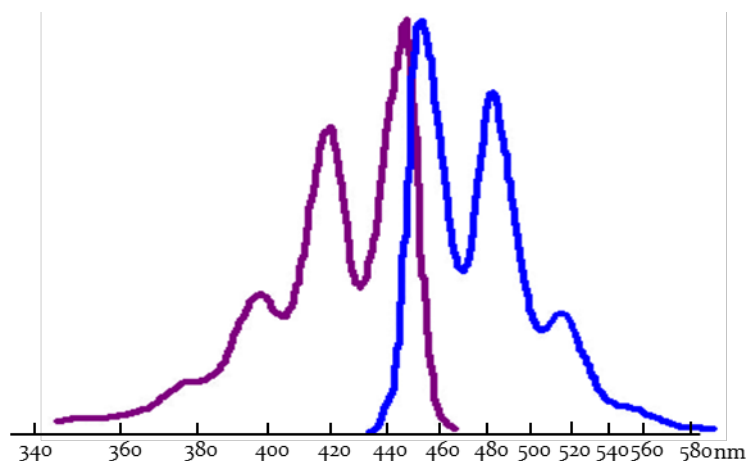


Figure 4.2 Absorption and emission spectra of Perylene

The final UV dye tested is a petroleum based UV dye, DFSB K-175 manufactured by Risk Reactor. One batch of luminescent oil is produced by mixing the dye and silicone at a ratio of 0.5 ml to 100 ml respectively. Figure 4.3 is a plot of the absorption spectrum of the DFSB K-175 dye. The dye has two absorption maxima, 280 nm and 365 nm corresponding to the light spectrum of short wave UV and long wave UV, respectively. Short wave UV has a wavelength range of 100 – 280 nm and is not a suitable excitation source due to its inability to penetrate through glass which rules it out of being used for wind tunnel testing as well as being a hazardous and potentially carcinogenic illumination source. Long wave UV is a suitable excitation source easily available as end user equipment.

Table 4.1 Summary of strengths and weaknesses of luminescent molecules evaluated

| Molecule | Strength | Weakness |
|-----------------|--|---|
| EuTTA | <ul style="list-style-type: none"> • Excellent luminescence • Distinct excitation and emission wavelengths | <ul style="list-style-type: none"> • Adherence to model surface • Requires dissolution in a solvent |
| UVXPBR | <ul style="list-style-type: none"> • Good luminescence | <ul style="list-style-type: none"> • Adherence to model surface |
| Perylene | <ul style="list-style-type: none"> • Excellent luminescence | <ul style="list-style-type: none"> • Excitation and emission peaks not distinctly separated |
| DFSB K-175 | <ul style="list-style-type: none"> • Excellent luminescence | <ul style="list-style-type: none"> • Excitation and emission peaks distinctly separated. |

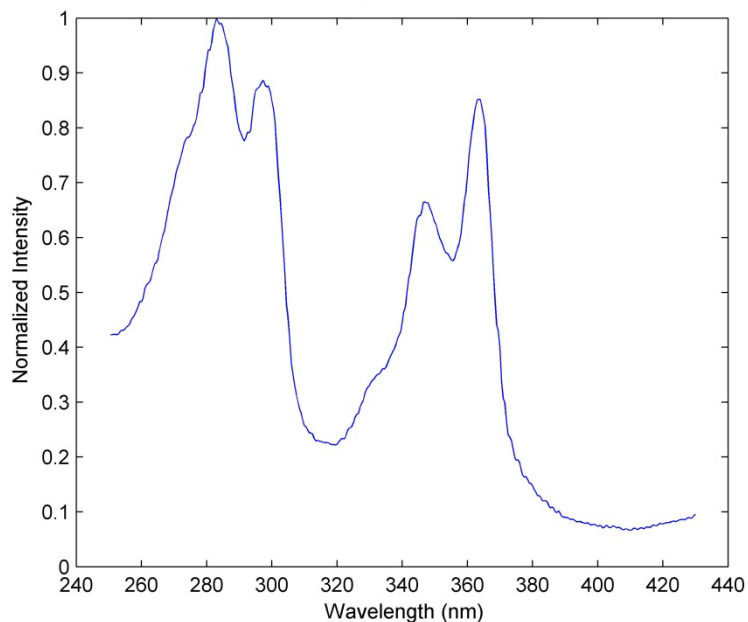


Figure 4.3 Absorption spectrum of DFSB K-175

Two typical excitation wavelengths for commercially available long wave UV illumination are 365 nm and 400 nm. Figure 4.4 is a plot of the emission spectra of the dye with 365 nm and 400 nm excitation. The plot shows the emission peak at 530 nm for both excitation wavelengths which is a bright green emission. The plot also highlights the emission intensity of the dye for both excitation wavelengths. It is clear that 365 nm excitation produces the highest emission intensity, almost 21 times higher than 400 nm excitation. DFSB K-175 is clearly the leading candidate among all the luminescent dyes tested and has several favorable traits. It easily soluble in silicone oil, non-reactive to test model surfaces, possesses an absorption wavelength easily excitable by commercially available UV excitation and it has a distinctly separated absorption and emission spectrum making it the chosen luminescent dye for the GLOF technique.

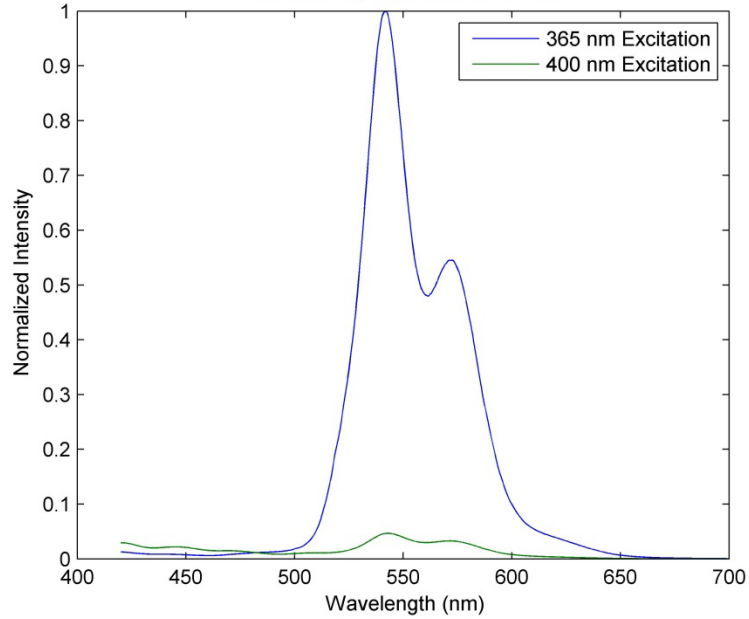


Figure 4.4 Emission spectrum of DFSB K-175 with 365 and 400 nm excitation

4.3 UV Excitation

UV excitation is another critical component of the GLOF technique. A suitable UV excitation source is required to produce the best luminescent signal. Two excitation sources were evaluated to be used for the technique. They were a commercially available blacklight lamp manufactured by GE (Model: 35884) and a UV LED array with 192 UV LEDs manufactured by Chauvet Lightning (Model: LED Shadow) as seen in Figure 4.5.



Figure 4.5 UV excitation sources (from left to right) – UV LED array, blacklight lamp

Figure 4.6 is a plot of the emission spectra of the blacklight lamp and UV LED. The blacklight lamp has a strong peak emission wavelength centered at approximately 367 nm. It also possesses a second peak emission wavelength at approximately 402 nm at 30% of the intensity of the peak at 367 nm. The UV LED on the other hand possesses only a single peak emission wavelength centered at approximately 400 nm as shown in Figure 4.6.

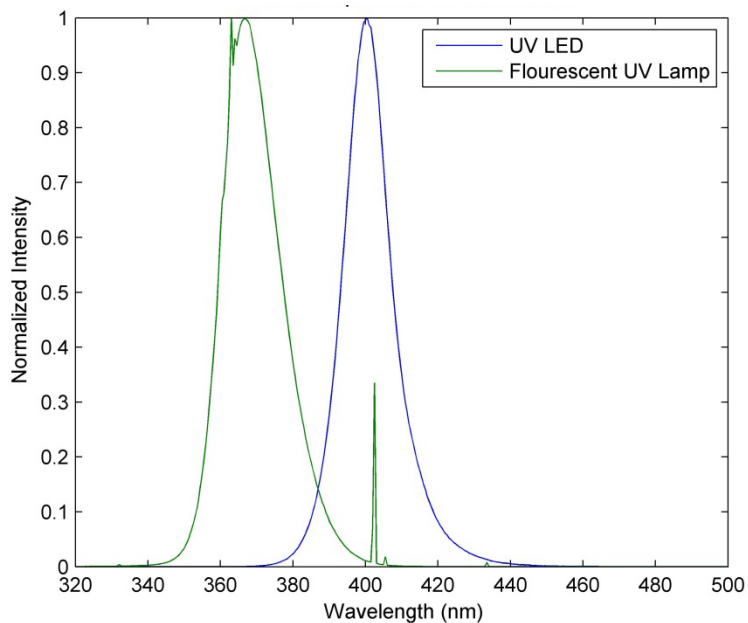


Figure 4.6 Emission spectrum of UV illumination sources

Figure 4.7 shows the emission spectra of the dye with the blacklight lamp and UV LED excitation. It is clearly visible that a similar emission spectrum of the dye occurs for both excitation sources. As discussed in the previous section, the emission intensity of DFSB K-175 for excitation at 365 nm is 21 times higher than that at 400 nm. Although this indicates that the UV LED might not be a suitable excitation source, its emission strength is significantly higher than the fluorescent blacklight, which results in a similar dye emission intensity when excited by either source.

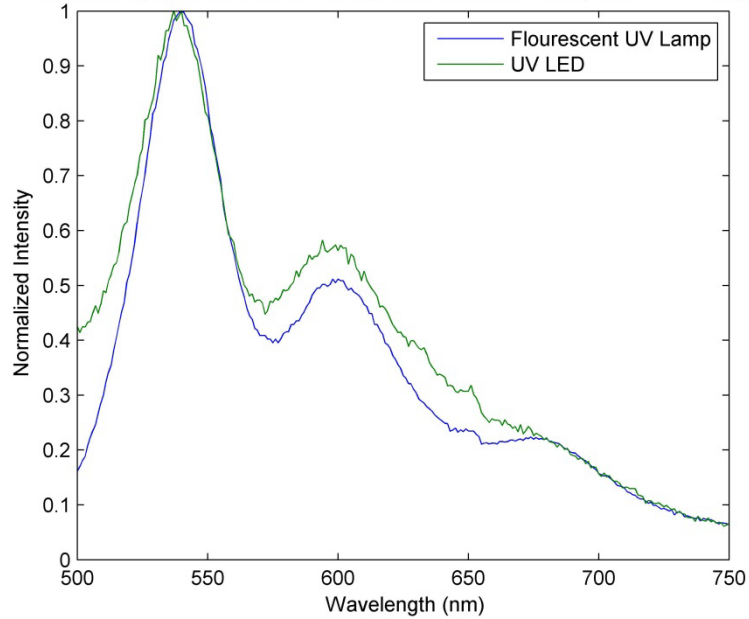
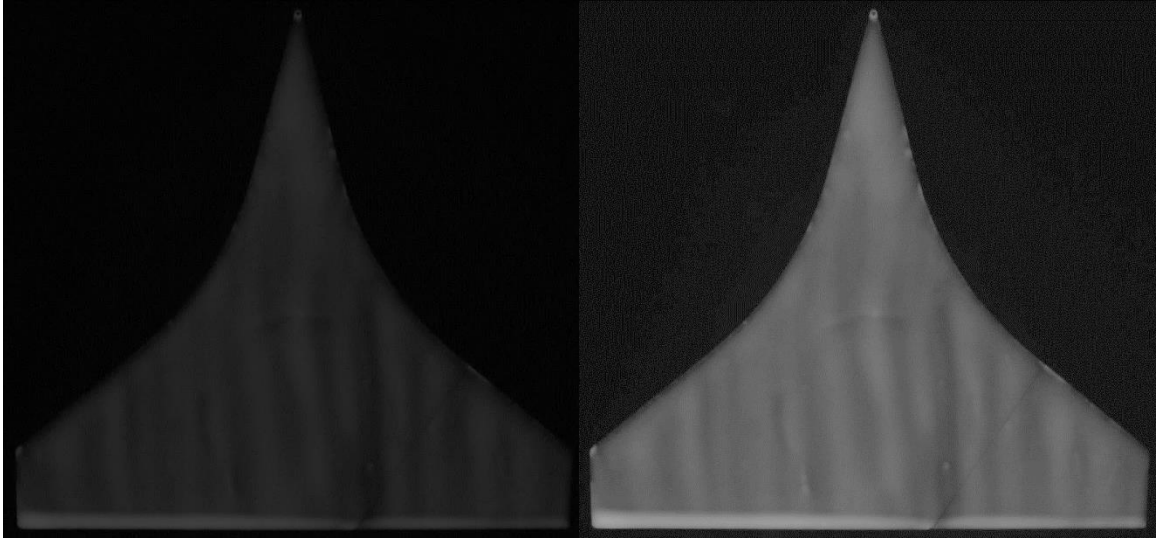
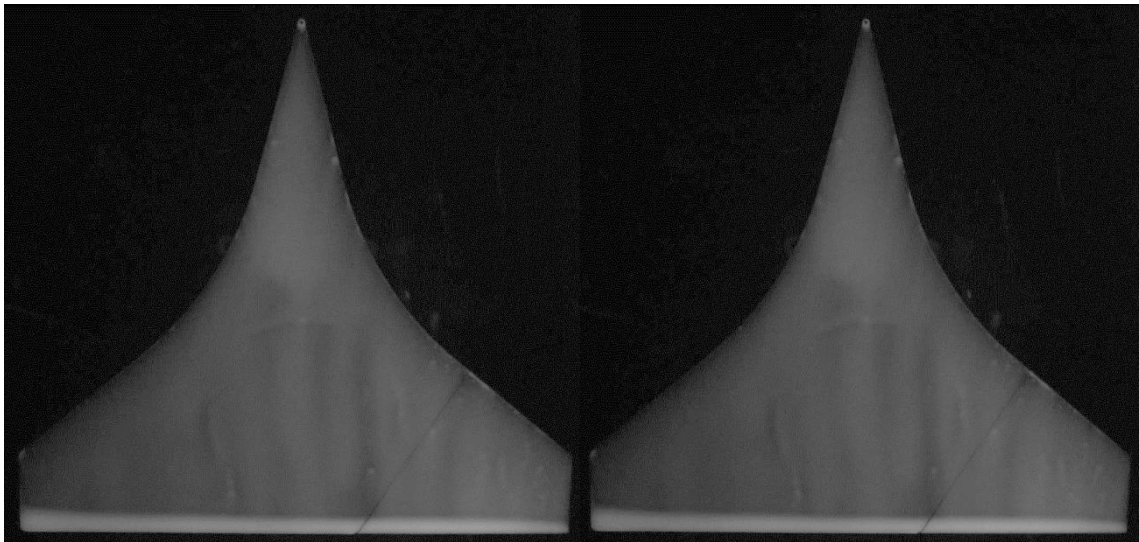


Figure 4.7 Emission spectrum of DFSB K-175 with blacklight lamp and UV LED excitation

Figures 4.8 (a) and (b) and 4.8 (a) and (b) show raw images for a delta wing with a uniform coat of luminescent oil for fluorescent blacklight and UV LED array excitation respectively. The conditions are with no wind, thus no oil film development or thickness change occurs. This implies that the intensity on the acquired images should not change between frames. Figure 4.8 clearly highlights an intensity change between two successive frames in contrast to Figure 4.9 which shows similar intensity between the frames. An analysis of pixel intensity values for the fluorescent UV lamp images shows a difference of approximately 30% between the frames compared to 0% for the UV LED array images. This occurs due to the sinusoidal output nature of fluorescent lamps and when combined with a particular acquisition frame rate contributes to this observation. Since this intensity variation occurs only at certain camera acquisition frame rates, it is still a viable option for UV excitation. In situations that require a particular acquisition frame rate which causes intensity variations not related to oil film development, the UV LED array can be utilized.



(a) (b)
Figure 4.8 Successive image frames for a delta wing with a luminescent oil film excited by a fluorescent UV lamp source



(a) (b)
Figure 4.9 Successive image frames for a delta wing with a luminescent oil film excited by a UV LED array source

Table 4.2 Summary of strengths and weaknesses of excitation sources

| Excitation Source | Strength | Weakness |
|--------------------|--|--|
| UV blacklight lamp | <ul style="list-style-type: none"> • Low cost • Best excitation wavelength | <ul style="list-style-type: none"> • Fluctuating intensity due to sinusoidal output of lamp |
| UV LED array | <ul style="list-style-type: none"> • Constant intensity due to DC output of LED | <ul style="list-style-type: none"> • Non-ideal excitation wavelength |

4.4 Oil Film Application

Two critical components of the GLOF technique measurement system, luminescent oil and UV excitation have been discussed in the preceding sections. The final component is the application method of the luminescent oil film on the model surface. It is important that a uniform oil film is applied to the model surface to ensure proper oil film development that subsequently leads to the extraction of high quality skin friction fields through data reduction. In the initial phases of development of the GLOF technique, the oil film was applied to the model surface using a paint brush. It is a simple and rapid approach to coating small models (150 x 150 mm). The application of luminescent oil using a paint brush must be done with care to ensure a uniform oil film application. A foam brush can also be used in place of a paint brush. For large surface areas, an alternate application method is desirable to ensure the application of a uniform oil film. A compressed air spray paint gun was evaluated as an approach to applying the luminescent oil on large surface areas. Figure 4.10 is an image of the three oil application apparatus, paint brush, foam brush and spray gun from left to right.

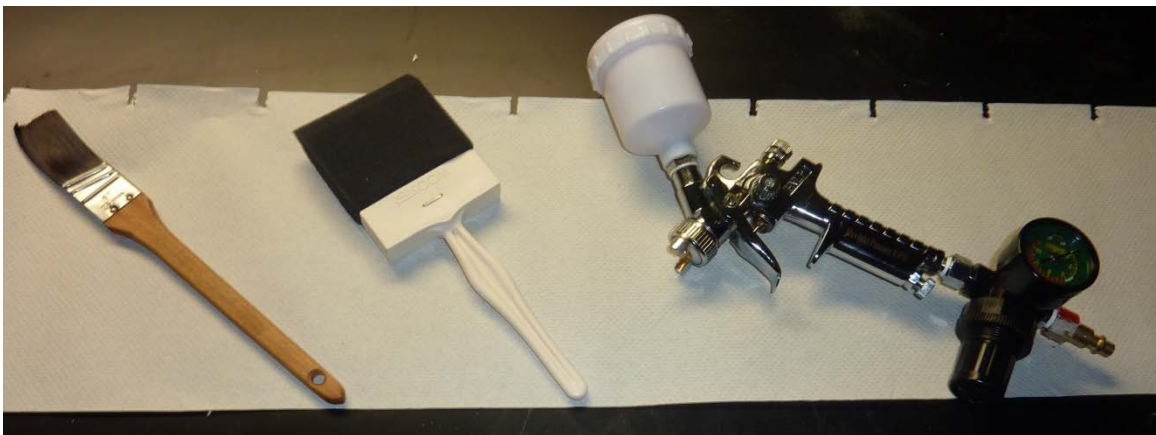
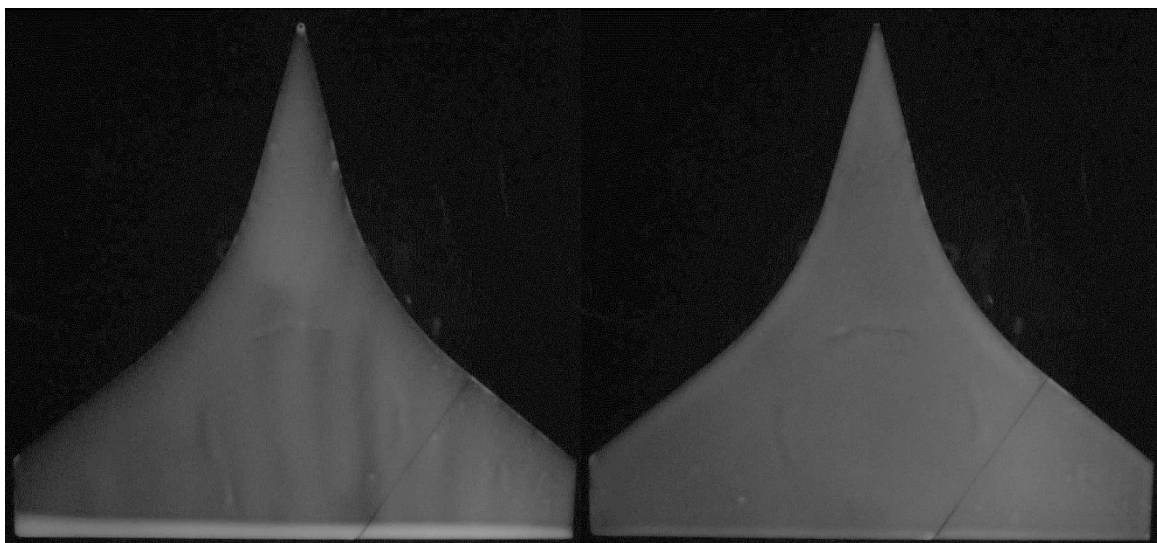


Figure 4.10 Oil application apparatus (from left to right) - paint brush, foam brush, HVLP spray gun

The spray paint gun used was a high volume low pressure (HVLP) gravity feed spray gun manufactured by Central Pneumatic (Model: 46719). The spray gun was set at an air input pressure of 30 pounds per square inch (psi). The spray gun was tested with oil viscosities of 50, 100, 200 and 350 cs. The resulting oil film applied with the spray gun had excellent uniformity and good coverage for all viscosities tested. Higher oil viscosities were not tested but will most likely work with increased air input pressure.

Figure 4.11 (a) and (b) are images comparing luminescent oil application by a paint brush and spray gun respectively. The oil film applied using the spray gun is relatively more uniform than that by a paint brush which exhibits a streaky nature. Naturally, from observing the images, the spray gun application method is preferred although there are instances where it is not feasible to use a spray gun such as a wind tunnel with limited access or a setup which does not permit potential overspray affecting it due to the presence of sensitive instrumentation. In situations that do not permit the use of a spray gun, a foam brush can be used instead of a paint brush and the resulting applied oil film does not exhibit the streaky nature of a paint brush.



(a) (b)
Figure 4.11 Oil film applied to model by (a)paint brush, (b)spray gun

The selection of an application method is highly dependent on two factors, the model size and experimental setup. A foam brush is sufficient for a small models or setups that do not permit the use of a spray gun. A spray gun is the preferable method for larger models as it is impossible to coat these models with a paint or foam brush with sufficient coating coverage and uniformity.

Table 4.3 Summary of strengths and weaknesses of oil film application methods evaluated

| Oil Film Application Method | Pros | Cons |
|------------------------------------|---|--|
| Bristle brush | <ul style="list-style-type: none"> • Ease of use | <ul style="list-style-type: none"> • Slightly uneven oil film coating |
| Foam brush | <ul style="list-style-type: none"> • Ease of use • More even oil film coating compared to bristle brush | <ul style="list-style-type: none"> • Better oil film coat compared to bristle brush but not as uniform as a spray gun |
| Spray gun | <ul style="list-style-type: none"> • Very even oil film coating | <ul style="list-style-type: none"> • Elaborate setup required |

4.5 Summary

The study of refining various aspects of the GLOF technique such as data reduction code, luminescent oil, UV excitation and oil film application was performed. A streamlined data reduction code was written in MATLAB that enables a systematic data reduction procedure. Four modules were written – preprocessor, processor, postprocessor and image manipulation. The preprocessor module receives processing parameter settings including start and end points, time step, masking and filtering and displays the corresponding image sequence related to the set parameters. The processor module performs data reduction using the optical flow algorithm using settings generated by the preprocessor module. The postprocessor module generates high quality visual representations of the calculated skin friction data while the image manipulation module performs spatial transformation and downsampling to selected images.

A few luminescent dyes were also identified and tested. The DFSB K-175 petroleum based dye was selected as a suitable candidate for luminescent oil preparation due to its good mixing characteristics in silicone oil as well as its excellent luminescent properties. Two UV illumination sources; a blacklight lamp and UV LED array were also identified and characterized. It was found that both illumination sources were appropriate in most test cases although the blacklight lamp was limited in a certain applications, particularly in a certain range of image acquisition frame rates due to its sinusoidal light output. Finally, a few oil film application methods were evaluated. Paint and foam brushes were found to be appropriate for luminescent oil film application to small surface areas whereas large surface areas are more suited for a spray gun to ensure a uniform oil film application.

CHAPTER 5

PARAMETRIC ANALYSIS OF DATA REDUCTION VARIABLES

Variables such as spatial resolution, time step, Lagrange multiplier, image filtering and image file format are important in the data reduction phase of the GLOF technique. Therefore, it is essential that a parametric analysis is conducted to study the sensitivity of calculated skin friction fields to these variables. A standard case of a NACA 2412 airfoil is selected for systematic analysis of data reduction variables. The airfoil is set at an angle of attack (AoA) of 0° with a flow speed of 16 m/s corresponding to a Reynolds number of 305,000 based on chord length. The data reduction variables are systematically varied and the corresponding results are compared against computational fluid dynamics (CFD) results from Xfoil using the e^N criterion with $N = 9$ by plotting coefficient of friction (C_f) against streamwise position normalized by chord length (x/c). The value of C_f at 20% chord from Xfoil is used to compute the proportional constant for GLOF measurements to obtain absolute skin friction values. The results obtained from GLOF measurements are in good agreement with predictions from Xfoil. Near the leading edge, it appears that GLOF measurements underestimate the value of C_f due to the angular effect of the luminescent emission resulting from the large surface curvature near the leading edge. GLOF measurements also reveal a separation bubble between 70% to 75% chord before transition which is in agreement with Xfoil predictions. In the turbulent region, GLOF measurements show a larger C_f

magnitude than Xfoil predictions

5.1 Spatial Resolution

Spatial resolution is a parameter that can be adjusted in the image acquisition phase or by performing software based image downsampling. Ideally it is desirable to perform data reduction on the highest resolution image possible to capture the fine details or features such as critical points and separation and reattachment lines in the skin friction fields. Certain restrictions such as camera or lensing setups for a given test facility or computational resource availability might prevent the use of high resolution images. It is then important to study the effects of spatial resolution for a given test case. Figure 5.1 is a plot of the skin friction coefficient vs. streamwise position normalized by the chord length (x/c) for the standard NACA 2412 airfoil test case.

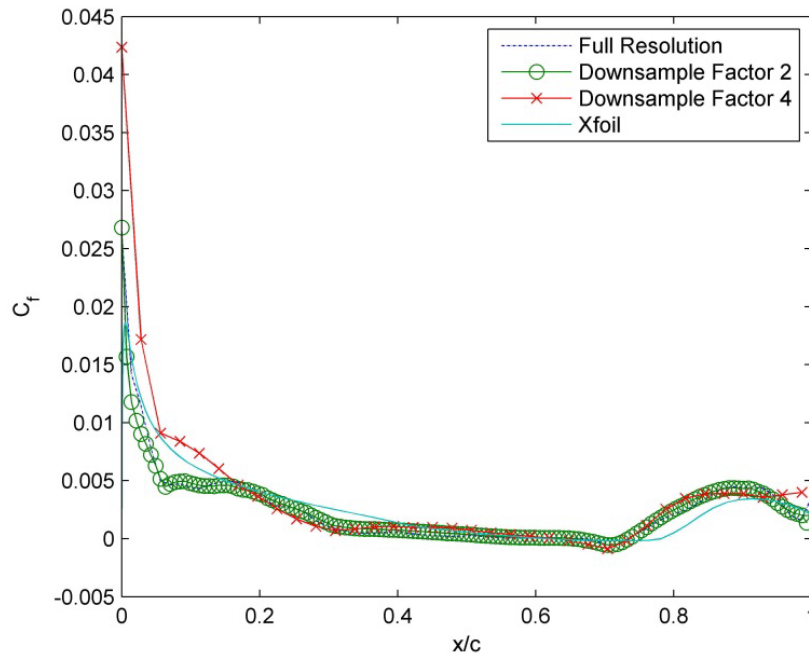


Figure 5.1 Spatial resolution effect on GLOF measurements

Three cases were analyzed - full resolution and two downsample factors of 2 and 4. The downsample factor represents the reduction of the image resolution by a factor of

2 and 4 at 284×31 pixels and 142×17 pixels, respectively, from an original resolution of 569×53 pixels. The downsampling factor of 2 shows good agreement with the full resolution results and Xfoil predictions. For the downsampling factor of 4, the general trend is similar to the full resolution and Xfoil predictions except at the leading edge where it overestimates the value of C_f and can be attributed to the loss of information by downsampling.

To better demonstrate the effects of spatial resolution, a square cylinder junction flow which is a more complicated separated flow case will be considered. The region examined is near the leading edge of a square cylinder on the cylinder-floor junction surface. Figures 5.2 (a), (b) and (c) and 5.3 (a), (b) and (c) are a typical raw image, skin friction magnitude plot and skin friction line plot for the full resolution and downsampled image cases, respectively. Downsampling is performed by a factor of 3 at 190×167 pixels from an original resolution of 550×490 pixels. In examining the skin friction line plots for both cases, the effect of spatial resolution on extraction of the details of a skin friction field is clearly illustrated. The raw images and skin friction magnitude plots for both cases appear to be qualitatively similar especially near the leading edge where multiple bands of high and low oil film intensity exist inferring multiple zones of high and low skin friction which the presence of multiple separation and reattachment lines. When examining the skin friction line plots, the results from the downsampled image set in Figure 5.3 (c) fails to show the secondary separation and reattachment lines as compared to the full resolution case in Figure 5.2 (a) which shows the presence of these lines. This clearly highlights the need to acquire images at a sufficiently high resolution to reconstruct the fine details of a skin friction field.

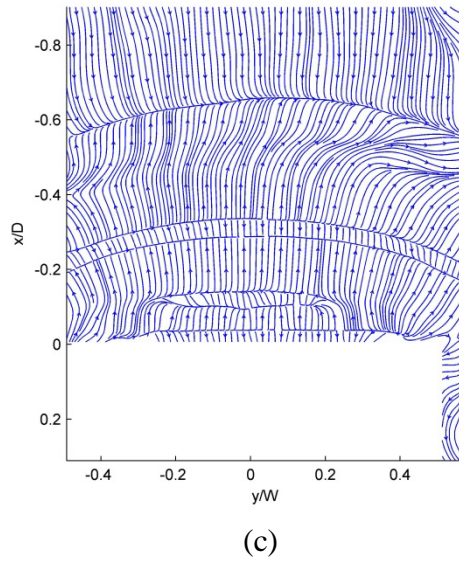
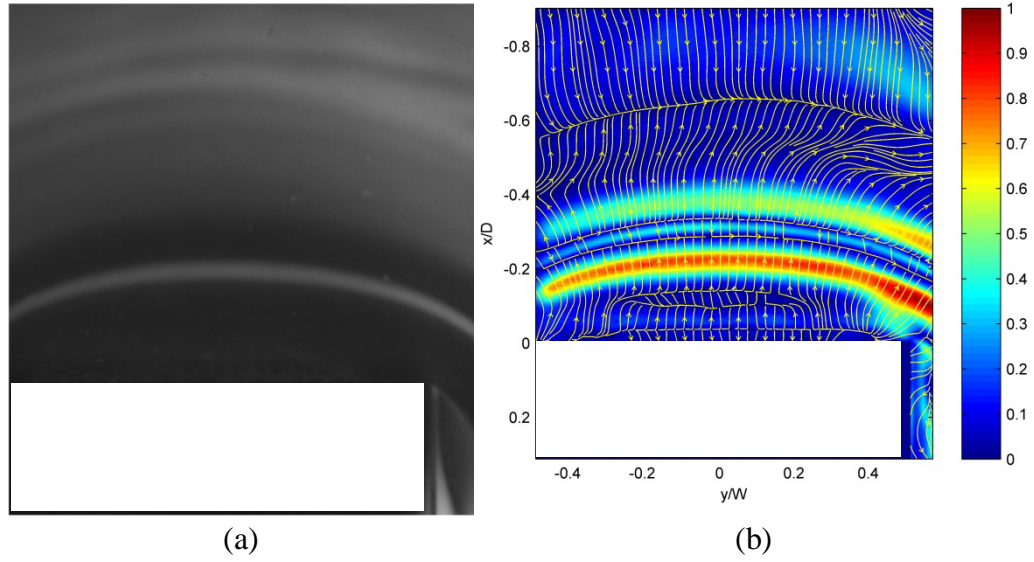


Figure 5.2 GLOF measurements near the leading edge of a square cylinder-floor junction surface for full resolution images, (a) typical raw image, (b) skin friction magnitude plot, (c) skin friction line plot

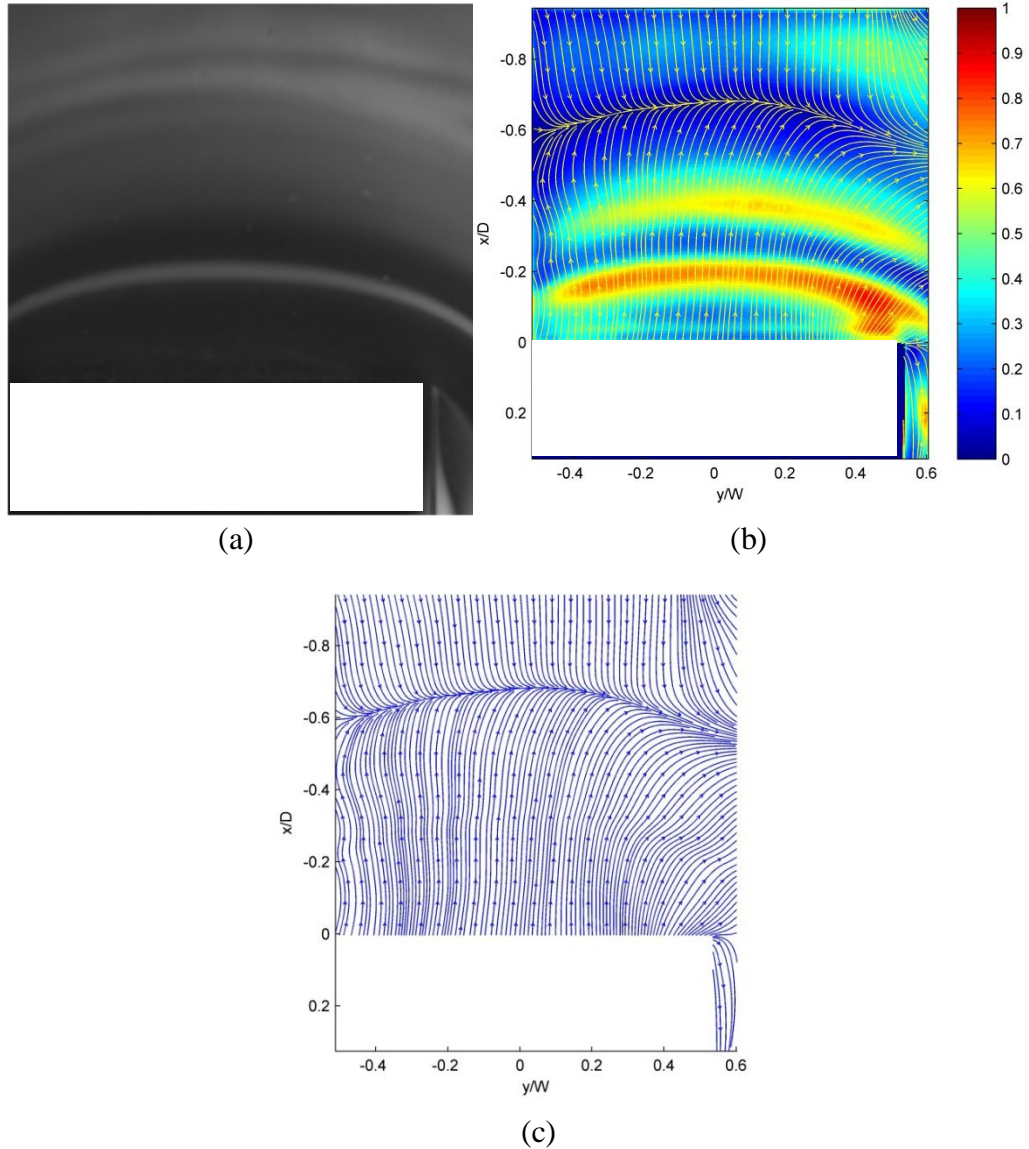


Figure 5.3 GLOF measurements near the leading edge of a square cylinder-floor junction surface for downsampled images, (a)typical raw image, (b)skin friction magnitude plot, (c)skin friction line plot

5.2 Time Step

Time step is another critical parameter in the data reduction process and is comprised of two parameters, time step between images (dt) and the number of snapshot solutions (ns). The time step (dt) represents the time step between images pairs for a single snapshot solution. Typically, dt is selected by observing the oil film development process, ensuring that sufficient change occurs in the oil film between the image pairs.

Along with determining an appropriate dt , a start and end point in the image set is selected such that at the start point, the oil film is just beginning to develop and at the end point the oil film has completely developed. The second parameter, ns is calculated after dt and the start and end points are selected. Since the selection of dt and ns is based on observations, experience and a particular flow case, it is essential to evaluate the effects of these parameters on the calculated skin friction fields. Three different studies were performed, the first setting a fixed dt of 4 seconds and increasing ns from 10 to 30 at a step size of 5. The effect of this is changing the end point of the processed image set. Figure 5.4 is a plot of C_f vs x/c for this case. The plot clearly shows that all the solutions are convergent as the number of solutions is increased in good agreement with Xfoil predictions. The plot also shows that beyond ns of 15, the solutions are collapsed onto each other, thus 15 snapshot solutions is selected as the appropriate number of solutions for a dt of 4 seconds and is used as a benchmark for the subsequent cases.

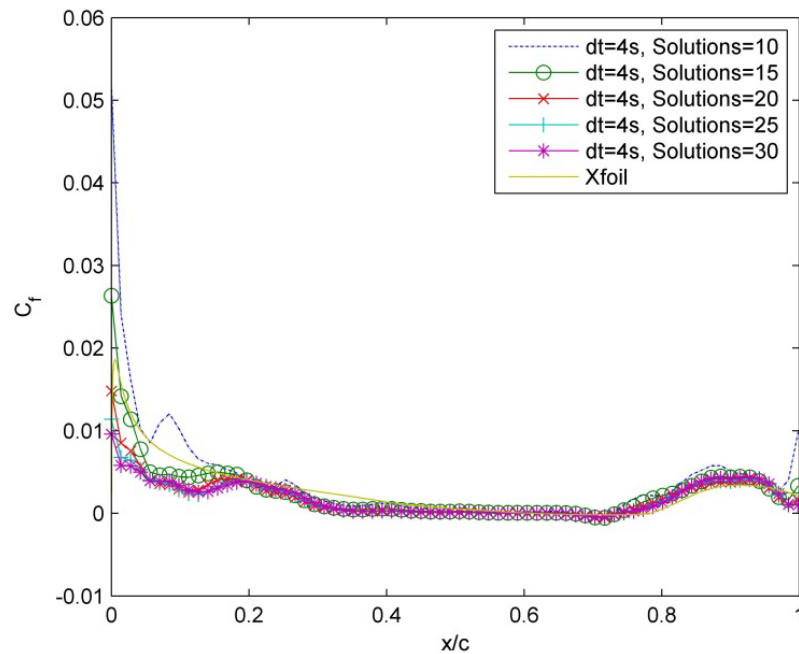


Figure 5.4 Time step effect on GLOF measurements - fixed dt , varying ns

The next case studied was setting a fixed number of solutions and varying dt to lower values. The effect of this is changing the end point of the processed image set, effectively bringing it forward with decreasing dt . Figure 5.5 shows the effects of this case. A fixed number of solutions with decreasing dt causes an inadequate number of images to be processed as the oil film has not completely developed at the end point. Decreasing dt between images also results in a small intensity gradient between image pairs as the oil film has not developed sufficiently between the image pairs. The effects in this case are twofold since fixing the number of solutions coupled with an decreasing dt both have a similar effect on the intensity gradient between image pairs. As discussed in Chapter 2 in Section 2.3, a small intensity gradient is a potential source of error. This is clearly highlighted in Figure 5.5 where the solutions show increased noise as dt is reduced while fixing the number of solutions. This emphasizes that it is necessary to determine a minimum value for dt and ns .

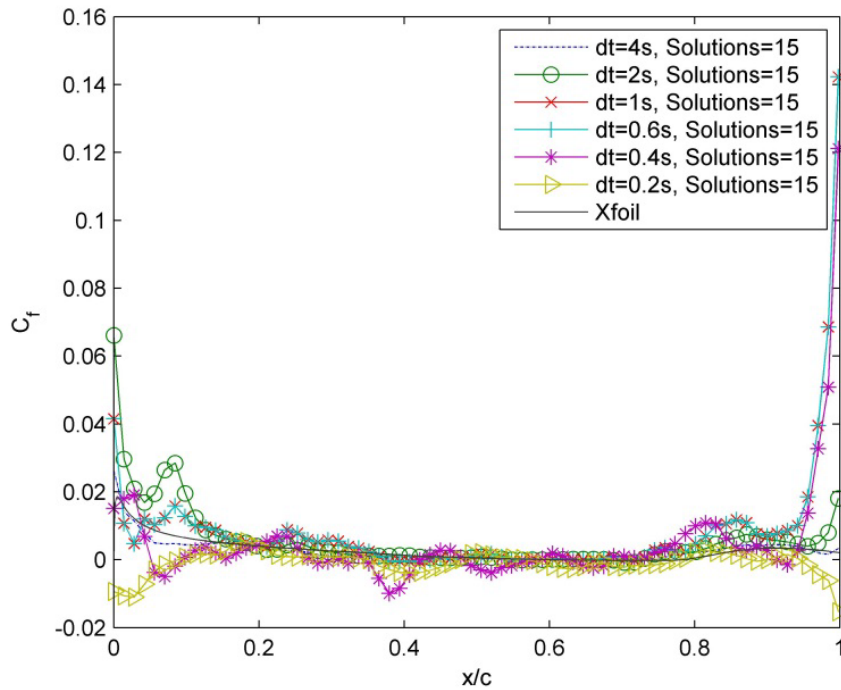


Figure 5.5 Time step effect on GLOF measurements - fixed ns , varying dt

The final case studied was setting a fixed start and end point for the images, and varying dt and number of solutions together to ensure a fixed end point. The case of dt of 4 seconds and number of solutions of 15 is selected as a benchmark, setting the end point at 60 seconds. As dt is reduced, the number of solutions is increased to keep the end point at 60 seconds. Figure 5.6 is the plot of this study. Overall, the solutions are in agreement with the benchmark case, except in the region near the leading edge. The large discrepancy near the leading edge is related to the selection of dt as discussed in the previous case, whereby if a selected dt is too small, the intensity gradient between image pairs is small which leads to large errors near the leading edge although the effect is not as pronounced as the previous case since more solutions are processed and the oil film is completely developed at the end point.

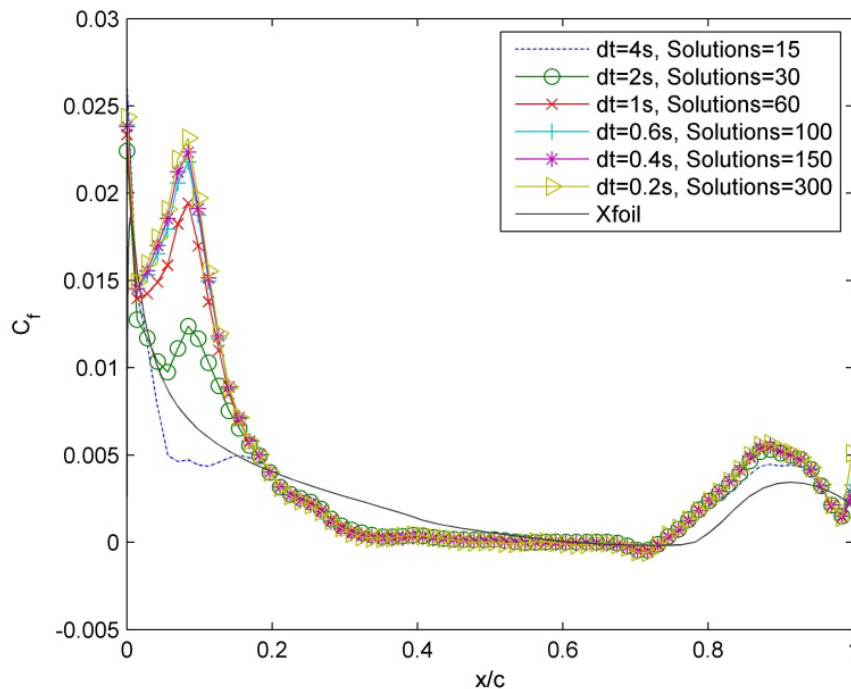


Figure 5.6 Time step effect on GLOF measurements - fixed end point, varying dt and ns

5.3 Lagrange Multiplier

The Lagrange multiplier is a variable in the data reduction algorithm that is typically not manipulated. If the Euler-Lagrange equations (Equation 2.6) are examined, the last term on the left hand side contains the Lagrange multiplier. If this term is examined closely, it is in the same form as the diffusion equation and has an effect of smoothing out the skin friction field. Figure 5.7 is a plot of the effect of the Lagrange multiplier for the benchmark case of dt of 4 seconds with 15 solutions. As can be seen in the plot, varying the Lagrange multiplier has no effect on the computed skin friction values, signaling that the technique is not sensitive to the Lagrange multiplier for this measurement case.

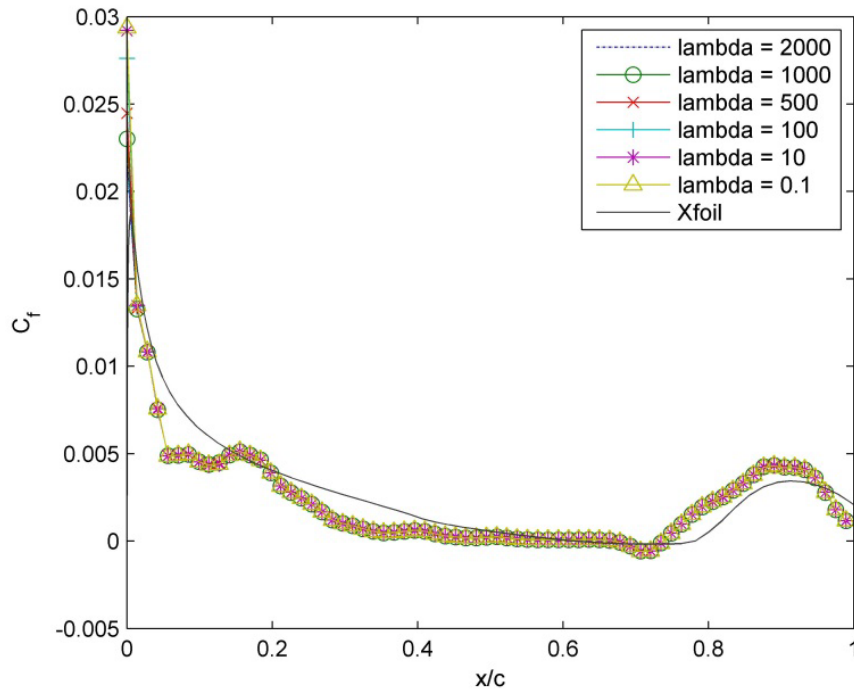


Figure 5.7 Lagrange multiplier effect on GLOF measurements

Lagrange multiplier selection might exhibit some effects in measurement cases where a number of small features in the skin friction field might be smoothed out due to an inappropriately large selection of a Lagrange multiplier. Conversely, a low quality

image set, with a low signal to noise ratio might produce artificial features in the skin friction field which may be alleviated with a large value of the Lagrange multiplier.

5.4 Image Filtering

A Gaussian filter can be applied to an image to reduce noise apparent in images with low signal to noise ratio. Figure 5.8 is a plot of the Gaussian filter effect on GLOF measurements. Overall the application of a Gaussian filter to processed images does not appear to affect the GLOF measurements. A Gaussian filter of 5 square pixels and a standard deviation value of 0.6 shows good agreement with the unfiltered results and XFOIL predictions. When the size of the Gaussian filter is increased to 10 square pixels, the calculated value near the leading edge increases.

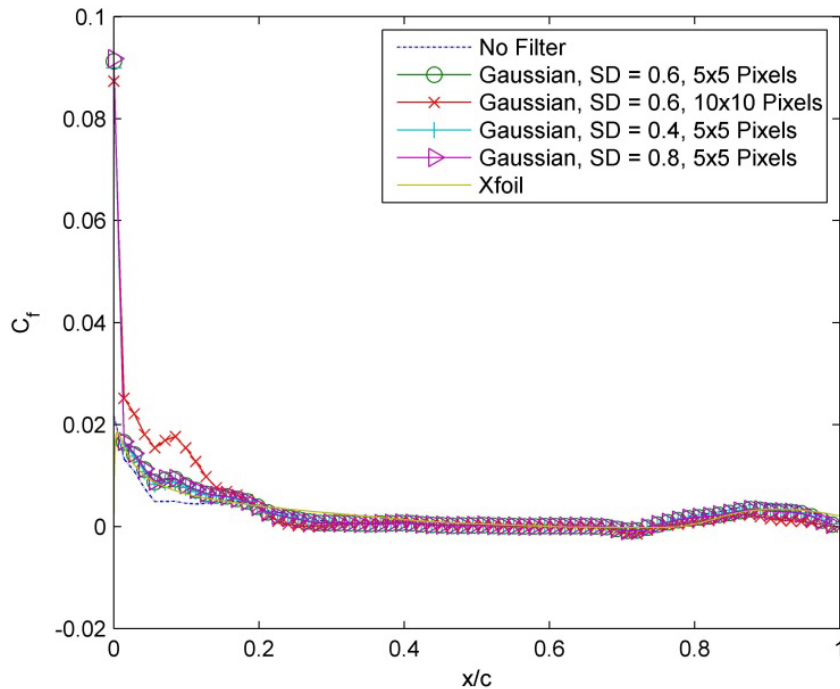


Figure 5.8 Gaussian filter effect on GLOF measurements

This is a plausible effect since a Gaussian filter causes a change in intensity in its domain particularly near the edges of the filter where the values are low. This leads to observed increase in magnitude particularly near the wing leading edge when the filter

size is increased. With a filter size of 5 square pixels, varying the standard deviation does not cause a change in the measured skin friction values. The dominant effect in applying a Gaussian filter is determined to be the size of the filter. A Gaussian filter can be useful in situations where acquired images need to be filtered to improve the signal to noise ratio, although care must be taken in selecting the size of the filter.

5.5 Image File Format

The format of the image file is another variable of interest since different certain file formats such as JPEG employ a compression algorithm to reduce the file size resulting in efficient storage space utilization. Typically an uncompressed image file such as a TIFF file takes up as much as 10 times the storage space of a JPEG file. In applying the JPEG compression algorithm, some information in the image is potentially lost and could affect the calculation of skin friction values. Figure 5.9 shows the comparison of various JPEG formats and the uncompressed TIFF image.

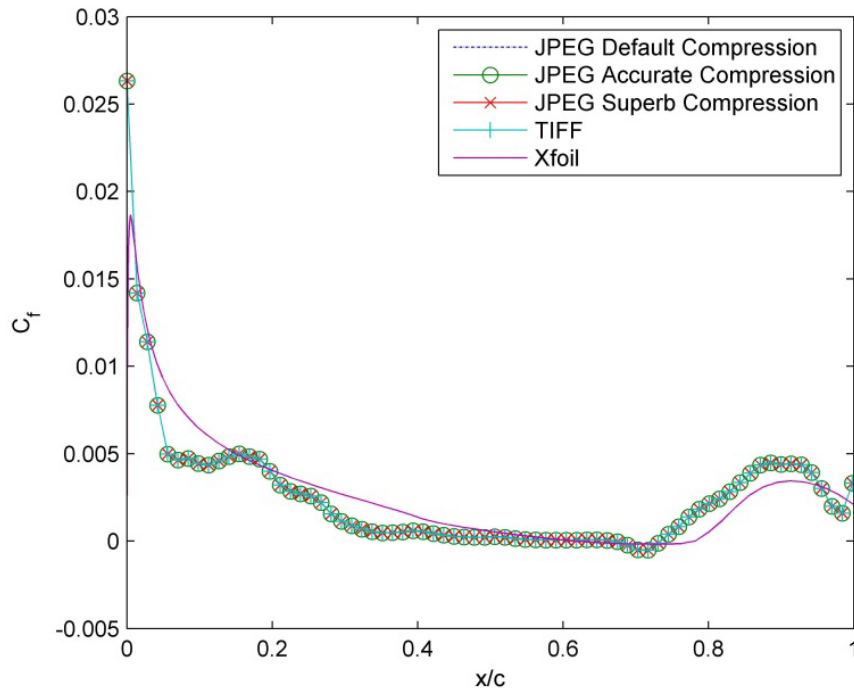


Figure 5.9 Image file format effect on GLOF measurements

The three JPEG formats, default, accurate and superb are at various compression levels in decreasing order, i.e. less compression. Figure 5.9 clearly shows that no difference exists between the calculated skin friction values for compressed and uncompressed formats (JPEG vs. TIFF) although a small standard deviation exists between the respective formats when the raw images are compared against the TIFF image. A standard deviation of 0.08%, 0.07% and 0.02% exists for the default, accurate and superb JPEG compression levels when compared against the TIFF file. This is a very small value of standard deviation that will not give rise to any differences in calculated skin friction values.

5.6 Summary

The parametric analysis of data reduction variables has shown that time step and spatial resolution are sensitive parameters that have to be selected with care to ensure that appropriate results are obtained from the data reduction routine. The proper procedure in selecting time step is setting a start and end point in the image set and subsequently selecting image pairs at a time step that shows sufficient change in the oil film. Spatial resolution should always be maximized. Applying a Gaussian filter to the image introduces a diffusion effect to the image intensity field, particularly on the edges of the filter domain. This effect could subsequently alter the calculated skin friction values in certain regions. Image file format and Lagrange multiplier selection appear to be the least sensitive parameters in this study although there might be certain cases where these parameters might affect the calculated skin friction fields drastically.

CHAPTER 6

LOW ASPECT RATIO NACA 0012 WING

Unmanned aerial vehicles (UAVs) have garnered a lot of attention lately with widespread adoption from hobbyist to scientific and military applications. UAVs are advantageous in situations where a manned aircraft is not practical because of flight envelope, cost or safety constraints. Micro UAVs (MAVs) are a subset of UAVs that as the name suggests, are small in scale. MAVs are typically on the order of tenths of a meter square footprint and sub 100 gram weight including payload. MAVs typically operate in the Reynolds number range of 30,000 to 500,000. The sizing of an MAV is restricted by packaging, handling and mission requirements typically leading to the use of a low aspect ratio (LAR) wing. Numerous experimental [60-65] and numerical [66-67] studies have been performed by researchers on LAR wings. Mueller and DeLaurier [60] presented a comprehensive review of aerodynamics of small vehicles concentrating on fixed and flapping wing MAVs operating in a Reynolds number range below 500,000. They discussed the unique performance characteristics of LAR wings, specifically delayed stall compared to a similar high aspect ratio wing planform. This occurs due to the combination of linear and non-linear lifting mechanisms, linear lift being the lift due to circulation and non-linear lift related to the interaction between the tip vortices and suction side of the wing post separation. The tip vortex is formed due to the pressure difference between the wing lower surface (pressure side) and upper surface (suction

side) causing a vortex to roll up towards the suction side. Once flow separation occurs, the tip vortices interact with the separated flow region on the wing upper surface forming counter rotating vortices which create a low pressure region on the suction side of the wing. This leads to an increase in the lift curve slope and maximum lift coefficient compared to a high aspect ratio wing of the same planform. This non-linear lifting mechanism is similar to the flow over a delta wing which is dominated by the leading edge vortices formed on the upper surface of the delta wing. Extensive experimental work has been performed by various researchers on the effects of aspect ratio on the lifting characteristics of various wing planforms. Mueller et.al [62, 63] summarized that aspect ratio is a dominant factor followed by planform shape and Reynolds number in the lifting characteristics of finite (low aspect ratio) wings. It is especially apparent at aspect ratios below 1.25 where lifting characteristics are largely non-linear.

Previous work has focused on force measurements and particle image velocimetry (PIV) measurements and limited qualitative cross flow and surface flow visualizations of the vortical structures associated with the LAR wing. No quantitative global skin friction diagnostics have been performed on LAR wings in the past. The availability of the GLOF technique enables quantitative measurements of skin friction fields which will allow the study of the complex flow structures on the upper surface of the LAR wing by analyzing the skin friction topology.

6.1 Experimental Setup

In this study, the global skin friction fields on a LAR ($AR = 1.2$) NACA 0012 wing will be measured with the GLOF technique. The measurements will be focused on the evolution of the skin friction fields as the angle of attack (AoA) is increased. The

wing used was made of plastic sprayed with a white base paint (LustreKote manufactured by MonoKote). The wing had a span and chord length of 153 mm and 127 mm, respectively with cropped wing tips. Figure 6.1 is an image of the LAR wing used for tests.



Figure 6.1 Image of LAR NACA 0012 Wing

Experiments were conducted in the Western Michigan University Small Wind Tunnel (SWT) facility at a flow speed of 20 m/s corresponding to a Reynolds number based on chord length (Re_c) of 159,000. Measurements were performed at AoAs of 0° , 5° , 12° , 13.5° , 14° , 16° and 18° for the wing upper surface and AoA of 18° for the wing side surface and upper surface with a leading edge roughness strip. Figure 6.2 is an illustration of the experimental setup used for this measurement and Figures 6.3 (a), (b), (c) and (d) are a typical luminescent oil image, skin friction line plot, skin friction vector plot and skin friction magnitude plot, respectively for the wing upper surface at 18° AoA.

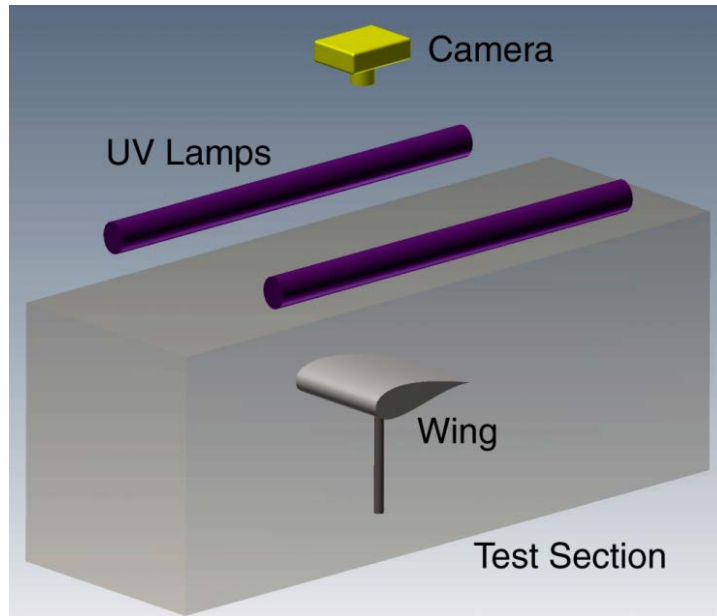


Figure 6.2 Illustration of experimental setup for GLOF measurements on a LAR NACA 0012 wing

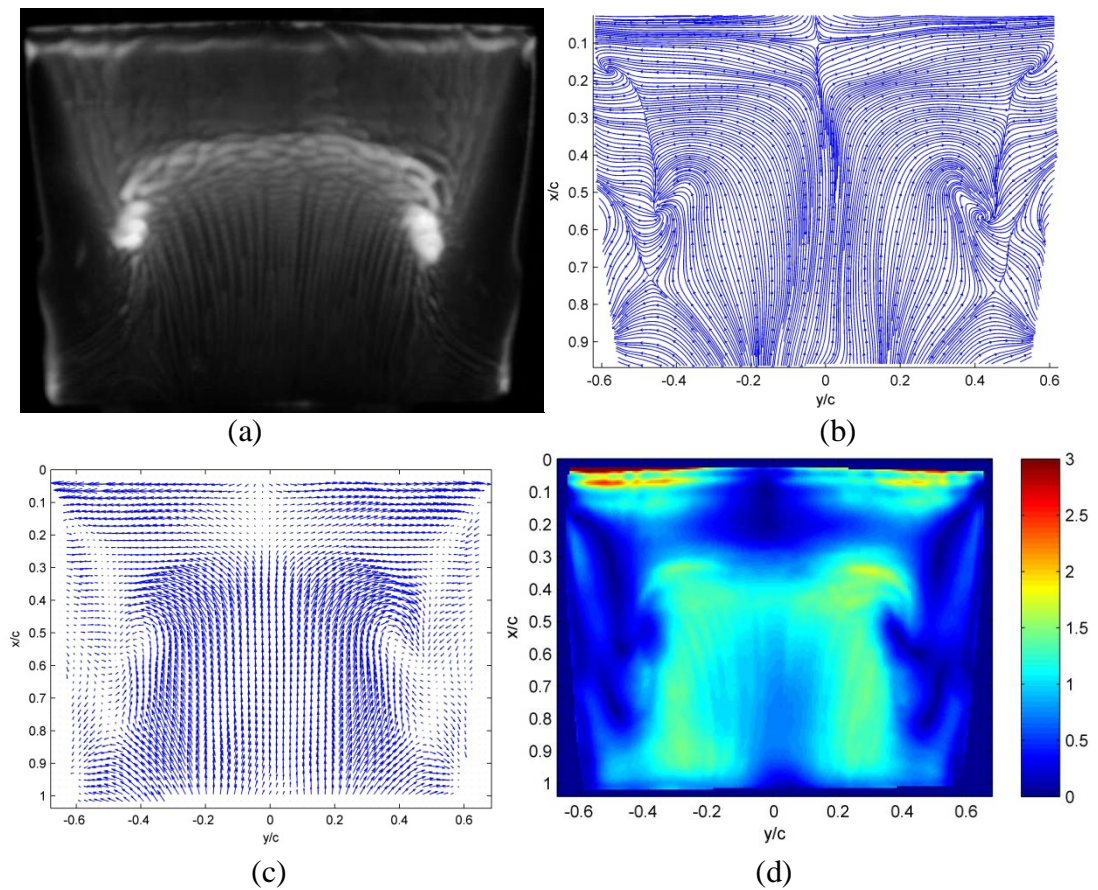


Figure 6.3 NACA 0012 LAR wing at 18° AoA, (a) typical luminescent oil image, (b) skin friction lines, (c) skin friction vectors and (d) relative skin friction magnitude

6.2 Evolution of Skin Friction Field Topology by Varying Angle of Attack

The evolution of the skin friction field on the upper surface of the LAR NACA 0012 wing is shown in Figures 6.4 through 6.9 for AoAs of 0° , 5° , 12° , 13.5° , 14° and 16° , respectively. For AoA of 0° , as shown in Figure 6.4, the flow is mainly 2D near the leading edge and mid-span of the wing from leading edge to trailing edge with 3D effects visible near the wing tips. For AoA of 5° , although the flow remains nearly 2D along the leading edge, the skin friction lines are considerably bent and converged along the spanwise direction at about 30% chord as indicated in Figure 6.5. The converged skin friction lines indicate the beginning of the formation of a separation line.

As the AoA is increased to 12° , the skin friction lines are converged along the leading edge toward mid span from the wing tips as illustrated in Figure 6.6. This indicates that the flow is separated partially near the tips along the leading edge, while the flow remains attached near the middle section of the wing. Two attachment lines are formed at about 20% chord on the left and right sides of the wing, but they are not connected. Since the converged skin friction lines do not originate from a saddle or node, the flow separation near the leading edge is open, similar to observations by Wang [45]. No isolated singular point is identified on the wing upper surface in this case. The evolution of the flow on the upper surface of the LAR wing into open separation before reaching a critical AoA at which the isolated singular points occur is similar to an example presented by Tobak and Peake [44] for a body of revolution.

As indicated in Figure 6.7, a saddle (S_1) occurs near the middle of the leading edge at AoA of 13.5° . This is a critical AoA just before the flow becomes fully separated. In contrast to the case of AoA of 12° , the two attachment lines on the left and

right sides of the wing are connected at S_1 . The leading-edge separation bubble extends from the left to right wing tip. As AoA is increased to 14° , a catastrophic topological change takes place related to the bursting of the leading edge separation bubble formed at AoA of 13.5° . This phenomenon is clearly seen in Figure 6.8. Also visible in Figure 6.8 are two primary spiraling nodes N_1 and N_2 associated with tornado-like vortices. Two saddles S_1 and S_2 occur near the trailing edge in the region of the wing tips. As the AoA is increased to 16° , the skin friction fields observed are qualitatively similar to the case of AoA of 18° as seen in Figure 6.3 (b).

Lift and drag measurements were also conducted for the wing at AoAs of 0° , 5° , 10° , 12° , 13.5° , 14° , 16° , 18° and 20° . Lift measurements were compared to the Helmbold approximation [2] as seen in the coefficient of lift (C_L) vs. AoA plot in Figure 6.10 (a). The Helmbold approximation is a reasonable approximation given for wings of finite aspect ratio. As seen in Figure 6.10 (a), the lift curve for the experimental measurements agrees well with the Helmbold approximation. The experimental measurements start to deviate from the approximation as the AoA increases above 14° at which full flow separation occurs. It is also clearly seen that beyond 14° AoA, the lift does not decrease as is typically observed with high aspect ratio wings; instead it increases due to the non-linear lifting mechanism discussed earlier. Figure 6.10 (b) is a plot of the drag coefficient (C_D) vs AoA for experimental measurements compared with the induced drag approximation. The Oswald efficiency factor (e) is set as a fitting parameter at a value of 0.6. The drag curve for the experimental and induced drag approximation agrees well up to an AoA of 13.5° where it starts to deviate and increase drastically due to the formation of vortical structures on the upper surface post separation.

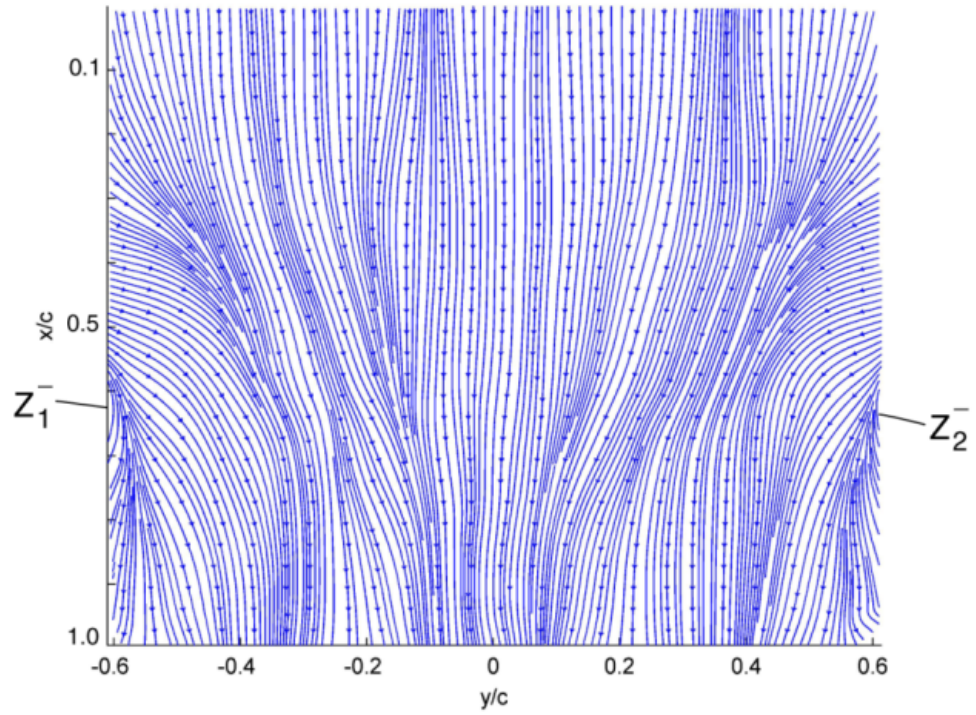


Figure 6.4 Skin friction lines on the upper surface of a LAR NACA 0012 wing at 0° AoA

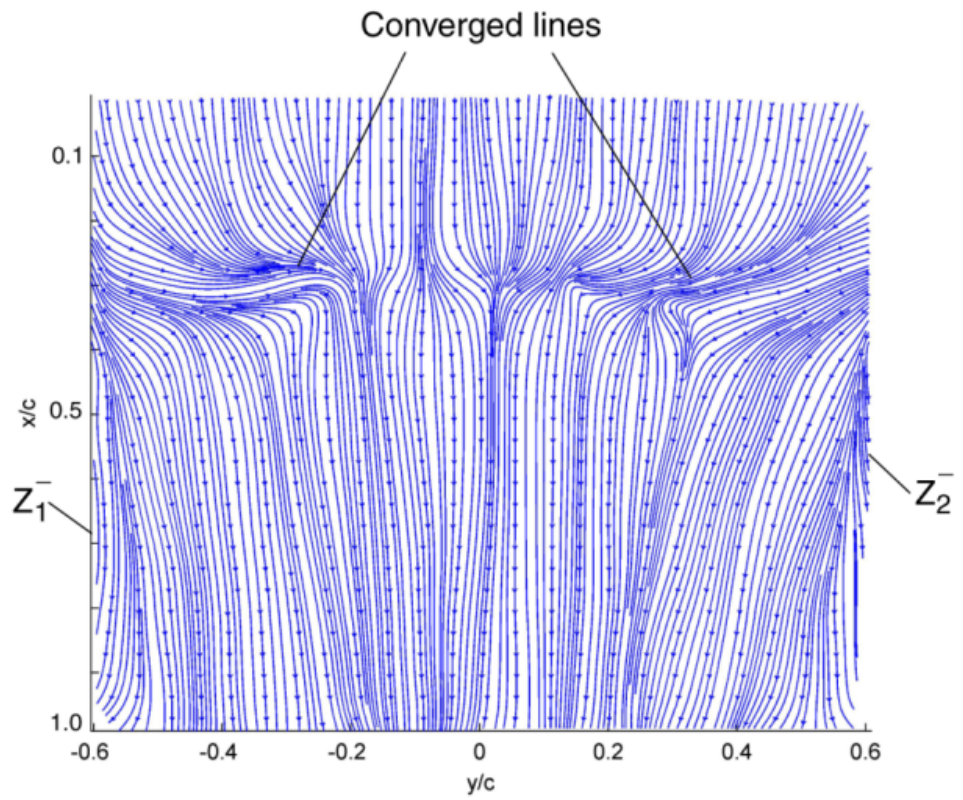


Figure 6.5 Skin friction lines on the upper surface of a LAR NACA 0012 wing at 5° AoA

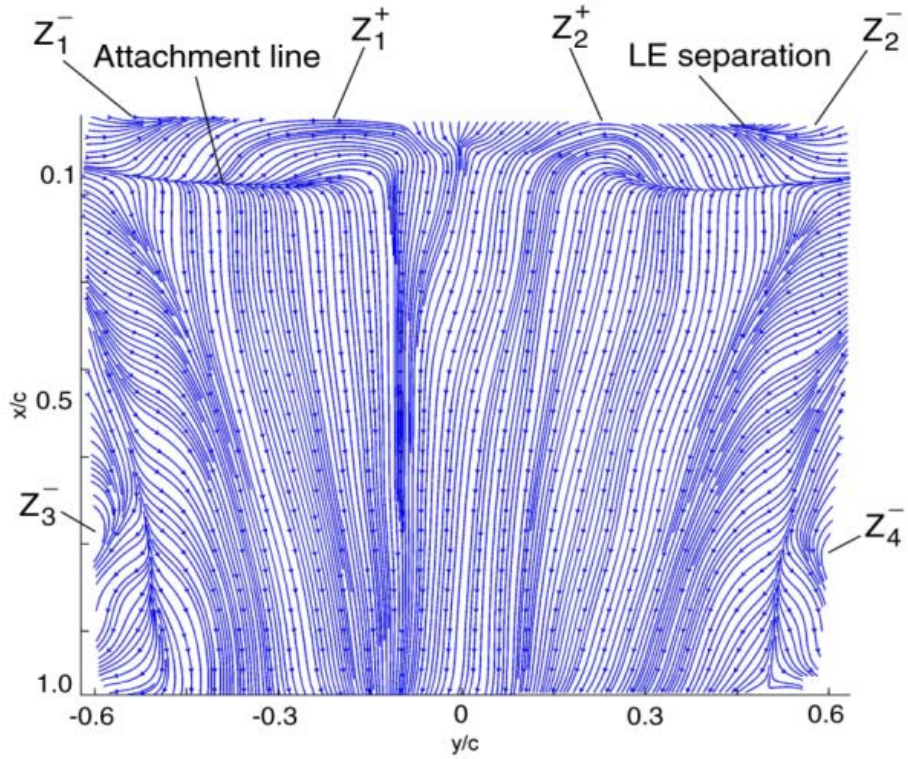


Figure 6.6 Skin friction lines on the upper surface of a LAR NACA 0012 wing at 12° AoA

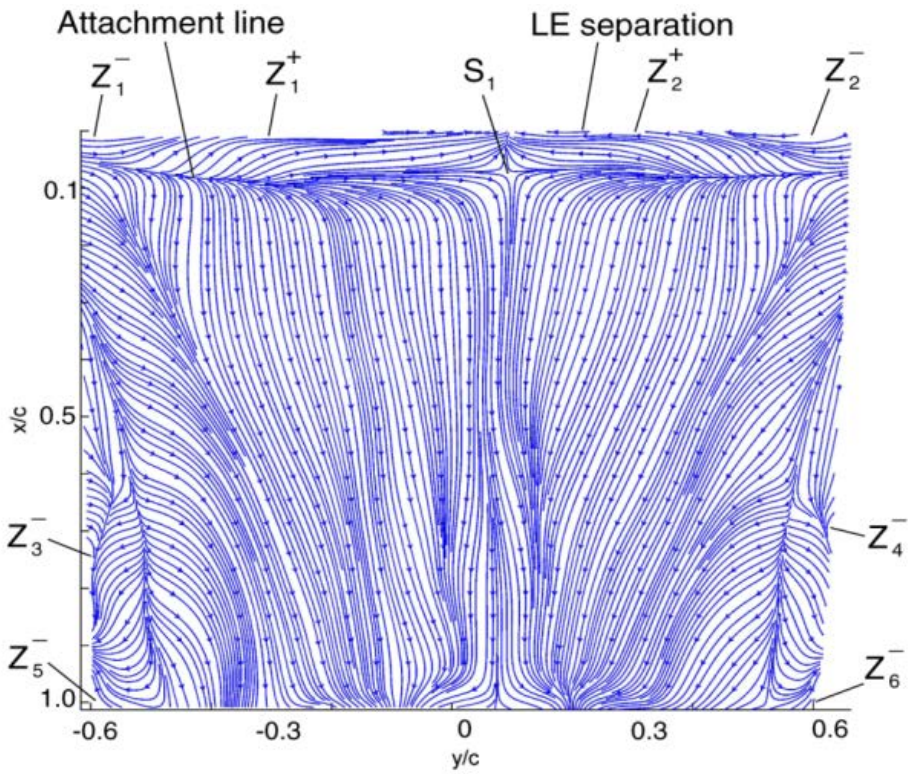


Figure 6.7 Skin friction lines on the upper surface of a LAR NACA 0012 wing at 13.5° AoA

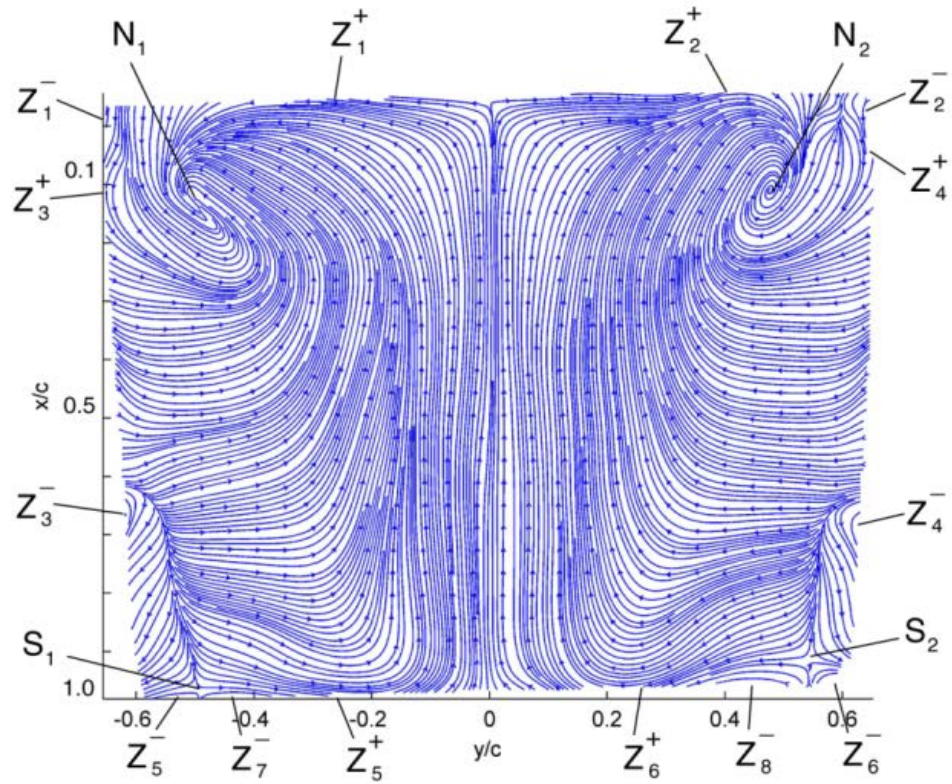


Figure 6.8 Skin friction lines on the upper Surface of a LAR NACA 0012 wing at 14° AoA

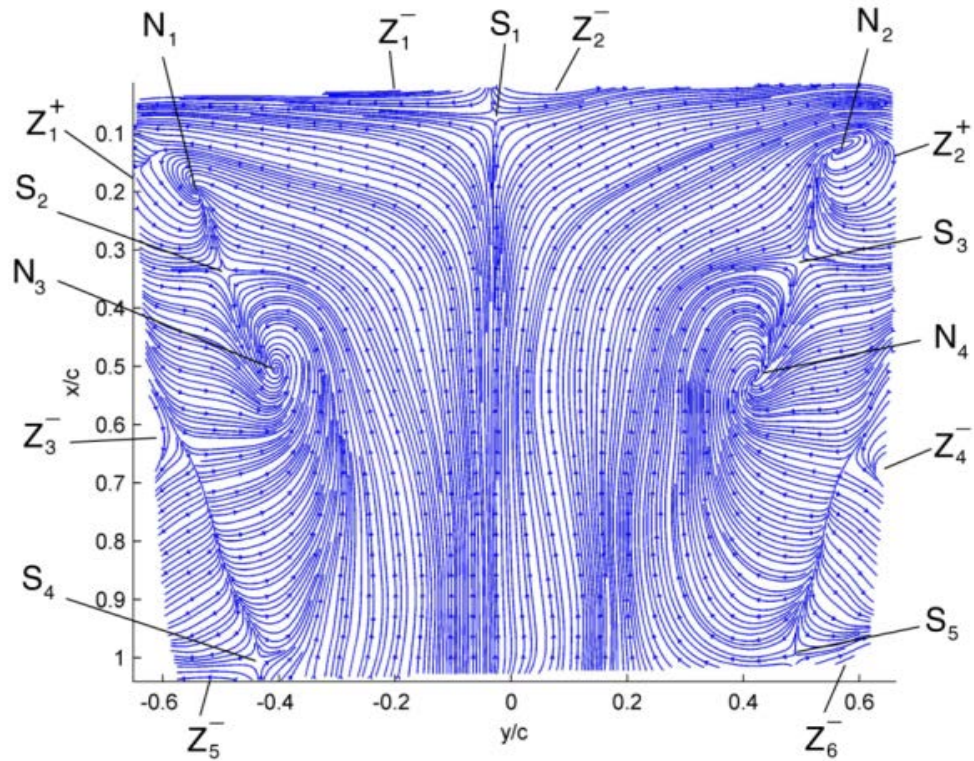
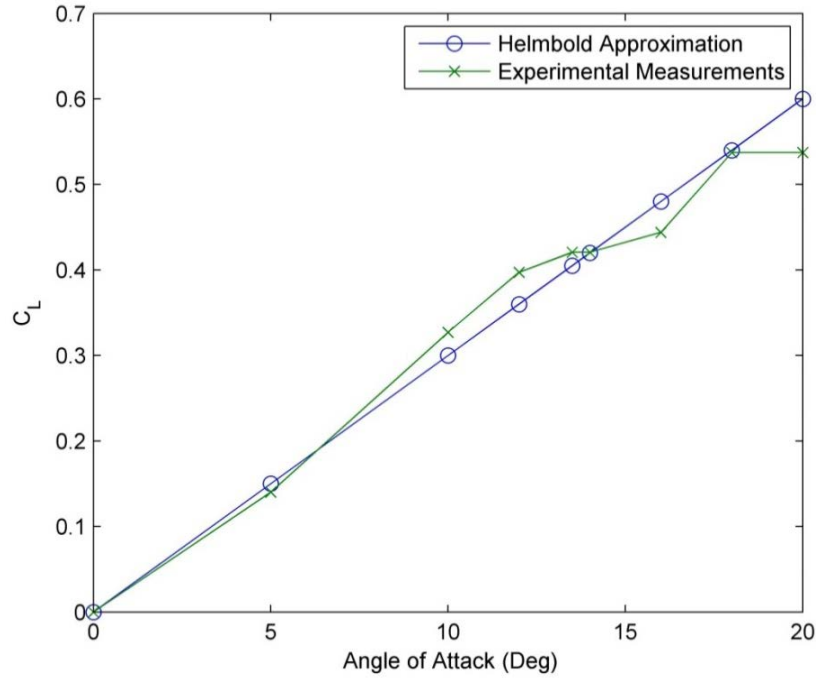
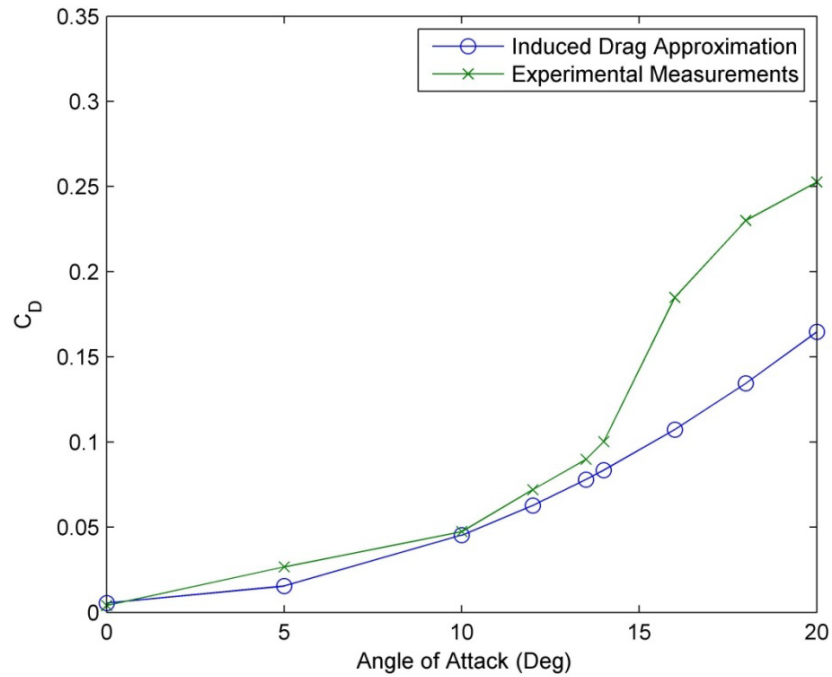


Figure 6.9 Skin friction lines on the upper surface of a LAR NACA 0012 wing at 16° AoA



(a)



(b)

Figure 6.10 Force data vs. angle of attack, (a) C_L vs. AoA (experimental measurements vs. Helmbold approximation) and (b) C_D vs. AoA (experimental measurements vs. induced drag approximation)

6.3 Skin Friction Topology Constraint Analysis

Detailed topological analysis is conducted on the skin friction fields. Isolated singular points and boundary switch points are identified and the Poincare-Bendixson (P-B) index formula is applied to verify that the skin friction vector fields obey the conservation law. The case of the LAR wing at 18° AoA is selected as a typical case for detailed analysis. For this case, the upper surface, side surface and upper surface with a leading edge trip are analyzed in detail. The skin friction fields for AoAs of 0° , 5° , 12° , 13.5° , 14° and 16° are also analyzed to verify the compliance with the conservation law given by the P-B index formula.

6.3.1 Wing Upper Surface at 18° AoA

The skin friction field on the upper surface of the LAR wing at 18° AoA is shown in Figure 6.11, indicating the complex topological structures in this separated flow. First, a closed boundary that consists of the leading, side and trailing edges of the wing is considered and the isolated singular points enclosed by the boundary and the switch points on the boundary are identified. Flow separation starts at saddle (S_1) near the leading edge. Separation lines extend from S_1 along the spanwise direction towards the wing tips. There are two small spiraling nodes N_1 and N_2 near the wing tips that are connected to saddles S_2 and S_3 , respectively. The primary spiraling nodes N_3 and N_4 on the surface are also connected to saddles S_2 and S_3 , respectively. Two other saddles S_4 and S_5 occur below the primary spiraling nodes, N_3 and N_4 . There are a total number of 4 nodes and 5 saddles on the upper surface. The zoomed-in views of the singular points and switch points are shown in Fig. 6.12 (a), (b) and (c). The separation and attachment lines between the isolated singular points are clearly identified in Figure 6.11. The

typical closed separation patterns from a saddle to a spiraling node are seen in this case, such as the combinations of $S_2 - N_1$, $S_3 - N_2$, $S_4 - N_3$, and $S_5 - N_4$ as observed in previous work by Tobak and Peake [44], Perry and Chong [55] and Surana et al. [42-43]. Since a spiraling node is commonly associated with the presence of a standing vortex as described by Délery [33], the skin friction topology on the upper surface of the wing is a result of the interaction between the tip vortices and the separated flow.

The switch points on a closed boundary that consists of the leading, side and trailing edges are identified as shown in Figure 6.11 denoted by Z^+ or Z^- for positive or negative switch points, respectively. There are inflow and outflow segments near the leading edge, which are separated by the negative switch points Z_1^- and Z_2^- . Two positive switch points Z_1^+ and Z_2^+ on the side edges are identified, which are primarily induced by the spiraling nodes N_1 and N_2 that are associated with the tornado-like vortices. The negative switch points Z_3^- and Z_4^- near the side edges of the boundary (wing tips) are induced by the interaction between the tip vortices and the standing vortices connected with the primary spiraling nodes N_3 and N_4 . On the trailing edge, the negative switch points Z_5^- and Z_6^- are located at the corners where the inflow and outflow segments are separated. A negative switch point is often identified at a sharp corner of a boundary where the flow enters the region from one edge and leaves through another.

The skin friction field on the upper surface at AoA of 18° contains 4 nodes and 5 saddles, 2 positive switch points and 6 negative switch points. The boundary encloses a total number of 4 nodes ($\#N = 4$), 5 saddles ($\#S = 5$), 2 positive switch points ($Z^+=2$) and 6 negative switch points ($Z^-=6$). Applying the P-B index formula $\#N - \#S = 1 + (\#Z^+ - \#Z^-)/2$ shows that the conservation law is satisfied for the

skin friction field in this case. The P-B formula is also satisfied in a local region enclosed by an arbitrary penetrable boundary in a 2D vector field. The zoomed-in views in Figures 6.12 (a) through (c) are a good example of local separation patterns for illustration, in which new boundary switch points are generated by selection of an arbitrary boundary in these local regions. The boundary switch points are easily identifiable. In Figure 6.12(a), only one saddle exists. Thus $\#N = 0$, $\#S = 1$, $Z^+ = 0$ and $\#Z^- = 4$. Applying the P-B index formula confirms that the conservation law is satisfied. Similar results are obtained when analysis is performed on local regions of N_2 and N_4 , shown in Figures 6.12 (b) and (c). In both Figures 6.12(b) and (c), $\#N = 1$, $\#S = 1$, $Z^+ = 1$ and $\#Z^- = 3$. Applying the P-B index formula clearly shows the conservation law is satisfied in these local regions.

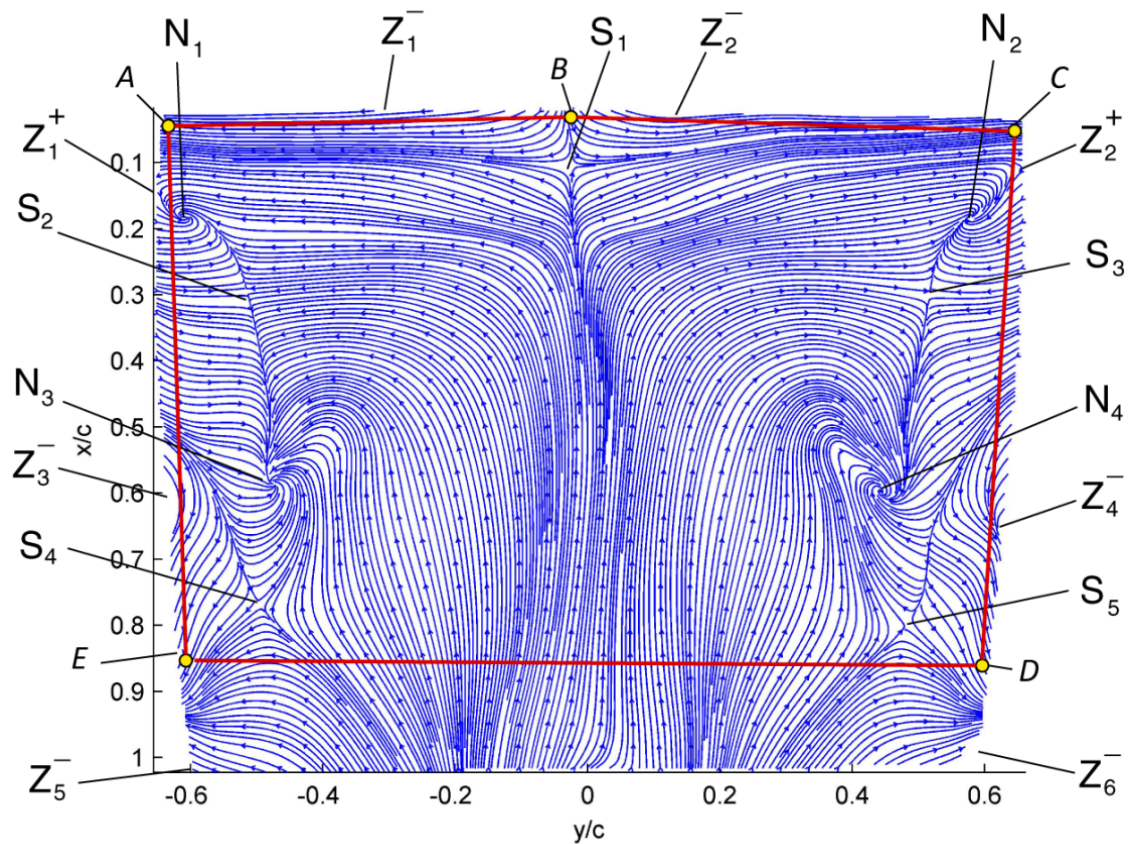


Figure 6.11 Skin friction lines on the upper surface of a LAR NACA 0012 wing at 18° AoA

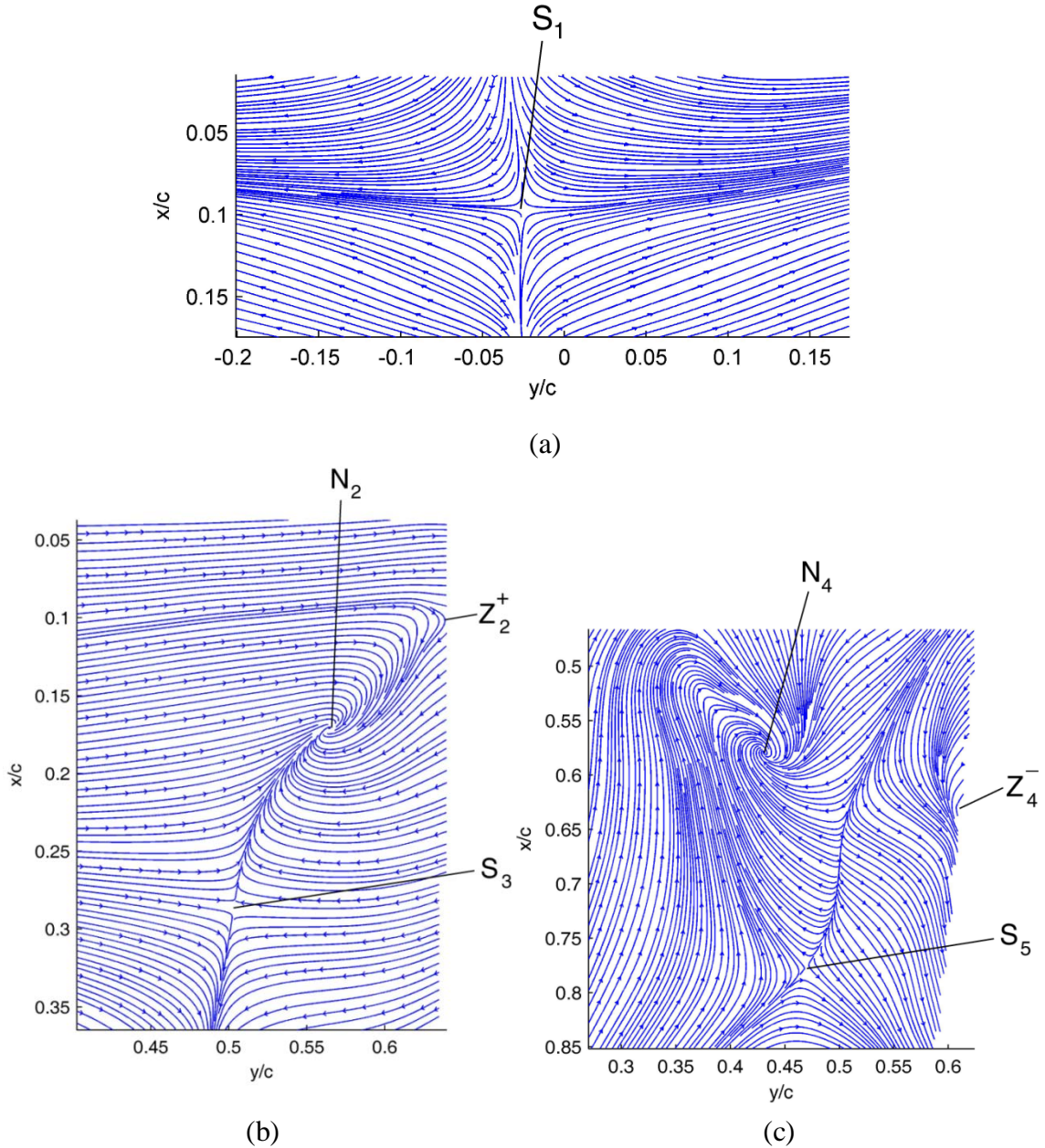


Figure 6.12 Zoomed-in views near singular points (a) S_1 , (b) N_2 and (c) N_4 on the upper surface of a LAR NACA 0012 wing at 18° AoA

6.3.2 Wing Side Surface at 18° AoA

Skin friction measurements were also conducted on the wing side surface at 18° AoA. Figure 6.13 shows the skin friction lines on the side surface of the wing at its tip. The zoomed-in view near the leading edge indicates that an attachment line and a separation line originate from the source node (N_1) and saddle (S_1), respectively. The

connection between N_1 and S_1 is clearly visible in Figure 6.13 although the separation line that originates from the saddle (S_1) does not end at a spiraling or sink node. The boundary switch points are clearly identified in Figure 6.13. The two negative switch points Z_1^- and Z_2^- are also clearly visualized in Figure 6.13 near the leading edge. A local boundary ABCDA is defined and the P-B formula is applied. The conservation law is shown to be satisfied in this case. It can also be observed that a number of inflow and outflow segments exist towards the trailing edge of the wing where no isolated singular points exist. Three positive switch points Z_2^+ , Z_3^+ , and Z_4^+ and 4 negative switch points Z_3^- , Z_4^- , Z_5^- and Z_6^- are identified. The zoomed-in views near these switch points are shown in Figures 6.14 (a) and (b). In applying the P-B formula to this surface, with $\#N = 1$, $\#S = 1$, $Z^+ = 4$ and $\#Z^- = 6$ the conservation law is satisfied.

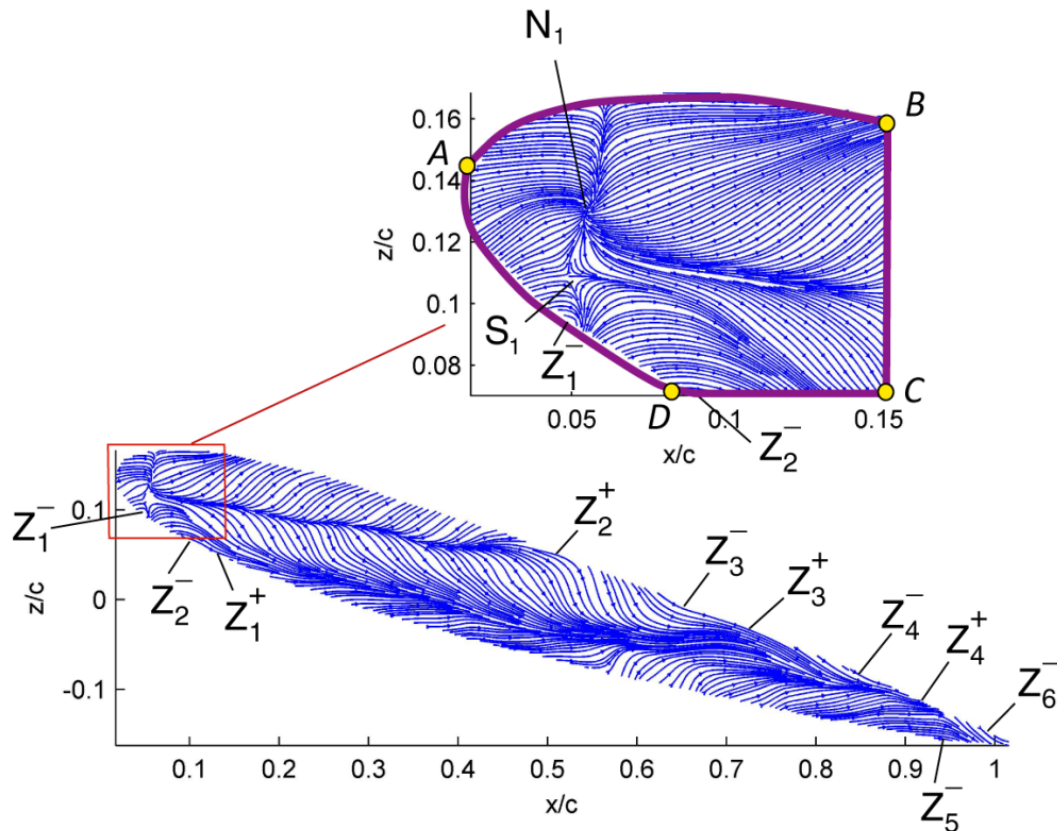
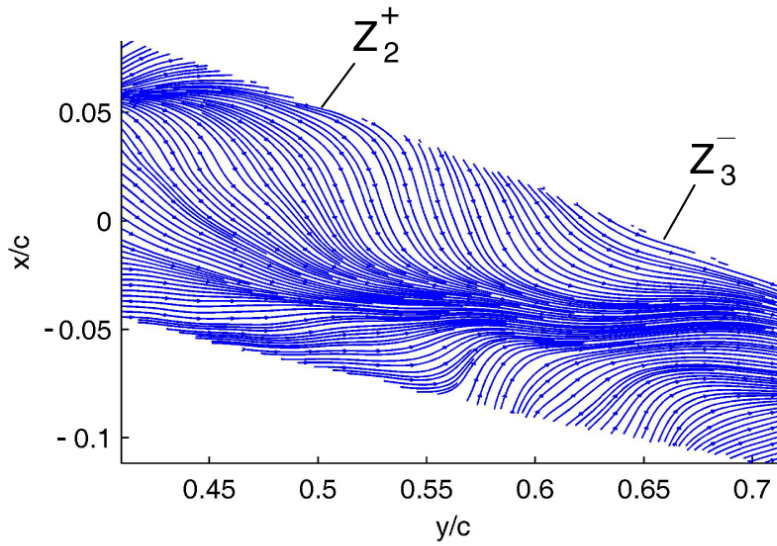
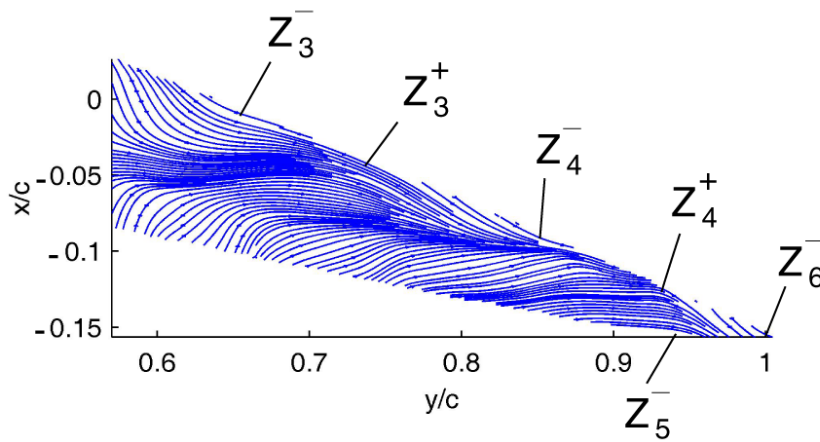


Figure 6.13 Skin friction lines on the side surface of a LAR NACA 0012 wing at 18° AoA



(a)



(b)

Figure 6.14 Zoomed-in views near boundary switch points (a) Z_2^+ and Z_3^- and (b) Z_3^+ , Z_4^+ and Z_3^- , Z_4^- , Z_5^- , Z_6^- on the side surface of a LAR NACA 0012 wing at 18° AoA

6.3.3 Wing Upper Surface with Leading Edge Roughness Strip at 18° AoA

An interesting topological change occurs when the flow is tripped by a roughness strip placed along the leading edge. The roughness strip is formed by placing a 0.075 mm thick white Mylar sheet from the leading edge to the trailing edge i.e., there is a 0.075 mm high step at the leading edge, as illustrated in Figure 6.15. The skin friction line plot of the tripped flow on the upper surface at AoA 18° is shown in Figure 6.15 with

the zoomed-in views of skin friction lines in the vicinity of singular points and boundary switch points shown in Figures 6.16 (a) through (c). In comparison to the non-tripped case in Figure 6.11, it is found that the two primary spiraling nodes are located at approximately the same positions. The topological structures near the leading edge however, are significantly altered. The skin friction lines are observed to converge along the corners of leading edge, indicating the beginning of separation. As shown in Figure 6.15, the flow is partially reattached at source node (N_1), followed by secondary separation at saddle (S_1). As indicated in Figure 6.16 (b), the positive switch point Z_1^+ and the negative switch point Z_1^- occur along the left side of the leading edge and conversely Z_2^+ and Z_2^- on the right side. The negative switch points Z_3^- and Z_4^- on the side edges close to the wing tip near the leading edge are associated with saddles S_2 and S_3 . The interaction between the saddles S_4 and S_5 and the spiraling nodes N_2 and N_3 are responsible in generating the negative switch points Z_5^- , Z_6^- , Z_7^- and Z_8^- .

To highlight the change caused by the roughness strip towards the formation of the boundary switch points, a polygon ABCDA is defined in Figure 6.15, in which all the isolated singular points are enclosed. When compared with the case of the non-tripped wing at 18° AoA in Figure 6.11, a qualitative change observed is the occurrence of positive switch points Z_1^+ and Z_2^+ along the leading edge due to the influence of the roughness strip. The locations of other switch points in the tripped and non-tripped flows are unchanged. The number of the singular points and switch points on the upper surface in Figure 6.15 are $\#N = 3$, $\#S = 5$, $Z^+ = 2$ and $\#Z^- = 8$. Applying the P-B index formula, the conservation law is satisfied. The conservation law is also satisfied for the local regions defined in Figures 6.16 (a) through (c).

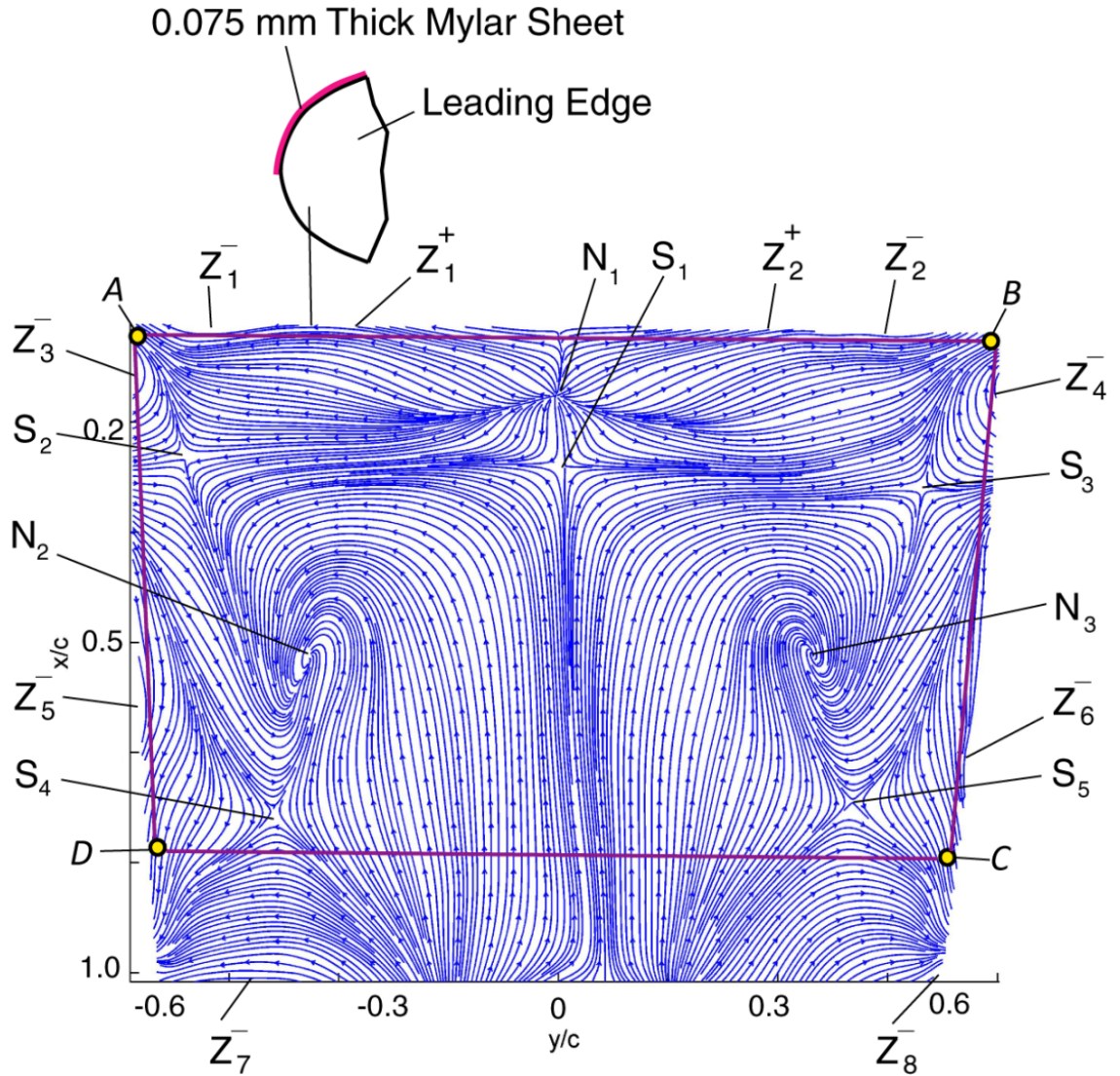
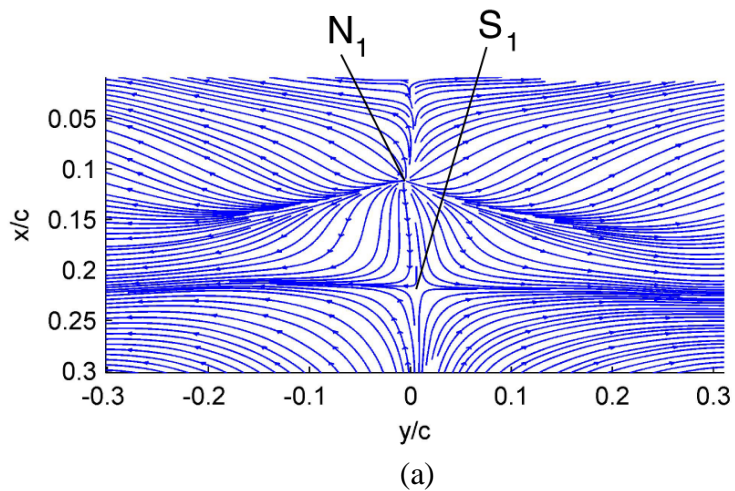
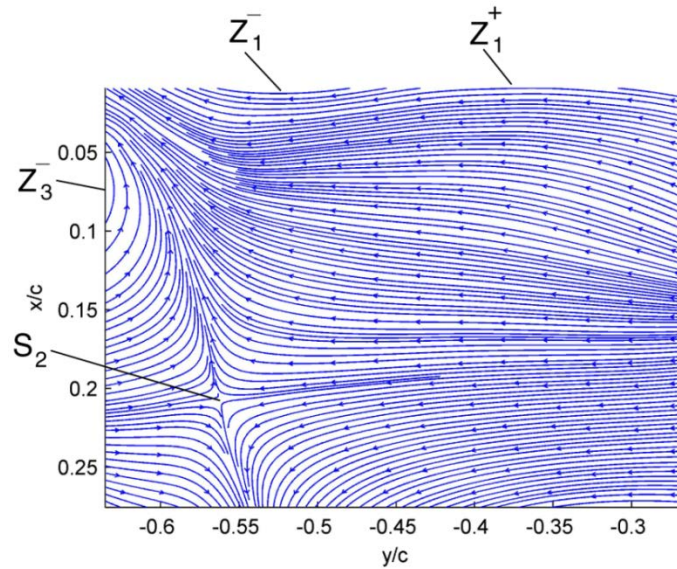
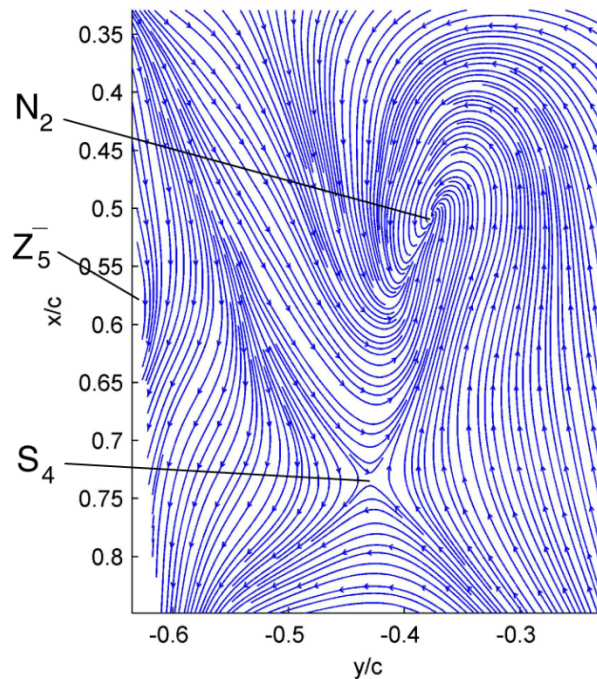


Figure 6.15 Skin friction lines on the upper surface of a tripped LAR NACA 0012 wing at 18° AoA





(b)



(c)

Figure 6.16 Zoomed-in views near singular points (a) N_1 and S_1 , (b) S_2 , Z_1^- , Z_3^- , and Z_1^+ and (c) N_2 , S_4 and Z_5^- on top surface of a tripped LAR NACA 0012 wing at 18° AoA

6.3.4 Wing Upper Surface at 0° , 5° , 12° , 13.5° , 14° and 16° AoA

The skin friction fields at AoA of 0° , 5° , 12° , 13.5° , 14° and 16° and shown in Figures 6.4 through 6.9, respectively. As discussed earlier, AoA of 0° and 5° exhibit largely 2D skin friction field features with 3D effects visible near the wing tips related to

interaction with the tip vortices. As the AoA is increased to 12° and above, 3D effects start to manifest on the skin friction fields with the formation of isolated singular points. All these cases are analyzed by applying the P-B index formula to skin friction fields bounded by the wing leading edge, trailing edge and tip edges. For all cases, boundary switch points and isolated singular points are identified to be used in the P-B index formula. It was found that all cases satisfied the conservation law given by the P-B index formula. Table 6.1 below summarizes all the test cases analyzed and the corresponding values of the left and right hand side of the P-B index formula.

Table 6.1 Summary of isolated singular points, boundary switch points and left and right hand side values of P-B Index Formula

| Cases | #N | #S | #Z ⁺ | #Z ⁻ | #N - #S | $1 + (\#Z^+ - \#Z^-)/2$ |
|--|----|----|-----------------|-----------------|---------|-------------------------|
| Upper surface, AoA = 0° | 0 | 0 | 0 | 2 | 0 | 0 |
| Upper surface, AoA = 5° | 0 | 0 | 0 | 2 | 0 | 0 |
| Upper surface, AoA = 12° | 0 | 0 | 2 | 4 | 0 | 0 |
| Upper surface, AoA = 13.5° | 0 | 1 | 2 | 6 | -1 | -1 |
| Upper surface, AoA = 14° | 2 | 2 | 6 | 8 | 0 | 0 |
| Upper surface, AoA = 16° | 4 | 5 | 2 | 6 | -1 | -1 |
| Upper surface, AoA = 18° | 4 | 5 | 2 | 6 | -1 | -1 |
| Side surface, AoA = 18° | 1 | 1 | 4 | 6 | 0 | 0 |
| Upper surface with LE roughness strip, AoA = 18° | 3 | 5 | 2 | 8 | -2 | -2 |

6.4 Summary

High resolution global skin friction diagnostics were performed on a LAR NACA 0012 wing at AoAs of 0°, 5°, 12°, 13.5°, 14°, 16° and 18°. Skin friction topological features such as isolated singular points, separation and reattachment lines and boundary switch points were identified from the resulting skin friction fields. These topological features were analyzed as the AoA was varied. It was found that the skin friction fields were largely 2D with no isolated singular points observed up to AoA of 5°. At AoA of 12° and above, isolated singular points were identified along with the formation of a

leading edge separation bubble. The case of AoA of 13.5° was also identified as the critical AoA, beyond which the leading edge separation bubble bursts and complex skin friction field features were generated associated with the three dimensional separated flow. Lift and drag measurements were also conducted. It was found that the lift and drag measurements largely agreed with the selected approximations for both forces except beyond the AoA of 14° , where flow separation has occurred. Lift was observed to increase post separation, which can be attributed to the non-linear lifting mechanism associated with the counter rotating vortices formed on the wing upper surface. Drag is observed to increase dramatically post separation which can also be attributed to the formation of the vortical structures on the wing upper surface (suction side).

The skin friction topology was also analyzed from the perspective of topological constraint application, specifically the P-B formula. Topological analysis of the skin friction fields on the upper surface of the LAR wing indicate that the conservation law given by the P-B formula is satisfied for all test cases even though the skin friction topology is drastically altered as the AoA is increased or the model geometry is altered by a leading edge roughness strip. Analysis of the wing side surface was also shown to satisfy the conservation law.

From a broader perspective, since the measured skin friction topology has been shown to satisfy the conservation law given by the P-B formula, the quantitative mapping capability of the GLOF technique in complex separated flows is validated. Generally, topological analysis of a skin friction field should take into account not only the isolated singular points in a region, but also the switch points on a defined penetrable boundary as described by the P-B formula.

CHAPTER 7

DELTA WINGS

A delta wing is a type of low aspect ratio wing with a triangular planform typically defined by its sweep angle, which is the angle from the horizontal to the wing leading edge. Delta wings have been widely utilized in high performance combat aircraft, supersonic civil aircraft, hypersonic aircraft and the space shuttle orbiter. These flight vehicles operate in the transonic to hypersonic speed range. One of the advantages of a using a delta wing for flight vehicles operating at these speeds is the reduction in transonic or supersonic wave drag. This is related to the high sweep angle of a delta wing and its position behind the bow shock that forms at the nose of the aircraft. Another advantage of a delta wing is its capability for high angle of attack (AoA) operations. At high AoA, a conventional wing would stall due to flow separation whereas a delta wing is still able to operate effectively due to the non-linear lifting mechanism of vortex lift. A delta wing generates a leading edge vortex (LEV) which remains attached to the upper surface of the wing even at high AoA, causing suction on the wing upper surface subsequently augmenting lift, allowing the delta wing to operate in flight envelopes not attainable by conventional wings. Although these unique characteristics of a delta wing allow it to operate in flight envelopes restricted to conventional wings, it possesses one inherent drawback. A delta wing typically possesses degraded low speed performance due to its high sweep angle and typically requires a larger wing surface compared to a

conventional wing to attain acceptable low speed performance for a given aircraft platform.

A double delta wing is also known as a strake/wing configuration. It has the general geometric characteristics of a delta wing with a discontinuity or a kink in its leading edge. This discontinuity separates the strake (forward) and wing (aft) sections of the double-delta wing. The strake is set at a higher sweep angle than the wing. The highly swept strake acts as an additional lifting surface forming a stable vortex structure above it. This strake vortex carries on through the wing section which keeps the flow attached to the wing to a higher angle of attack than the case of a wing without a strake or a conventional delta wing. This also allows for the wing section to be at a lower sweep angle mitigating the degraded low speed performance of a conventional delta wing. At the junction between the strake and wing sections, a wing vortex is formed. At low AoA, the wing and strake vortices form distinct trajectories. As the AoA is increased, the trajectories of the strake and wing vortices tighten up and move outboard as observed by Hebbar et al. [68]. The strake and wing vortices have also been observed to intertwine at certain conditions. The conditions described by Hebbar et al. [68] for wing and strake vortex intertwining are related to Reynolds number (Re). It was observed that at lower Re ($Re_c = 15,000$), the wing and strake vortices exhibited intertwining that was not apparent when Re was increased. Increasing Re caused the vortex trajectories to tighten up and move outboard laterally for a fixed AoA. For a fixed Re , similar effects were observed by increasing AoA.

Juncture fillets are additions to the double delta wing at the strake-wing junction with the objective of controlling the LEVs on the double delta wing. Juncture fillets have

been studied in depth by Hebbar et al. [69] and Erickson and Gonzalez [70]. Two types of fillets have been studied – diamond and parabolic. The diamond fillet adds more leading edge discontinuities with the purpose of generating additional vortices. These additional vortices energize the boundary layer, delaying vortex breakdown and flow separation. The parabolic fillet is a smooth curved section which aims to create a single dominant vortex system over the wing upper surface by removing the strake-wing junction discontinuity. Extensive force measurements and flow visualization by Hebbar et al. [69] have shown the effectiveness of the diamond and parabolic fillets in delaying vortex breakdown and augmenting lift. These observations were confirmed in flow visualization experiments by Verhaagen et al. [71] and numerical simulations by Kern [72-73]. Erickson and Gonzalez [70] have also shown similar characteristics of diamond and parabolic juncture fillets. In their work, Erickson and Gonzalez performed surface pressure and force measurements on a $76/40^\circ$ double delta wing with juncture fillets. The surface pressure signatures confirm the hypothesis that juncture fillets augment lift, as higher suction peaks and increased overall surface pressure levels were detected with a parabolic and diamond fillet. This was supported by force measurements, indicating increased lifting performance with juncture fillets. It was also observed that symmetric vortex breakdown occurred with the diamond fillet and conversely, asymmetric vortex breakdown was observed with the parabolic fillet.

As the preceding paragraphs have established, the vortical structures associated with delta wings contribute to interesting aerodynamic phenomena that augment the performance of these wings. These vortical structures have been the focus of extensive experimental and numerical studies [74-77]. To study the underlying mechanisms of

such complex separated flows Délerly [33] and Tobak et al. [44] analyzed the topological structures of skin friction fields on delta wings. A number of researchers have used oil flow visualization to study the flow on the surface of delta wings [71, 76, 78-80]. This approach is qualitative and somewhat subjective, although it has been used to obtain a vast amount of information on the topology of skin friction fields on delta wings. Numerical simulations have also been conducted to understand the flow structures over delta wings [72-73, 81-84] although high-fidelity skin friction fields generated by CFD are rare for systematic comparisons with experimental observation.

The GLOF technique allows for quantitative measurements of skin friction fields. This enables the mapping of topological features such as reattachment and separation lines, and other subtle features associated with vortex bursting and vortex interactions as demonstrated by previous work conducted here at Western Michigan University [85]. The previous study focused on studying the changes in the topological structures of skin friction fields for a 65° delta wing and a $76/40^\circ$ double delta wing with juncture fillets as AoA was increased. The effects of juncture fillets on vortex breakdown and performance characteristics of a $76/40^\circ$ double delta wing were also evaluated. It was found that juncture fillets augmented lift and improved the lift to drag ratio of the wings. It was also observed that juncture fillets delayed vortex breakdown from the investigation of skin friction fields obtained using the GLOF technique.

This study will focus on the effects of yaw and roll on the skin friction fields on a 65° delta wing and a $76/40^\circ$ double-delta wing with different fillets at different YA and RA using the GLOF technique. The $76/40^\circ$ double-delta wing used in this study is a half scale models of the wing studied by Erickson and Gonzales [70].

7.1 Experimental Setup

The wings used in this study were CNC machined out of 1/4 inch steel plate with a flat upper surface and 45° leading edge bevel. The upper surface of the wings was covered with a 0.075mm white MonoKote adhesive trim sheet. Figures 7.1 (a) through (d) are images of the 65° delta wing, baseline $76/40^\circ$ double delta wing and $76/40^\circ$ double delta wing with diamond and parabolic juncture fillets, respectively.

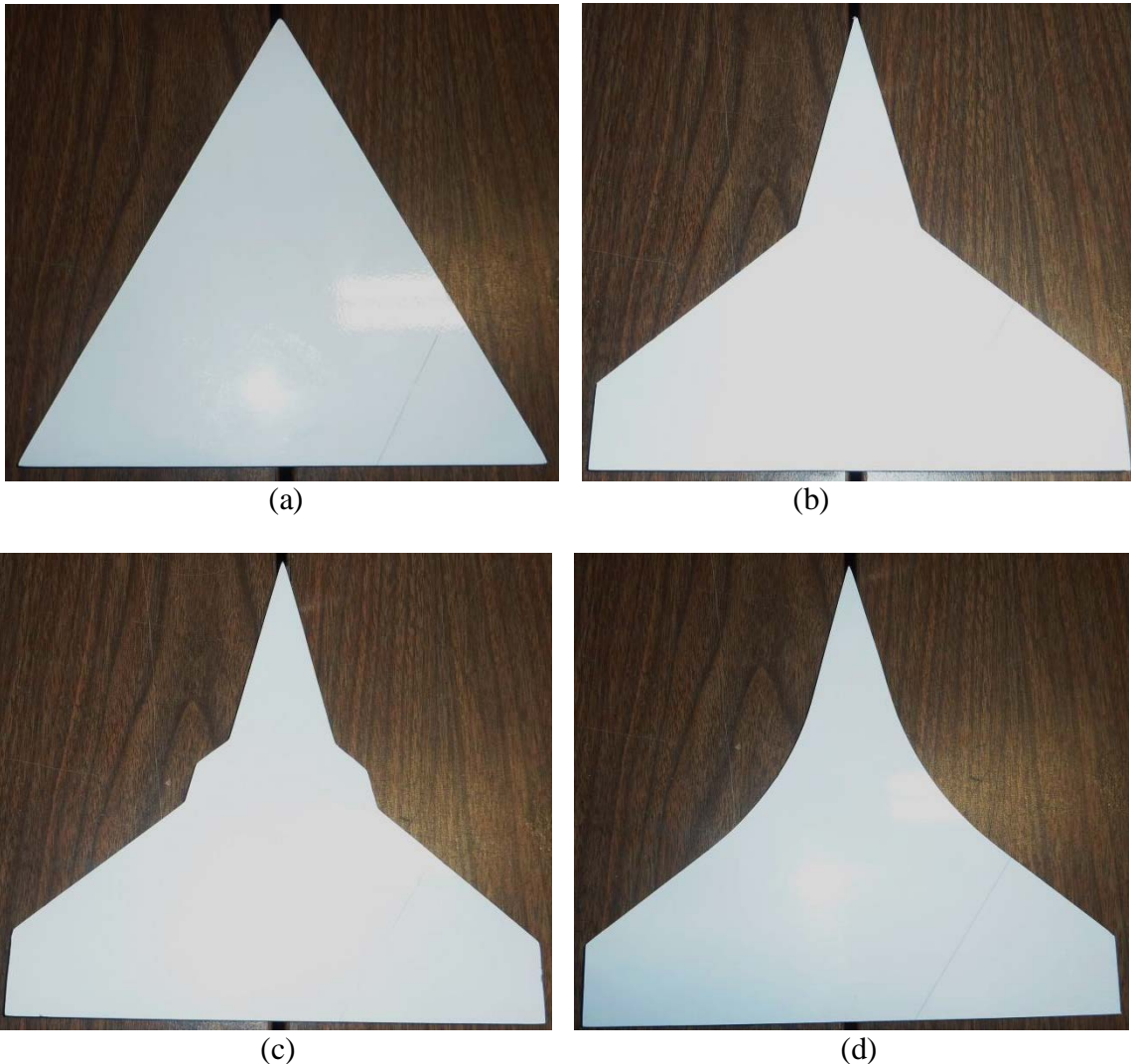


Figure 7.1 Images of (a) 65° delta wing, (b)baseline $76/40^\circ$ double delta wing, (c) $76/40^\circ$ double delta wing with a diamond fillet and (d) $76/40^\circ$ double delta wing with a parabolic fillet

The 65° delta wing had a root chord and span of 203mm and 185 mm, respectively while the 76/40° double delta wing with juncture fillets had a root chord and span of 203 mm and 207 mm, respectively. Experiments were conducted in the Western Michigan University Small Wind Tunnel (SWT) facility at a flow speed of 20 m/s corresponding to a Reynolds number based on chord length (Re_c) of 275,000 for all the wings. Figures 7.2 (a) and (b) are images of the wind tunnel attachment mechanism for yaw and roll adjustments and the baseline 76/40° double delta wing mounted on the adjustment mechanism, respectively.

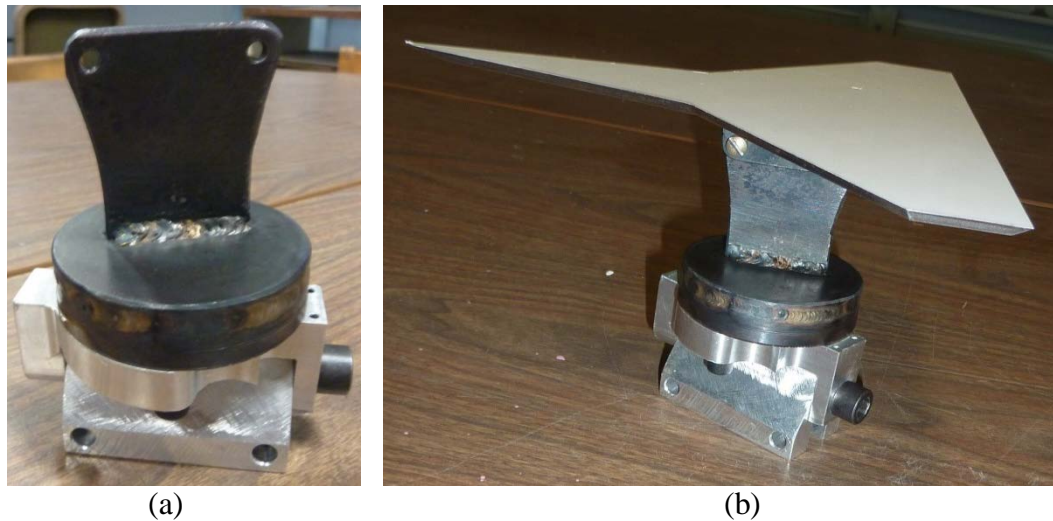


Figure 7.2 Images of (a) yaw and roll adjustment mechanism and (b) 76/40° baseline double delta wing mounted on the adjustment mechanism

Measurements were performed at AoAs of 10° and 20° with a combination of yaw (YA) and roll (RA) angles of 10°, 15° and 20°. Table 7.1 is a test matrix detailing the combination of AoA, YA and RA performed for each wing.

Table 7.1 Test matrix for wind tunnel testing of the delta wings

| Parameter/Case | 1 | 2 | 3 | 4 | 5 | 6 |
|----------------|----|----|----|----|----|----|
| AoA (°) | 10 | 20 | 10 | 10 | 20 | 20 |
| YA (°) | 0 | 0 | 10 | 15 | 0 | 0 |
| RA (°) | 0 | 0 | 0 | 0 | 10 | 20 |

Figures 7.3 (a), (b), (c) and (d) are a typical luminescent oil image, skin friction line plot, skin friction vector plot and skin friction magnitude plot, respectively for the 65° delta wing at 10° AoA.

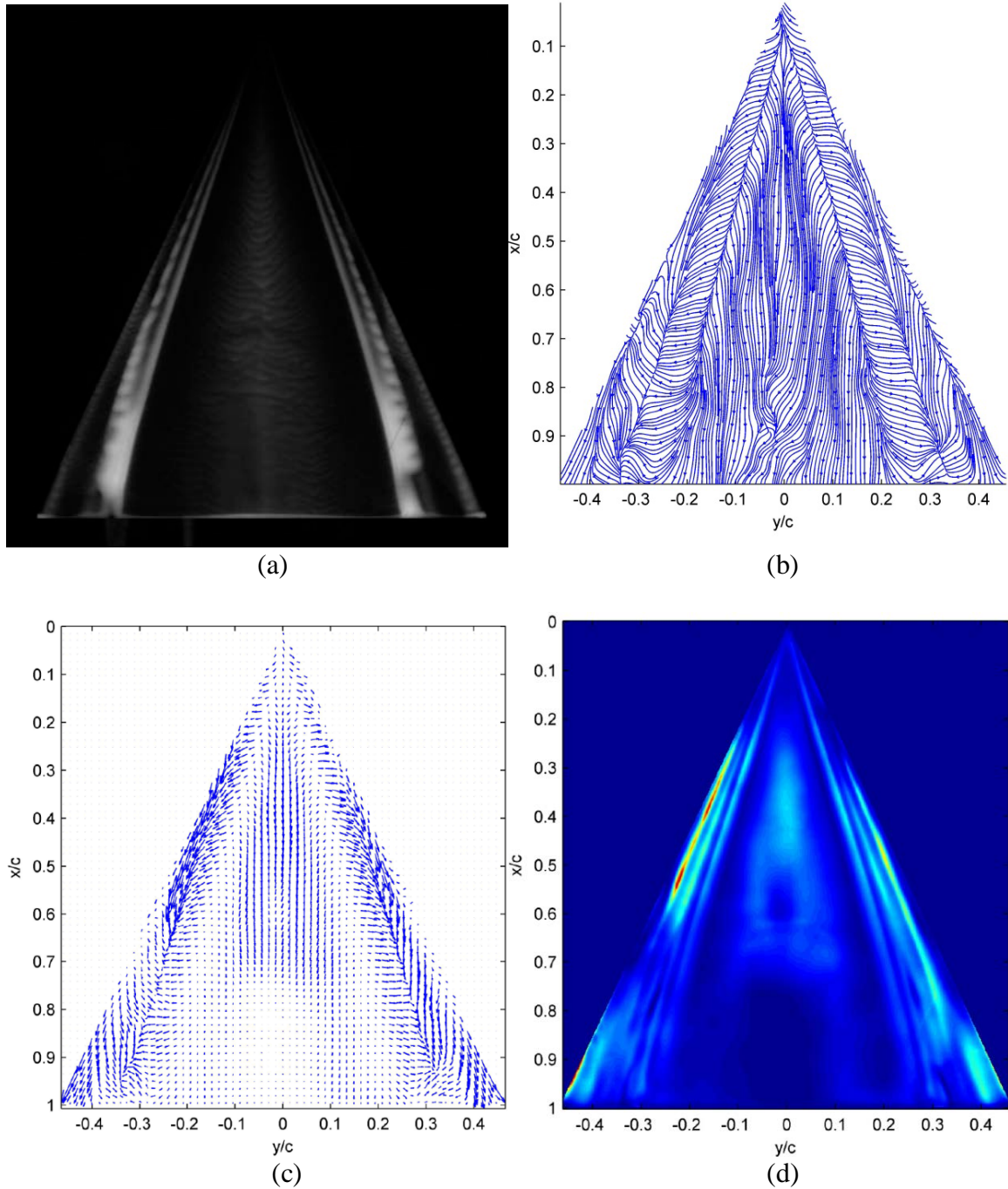


Figure 7.3 65° delta wing at 10° AoA, (a)typical luminescent oil image, (b)skin friction line plot, (c)skin friction vector plot and (d)skin friction magnitude plot

7.2 65° Delta Wing

A number of studies have been conducted by Verhaagen et al. [86-88] and Huang et al. [76] on the effects of yaw and roll on delta wings, respectively. For a delta wing in yaw, the windward side of the wing experiences an effective reduced sweep angle while, the leeward side of the wing experiences an effective increase in sweep angle. This causes the windward and leeward LEV vortex trajectories to move inboard towards the leeward side of the wing with increasing YA. The windward side vortex burst (VB) location has been observed to move towards the apex of the wing with increasing YA while the leeward side vortex tends to move off the surface of the wing with VB location moving towards the wing trailing edge (TE). For the delta wing in roll, the effects experienced by the upward leading edge (ULE) and downward leading edge (DLE) are combined effective AoA and sweep angle change. In numerical simulations by Gordnier [89], the results have shown an outboard and off surface movement of the LEV on the ULE side and inboard, towards surface movement of the LEV on the DLE side.

Figures 7.4 (a) and (b), 7.5 (a) and (b) and 7.6 (a) and (b) are skin friction line plots for the six test cases of $AoA = 10^\circ$, $AoA = 20^\circ$, $(AoA, YA) = (10^\circ, 10^\circ)$ and $(AoA, YA) = (10^\circ, 15^\circ)$, $(AoA, RA) = (20^\circ, 10^\circ)$ and $(AoA, RA) = (20^\circ, 20^\circ)$, respectively. The x (chordwise) and y (spanwise) coordinates are normalized by the root chord, c.

For the case of increasing AoA as shown by Figures 7.4 (a) and (b), the reattachment line associated with the primary leading edge vortex and the secondary separation line between the primary and secondary vortex is clearly identified. These features are symmetric about the wing root chord. The primary reattachment line moves inboard with increasing AoA. As AoA is increased from 10° to 20° , the primary

reattachment line on the right side of the wing moves inboard from $(y/c) = 0.06$ to $(y/c) = 0.04$ at $(x/c) = 0.2$. Similarly, the secondary separation line moved inboard from $(y/c) = 0.36$ to $(y/c) = 0.34$ at $(x/c) = 1.0$ when AoA was increased from 10° to 20° .

The skin friction line plots for the wing at $(\text{AoA}, \text{YA}) = (10^\circ, 10^\circ)$ and $(10^\circ, 15^\circ)$ are shown in Figures 7.5 (a) and (b). The reattachment line of the primary LEV on the windward side of the wing moves inboard with increasing YA. For YA of 10° and 15° , the reattachment line is located at $(y/c) = 0.1$ and $(y/c) = 0.08$ at $(x/c) = 0.5$, respectively. There is no obvious indication of the reattachment line associated with the LEV on the leeward side of the wing for both cases. VB is observed for the windward side LEV, identifiable by the sudden expansion of the well-defined reattachment line. The VB location is seen to move upstream towards the apex of the wing with increasing YA. VB is observed at $(x/c) = 0.72$ moving upstream to $(x/c) = 0.58$ for YA of 10° and 15° , respectively. This trend of upstream movement of VB location with increasing yaw angle is consistent with previous observations by Verhaagen et al. [86-88].

Figures 7.6 (a) and (b) show the skin friction line plots of the wing at $(\text{AoA}, \text{RA}) = (20^\circ, 10^\circ)$ and $(20^\circ, 20^\circ)$. Between the two RAs, the skin friction fields are qualitatively similar. For both cases, the secondary separation lines are observed to move inboard towards the DLE side.

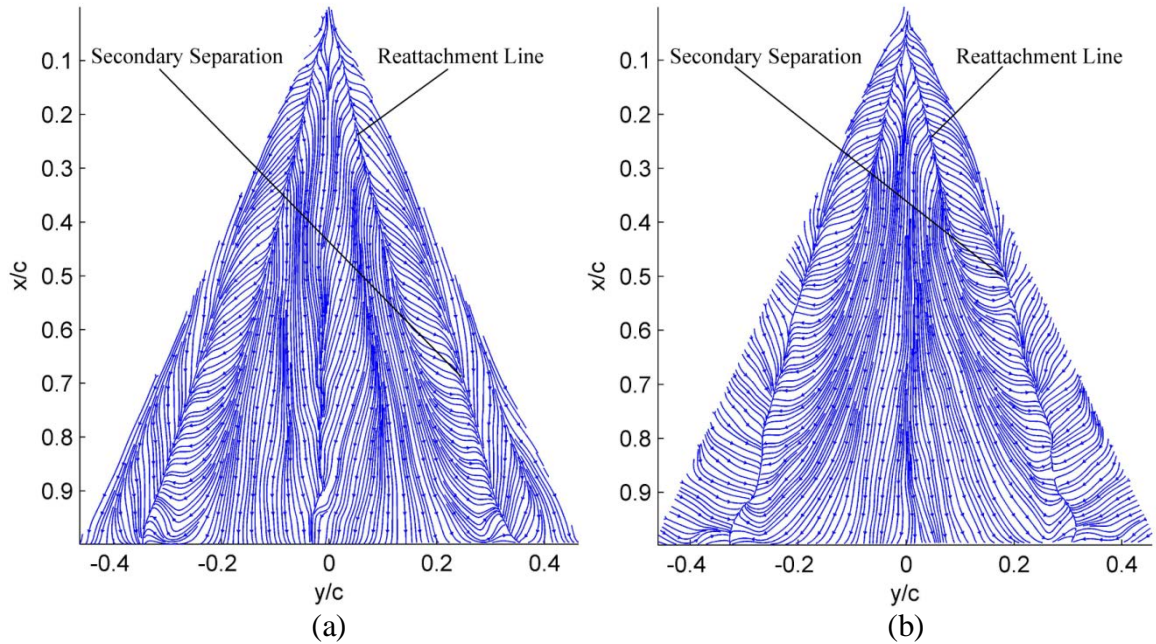


Figure 7.4 Skin friction line plots for a 65° delta wing at AoA, (a)10° and (b)20°

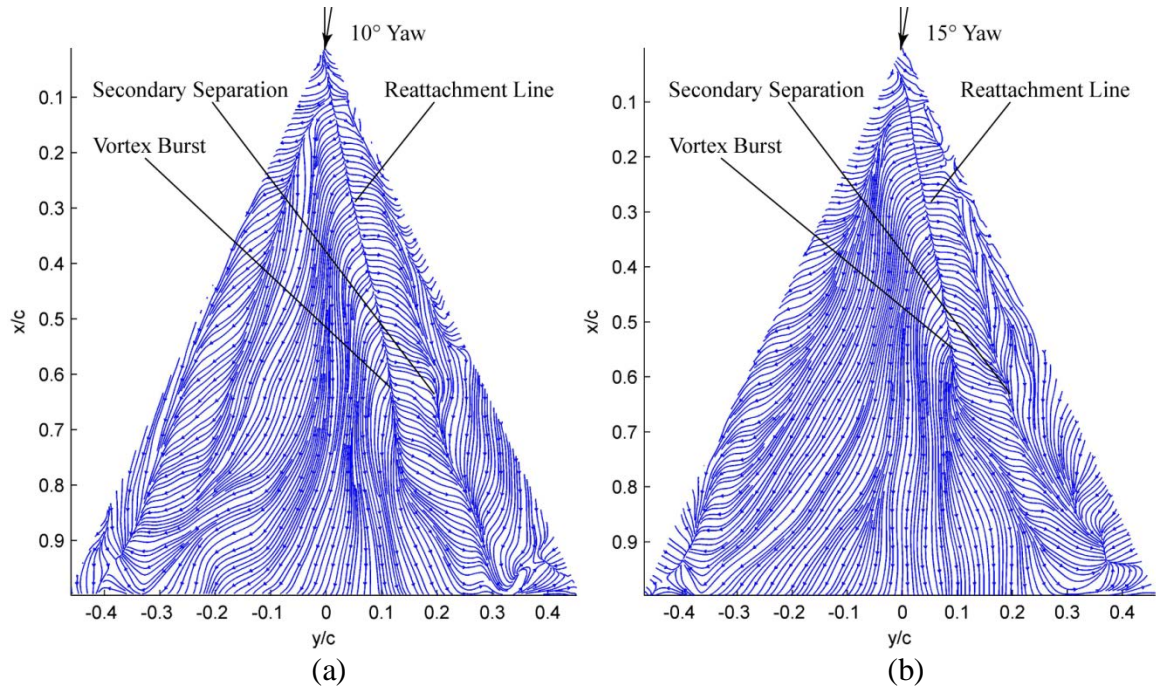


Figure 7.5 Skin friction line plots for a 65° delta wing at (AoA, YA), (a)(10°, 10°) and (b)(10°, 15°)

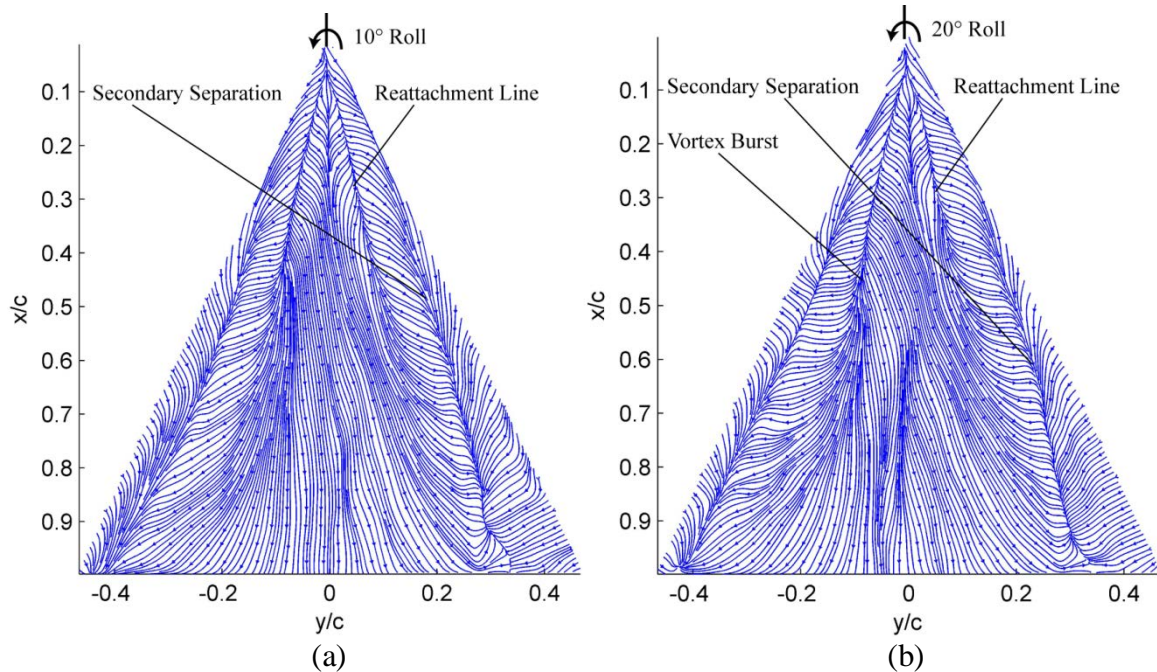


Figure 7.6 Skin friction line plots for a 65° delta wing at (AoA, RA), (a)(20°, 10°) and (b)(20°, 20°)

7.3 76/40° Double Delta Wing

The observations of LEV behavior for a double delta wing are similar for a delta wing in static yaw and roll cases as described in experimental work by Grismer et al. [90] and Hebbar et al. [91] although the effects are slightly more complex for the double delta wing because of the interaction between the wing and strake vortices. Hebbar et al. [91] have also shown vortex flow control for a yawing delta wing by demonstrating the delay in vortex burst for a double delta wing with a diamond juncture fillet at low Re ($Re_c = 18750$).

7.3.1 76/40° Double Delta Wing – Baseline

Figures 7.7 (a) and (b), 7.8 (a) and (b) and 7.9 (a) and (b) are skin friction line plots for the six test cases of AoA = 10°, AoA = 20°, (AoA, YA) = (10°, 10°) and (AoA, YA) = (10°, 15°), (AoA, RA) = (20°, 10°) and (AoA, RA) = (20°, 20°), respectively for

the baseline $76/40^\circ$ double delta wing. The x (chordwise) and y (spanwise) coordinates are normalized by the root chord, c .

As shown in Figure 7.7 (a) for the case of the wing at AoA of 10° , the primary LEV reattachment line is clearly visible along with the secondary separation and reattachment lines. The reattachment lines appear to curve outboard at $(x/c) = 0.7$ indicating the interaction of the strake and wing vortices. As AoA is increased to 20° asymmetric VB is observed. VB occurs at $(x/c) = 0.68$ for the left side of the wing and $(x/c) = 0.78$ for the right side of the wing as seen in Figure 7.7 (b). A spiral feature is also observed on the right side leading edge close to the strake-wing junction.

For the cases of the wing at $(\text{AoA}, \text{YA}) = (10^\circ, 10^\circ)$ and $(10^\circ, 15^\circ)$ as illustrated by Figures 7.8 (a) and (b), the reattachment line of the primary windward side LEV is clearly seen. The reattachment line is observed to move inboard with increasing YA from $(y/c) = 0.08$ to $(y/c) = 0.03$ at $(x/c) = 0.6$ for YA of 10° and 15° respectively. The VB location of the windward side LEV is located at $(x/c) = 0.72$ and $(x/c) = 0.68$ for YA of 10° and 15° , respectively. This indicates an upstream movement of VB with increasing YA consistent with previous observations by Hebbar et al. [91].

Figures 7.9 (a) and (b) show the skin friction line plots of the wing at $(\text{AoA}, \text{RA}) = (20^\circ, 10^\circ)$ and $(20^\circ, 20^\circ)$. The primary reattachment lines are observed to move inboard towards the ULE side of the wing from $(y/c) = -0.03$ at $(x/c) = 0.2$ for the wing at RA of 0° to $(y/c) = 0$ at $(x/c) = 0.2$ for the wing at both RAs. Asymmetric VB is also observed for both RAs. For RA of 10° , VB occurs at $(x/c) = 0.63$ on the DLE side of the wing, and $(x/c) = 0.83$ for the ULE side of the wing. As RA is increased to 20° , VB moves upstream towards the apex of the wing at $(x/c) = 0.57$ on the DLE side of the

wing, and downstream towards the TE of the wing at $(x/c) = 0.93$ for the ULE side of the wing.

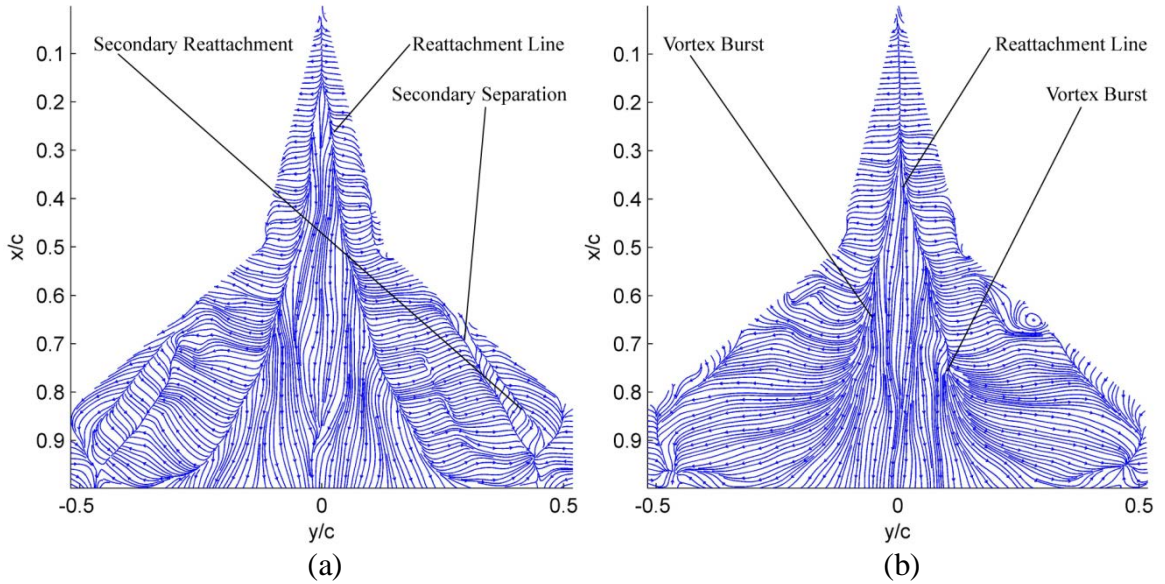


Figure 7.7 Skin friction line plots for a baseline 76/40° double delta wing at AoA, (a)10° and (b)20°

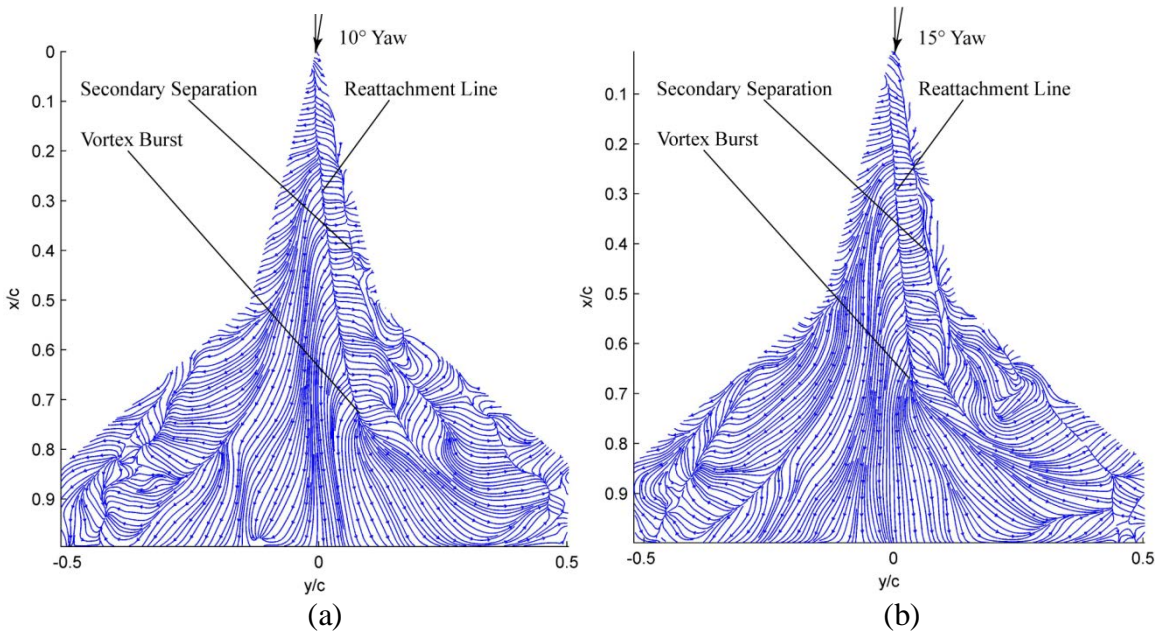


Figure 7.8 Skin friction line plots for a baseline 76/40° double delta wing at (AoA, YA), (a)(10°, 10°) and (b)(10°, 15°)

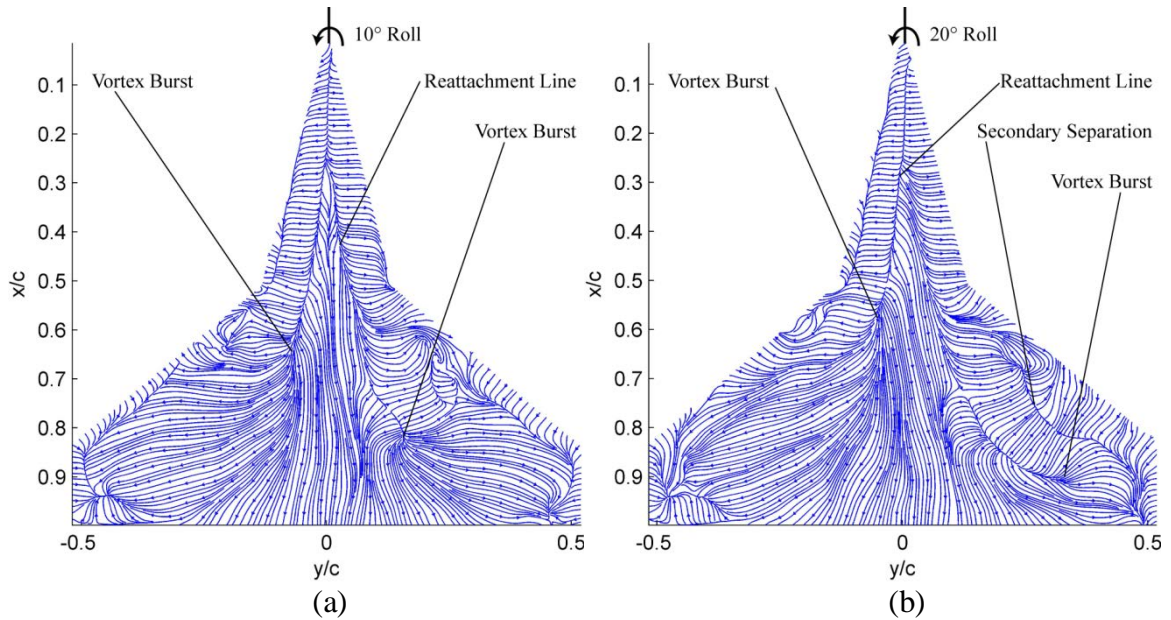


Figure 7.9 Skin friction line plots for a baseline 76/40 double delta wing at (AoA, RA), (a)(20°, 10°) and (b)(20°, 20°)

7.3.2 76/40° Double Delta Wing – Diamond Fillet

Figures 7.10 (a) and (b), 7.11 (a) and (b) and 7.12 (a) and (b) are skin friction line plots for the six test cases of AoA = 10°, AoA = 20°, (AoA, YA) = (10°, 10°) and (AoA, YA) = (10°, 15°), (AoA, RA) = (20°, 10°) and (AoA, RA) = (20°, 20°), respectively for the 76/40° double delta wing with a diamond juncture fillet.

As shown in Figure 7.10 (a), at AoA of 10°, the primary LEV reattachment line is clearly seen with the secondary separation and reattachment lines. A set of separation and reattachment lines is also observed near the diamond fillet junction related to the vortex structures created by the additional discontinuities created by the diamond shaped junction. The reattachment lines curve outboard at $(x/c) = 0.65$ indicating interaction of the strake and wing vortices. The curving of the line occurs earlier compared to the baseline wing possibly related to additional vortices created by the diamond junction. As AoA is increased to 20° symmetric VB is observed at $(x/c) = 0.73$ in Figure 7.10 (b).

In the case of the wing at $(\text{AoA}, \text{YA}) = (10^\circ, 10^\circ)$ and $(10^\circ, 15^\circ)$, the reattachment line of the primary LEV of the windward side of the wing is observed to move inboard towards the leeward side of the wing with increasing YA as seen in Figures 7.11 (a) and (b). The reattachment line is located at $(y/c) = 0.08$ and $(y/c) = 0.05$ at $(x/c) = 0.6$ for YA of 10° and 15° , respectively. The primary LEV is observed to burst at $(x/c) = 0.7$ and $(x/c) = 0.68$ for YA of 10° and 15° , respectively. The VB location also moves upstream towards the apex of the wing with increasing YA. The delay of VB is not observed when compared to the baseline wing for the wing with YA, as reported by Hebbar et al. [91].

Figures 7.12 (a) and (b) show the skin friction line plots of the wing at $(\text{AoA}, \text{RA}) = (20^\circ, 10^\circ)$ and $(20^\circ, 20^\circ)$. The primary reattachment lines are observed to move inboard towards the ULE side of the wing from $(y/c) = -0.03$ at $(x/c) = 0.2$ for the wing at RA of 0° to $(y/c) = 0$ at $(x/c) = 0.2$ for the wing at RA of both 10° and 20° . Asymmetric VB is also observed for both RAs. For RA of 10° , VB occurs at $(x/c) = 0.63$ on the DLE side of the wing, and $(x/c) = 0.80$ for the ULE side of the wing. As RA is increased to 20° , VB moves upstream towards the apex of the wing at $(x/c) = 0.53$ on the DLE side of the wing, and downstream towards the TE of the wing at $(x/c) = 0.94$ for the ULE side of the wing in a similar trend to the baseline wing.

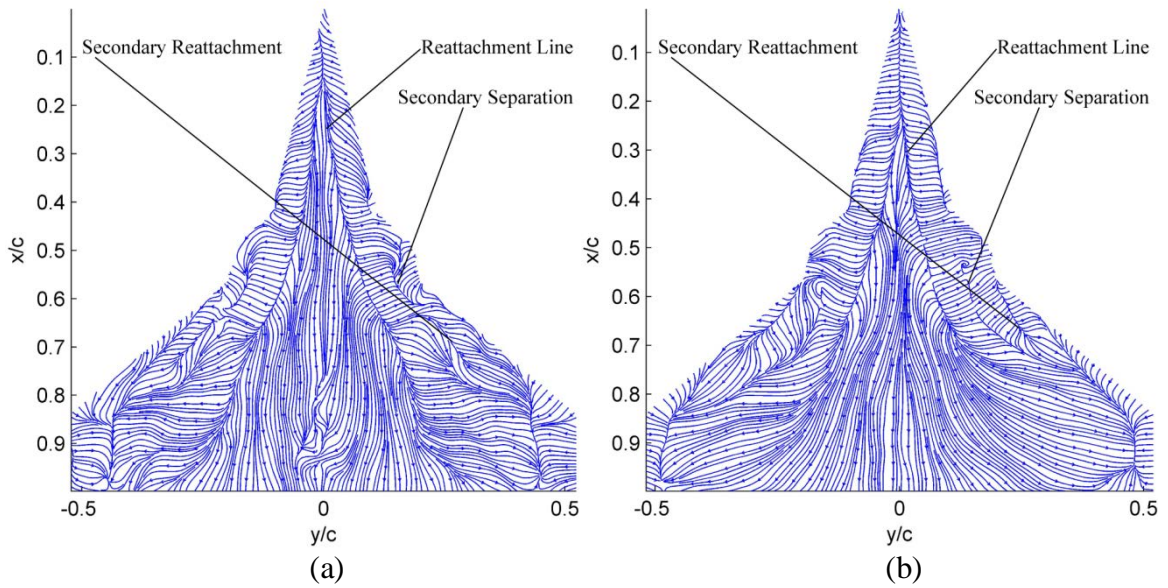


Figure 7.10 Skin friction line plots for a 76/40° double delta wing with a diamond junction fillet at AoA, (a)10° and (b)20°

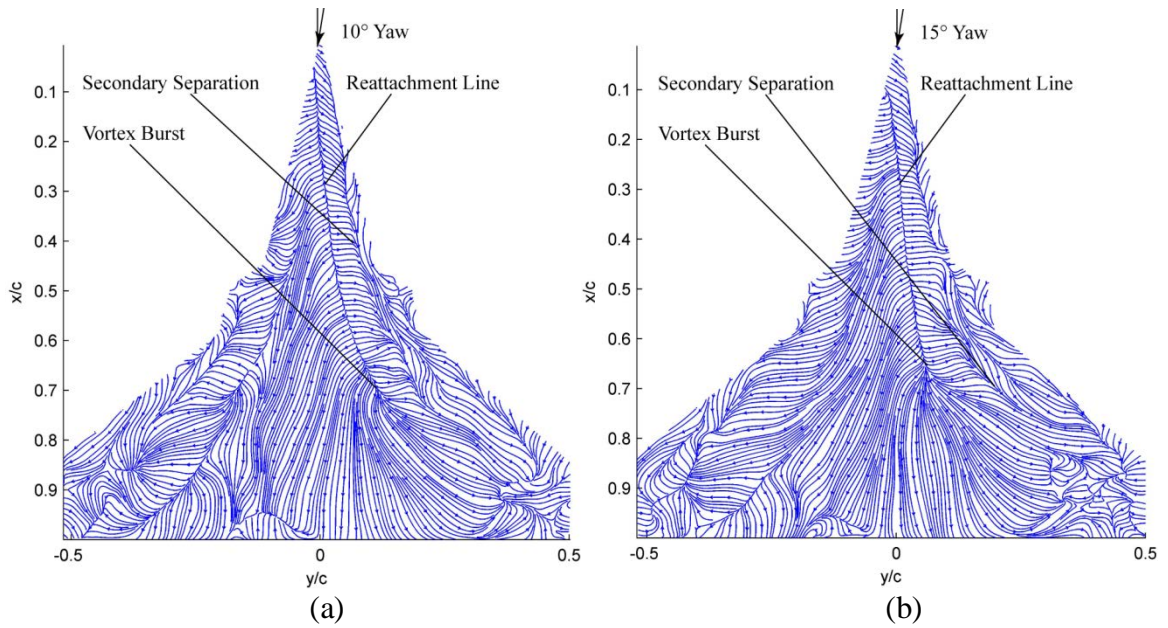


Figure 7.11 Skin friction line plots for a 76/40° double delta wing with a diamond junction fillet at (AoA, YA), (a)(10°, 10°) and (b)(10°, 15°)

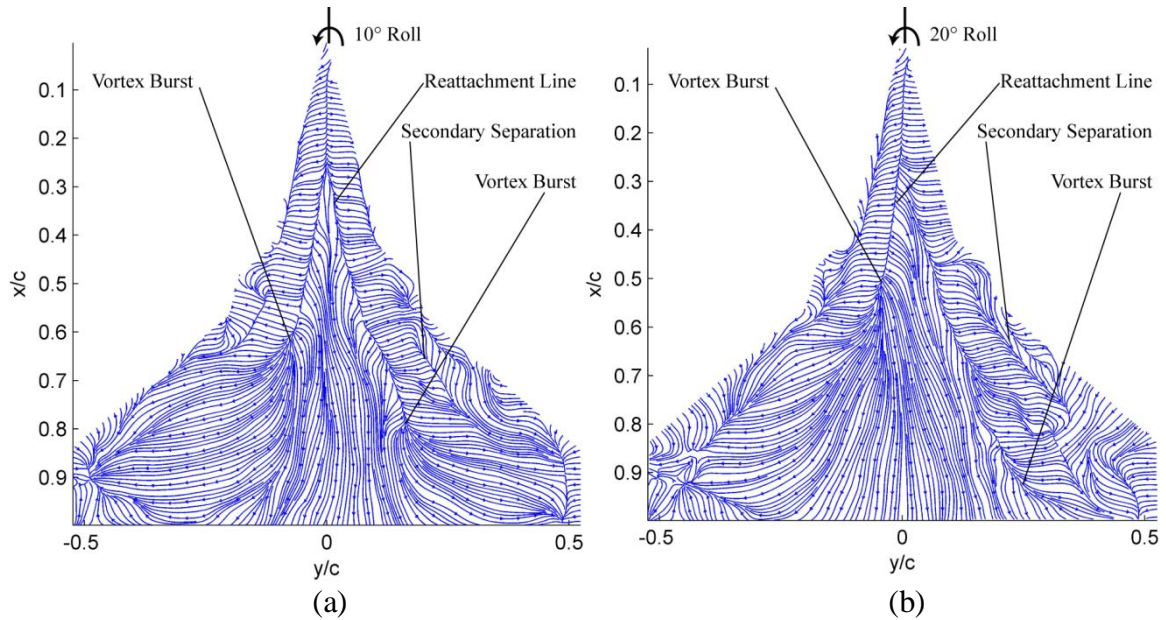


Figure 7.12 Skin friction line plots for a 76/40° double delta wing with a diamond juncture fillet at (AoA, RA), (a)(20°, 10°) and (b)(20°, 20°)

7.3.3 76/40° Double Delta Wing – Parabolic Fillet

Figures 7.13 (a) and (b), 7.14 (a) and (b) and 7.15 (a) and (b) are skin friction line plots for the six test cases of AoA = 10°, AoA = 20°, (AoA, YA) = (10°, 10°) and (AoA, YA) = (10°, 15°), (AoA, RA) = (20°, 10°) and (AoA, RA) = (20°, 20°), respectively for the 76/40° double delta wing with a parabolic juncture fillet.

As shown in Figure 7.13 (a), at AoA of 10°, the primary LEV reattachment line is clearly visible along with the secondary separation and reattachment lines. As discussed earlier, the purpose of the parabolic fillet is to create a single dominant vortex system and it appears to achieve that goal as illustrated by the skin friction line plot in Figure 7.13 (a). The reattachment lines curve outboard at $(x/c) = 0.6$ indicating interaction between the strake and wing vortices. As AoA is increased to 20° asymmetric VB is observed at $(x/c) = 0.75$ for the left side LEV and $(x/c) = 0.68$ for the right side LEV as seen in Figure 7.13 (b).

In the case of the parabolic wing with YA of 10° , the windward side LEV reattachment line is seen as illustrated in Figure 7.14 (a). A reattachment line and separation line are also observed on the leeward side of the wing from approximately $(x/c) = 0.65$ to the TE of the wing. When YA is increased to 15° , the reattachment line of the primary LEV on the windward side moves inboard to $(y/c) = 0.05$ from $(y/c) = 0.08$ at $(x/c) = 0.6$ for YA of 10° . The reattachment line previously observed on the leeward side of the wing is not present for YA of 15° as illustrated by Figure 7.14 (b). Similar to the baseline and diamond juncture fillet wings, the VB location moves upstream from $(x/c) = 0.68$ to $(x/c) = 0.63$ as YA is increased from 10° to 15° .

Figures 7.15 (a) and (b) show the skin friction line plots of the wing at $(\text{AoA}, \text{RA}) = (20^\circ, 10^\circ)$ and $(20^\circ, 20^\circ)$. The primary reattachment lines are observed to move inboard towards the ULE side of the wing from $(y/c) = -0.03$ at $(x/c) = 0.2$ for the wing at RA of 0° to $(y/c) = 0$ at $(x/c) = 0.2$ for the wing at RA of both 10° and 20° . Asymmetric VB is also observed for both RAs similar to the baseline and diamond fillet wings. For RA of 10° , VB occurs at $(x/c) = 0.6$ on the DLE side of the wing, and $(x/c) = 0.81$ for the ULE side of the wing. As RA is increased to 20° , VB moves upstream towards the apex of the wing at $(x/c) = 0.5$ on the DLE side of the wing, and downstream towards the TE of the wing at $(x/c) = 0.82$ for the ULE side of the wing in a similar trend to the baseline and diamond fillet wings.

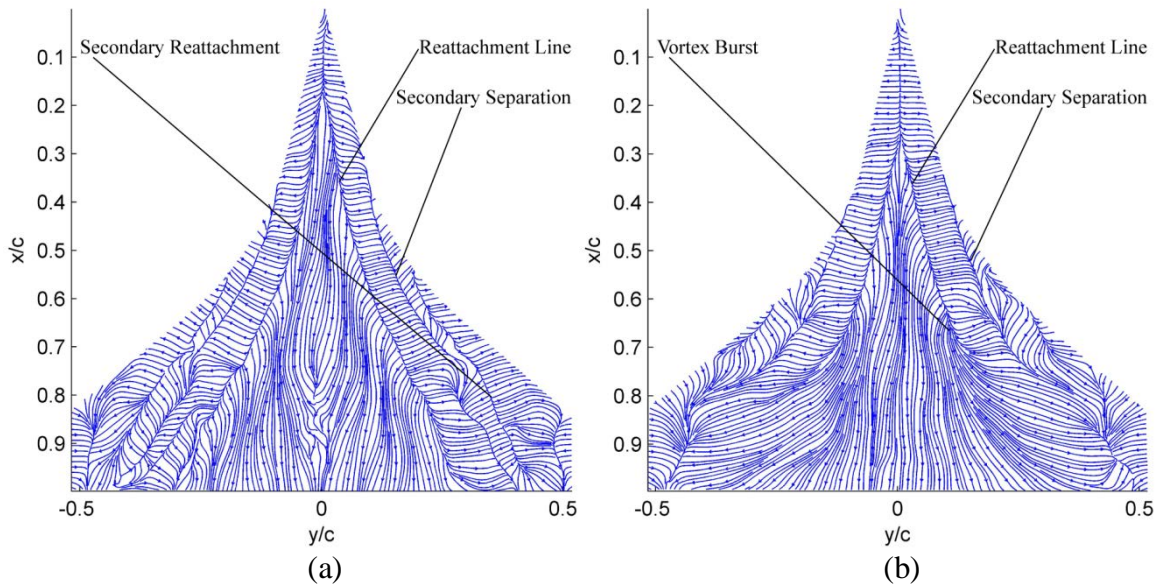


Figure 7.13 Skin friction line plots for a 76/40° double delta wing with a parabolic juncture fillet at AoA, (a)10° and (b)20°

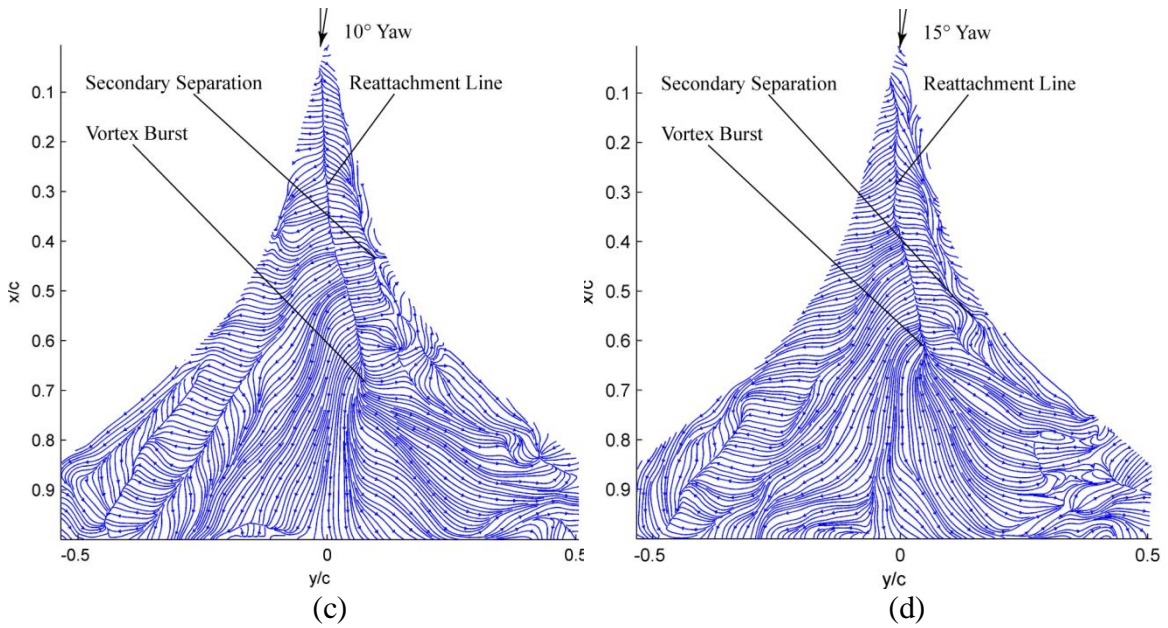


Figure 7.14 Skin friction line plots for a 76/40° double delta wing with a parabolic juncture fillet at (AoA, YA), (a)(10°, 10°) and (b)(10°, 15°)

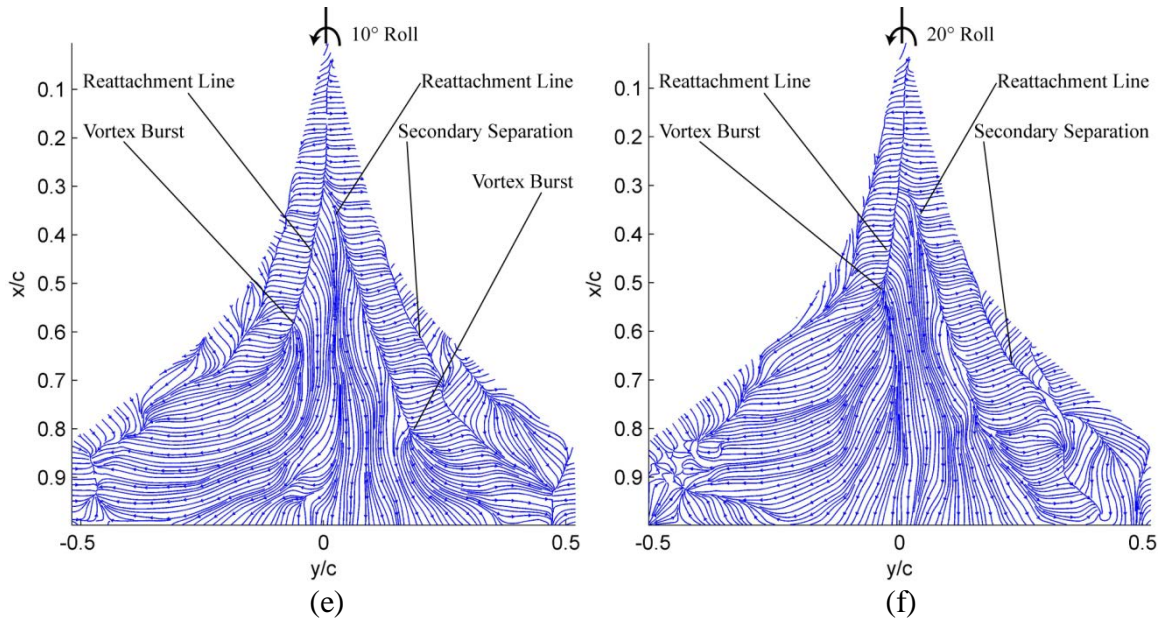


Figure 7.15 Skin friction line plots for a 76/40° double delta wing with a diamond juncture fillet at (AoA, RA), (a)(20°, 10°) and (b)(20°, 20°)

7.4 Skin Friction Topology Constraint Analysis

In previous oil streak visualizations of skin friction topology on delta wings by Huang et al. [76-77] and Su et al. [92], singular points were summed up although the key relevance of switch points on a boundary to the distribution of the singular points in the region enclosed by the boundary was not recognized. Consequently, the topological analysis based on the statistics of singular points on delta wings is not complete and universal. Near wall streamline patterns on a low sweep angle delta wing were measured by Yavuz et al. [93] using near wall PIV. The detailed surface streamline patterns enclosed by the leading and trailing edges of the delta wing as a closed penetrable boundary can be analyzed using the Poincare-Bendixson (P-B) index formula. For instance, in the time-averaged surface streamline pattern on the stationary delta wing (Figure 2 in [93]), two saddles and two sink nodes are identified near the leading edge on the wing upper surface. Two positive switch points associated with the large scale swirling pattern of the streamlines are identified on the trailing edge. Two negative

switch points are located at the sharp wing tips along with two more negative switch points on the trailing edge are identified between the saddle and the wing tip on each side of the wing. Summarizing the number of singular points and boundary switch points we have, $\#N = 2$, $\#S = 2$, $\#Z^+ = 2$ and $\#Z^- = 4$. Applying the P-B index formula given by $\#N - \#S = 1 + (\#Z^+ - \#Z^-) / 2 = 0$ shows that the conservation law is satisfied. Yavuz et al. [93] also obtained the instantaneous streamline patterns responding to the small unsteady motions of the wing. The application of the P-B index formula to these instantaneous streamline patterns showed that they satisfied the conservation law.

Figures 7.16 (a) and (b) are skin friction line plots for the baseline 76/40° double delta wing at $(AoA, YA) = (16^\circ, 6^\circ)$ and $(24^\circ, 6^\circ)$, respectively. The distinct features visible are saddle (S_1) and the spiraling node (N_1) that occur on the left side of the wing due to the YA. The combination of $S_1 - N_1$ indicates a typical closed type separation. Complex inflow and outflow behavior along the right side leading edge is observed for both cases. To simplify topological analysis, a polygon ABCDEFA is considered, which encloses all the singular points excluding the right side leading edge. The singular points and boundary switch points are indicated in Figures 7.16 (a) and (b), where $\#N = 2$, $\#S = 2$, $\#Z^+ = 1$ and $\#Z^- = 3$ for both cases of AoA of 16° and 24°. Applying the P-B index formula to the area enclosed polygon ABCDEFA for both cases satisfies the conservation law. The magnified views of the singular points and boundary switch points are shown in Figures 7.17 (a) and (b) for AoA of 16° and 24°, respectively. Applying the P-B index formula to these isolated regions also shows that the conservation law is satisfied.

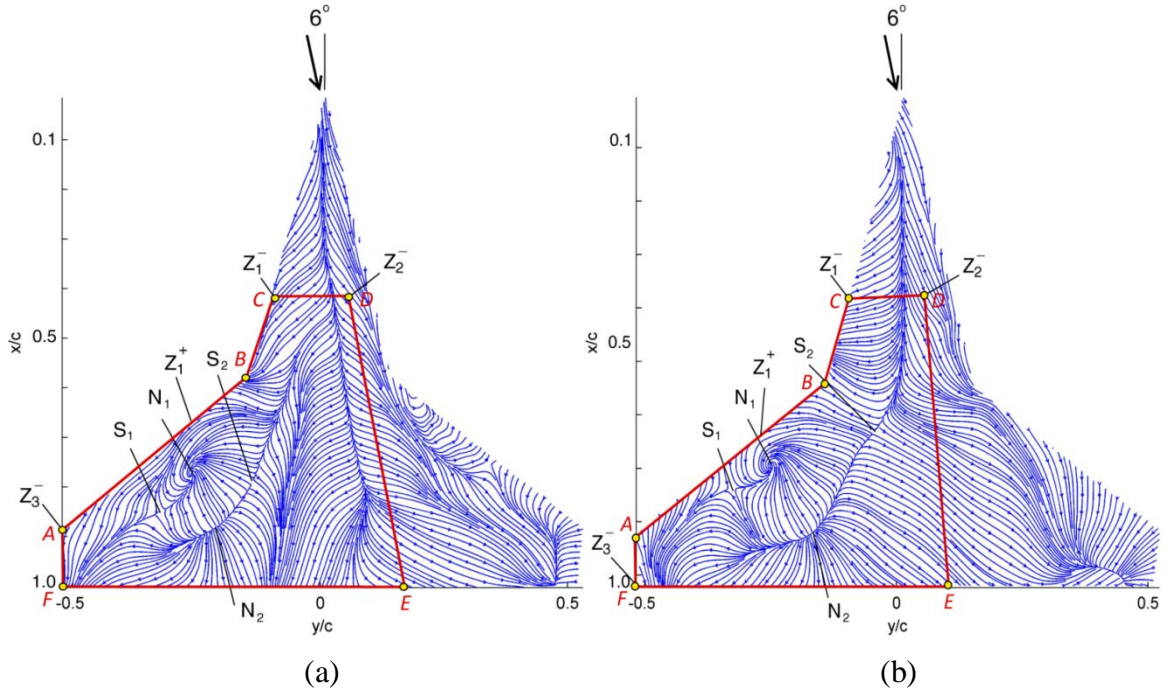


Figure 7.16 Skin friction lines on a baseline 76/40° double delta wing at (AoA, YA) (a) (16°, 6°) and (b) (24°, 6°)

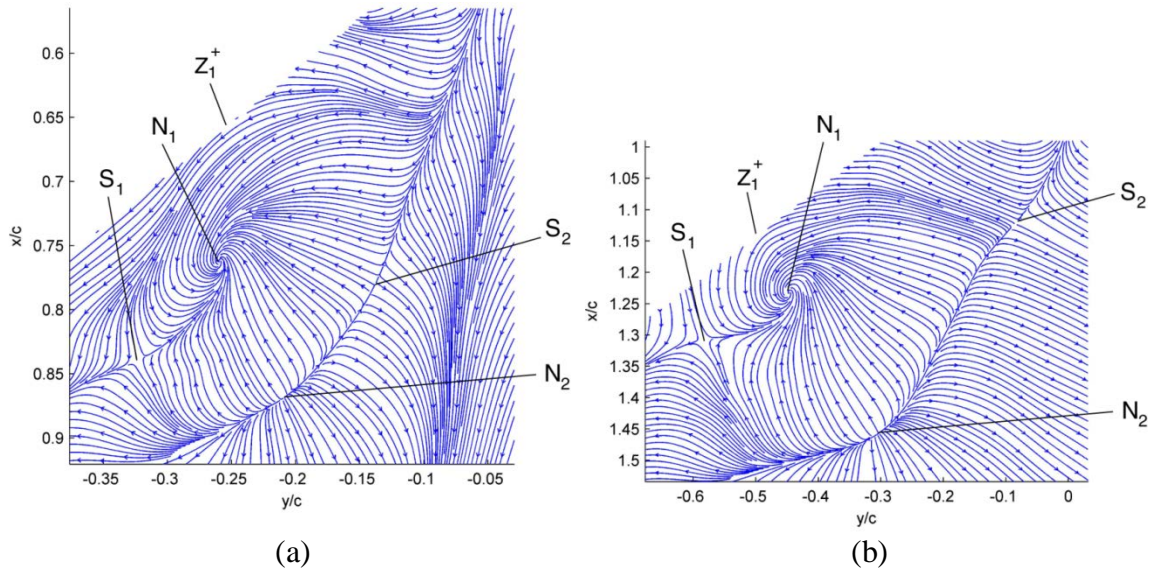


Figure 7.17 Magnified views of singular points on the skin friction fields of a baseline 76/40° double delta wing at (AoA, YA), (a) (16°, 6°) and (b) (24°, 6°)

7.5 Summary

High resolution skin friction diagnostics were performed on a 65° delta wing and a $76/40^\circ$ double delta wing with juncture fillets. Skin friction fields were evaluated for six different angle of attack (AoA), yaw angle (YA) and roll angle (RA) combinations. Changing the YA resulted in an effective change in sweep angle of the windward and leeward sides of the wings while changing RA resulted in a combined effective sweep angle and AoA change for the upward leading edge (ULE) and downward leading edge (DLE) sides of the wing.

In the case of the 65° delta wing, increasing AoA resulted in the inboard movement of the reattachment and separation lines. As YA was introduced, vortex burst (VB) is observed for the windward side leading edge vortex (LEV) which moves upstream towards the apex of the wing with increasing YA. As RA is introduced, no distinct changes are observed in the skin friction fields except for the inboard movement of the reattachment and secondary separation lines towards the DLE side of the wing.

For the $76/40^\circ$ double delta wing, the effects on the skin friction fields generally follow the same trend for all three wing configurations. The primary reattachment line is highly curved, due to interaction between the strake and wing vortices. For the wing with the diamond juncture fillet, additional separation and reattachment lines are observed near the strake-wing junction as well as the wing section leading edge related to the vortices generated by the additional discontinuities resulting from the diamond junction shape. For the parabolic juncture fillet, a single dominant vortex structure is seen in the skin friction fields for AoA of 10° and 20° .

As YA is introduced to the wings, the primary reattachment line of the windward side LEV is observed to move inboard towards the leeward side of the wings. VB location is observed to move upstream as YA is increased. Asymmetric VB is observed when RA is added to the wings. The VB location for the DLE side moves upstream towards the apex of the wing while the VB location for the ULE side moves downstream towards the wing trailing edge with increasing RA. VB delay is not apparent for the wings with juncture fillets as reported in the literature.

Application of the P-B index formula has also been demonstrated in studying the skin friction field topology on a double delta wing. The skin friction fields of a 76/40° baseline double delta wing at (AoA, YA) of (16°, 6°) and (24°, 6°) were analyzed as a typical case by applying the P-B index formula. The conservation law given by the P-B index formula was found to be satisfied for all cases.

CHAPTER 8

WING-BODY JUNCTION FLOW AND MAPPING OF SKIN FRICTION VECTORS FROM THE IMAGE PLANE TO A 3D MODEL IN THE OBJECT SPACE

Junction flows around wall mounted obstacles are often seen in various engineering applications such as wing-body junctions in aircraft, wall-vane junctions in gas turbines, appendage-body junctions in submarines and bridge piers. The flow associated with junction flows are complex, typically involving a primary horseshoe vortex and multiple vortices interacting with the unsteady separated flow behind the obstacle. The complex three dimensional separated flows, induced unsteady pressure oscillations and interference drag associated with junction flows are detrimental from the perspective of fluid and structural mechanics, e.g., wing-body junctions for aircraft and submarines which cause interference drag and bridge supports in civil engineering applications that experience bridge scour which affects the structural integrity of bridges.

Junction flows have been studied extensively over the years. Numerous researchers have studied junction flows over obstacles including circular cylinders, rectangular blocks, cubes, vertical plates and hemispheres [94-102]. Wing-body junction flows have also been rigorously investigated due to their relevance in aeronautical and naval applications. The studies of wing-body junction flows have encompassed the measurements of flow quantities such as velocity and pressure fields using laser Doppler velocimetry (LDV), particle image velocimetry (PIV), pressure sensors and flow

visualizations [10-14]. A comprehensive review of junction flows including wing-body junction flows has been given by Simpson [113]. Computational fluid dynamics (CFD) studies have also been conducted to provide detailed flow structures for wing-body junction flows [108-112].

Skin friction fields in junction flows have also been studied, although in a qualitative sense using surface oil streak visualizations. This approach has been utilized to provide qualitative information of skin friction topology in junction flows. However, this approach is rather ambiguous since it relies on the physical intuition of observers. To counter this issue, the topological analysis of skin friction fields based on a topological rule or constraint has been utilized to understand the complex near-wall flows in junction flows [35-36, 38, 44, 114]. A simple topological rule has been derived by Hunt et al. [38] for junction flows on a base surface plus the surface of an obstacle, which states that the number of nodes equals to that of saddles. Even though these topological rules as based on rigorous mathematical formulations, the issue of ambiguity still exists when applied to surface oil visualization images since the topological features are highly conjectured depending on the complexity of the flows. The availability of the GLOF technique solves the fundamental issue in studying skin friction topology by providing the means to perform high resolution quantitative global skin friction diagnostics. The GLOF technique has previously been utilized to study the skin friction topology on delta wings [85], a low-aspect ratio rectangular wing [57] and junction flows [28].

Previous measurements using the GLOF technique were conducted on flat or relatively flat surfaces that were viewed perpendicularly by a camera such that the perspective projection transformation between the surface and the image plane was

simplified. However, for a large complex model such as the wing-body junction model in this study, a single fixed camera can only view a part of the surface, therefore multiple images from different viewing angles and positions must be acquired to cover all surfaces of the model. Moreover, skin friction vectors extracted from GLOF images must be mapped onto a surface grid in the 3D object space to reconstruct a complete skin friction field on the entire surface, which will enable the correct interpretation of skin friction topology on a complex surface.

The objective of this work is to reconstruct skin friction fields on the complete wing-body junction model from GLOF images taken from multiple viewing angles and positions and perform topological analysis of the extracted skin friction fields. The projection mapping from multiple images onto a surface grid is developed and topological analysis is conducted using the topological rule given by Hunt et al. [38] for junction flows and the Poincare-Bendixson index formula for a region enclosed by a penetrable boundary. Skin friction vectors on the surface of the wing-body junction model at angles of attack (AoA) of 0° , 6° and 12° are extracted from GLOF images taken at different viewing angles and positions, and mapped onto the surface grids to reconstruct the complete skin friction fields in the 3D object space. Isolated singular points and separation and reattachment lines are identified from the extracted skin friction fields and topological analysis is performed using the described topological rules. The relationship between the topological features on the surface and corresponding flow structures is explored and discussed.

8.1 Mapping Skin Friction Vectors from the Image Plane to the Object Space

The projected skin friction vectors extracted by the GLOF technique are mapped onto a surface grid in the object space utilizing the photogrammetry approach. Photogrammetry provides the relationship between the image coordinate and the object space coordinate described by the collinearity equations [34-36]. In this work, the Direct Linear Transformation (DLT) is used as a linear treatment of the nonlinear collinearity equations with reasonable accuracy when the lens distortion can be neglected [123]. The DLT equations for the image coordinates (x_1, x_2) and the designated object-space coordinates (X_1, X_2, X_3) are written as

$$x_1 = \frac{m_{11}X_1 + m_{12}X_2 + m_{13}X_3 + m_{14}}{m_{31}X_1 + m_{32}X_2 + m_{33}X_3 + 1}, x_2 = \frac{m_{21}X_1 + m_{22}X_2 + m_{23}X_3 + m_{24}}{m_{31}X_1 + m_{32}X_2 + m_{33}X_3 + 1}, \quad (8.1)$$

where m_{ij} are the 11 DLT parameters determined by camera calibration. The advantage of utilizing the DLT approach is that the DLT parameters can be determined using a linear least-squares method. When the lens distortion is small, the DLT approach is reasonably accurate. However, when the lens distortion is large, a nonlinear optimization method should be employed to obtain a refined solution for the camera exterior and interior parameters [117]. The data reduction routines including camera calibration/orientation algorithms for aerospace applications are comprehensively documented [125]. Once the DLT parameters in Equation 8.1 are computed based on known targets on a surface, mapping of scalar fields such as image intensity, pressure and temperature from the image plane onto the object surface is possible. For a point (X_1, X_2, X_3) on a surface $X_3 = f(X_1, X_2)$, the corresponding image point (x_1, x_2) can be found using Equation 8.1. The value of the scalar quantity at (X_1, X_2, X_3) on

the surface grid is directly associated with that at the image point (x_1, x_2) by interpolation of the values at neighboring points. A third-order B-spline scheme is utilized for interpolation in this work. This approach is typically used in pressure and temperature sensitive paint (PSP and TSP) measurements [25].

The next challenge is transforming a projected skin-friction vector $\bar{\boldsymbol{\tau}} = (\bar{\tau}_1, \bar{\tau}_2)$ in the image plane to a skin friction vector $\boldsymbol{\tau} = (\tau_1, \tau_2, \tau_3)$ on the surface in the object space. Along a skin friction line on a surface in the object space, $\tau_j = \|\boldsymbol{\tau}\| dX_j / dS$ is defined where the derivative with respect to the arc length S , dX_j / dS , is the unit tangent vector of the skin friction line on the surface and $\|\boldsymbol{\tau}\|$ is the skin friction magnitude on the surface. The corresponding relationship in the image plane is defined as $\bar{\tau}_j = \|\bar{\boldsymbol{\tau}}\| dx_j / ds$, where dx_j / ds is the derivative with respect to the arc length s in the image plane and $\|\bar{\boldsymbol{\tau}}\|$ is the magnitude of the projected skin friction vector which results in the following relationship

$$\begin{pmatrix} \bar{\tau}_1 \\ \bar{\tau}_2 \end{pmatrix} = \begin{pmatrix} \frac{\partial x_1}{\partial X_1} & \frac{\partial x_1}{\partial X_2} & \frac{\partial x_1}{\partial X_3} \\ \frac{\partial x_2}{\partial X_1} & \frac{\partial x_2}{\partial X_2} & \frac{\partial x_2}{\partial X_3} \end{pmatrix} \begin{pmatrix} \tau_1 \\ \tau_2 \\ \tau_3 \end{pmatrix} \quad (8.2)$$

where the elements in the coefficient matrix is computed from Equation 8.1. Equation 8.2 is made of two equations for the three unknowns (τ_1, τ_2, τ_3) , thus, the orthogonality condition $\boldsymbol{\tau} \cdot \mathbf{n} = \tau_j n_j = 0$ ($j = 1, 2, 3$) is imposed as an extra constraint, where $\mathbf{n} = (n_1, n_2, n_3)$ is the unit normal vector of a surface. The inverse relation described by Equation 8.3 gives the one-to-one mapping between $\bar{\boldsymbol{\tau}} = (\bar{\tau}_1, \bar{\tau}_2)$ and $\boldsymbol{\tau} = (\tau_1, \tau_2, \tau_3)$.

$$\begin{pmatrix} \tau_1 \\ \tau_2 \\ \tau_3 \end{pmatrix} = \begin{pmatrix} \frac{\partial x_1}{\partial X_1} & \frac{\partial x_1}{\partial X_2} & \frac{\partial x_1}{\partial X_3} \\ \frac{\partial x_2}{\partial X_1} & \frac{\partial x_2}{\partial X_2} & \frac{\partial x_2}{\partial X_3} \\ n_1 & n_2 & n_3 \end{pmatrix}^{-1} \begin{pmatrix} \bar{\tau}_1 \\ \bar{\tau}_2 \\ 0 \end{pmatrix}. \quad (8.3)$$

Once the DLT parameters in Equation 8.1 are determined by camera calibration and the projected skin friction field, $\bar{\tau} = (\bar{\tau}_1, \bar{\tau}_2)$, is extracted by the GLOF technique, the skin friction distribution $\tau = (\tau_1, \tau_2, \tau_3)$ on a surface in the object space can be computed by Equation 8.3. The reconstructed 3D skin friction vector field on a 3D model surface is a relative or normalized field and the absolute field can be computed by multiplying a coefficient determined by in-situ calibration at one or several locations.

The data reduction procedures in this study are summarized as follows:

- 1) Surface meshes of the wing-body junction model in the 3D object space are generated for AoAs of 0° , 6° and 12° .
- 2) The camera is calibrated for the different viewing angles and positions using several (at least 6) targets with known coordinates on the model surface in the body coordinate system. The computed DLT parameters in Equation 8.1 are stored for mapping from the image plane to the surface.
- 3) The luminescent oil images acquired for different viewing angles and positions are mapped onto the surface mesh using Equation 8.3 to reconstruct the luminescent oil flow fields on the surface. This step is useful to examine the accuracy of mapping procedure from images onto the model surface.

- 4) The projected skin friction vectors in the image plane are extracted from a time sequence of GLOF images taken from different viewing angles and positions using a suite of in-house developed MATLAB algorithms for the GLOF technique.
- 5) The complete skin friction vector field on the surface mesh in the object space is reconstructed using Equation 8.5 utilizing the projected skin friction vectors in different sections in the image plane. In this step, interpolations of the skin friction data between surface grid points are performed using a third-order B-spline scheme.

8.2 Experimental Setup

Experiments were conducted in a low speed recirculation wind tunnel at Shenyang Aerospace University. The dimensions of the test section are 3 m, 1.2 m and 1m in length, width and height, respectively. The test section flow speed ranges from 2 m/s to 55 m/s with a freestream turbulence intensity of less than 0.2 %. The wing used in the experiments is also known as the Rood Wing as documented by Simpson [113]. The wing cross section is a fusion of two sections – a 3:2 elliptic nose attached to a NACA 0020 tail section at its maximum thickness. Figures 8.1 and 8.2 are images of the wind tunnel and the Rood wing model mounted vertically on an aluminum flat plate. The wing had a chord length (c), maximum thickness (T) and height (H) of 383.3 mm, 90.0 mm, and 235.1 mm, respectively with a height-to-thickness ratio of 2.61. The flat plate was 1.25 m, 0.5 m and 9 mm in length, width and thickness, respectively with a blunt leading edge. The plate was supported by four struts and aligned parallel to the wind tunnel floor and side walls. The flat plate was at a height of 70 mm above the floor to avoid

interaction with the wind tunnel floor boundary layer. The wing and the plate were connected by a threaded rod joint and secured by tightening a nut on the threaded rod below the flat plate. The AoA of the wing is adjusted by pivoting it about the threaded rod joint.

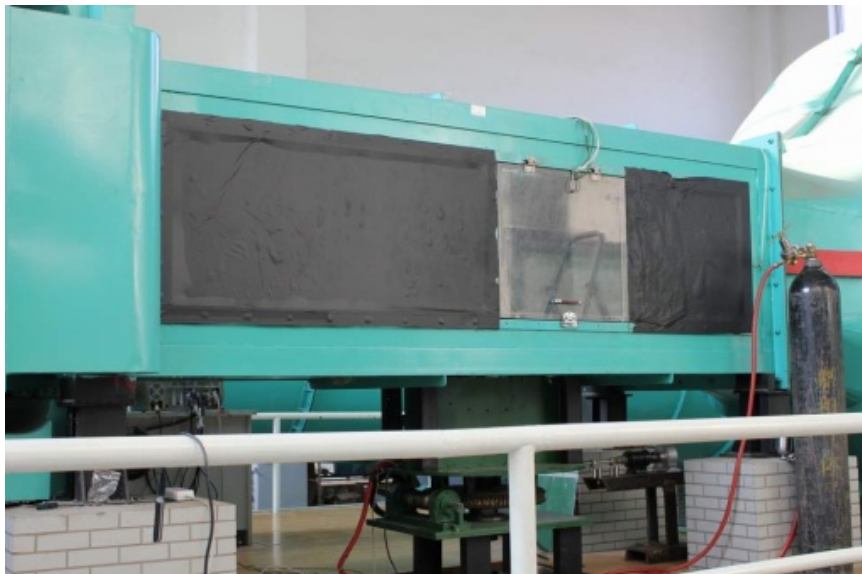


Figure 8.1 Shenyang Aerospace University low speed wind tunnel



Figure 8.2 Rood wing mounted on an elevated flat plate in the wind tunnel test section

The wing and flat plate surfaces were painted white to enhance the luminescent emission of the luminescent oil. Luminescent oil was prepared by mixing a commercial

ultraviolet (UV) dye for leak detection with silicone oil with a viscosity of 200 cs. The luminescent oil was sprayed onto the model surface using an automotive grade paint spray gun. The spray approach ensured that a uniform coat of luminescent oil was applied to the large model surface area. Based on the amount of oil consumed and the surface area covered, it is estimated that the oil film thickness was between 20 to 40 μm . On the vertical surfaces of the wing, no significant downward oil flow was observed even after five minutes post application of the oil film indicating minimal influence of gravity on the oil film.

The luminescent oil was excited by four ultraviolet (UV) LED lamps with an emission wavelength of 365 nm and a total power of 12 Watts. The luminescent emission was yellowish green hue at the wavelength of approximately 530 nm. The UV LED lamps were arranged appropriately to ensure uniform illumination of the model surface. A CCD camera was used to record images at a resolution of 1024×1024 pixels as 25 frames per second. A 500 nm longpass filter was used to filter out the excitation light spectrum. For image acquisition, the model surface was divided into five regions of interest: wingtip surface, wing suction surface, wing pressure surface, floor suction surface and floor pressure surface. Using a single camera, tests were run to capture the oil film development sequence in one region of interest. Tests were then repeated for the other regions of interest until all five regions were imaged.

The single camera approach for a complex surface possesses some disadvantages although it is simple in implementation. Since the illumination fields at different positions are dissimilar and non-uniform, the extracted skin friction vectors on different images taken at multiple positions cannot be simply normalized by a value at a single

location of the surface. This problem is tackled by correcting for a non-uniform illumination field for each image and performing in-situ calibration using a reliable point based technique such as oil film interferometry at suitable positions in each image for the respective regions of interest. In this work, without in-situ calibration and correction for non-uniform illumination, extracted skin friction vectors have the correct directions although their magnitudes are not universally scaled. Fortunately, skin friction line fields are sufficient to study the topological structures without considering skin friction magnitude. Several error sources are present in these experiments. In the optical flow computation for a skin friction field, the effect of gravity on a thin oil film is ignored, which is legitimate in most circumstances. However, gravity effects could be influential in certain regions where the oil aggregates after a certain amount of tunnel run time. Similar to other surface measurements with fluorescent molecules such as pressure and temperature sensitive paints, self-illumination effects would influence the accuracy of the measurement as considerable inter-reflection could occur at corner regions. Further studies should be made to compensate these effects to ensure that the results obtained are of higher accuracy and fidelity.

The parameter used to characterize the wing-junction is the bluntness factor defined as [105]

$$BF = \frac{1}{2} \frac{R_0}{X_T} \left(\frac{T}{S_T} + \frac{S_T}{X_T} \right) \quad (8.4)$$

where R_0 is the leading-edge radius of the wing, X_T is the chordwise location of the maximum thickness of the wing, T is the maximum thickness and S_T is the distance from the leading edge along the airfoil surface to the location of maximum thickness. The Rood wing used in this work has $BF = 0.32$, similar to previous studies [103, 105-107].

To quantify the influence of the incoming boundary layer, another relevant parameter is the momentum deficit factor defined as $MDF = Re_T \cdot Re_\theta$, where Re_T and Re_θ are the Reynolds numbers based on wing thickness and incoming boundary layer momentum thickness, respectively [105].

Tests were run at the freestream velocity of 27 m/s for AoAs of 0° , 6° and 12° . The Reynolds number based on the maximum wing thickness (Re_T) was 151,000. In this study, since the incoming boundary layer was not surveyed, the boundary-layer momentum thickness was estimated based on the flat-plate laminar boundary-layer. The estimated Re_θ was 200-500 and MDF was 500,000 to 750,000. The values of BF and MDF in this study are in the parametric domain where the horseshoe vortices are dominant [111].

8.3 Skin Friction Fields Mapped onto a 3D Model Surface

Figure 8.3 shows typical GLOF images at one instance for the five regions of interest at AoA of 6° . In Figure 8.3, images 1 and 2 are the luminescent oil patterns on the base surface in the suction and pressure sides of the wing, respectively. Image 3 shows the luminescent oil pattern on the wingtip surface and images 4 and 5 are the luminescent oil patterns on the suction and pressure surfaces of the wing, respectively. Figure 8.4 shows the luminescent oil intensity field mapped onto the wing-body junction model surface from the five images in Figure 8.3 using the DLT approach described by Equation 8.3. Figures 8.5 through 8.7 shows the skin friction lines mapped onto the 3D model surface viewed from the suction and pressure sides of the wing for AoA of 0° , 6° and 12° , respectively, where the color map indicates the luminescent intensity

distribution of the oil film. The total number of the surface grid points is 240372, and most of the grid points are on the floor surface.

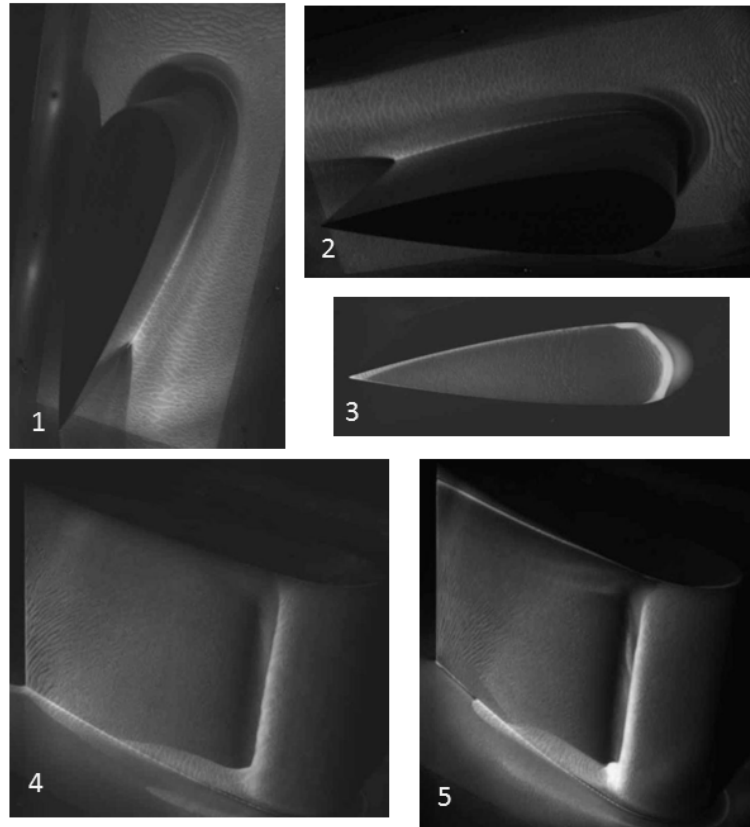


Figure 8.3 Typical GLOF images for the five regions of interest at $AoA = 6^\circ$, (1)wing suction side base surface, (2)wing pressure side base surface (3)wingtip surface (4)pressure side wing surface and (5)suction side wing surface

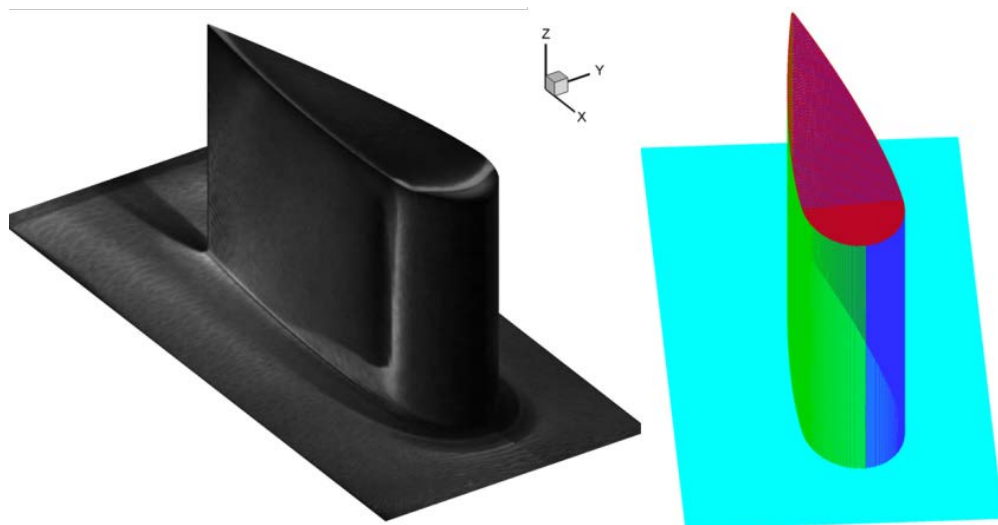
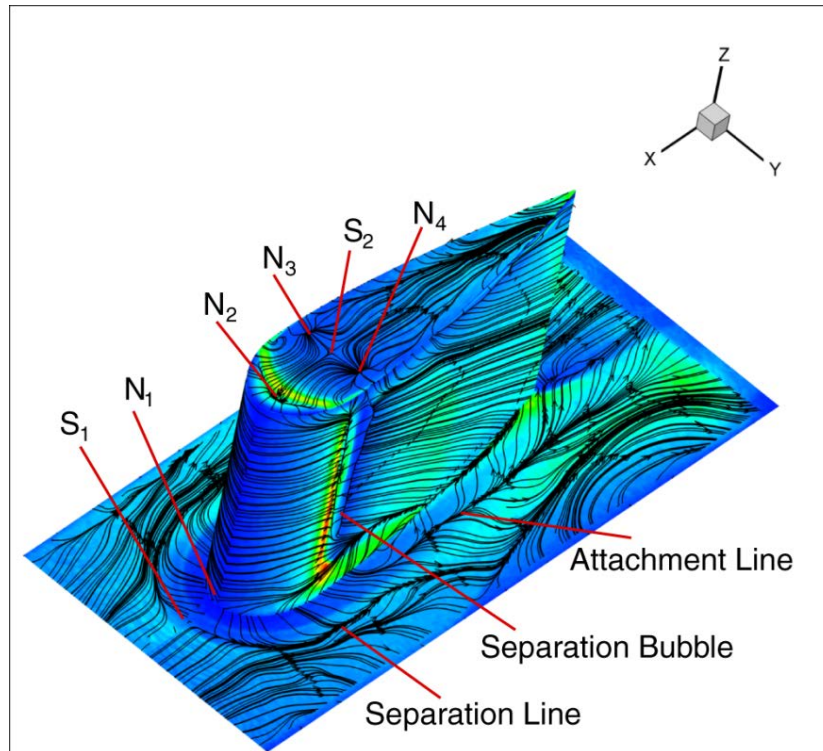
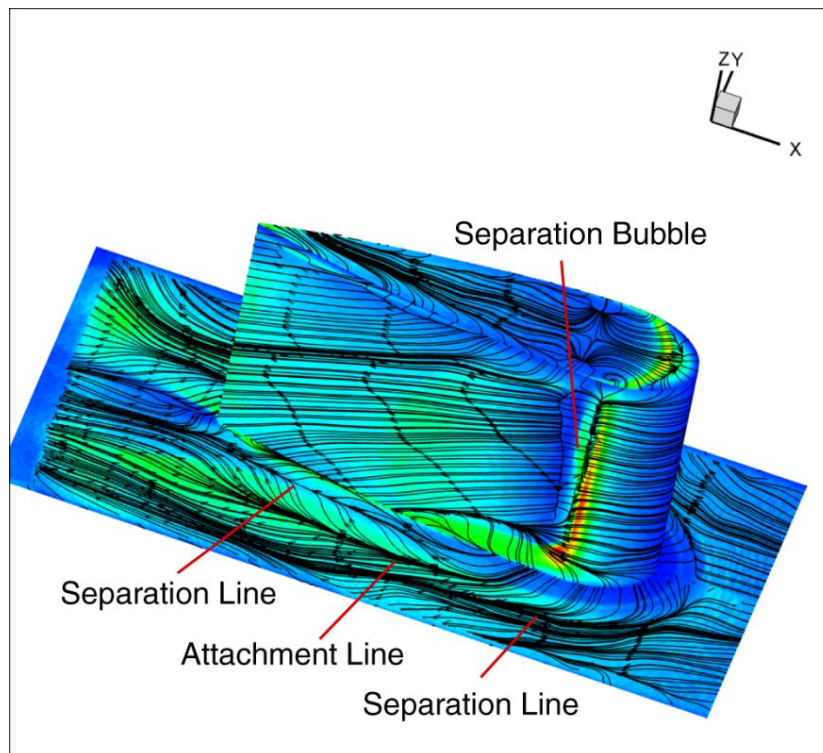


Figure 8.4 GLOF intensity field mapped on the surface of the wing-body junction flow model (left) and the mesh of the Rood wing model (right) at $AoA = 6^\circ$

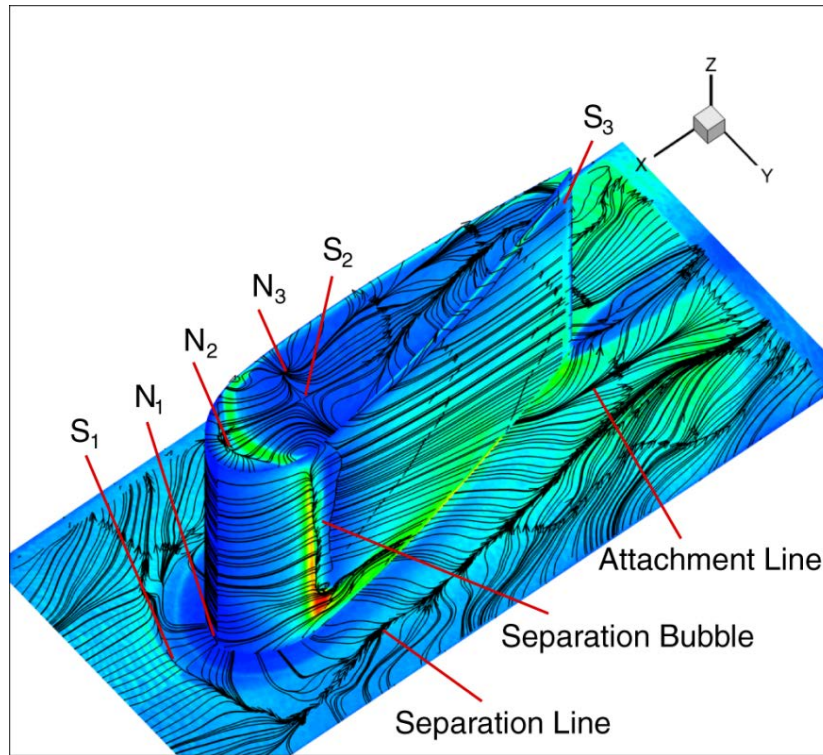


(a)

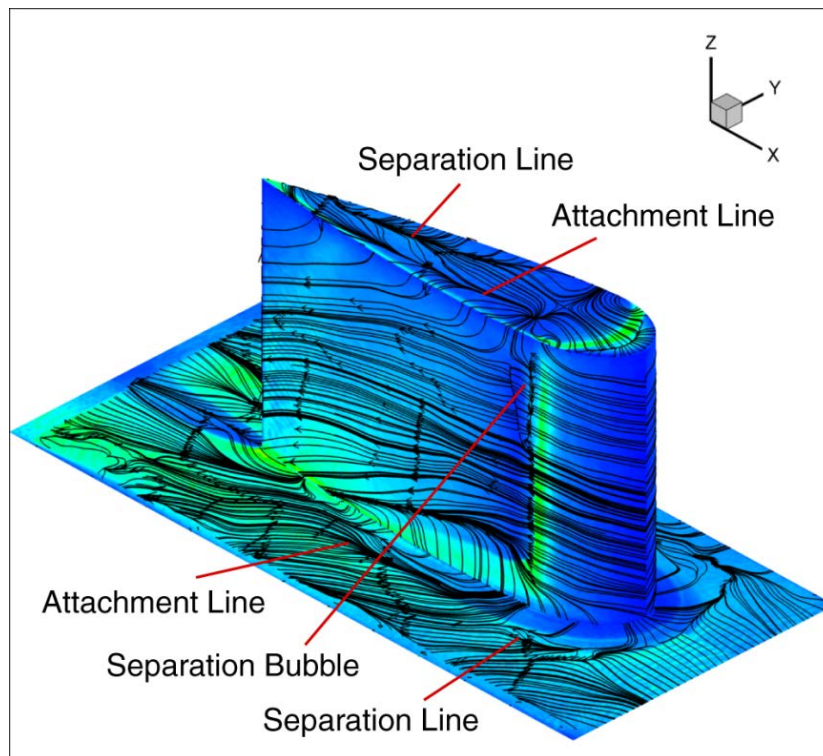


(b)

Figure 8.5 Skin friction lines mapped on the surface of the wing-body junction model viewed from (a) wing suction side and (b) wing pressure side, at AoA of 0° , where the color map indicates the luminescent intensity distribution of the oil film

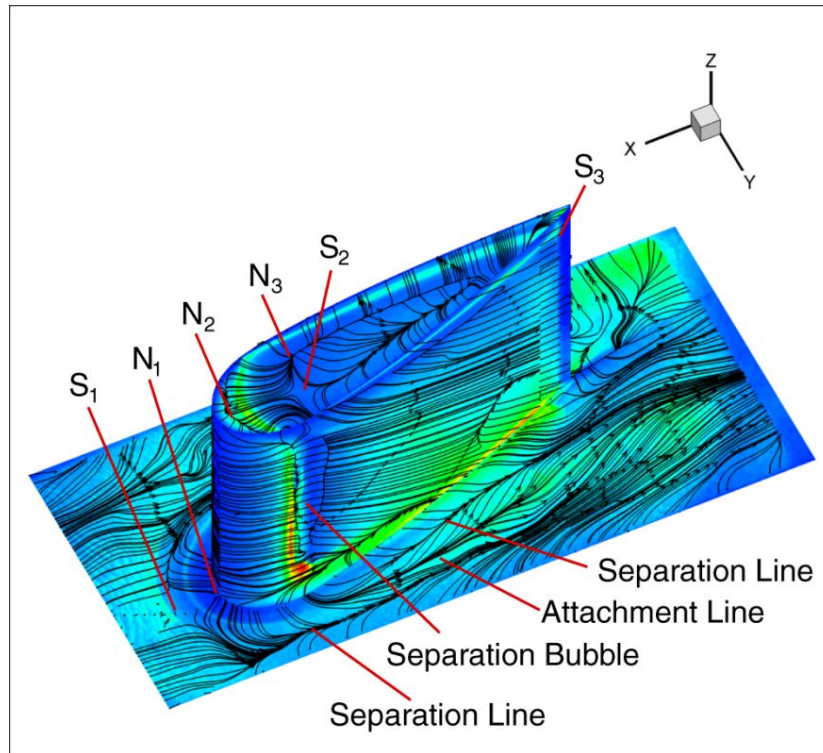


(a)

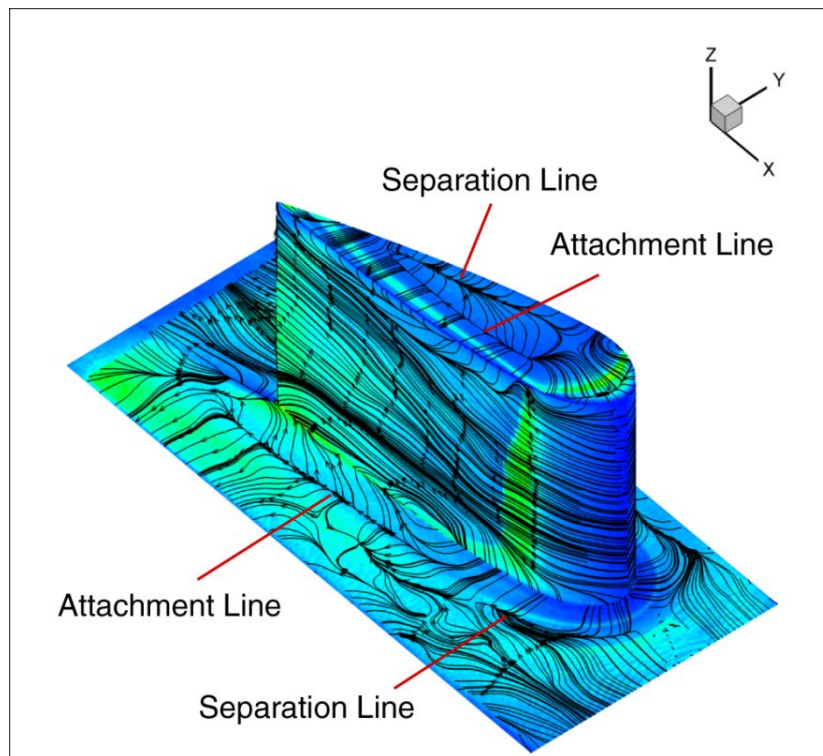


(b)

Figure 8.6 Skin friction lines mapped on the surface of the wing-body junction model viewed from (a) wing suction side and (b) wing pressure side, at AoA of 6° , where the color map indicates the luminescent intensity distribution of the oil film



(a)



(b)

Figure 8.7 Skin friction lines mapped on the surface of the wing-body junction model viewed from (a) wing suction side and (b) wing pressure side, at AoA of 12° , where the color map indicates the luminescent intensity distribution of the oil film

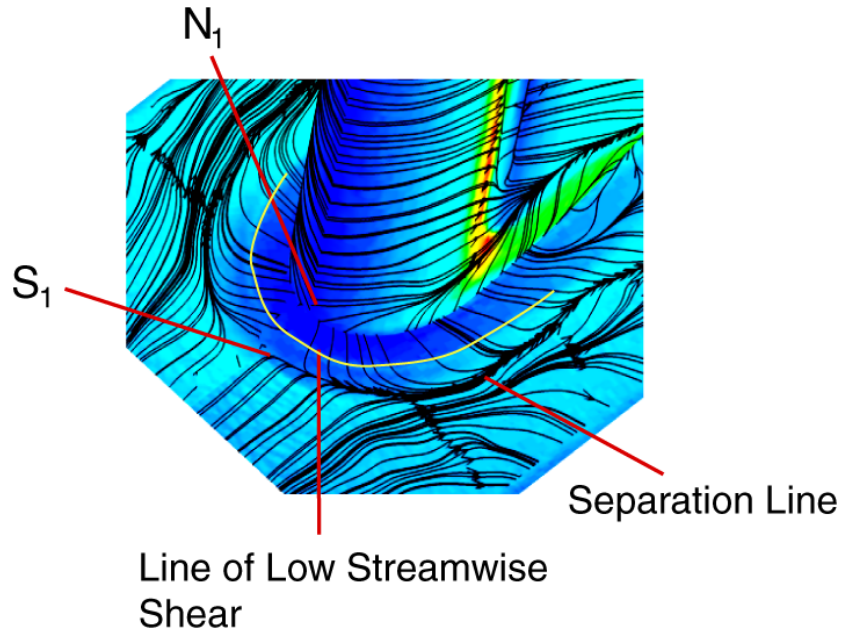


Figure 8.8 Illustration of the primary separation line and the line of low streamwise shear on the base surface of the wing-body junction model at AoA of 0°

8.4 Evolution of Skin Friction Field Topology by Varying Angle of Attack

Skin friction vectors were extracted from GLOF images taken from multiple viewing angles and positions for the specified regions of interest. Between 30 to 80 snapshot solutions were superposed to reconstruct the skin friction field for each region of interest using the GLOF technique. The selection of the number of snapshot solutions was dependent on specific regions being processed where the timescales of the oil evolution processes differed. Approximately 2 million skin friction vectors were extracted per test case.

The high resolution skin friction fields of the wing-body junction flow extracted in this study have provided useful data previously unavailable. Existing quantitative investigations of wing-body junction flows have focused on velocity fields around the wing-body junction from PIV measurements and numerical simulations. With the availability of high resolution skin friction fields, it is now worthwhile to examine the

relationship between the skin friction fields and the associated flow structures. Figures 8.5 through 8.7 are illustrations of the skin friction lines mapped on to the model surface for AoAs of 0° , 6° and 12° , respectively. As indicated in all three figures, the primary separation line originates from the saddle (S_1) and node (N_1) combination located at the intersection between the leading edge of the wing and the base surface. This saddle-node combination corresponds to a single large horseshoe vortex formed upstream of wing and has been previously observed in experiments [103] and numerical simulations [108, 110]. Another feature is also clearly observed for all cases. A distinct line has been observed in previous work [103, 108], that is the line of low streamwise shear between the saddle and node which divides a strip of a high skin friction region adjacent to the wing and a low skin friction region upstream. Figure 8.8 shows the primary separation line and the line of low streamwise shear on the surface of the wing-body junction model for AoA 0° . The color map in the figure indicates the luminescent intensity distribution of the oil film. Since the luminescent intensity of the oil film is inversely proportional to the oil film thickness and subsequently the skin friction magnitude, the line of low streamwise shear is delineated by the interface between the high and low intensity regions as indicated in Figure 8.6. The line of low streamwise shear is also clearly seen in both cases of AoA of 6° and 12° in Figures 8.6 and 8.7, respectively.

Additional separation and reattachment lines are also observed on the base surface near the wing side surfaces for all three cases. These structures are associated with the secondary separation induced by the interaction between the primary horseshoe vortex and floor boundary layer influenced by the wing side surface. Secondary separation is typically described by the presence secondary streamwise vortices parallel to the primary

horseshoe vortex in the proximity of the wing side surface. These secondary streamwise vortices have been observed in previous flow visualizations [107] of wing-body junction flow. This phenomenon is similar to the secondary separation induced by the primary vortex in a fin shock/boundary-layer interaction [125].

Figures 8.9 and 8.10 are plots of the extracted skin friction line fields for the various surfaces of the wing-body junction model at AoA of 0° and 6° , respectively. Isolated singular points and separation and reattachment lines are clearly visualized in Figures 8.9 and 8.10. For all cases a long separation bubble in the spanwise direction is observed near the location of the maximum thickness of the wing. On the pressure surface of the wing, the separation bubble is shorter at AoA of 6° , and it completely disappears at AoA of 12° as seen in Figures 8.6 and 8.7, respectively. The boundary layer on the wing suction side starts to separate due to the adverse pressure gradient at the location of the maximum thickness, and it subsequently reattaches due to flow transition. This phenomenon is usually observed in thick airfoils in a suitable range of Reynolds numbers. On the wing pressure side, the separation bubble decreases in size and eventually disappears due to the favorable pressure gradient as the AoA is increased. These separation bubbles are essentially 3D or quasi-2D.

Since the wing is of low aspect ratio ($AR = 0.61$), the flow on the wing surface is influenced by the vortices on the base surface as well as the wing tip vortex. On the suction side of the wing at AoA of 6° as seen in Figures 8.6 and 8.10, there is a distinct saddle near the upper corner of the trailing edge, and a long separation bubble in the spanwise direction near the location of the maximum thickness of the wing. Another observation on the wing suction side is that the skin friction lines are deflected downward

after the separation bubble compared to the horizontal skin friction lines near the leading edge of the wing before the separation bubble. This is clearly visible in Figures 8.5 through 8.7 and 8.9 through 8.10. This may be induced mainly by the downwash of the primary horseshoe vortex. On the wing pressure side, the downward direction of the skin friction lines is not obvious for AoA of 6° as seen in Figure 8.10, which is probably due to the competing influence between the primary vortex and the wingtip vortex. As the AoA is increased to 12° , the direction of the skin friction lines on the pressure surface of the wing is reversed upward, indicating stronger influence from the wingtip vortex. This is clearly illustrated in Figure 8.7 (b).

The skin friction topology on the wingtip surface is complex and intriguing since it is related to both the generation of the wingtip vortex and leading edge separation. For the case of 0° AoA, as shown in Figure 8.5 (a), the skin friction pattern is symmetric with respect to the centerline. A 3D separation bubble is formed from the wingtip leading edge, and its reattachment occurs at saddle S_2 between source nodes N_3 and N_4 . As the AoA is increased to 6° and 12° , a wingtip vortex is generated due to the pressure difference between the wing suction and pressure sides in addition to the 3D leading-edge separation bubble. At AoA of 6° as illustrated in Figure 8.6 (a), the saddle S_2 and source node N_3 remain on the surface, but source node N_4 moves off the wingtip surface towards the suction side of the wing. The skin friction field on the wingtip surface for AoA of 12° is qualitatively similar to that of 6° AoA. Separation and reattachment lines are also observed on the wingtip surface for non-zero AoAs as illustrated in Figures 8.6 (a) and 8.7 (a) for AoAs of 6° and 12° , respectively. These separation and reattachment lines are associated with the secondary structures formed within the wingtip vortex that is

formed at non-zero AoAs. The observed skin friction topology on the wingtip surface is similar to that observed on a low aspect ratio rectangular wing studied by Liu et al. [57]. Regions A and B in Figure 8.9 and A, B, C and D in Figure 8.10 are isolated regions selected for further topological constraint analysis and will be examined in detail in Section 8.5 of this chapter.

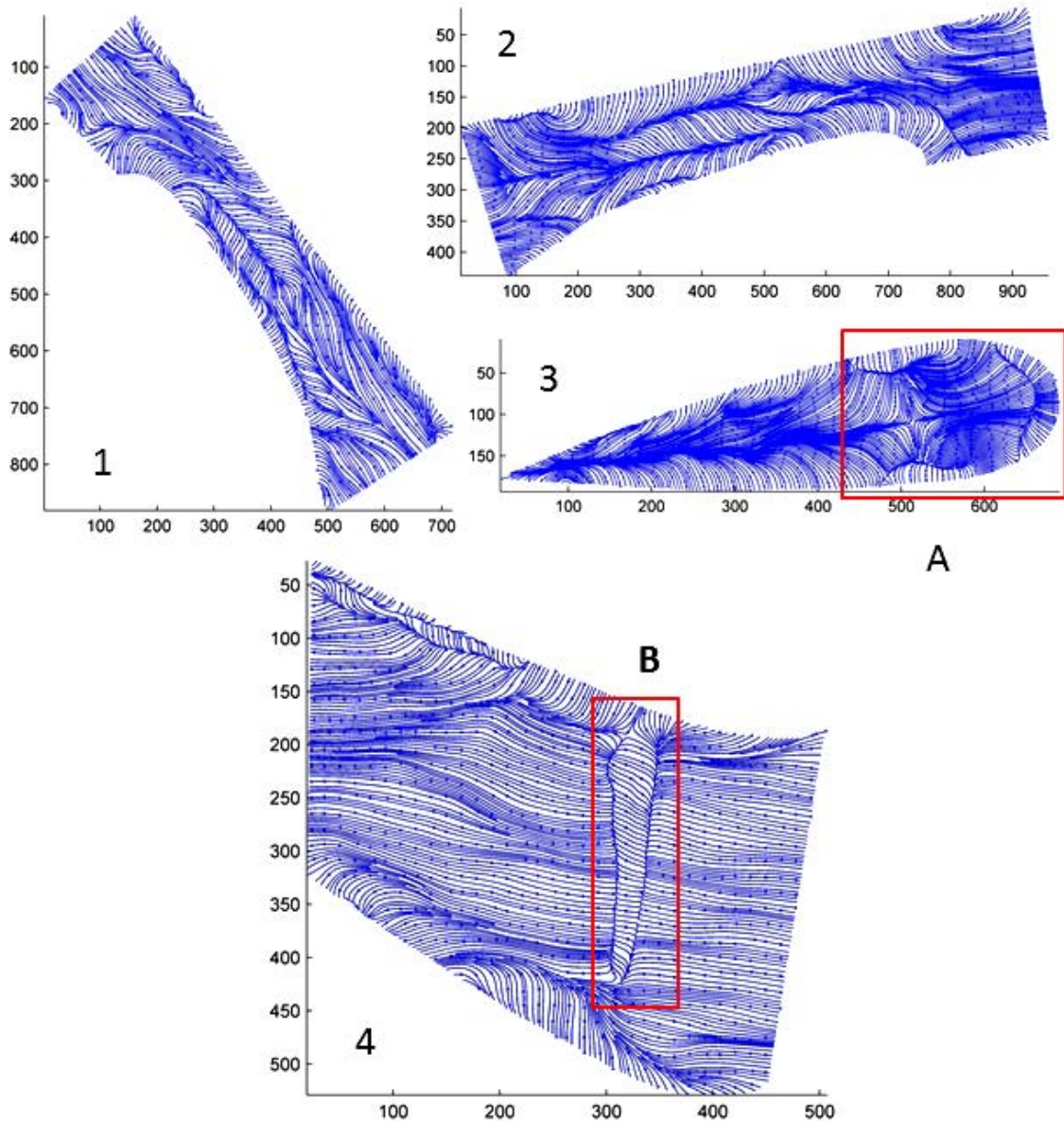


Figure 8.9 Skin friction lines extracted from GLOF images taken from five different viewing angles and positions for $\text{AoA} = 0^\circ$ on (1)base surface on the suction side of the wing, (2)base surface on the pressure side of the wing, (3)wingtip surface (4)wing surface

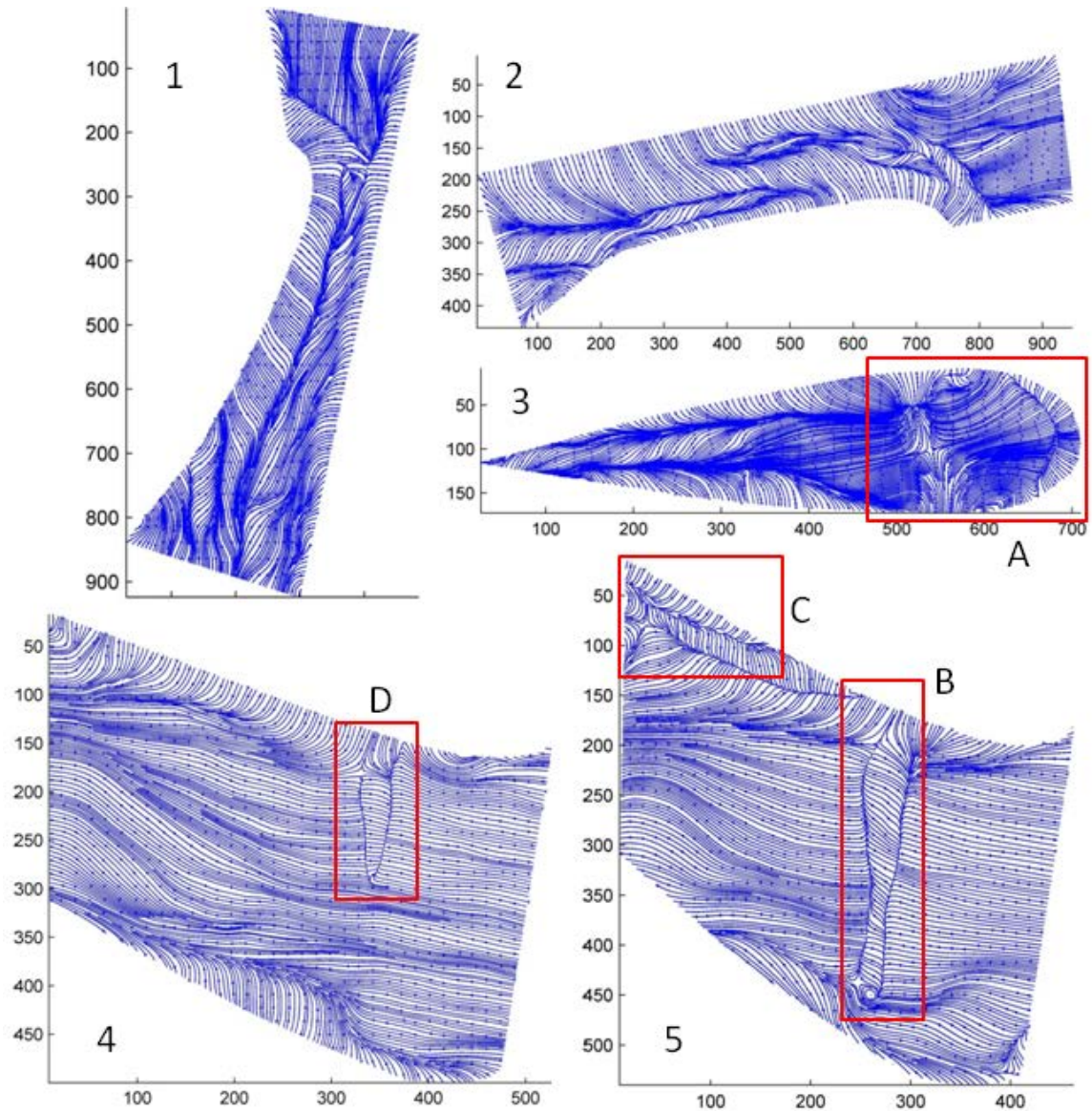


Figure 8.10 Skin friction lines extracted from GLOF images taken from five different viewing angles and positions for $AoA = 60$ on (1)base surface on the suction side of the wing, (2)base surface on the pressure side of the wing, (3)wingtip surface, (4)pressure surface of the wing and (5)suction surface of the wing

8.5 Skin Friction Topology Constraint Analysis

A topological rule was derived by Hunt et al. [38] for junction flows, utilizing the Euler characteristics of a torus defined by the Poincare-Hopf theorem resulting in the relation described by Equation 8.5 (referred to as Hunt's rule) below,

$$\#N - \#S = 0 \quad (8.5)$$

where #N and #S are the number of nodes and saddles on the surface of a cylinder and the base surface in a junction flow. Equation 8.5 is in fact a reduced case of the collapsed sphere method developed by Foss [35, 44].

For this study, skin friction topology constraint analysis will be performed using the Poincare-Bendixson index formula as described in Chapter 3 for selected isolated regions. The P-B index formula has previously been used in analysis of topological consistency of junction flows by Liu et al. [57]. The P-B index formula is defined as,

$$\#N - \#S = 1 + (\#Z^+ - \#Z^-) / 2 \quad (8.6)$$

where #N, #S, #Z⁺ and #Z⁻ is the number of the nodes, saddles, positive switch points, and negative switch points, respectively. Hunt's rule is directly obtainable using the P-B index formula as illustrated by Figure 8.11. A circle is defined around a wing-body junction as the penetrable boundary that encloses all the singular points on the surface. The circular boundary is selected to be sufficiently large such that the skin friction vectors on the front and back sections of the circumference go into and out of the circle, respectively. As a consequence, two negative switch points exist and applying Equation 8.6, the conservation law, #N - #S = 0, as given by Hunt's rule is obtained.

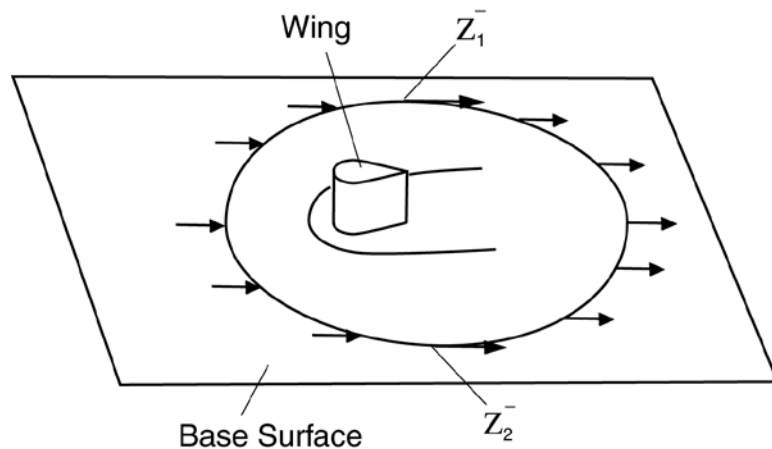


Figure 8.11 Illustration of a penetrable boundary defined for the base surface of a wing-body junction flow model

Hunt's rule is defined for application to a closed orientable surface. Typically, skin friction fields extracted by the GLOF technique present skin friction fields of isolated surfaces of a model e.g., the top or side surface of a wing. In certain situations, it is impossible to perform measurements on the whole surface of a model and in this case, the P-B index formula is able to provide a topological constraint for isolated regions bounded by a penetrable boundary. For this study, skin friction fields are analyzed for topological consistency using both Hunt's rule and the P-B index formula since skin friction measurements were performed for all surfaces of the wing-body junction model. Hunt's rule will be applied to the complete skin friction fields mapped onto the 3D model surface and the P-B index formula will be applied to selected isolated regions. These selected isolated regions are regions A and B in Figure 8.9 for the model at 0° AoA and regions A, B, C and D in Figure 8.10 for the model at 6° AoA

8.5.1 AoA = 0°

For this case, the skin friction topology on the wingtip surface of the Rood wing is symmetric about the centerline, which is characterized by node N_2 near the leading edge, nodes N_3 and N_4 about the centerline, and saddle S_2 between N_3 and N_4 at the centerline as illustrated by Figure 8.12 (a). Additionally, a pair of saddles, S_3 and S_4 is visible near the side edges. In this region, four negative and two positive boundary switch points are identified, therefore the conservation law given by the P-B index formula, $\#N - \#S = 1 + (\#Z^+ - \#Z^-) / 2 = 0$ is satisfied. On the side surface of the wing, a long separation bubble is observed, identified as region B in Figure 8.9. The magnified view of this region is shown in Figure 8.12 (b). A node-saddle pair (N_5 and S_5) is visible along with two negative boundary switch points. The conservation law given by the P-B

index formula, $\#N - \#S = 1 + (\#Z^+ - \#Z^-) / 2 = 0$, is also satisfied in this region. By examining the complete skin friction field of the wing-body junction model for this case as illustrated by Figure 8.5 and applying Hunt's rule, $\#N - \#S = 0$, it is clear that it is satisfied for this case with a total number of 6 nodes and 6 saddles identified on all surfaces.

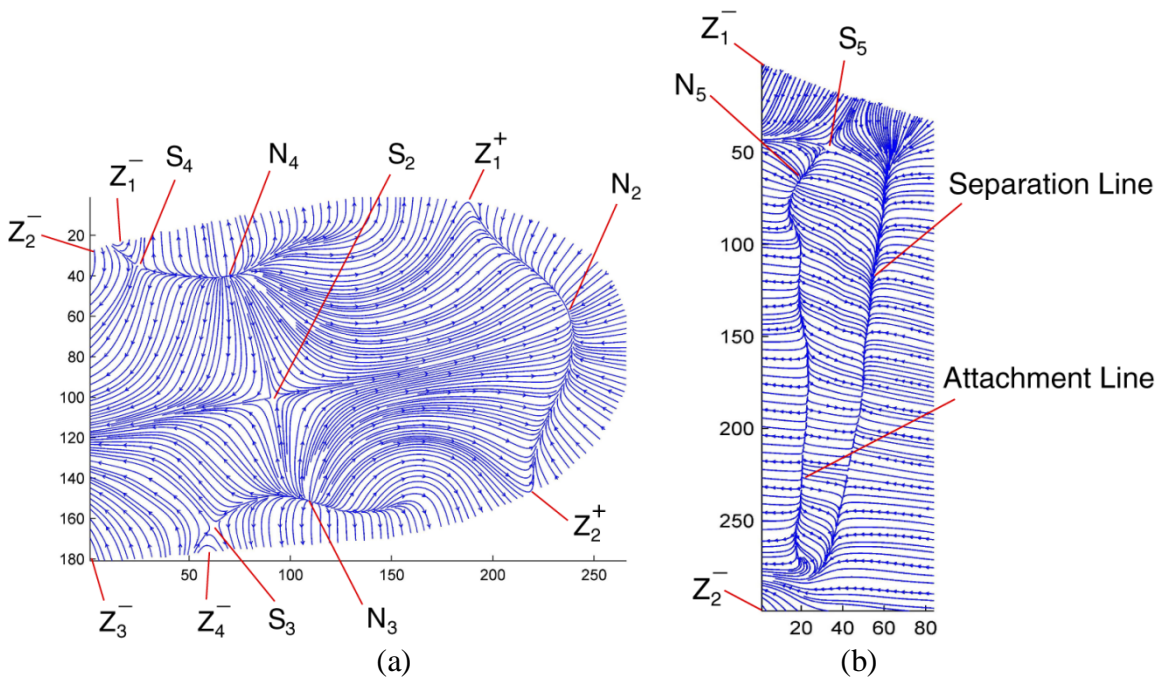


Figure 8.12 Magnified views of skin friction lines in selected regions on the wing-body junction model at AoA of 0° as defined in Figure 8.9 for regions, (a)A and (b)B

8.5.2 AoA = 6°

For the case of the wing-body junction model at AoA of 6° , the four regions, A, B, C and D, identified for further analysis in Figure 8.10 are shown in Figure 8.13 (a), (b), (c) and (d), respectively. Figure 8.13 (a) is a skin friction line plot of the magnified region near the leading edge of the wingtip surface. A sink node N_2 , source node N_3 and saddle S_2 are clearly identified. Two negative (Z_1^- and Z_2^-) and two positive (Z_1^+ and Z_2^+) are also identified. Applying the P-B index formula shows that the conservation

law, $\#N - \#S = 1 + (\#Z^+ - \#Z^-)/2 = 1$, is satisfied indicating topological consistency of the extracted skin friction field in Region A. Figure 8.13 (b) shows the skin friction topology of region B in the proximity of the long separation bubble on the suction surface of the wing. The node-saddle pairs (N_4 and S_4) and (N_5 and S_5) are visible in the separation bubble. Two negative switch points are also identified on the boundary. Applying the P-B index formula to this region, the conservation law $\#N - \#S = 1 + (\#Z^+ - \#Z^-)/2 = 0$ is satisfied region B. For region C, as shown in Figure 8.13 (c), a single saddle S_3 near the upper corner of the suction surface of the wing, along with 5 negative and 1 positive boundary switch points are identified. As a result, the conservation law, $\#N - \#S = 1 + (\#Z^+ - \#Z^-)/2 = -1$, is satisfied for region C. Similarly, for region D as shown in Figure 8.13 (d), a node-saddle pair (N_6 and S_6) and a negative boundary switch point (Z_1^+) is identified and the conservation law $\#N - \#S = 1 + (\#Z^+ - \#Z^-)/2 = 0$ is satisfied.

Applying Hunt's rule given by, $\#N - \#S = 0$, with 6 nodes and 6 saddles, the conservation law satisfied. Alternatively, summing the number of boundary switch points in all regions (A, B, C and D), it is also found that the conservation law $\#N - \#S = 1 + (\#Z^+ - \#Z^-)/2 = 0$ is satisfied. This indicates that the skin friction fields extracted by the GLOF technique are topologically consistent.

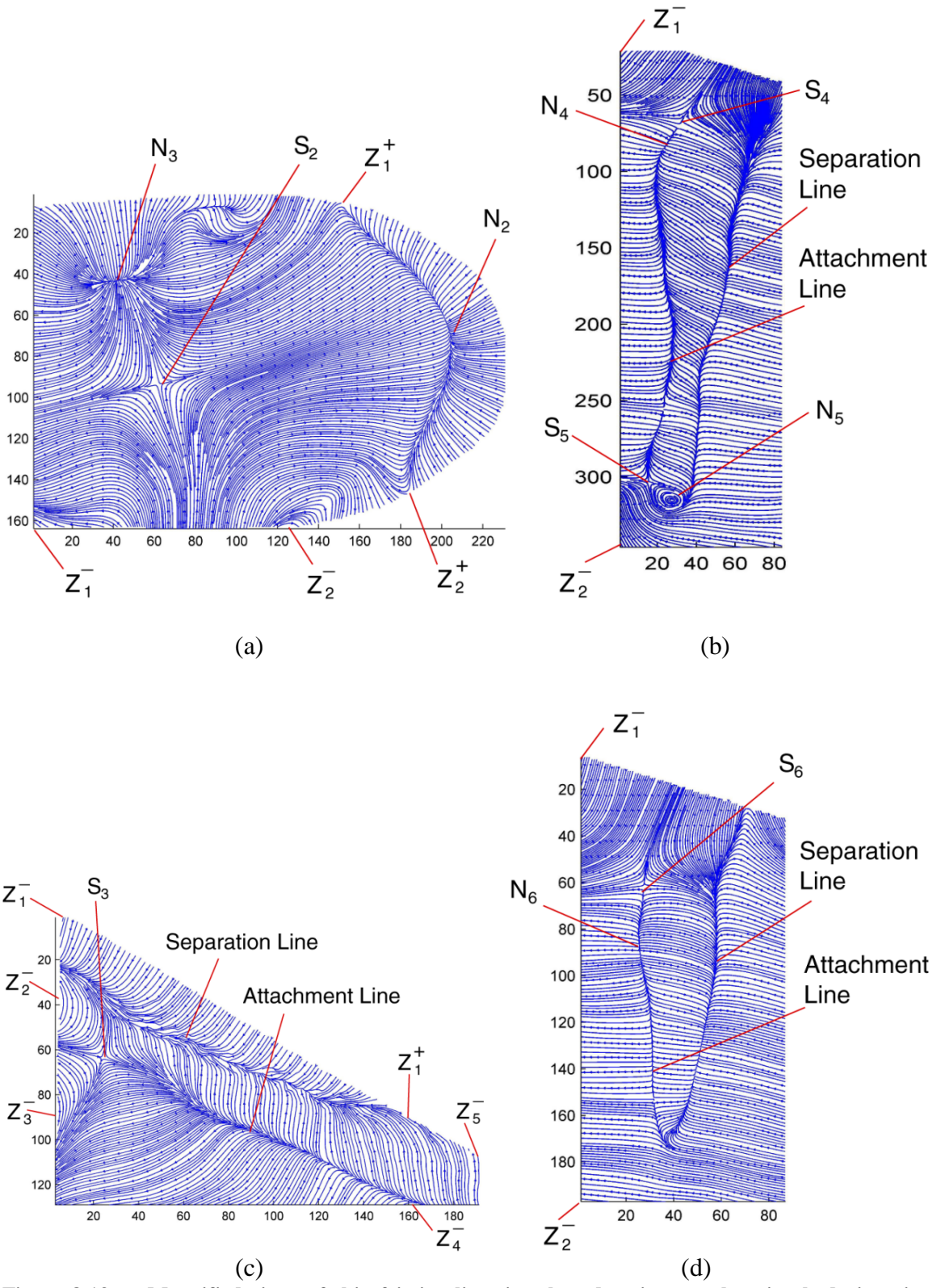


Figure 8.13 Magnified views of skin friction lines in selected regions on the wing-body junction model at AoA of 6° as defined in Figure 8.10 for regions, (a)A, (b)B, (c)C and (d)D

8.5.3 AoA = 12°

The wing-body junction flow model at AoA of 12° is considered as additional case to be analyzed. Figures 8.7 (a) and (b) are illustrations of the skin friction lines mapped on the 3D model surface viewed from the suction and pressure sides of the wing, respectively. The topological structures for AoA of 12° are qualitatively similar to that for AoA of 6°. The node-saddle combination (N_1 and S_1) associated with the primary horseshoe vortex on the base surface is similar to the previous cases. The reattachment and secondary separation lines are also observed on the base surface on the suction and pressure sides of the wing. The topological structure on the wingtip surface is similar to the case of AoA of 6°. On the pressure side surface of the wing, the separation bubble is not visible and no isolated singular points are identified. On the suction side surface of the wing, a long separation bubble is visible along with a saddle near the upper corner of the trailing edge and two node and saddle pairs occurring in the separation bubble. A total number of 5 nodes and 5 saddles are identified on all surfaces of the model. Applying Hunt's rule, $\#N - \#S = 0$, it is seen that the conservation law is satisfied.

8.6 Summary

This work has developed the procedures for implementing the GLOF technique for multiple images taken from different viewing angles and positions and subsequently mapping the extracted skin friction vectors to a 3D model surface. The GLOF technique was used to obtain high resolution skin friction vector fields and the photogrammetric method was applied to map the extracted skin friction vectors from the image plane onto the surface mesh of the wing-body junction model to reconstruct a complete skin friction field on the model surface in the 3D object space. The identified primary separation line

and line of low streamwise shear beginning upstream of the wing on the base surface are directly associated with the single primary horseshoe vortex. The reattachment and separation lines on the base surface in the proximity of the wing side surfaces are related to the secondary separation induced by the interaction between the primary horseshoe vortex and the floor boundary layer. Separation bubbles were also observed near the location of maximum thickness on the wing side surfaces. The separation bubble on the wing pressure side surface was observed to reduce in size at AoA of 6° and completely disappear at AoA of 12° . This occurs because a favorable pressure gradient on the wing pressure side surface as the AoA is increased. The complicated topological structures on the wingtip surface are associated with the leading edge separation and generation of the wingtip vortex.

Based on the extracted skin friction fields, the skin friction topology on the entire wing-body junction model and in selected isolated regions are studied, including isolated singular points and separation and attachment lines. The application of Hunt's rule to the skin friction fields on the complete wing-body junction model surface has been shown to obey the conservation law for all cases. This is the first experimental verification of the topological rule given by Hunt et al. [38] for junction flows. The application of the Poincare-Bendixson index formula to the selected isolated regions has also shown that the conservation law is satisfied. These topological constraints have typically been applied as a mathematical constraint to surface flow visualization patterns. This work has presented the first experimental verification of the topological rules due to the availability of the GLOF technique which provides a method for high resolution global skin friction diagnostics.

CHAPTER 9

COMBINED SURFACE PRESSURE AND GLOBAL SKIN FRICTION MEASUREMENTS

Skin friction vector fields are critical in understanding the flow topology near a wall in complex separated flows such as junction flows. The surface pressure field, along with skin friction, is another building block to reconstruct a near-wall flow field as described by Wu et al. [126] and Bewley and Protas [127]. However, skin friction and surface pressure field data for complex separated flows such as junction flows or flow about a simplified ground vehicle are not widely available due to a lack of quantitative global skin friction and surface pressure diagnostic tools.

The objective of this study is to measure skin friction and surface pressure fields on the floor surface around a square cylinder and a diamond cylinder in junction flows as well as the top and side surfaces of a simplified ground vehicle model (Ahmed model) using a combination of global luminescent oil film (GLOF) skin friction meter and pressure sensitive paint (PSP). Preliminary measurements of skin friction fields around cylinders in junction flows have been conducted using the S3F technique [9] and the GLOF technique [27]. This work will present combined measurements of skin friction and surface pressure fields which aims to further the understanding of the complex flow structures associated with junction flows and flow over an Ahmed model. The skin friction topology and corresponding surface pressure fields will be discussed in detail.

9.1 Experimental Setup

Measurements were conducted in the Tohoku University Basic Aerodynamic Research Wind Tunnel (T-BART) which is a suction-type wind tunnel. The test section is 300 mm by 300 mm by 760 mm in width, height and length, respectively with a flow uniformity of $\pm 1\%$ and turbulence intensity of 0.5%. For junction flow measurements, the test model was a 3D square cylinder with a 40×40 mm cross-section and 100 mm height mounted on a flat plate with turntable to adjust the incidence angle of the model relative to the incoming flow. The flat plate had a length, width and thickness of 600 mm, 297 mm and 15 mm, respectively and was painted white to enhance the luminescent emission of the oil. GLOF and PSP measurements were conducted on the base surface around the model. The turntable angle was set at 0° for the square cylinder and 45° for the diamond cylinder. Figure 9.1 is a schematic of the cylinder model and the flat plate.

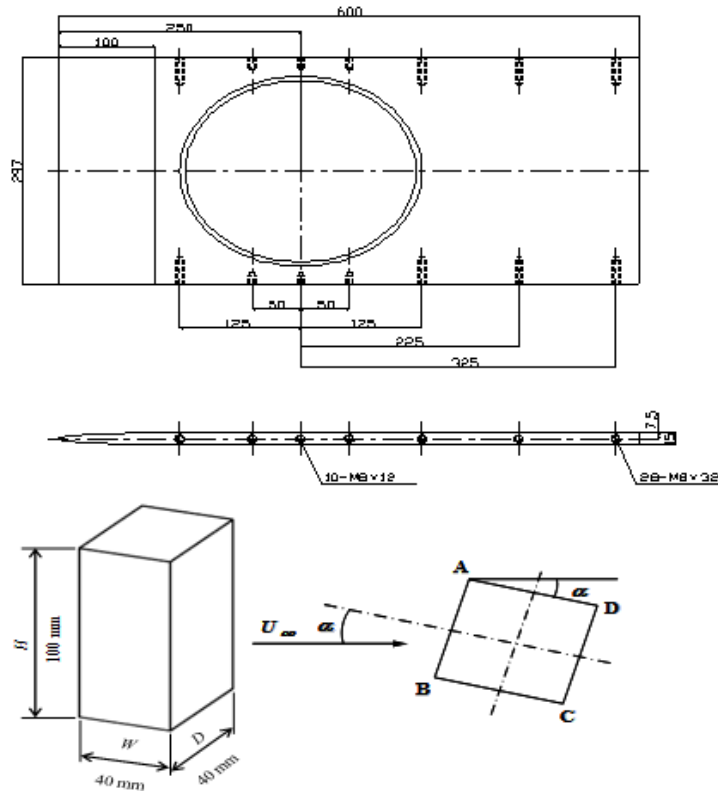


Figure 9.1 Schematic of junction flow setup

For Ahmed model measurements, the test model used is a 1/10th scale of the model used by Ahmed et al. [128]. The model had a length, height and depth of 104.4 mm, 28.8 mm and 38.9 mm, respectively with a 25° rear slant angle. The model was mounted on the same flat plate used in the junction flow tests. The turntable was used adjust the incidence angle of the model relative to the incoming flow. The angle was set at 0° and 20° to simulate the model in sideslip. GLOF and PSP measurements were conducted on the top and leeward side surface of the Ahmed model. Figure 9.2 is a schematic of the Ahmed model and the flat plate.

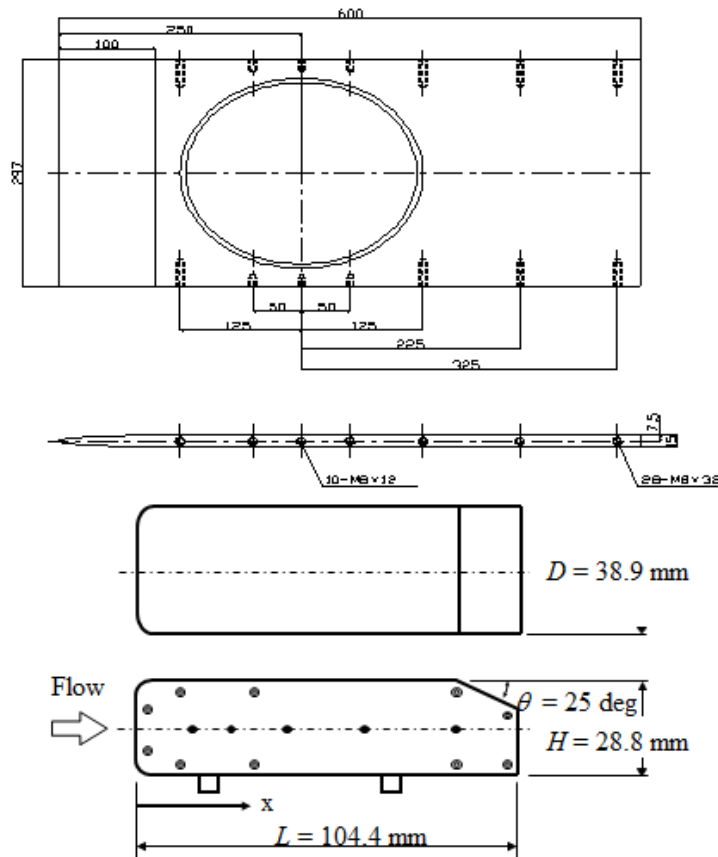


Figure 9.2 Schematic of Ahmed model setup

The freestream velocity was set at 50 m/s for all GLOF and PSP measurement. The Reynolds number based on the model length was 130,000 for the square cylinder, 180,000 for the diamond cylinder and 326,000 for the Ahmed model. Hot wire

measurements verified that the incoming boundary layer was laminar under these conditions. The Blasius solution for a laminar flat plate boundary layer estimates the boundary layer thickness at 1.3 mm.

9.1.1 GLOF

For GLOF measurements, Perylene was used as the luminescent molecule. Luminescent oil was made by mixing 5 milligrams of Perylene with 1 Liter of silicone oil. The viscosity of the silicon oil used was 350 cs. The luminescent oil has a peak emission wavelength of 450 nm when excited by a 395 nm source. Figure 9.3 shows the experimental setup for GLOF measurements in junction flows.

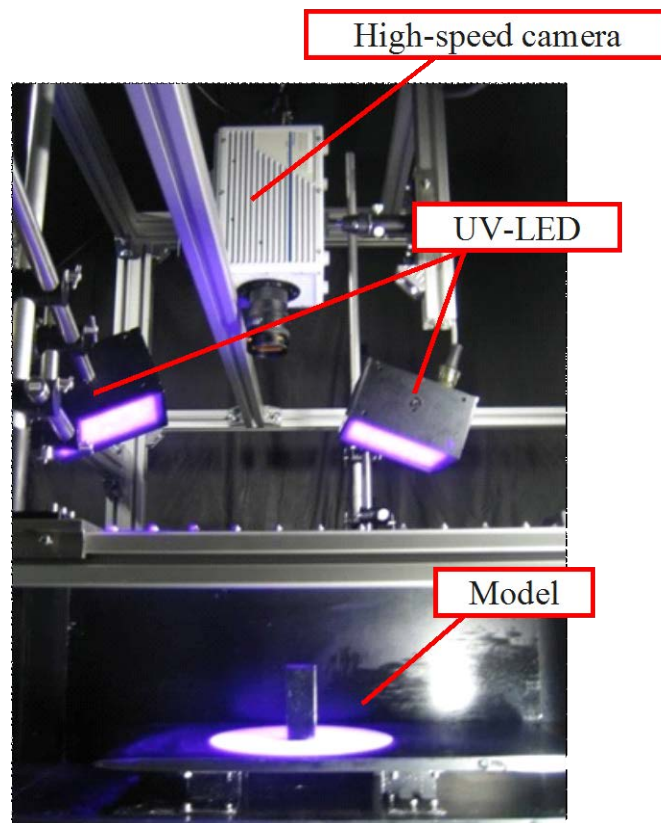


Figure 9.3 Image of experimental setup for GLOF measurements

The luminescent oil was brushed on the base surface and excited by two UV LED units manufactured by Hamamatsu (Model: LEDH576-395) with a peak emission

wavelength of 395 nm. The UV LED units were arranged to produce a uniform illumination field on the model surface. Image acquisition was performed using a 12-bit CMOS high-speed camera manufactured by Photron (Model: FASTCAM SA5). An optical bandpass filter with a transmission wavelength of 500 ± 50 nm was used to filter out the excitation source and capture the luminescent oil emission centered around 450 nm. Images were acquired at 60 frames per second with an exposure time of 16.6 ms. Skin friction fields were reconstructed from a set of between 40 to 80 snapshot solutions. The interval between image pairs for a single snapshot solution was set at 1 second.

9.1.2 PSP

Pressure sensitive paint (PSP) is a thin luminescent polymer coating used for measuring surface pressure fields in aerodynamics experiments. PSP utilizes the oxygen quenching mechanism of luminescence [25, 130-133]. In PSP, a luminescent molecule is used as a sensing probe. Generally, a luminophore and a polymer binder are dissolved in a solvent, and the resulting paint is applied to a surface using a spray gun or brush. Once the solvent evaporates, a solid polymer layer in which the luminescent molecule is immobilized remains on the surface. When an excitation source illuminates the coating, the luminescent molecule is excited and emits light at a longer wavelength due to Stokes shift.

The luminescent emission radiance from a coating can be affected by certain physical processes. The main photophysical process in PSP is oxygen quenching that causes a decrease of the luminescent intensity as the partial pressure of oxygen or air pressure increases. The polymer binder for PSP is oxygen permeable, which allows oxygen molecules to interact with the luminescent molecules in the binder. PSP is also

affected by the thermal quenching; therefore, it is intrinsically temperature sensitive. For oxygen quenching, the luminescent intensity (I) is described by the Stern-Volmer equation. According to Henry's law, the oxygen population in a polymer binder is proportional to the partial pressure (p) of oxygen or air pressure. By taking a luminescent intensity ratio between the wind-off and wind-on conditions, the Stern-Volmer equation suitable for aerodynamic applications is given by

$$\frac{I_{ref}}{I} = A(T) + B(T) \frac{P}{P_{ref}}, \quad (9.1)$$

where the Stern-Volmer coefficients $A(T)$ and $B(T)$ are temperature-dependent, and I_{ref} is the luminescent intensity at the wind-off reference condition. In principle, when the Stern-Volmer coefficients of PSP are determined through calibration, surface pressure can be remotely measured by detecting the luminescent emission radiance. Compared to conventional pressure measurement techniques, PSP is able to provide non-contact, high-resolution and quantitative mapping of surface pressure and temperature on complex aerodynamic models in a time and cost efficient manner. This enables experimental aerodynamicists to utilize PSP as a powerful flow diagnostics tool to investigate the rich physical phenomena in complex flows around flight vehicles and other bodies.

For PSP measurements in this work, UF470 manufactured by Innovative Scientific Solution Inc. was used as a PSP. This paint has a luminescent emission peak at 650 nm, when excited by a 395 nm light source. The experimental setup for PSP was similar to that of GLOF measurements. The UV LED excitation sources were arranged to provide uniform illumination of the model surface. Images acquisition was performed using a 16-bit CCD camera manufactured by Hamamatsu (Model: LEDH576-395). An

optical band-pass filter with a transmission wavelength band of 650 ± 20 nm was used. The model temperature was also monitored by a thermocouple installed within the model. Image acquisition and data reduction was based on the method proposed by Yamashita et al. [133]. A set of wind-on images was acquired after the rate of model temperature change approaches zero, and a set of wind-off images was acquired immediately after the tunnel was shut down. Each image set is comprised of 64 images. This data acquisition method is able to reduce the error resulting from model temperature changes. The data reduction procedure is made up of these sequential steps - subtraction of dark images to eliminate the CCD readout noise, ensemble averaging of 64 images, registration of the wind-on and wind-off images to account for model deformation or movement under wind-on conditions, computation of pressure by Equation 9.1 and finally correction of temperature effects from thermocouple measurements.

9.2 Junction Flows

Junction flows occur when a boundary layer interacts with an obstacle in aerodynamic and hydrodynamic configurations such as the junction between an aircraft fuselage and wing, wall and vanes in turbines, and river bed and bridge supports. In junction flows, the boundary layer on a surface separates upstream an obstacle to form horseshoe vortices around the obstacle with unsteady vortex shedding downstream of the obstacle. This implies that junction flows are highly three dimensional (3D) with complex flow structures. A vast amount of research has been conducted on junction flows from an experimental as well as numerical simulation standpoint. Simpson [113] has given a comprehensive review of junction flows. Considerable effort has also been made by Hunt et al. [38], Tobak and Peake [44], Martinuzzi and Tropea [95], Johnson

and Patel [114] and Coon and Tobak [134] on qualitative topological analysis based on surface oil-streak and flow visualizations. Recently, Depardon et al. [100] have performed near-wall PIV to give detailed near-wall streamline patterns in a junction flow over a cube mounted on a flat floor. Sattari et al. [102] and Ozturk et al. [135] have also performed PIV measurements to measure the flow around cylinders. Numerical simulations of laminar junction flows at low Reynolds numbers have been presented by Visbal [115], Lakehal and Rodi [136], Hung et al. [137] and Hwang and Yang [138], illustrating detailed flow fields and near-wall streamline patterns. Although a vast amount of work has been done on qualitative as well as quantitative measurements of various parameters in junction flows, the availability of combined skin friction and surface pressure measurements for junction flows will contribute greatly towards understanding the complex flow phenomenon associated with these types of flows.

9.2.1 Square Cylinder Junction Flow

Figure 9.4 (a), (b), (c) and (d) are a typical luminescent oil film image, skin friction line plot, skin friction vector plot and skin friction magnitude plot, respectively for the base surface of the square cylinder junction flow. The origin of the coordinate system is located at the center of the model leading edge, and the x- and y-coordinates are in the freestream and lateral directions, respectively. The x- and y- axes are normalized by the cylinder depth and width, respectively. Figure 9.4 (c) shows 284×269 skin friction vectors obtained from superposition of 80 snapshot solutions over a period of 80 seconds. Figure 9.4 (b) shows the skin friction line plot on the base surface around the square cylinder. The separation and reattachment lines related to the horseshoe vortices along

with a number of isolated singular points associated with the complex separated flow structures are clearly visible in the skin friction line plot.

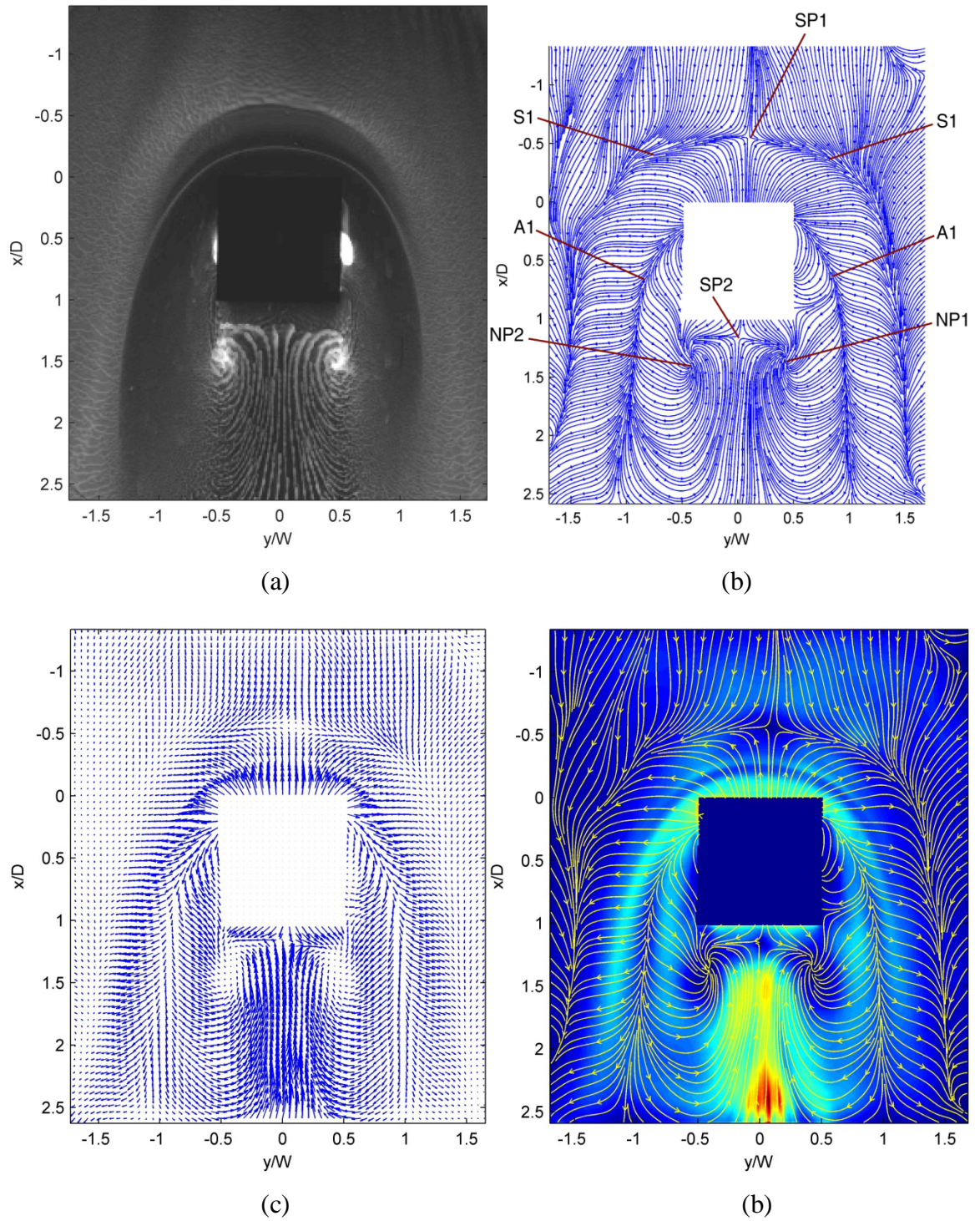


Figure 9.4 Square cylinder junction flow, (a) typical luminescent oil image, (b) skin friction line plot, (c) skin friction vector plot and (d) skin friction magnitude plot

A saddle point (SP1) is observed upstream of the cylinder leading edge. The primary separation line (S1) originating from SP1 and the reattachment line from the model leading edge (A1) form arc patterns induced by the horseshoe vortex formed around the square cylinder. At the rear portion of the cylinder, one saddle point (SP2) and a pair of foci (NP1 and NP2) are observed. These features at the rear portion of the cylinder are considered a time averaged skin friction field induced by von Karman vortex shedding. The global skin friction topology shown by the skin friction line plot in Figure 9.4 (b) is qualitatively consistent as observed in numerical simulations by Visbal [115], Hung et al. [137] and Hwang and Yang [138] and flow visualizations by Depardon et al. [100] and Simpson [113]. Figure 9.4 (d) shows the distribution of the skin friction magnitude normalized by the maximum magnitude. High skin friction magnitude regions are seen downstream of the square cylinder, around the reattachment line A1, and upstream of the saddle point SP1 in contrast to low skin- friction magnitude at the foci, saddles and in the proximity of the cylinder sides.

Figure 9.5 is a plot of the PSP derived pressure coefficient field with an overlay of the skin friction lines for the base surface of the square cylinder. The highest pressure is observed near the stagnation point at the leading edge of the cylinder. A high pressure region is also formed near the saddle point upstream of the cylinder and extends along the primary separation line while decreasing in magnitude. A low pressure region extends from the sharp leading corners to the rear section of the cylinder near the foci pair, which is delineated by the primary reattachment line A1. At this level of spatial resolution, the skin friction topology is reasonable from a topological standpoint (see Section 9.2.3) although the surface pressure field indicate more complicated patterns upstream of the

cylinder that is not captured in the extracted skin friction fields. It is speculated that GLOF fails to resolve the finer structures in this region due to a relatively low spatial resolution of images. In front of the square cylinder, the luminescent oil does not develop much after an initial transient stage. Such small oil film displacements are hard to detect if the spatial resolution of the GLOF image is not sufficiently large.

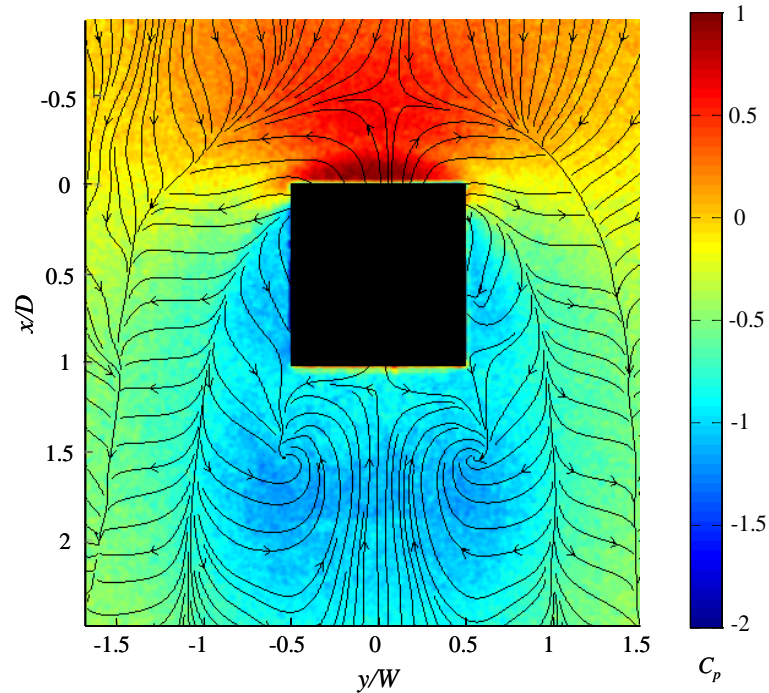


Figure 9.5 Surface pressure coefficient field with overlay of skin friction lines for the base surface of a square cylinder junction flow

This issue is examined by acquiring high resolution images of oil film development focusing on the region upstream of the cylinder. Tests were run at a free-stream velocity of 20 m/s using silicone oil with a viscosity of 200 cs with a corresponding Reynolds number based on cylinder width (Re_D) of 52,000. The incoming boundary layer was determined to be laminar based on Re_D . Figure 9.6 (a), (b), (c) and (d) are a typical luminescent oil intensity image, skin friction line plot, skin friction vector plot and skin friction magnitude plot of the zoomed in region upstream of the base

surface of the square cylinder junction flow. The region of interest contained 570×500 pixels. A series of 45 snapshot solutions were superposed over a time span of 15 seconds resulting in extraction of 570×500 skin friction vectors.

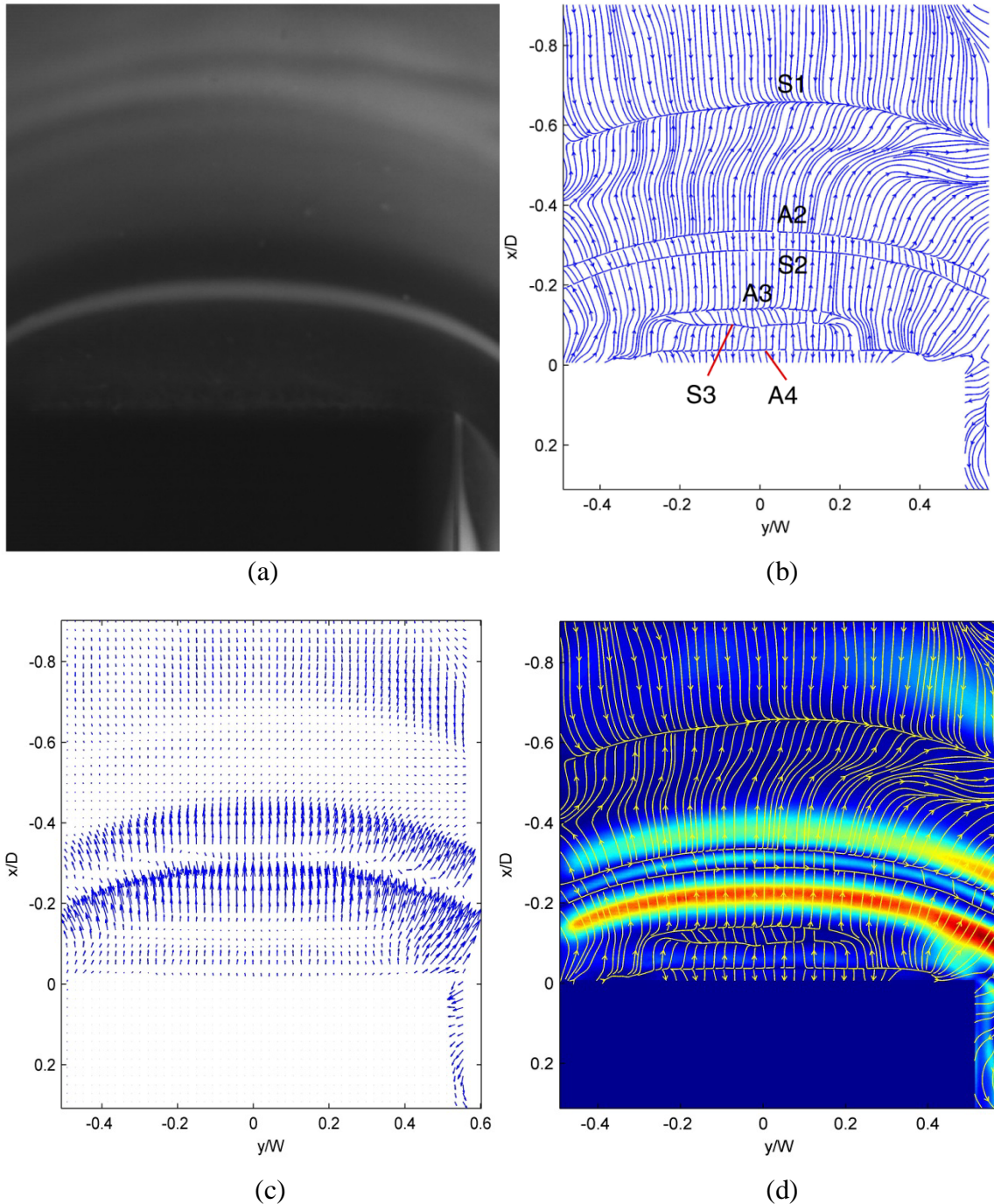


Figure 9.6 High spatial resolution images of square cylinder junction flow, (a) typical luminescent oil image, (b) skin friction line plot, (c) skin friction vector plot and (d) skin friction magnitude plot

The skin friction line plot in Figure 9.6 (b) clearly illustrates the topological structures that include the primary separation line S1, secondary separation lines S2 and S3 and the reattachment lines A2, A3 and A4. The conjectured flow topology associated with the extracted skin friction lines near the leading edge of the cylinder is illustrated in Figure 9.7. This flow topology is considered as a six vortex system with three primary vortices [113, 115, 137-139].

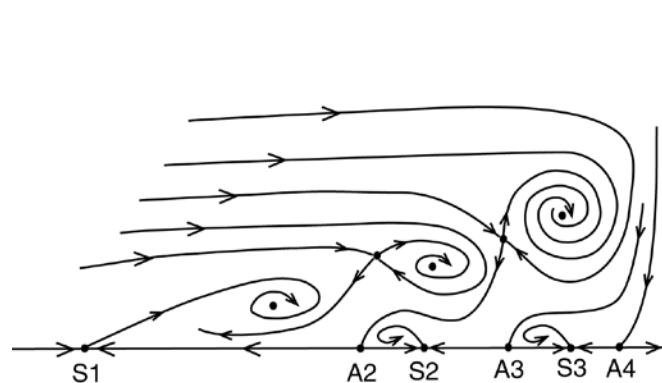
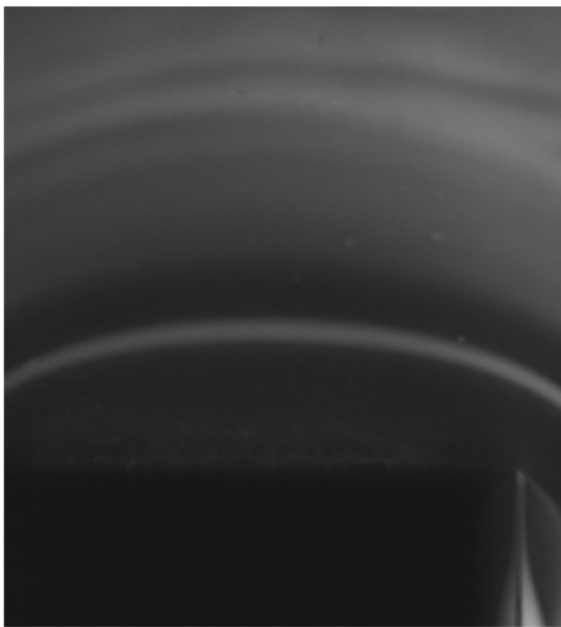


Figure 9.7 Conjectured flow topology of a six vortex system upstream of a square cylinder junction flow

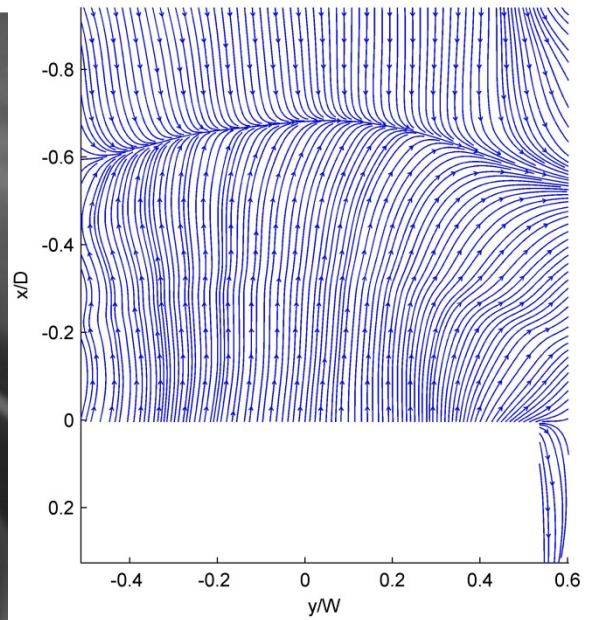
This flow structure has been described by several numerical simulations and flow visualizations of junction flows around circular cylinders when the Reynolds number is suitably large. Although Visbal [115] had proposed an alternate off surface flow topology, the resulting skin friction topology on the base surface remained the same. Inspecting Figure 9.6 (b) closely, it is observed that the secondary separation and reattachment lines S3, A3 and A4 are confined in a closed region in the front of the square cylinder, which is different from observations by Visbal [115] in junction flows around circular cylinders.

To demonstrate the effect of image spatial resolution on resolving details in the extracted skin friction fields, the zoomed in image set was downsampled to match the resolution of the original image set used to extract the skin friction fields in Figure 9.4.

The zoomed in image set was downsampled by a factor of 3 resulting in an image size of 190×167 pixels compared to the original resolution of 570×500 pixels for the zoomed in image set. Figure 9.8 (a), (b), (c) and (d) are a typical luminescent oil intensity image, skin friction line plot, skin friction vector plot and skin friction magnitude plot of the downsampled zoomed in region upstream of the base surface of the square cylinder junction flow.



(a)



(b)

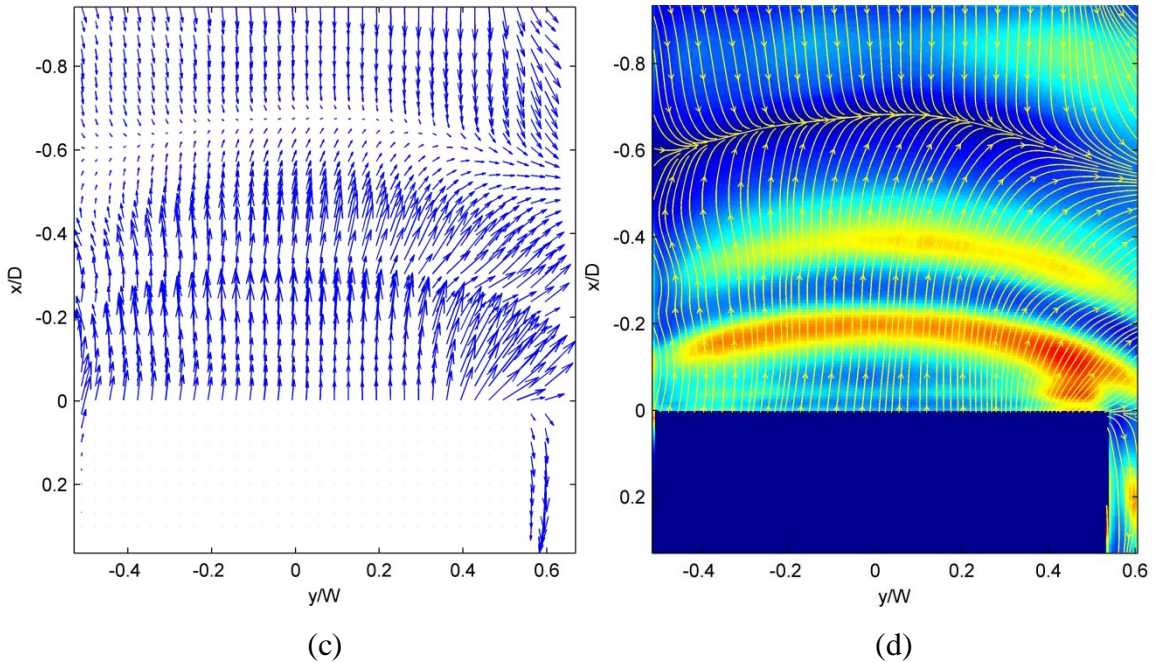


Figure 9.8 Downsampled high spatial resolution images of square cylinder junction flow, (a) typical luminescent oil image, (b) skin friction line plot, (c) skin friction vector plot and (d) skin friction magnitude plot

Figure 9.8 (c) illustrates the loss of detail in extracted skin friction fields for a downsampled image set. The secondary separation and reattachment lines were not visualized in skin friction fields extracted from the downsampled image set similar to the case of Figure 9.4 which presents the global view of the skin friction fields on the base surface of the square cylinder. This clearly emphasizes that the high resolution images are critical in resolving the finer details of a skin friction field particularly in a flow with complex skin friction topology such as that demonstrated by the square cylinder junction flow.

9.2.2 Diamond Cylinder Junction Flow

A diamond cylinder was generated by rotating the square cylinder 45° . GLOF measurements were conducted at the same conditions as those for the square cylinder. Figure 9.9 (a), (b), (c) and (d) are a typical luminescent oil intensity image, skin friction

line plot, skin friction vector plot and skin friction magnitude plot of the base surface of the diamond cylinder junction flow.

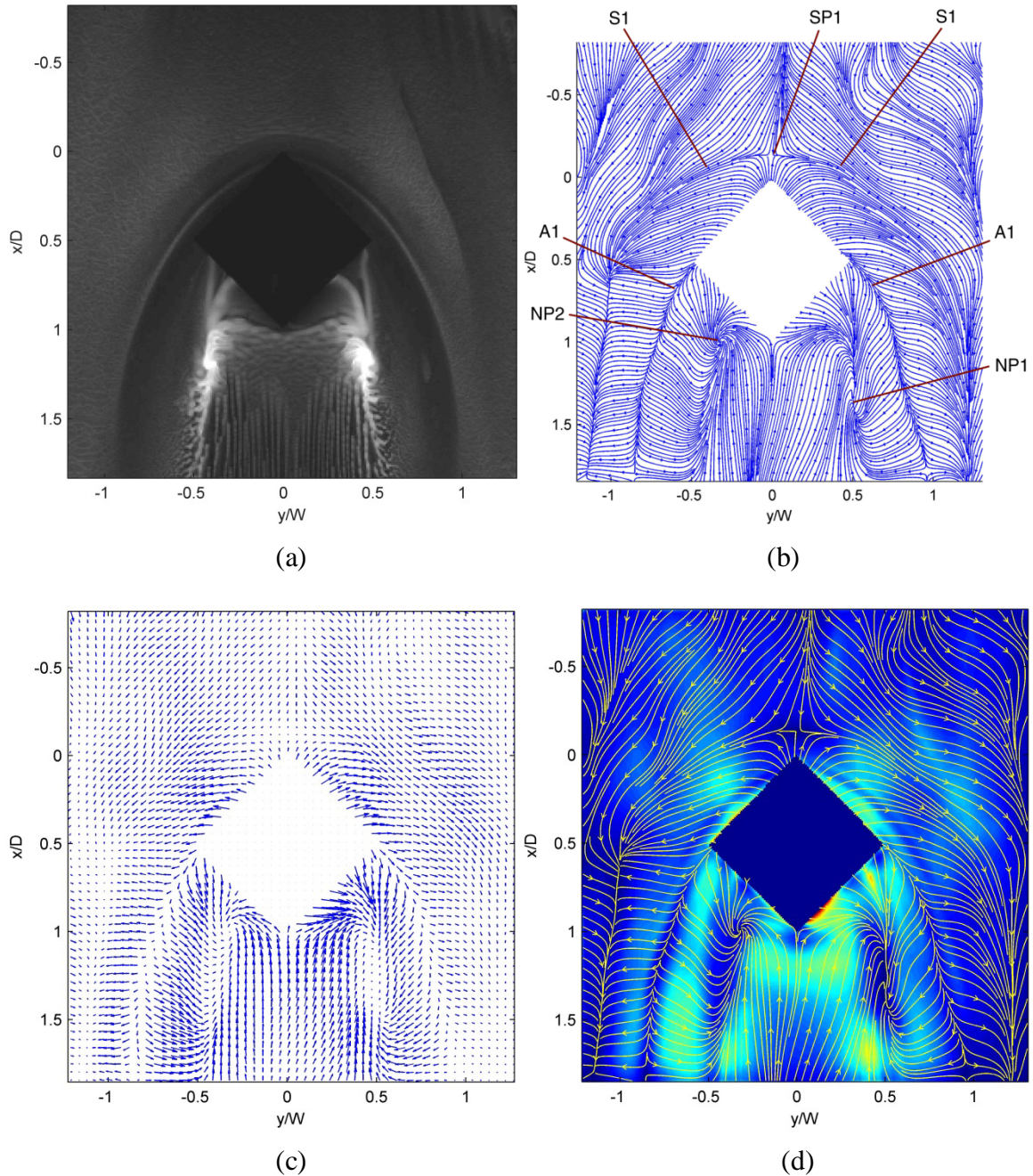


Figure 9.9 Diamond cylinder junction flow, (a) typical luminescent oil image, (b) skin friction line plot, (c) skin friction vector plot and (d) skin friction magnitude plot

The skin friction topology for the diamond cylinder is qualitatively similar to that of the square cylinder. Inspecting the skin friction line plot in Figure 9.9 (b), it is

observed that the primary separation line originates from the saddle point SP1 located upstream of the diamond cylinder. The separation line S1 is not as tightly converged in certain sections when compared to the square cylinder case illustrated in Figure 9.4 (b). The reattachment line A1 is seen to originate from the sharp corners of the cylinder. A pair of asymmetric foci (NP1 and NP2) is observed downstream of the diamond cylinder. The saddle point behind the cylinder is not observed in this case. The skin friction magnitude is high in the proximity of the diamond cylinder except near the foci. Figure 9.10 is a plot of the PSP-derived pressure coefficient field with an overlay of skin friction lines. A high pressure region is visible at the leading edge of the cylinder corresponding to the stagnation region. Similar to the square cylinder case, the low pressure region behind the cylinder is approximately delineated by the primary reattachment line A1.

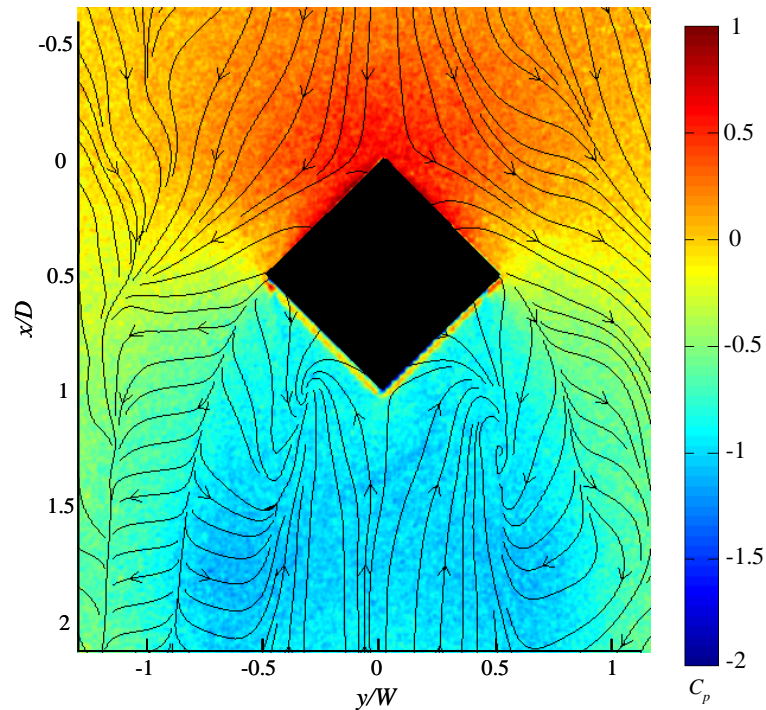
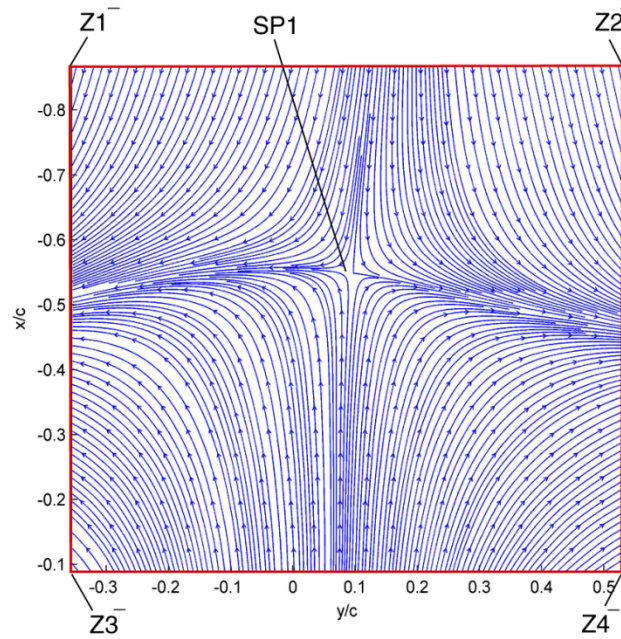


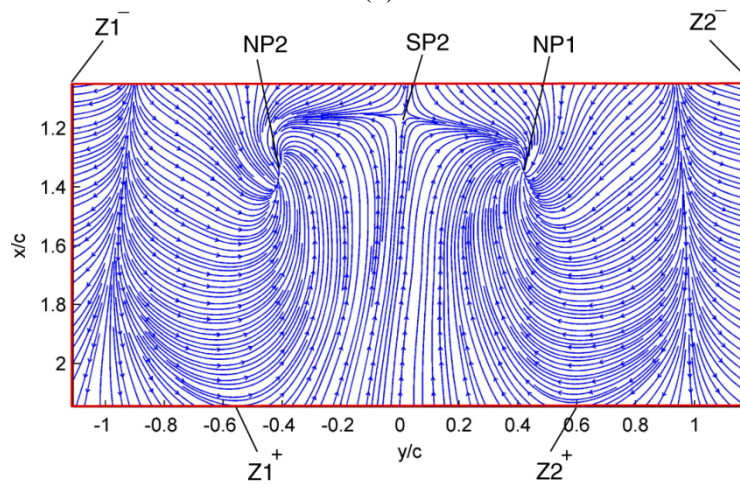
Figure 9.10 Surface pressure coefficient field with overlay of skin friction lines for the base surface of a diamond cylinder junction flow

9.2.3 Skin Friction Topology Constraint Analysis

The analysis of skin friction topology is performed for selected regions in both the cases of the square and diamond cylinder junction flows using the Poincare-Bendixson (P-B) index formula. For the junction flow around the square cylinder, two zoomed-in regions are selected for a topological analysis. The first is the region upstream of the square cylinder corresponding to the saddle point SP1 and the second the region immediately behind the square cylinder including the pair of foci (NP1 and NP2) and saddle point SP2. Figure 9.11(a) and (b) shows the isolated singular points and boundary switch points enclosed by rectangular boundaries near the saddle SP1 in the front of the cylinder and the nodes NP1 and NP2 and the saddle SP2 behind the cylinder. As illustrated by Figure 9.11 (a), one saddle and four negative switch points at the corners of the rectangular boundary are identified. Applying the P-B index formula given by $\#NP - \#SP = 1 + (\#Z^+ - \#Z^-)/2$, with $\#NP = 0$, $\#SP = 1$, $\#Z^+ = 0$, and $\#Z^- = 4$, shows that the conservation law $\#NP - \#SP = 1 + (\#Z^+ - \#Z^-)/2 = -1$ is satisfied in this region. For Figure 9.11 (b), there are two nodes, one saddle, two negative switch points and two positive switch points identified. Applying the P-B index formula shows that the conservation law $\#NP - \#SP = 1 + (\#Z^+ - \#Z^-)/2 = 1$ is satisfied.



(a)



(b)

Figure 9.11 Zoomed in views identifying singular points and boundary switch points for the region (a)upstream of the square cylinder junction flow base surface and (b)immediately behind the square cylinder junction flow base surface

Figure 9.12 shows the region selected immediately behind the diamond cylinder. A boundary behind the diamond cylinder is selected, where a contour is made on the selected boundary at the sharp trailing edge of the diamond cylinder for clear identification of the boundary switch points. The number of nodes, saddles, positive boundary switch points and negative boundary switch points are 2, 0, 4, and 2

respectively. Applying the P-B index formula results in $\#NP - \#SP = 1 + (\#Z^+ - \#Z^-) / 2 = 2$, which shows that the conservation law is satisfied. These cases clearly indicate that the extracted skin friction fields are topologically consistent in the selected regions.

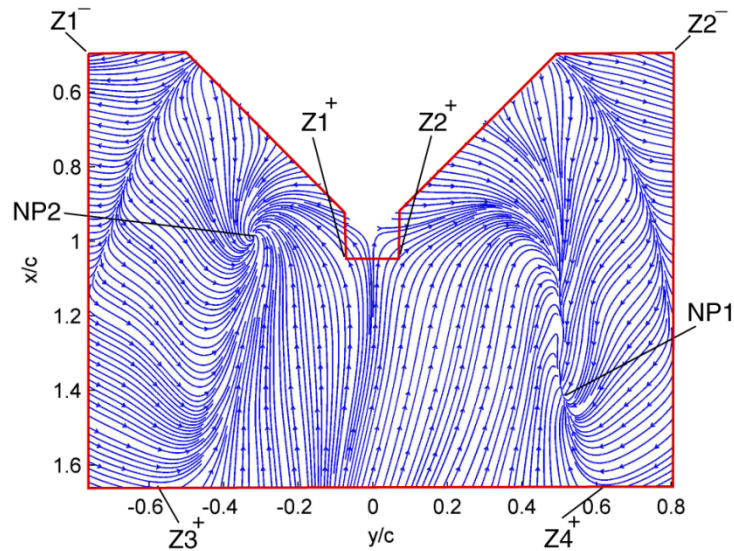


Figure 9.12 Zoomed in view identifying singular points and boundary switch points for the region immediately behind the diamond cylinder junction flow base surface

9.3 Ahmed Model

A considerable amount of effort has been put into studying the aerodynamics of ground vehicles. The aerodynamics of ground vehicles are complicated, typically at the rear end of the vehicle where flow separation occurs and vortices are formed. The separated flow region at the rear of the vehicle also referred to as the suction region since it has a negative value of coefficient of pressure (C_p). The frontal region of the vehicle is the stagnation region where the flow stagnates resulting in a high positive value of C_p . The difference between the pressure at the front and rear of the vehicle gives rise to pressure drag which is one of the major factors that affect the efficiency of the vehicle. With the rising cost of energy, it is important to ensure that the highest operating

efficiency of a vehicle is achieved. One of the critical areas in improving the efficiency of a ground vehicle is aerodynamics, specifically focused on the rear end of the vehicle where flow separation occurs. Numerous vehicle shapes and sizes exist, which make it difficult to systematically study effects of aerodynamic improvements for each individual comparison. Ahmed et al. [128] introduced a generic ground vehicle model as illustrated in Figure 9.2, referred to as the Ahmed model which represents a simplified ground vehicle. A number of numerical [139-140] and experimental [141] studies have been performed on the Ahmed model. This study will examine the skin friction and surface pressure fields on the top and leeward side surfaces of an Ahmed model at 0° and 20° sideslip. The complicated flow structures at the front and rear sections of the model will be identified, particularly at the curved leading edge and slanted trailing edge sections.

Figures 9.13 (a), (b), (c) and (d) are a typical luminescent oil intensity image, skin friction line plot, skin friction vector plot and skin friction magnitude plot with an overlay of skin friction lines of the top surface of the Ahmed model at 0° sideslip. A separation line is visualized at the leading edge curvature of the model consistent with observations by Spohn and Gillieron [141] along with the circular pool of oil in this region as shown in their oil flow visualizations experiments. They also presented the conjectured flow topology in this region, indicating the existence of two foci on either side of the model leading edge corresponding to the circular oil pool. These features are not visualized by the skin friction line plot possibly due to the low spatial resolution of the GLOF images. At the slant surface on the trailing edge of the model, reattachment lines are visible on either side, indicating the impingement of a vortex on the slant surface on both sides. Figure 9.14 is a surface pressure coefficient field plot of the top surface of the Ahmed

model at 0° sideslip. Low pressure regions are observed at the leading edge of the model where flow separation occurs as well as the sides of the slant surface where vortex structures are present as evidenced by the reattachment lines observed in this region.

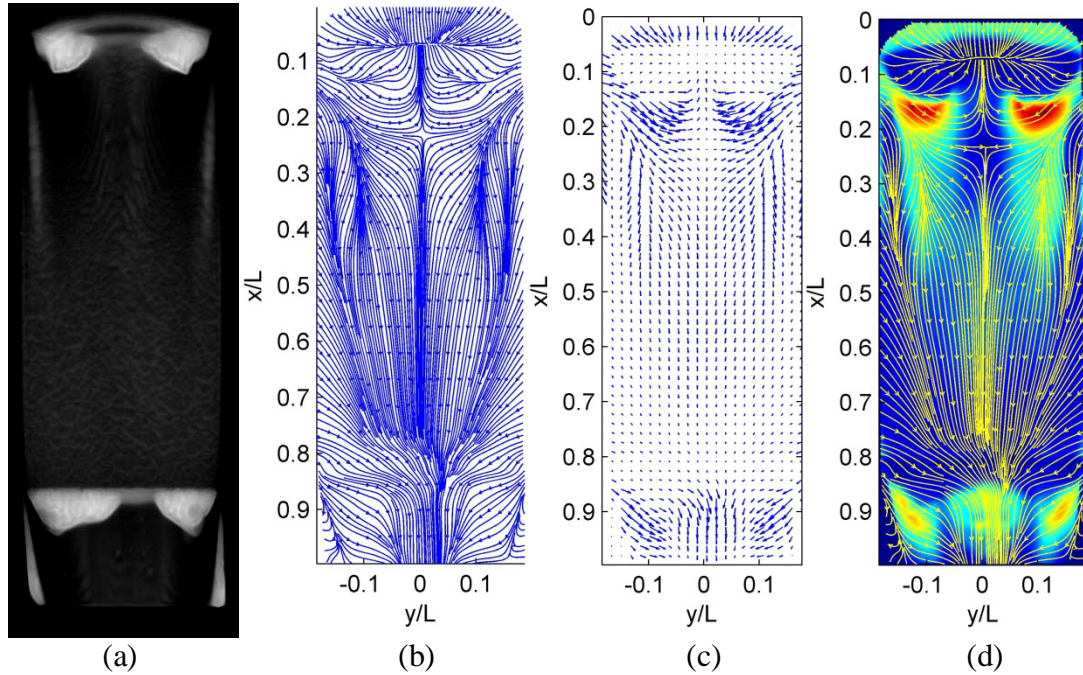


Figure 9.13 Top surface of an Ahmed model at 0° sideslip, (a) typical luminescent oil image, (b) skin friction line plot, (c) skin friction vector plot and (d) skin friction magnitude plot with an overlay of skin friction lines

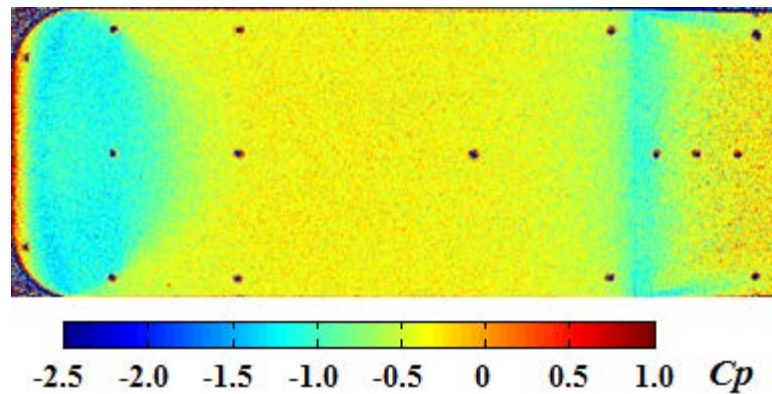


Figure 9.14 Surface pressure coefficient (C_p) field of the top surface of an Ahmed model at 0° sideslip

Figures 9.15 (a) and (b) are the skin friction line plot and skin friction magnitude plot with an overlay of skin friction lines for the top surface of the Ahmed model at 20° sideslip. The separation region at the leading edge of the model is asymmetric as seen in

the skin friction line plot in Figure 9.15 (a). The low pressure signature of the separation region is clearly visualized in the surface pressure coefficient field plot in Figure 9.16. Immediately downstream of the separation region a distinct reattachment line is observed along with a reattachment line on the windward side of the model with secondary separation and reattachment lines related to a vortex system formed at this location which propagates downstream to the slant surface also indicated in the surface pressure coefficient plot highlighting a low pressure region in the vicinity of the vortex system.

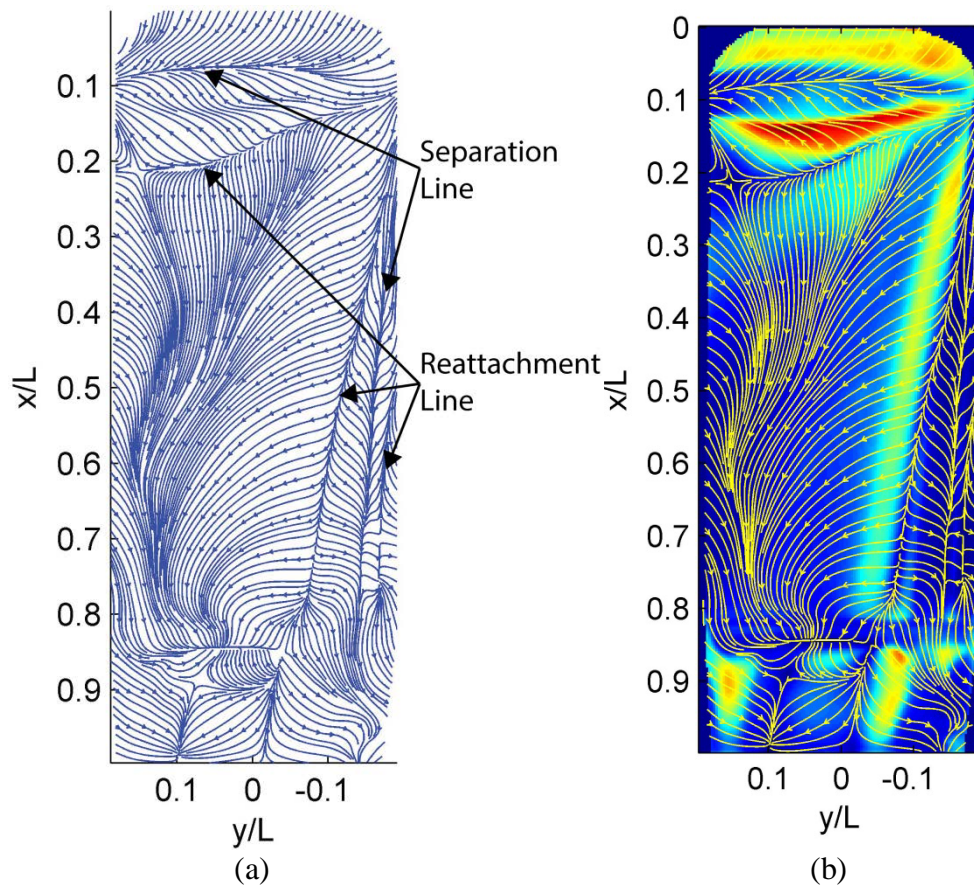


Figure 9.15 Top surface of an Ahmed model at 20° sideslip, (a) skin friction line plot and (b) skin friction magnitude plot with an overlay of skin friction lines

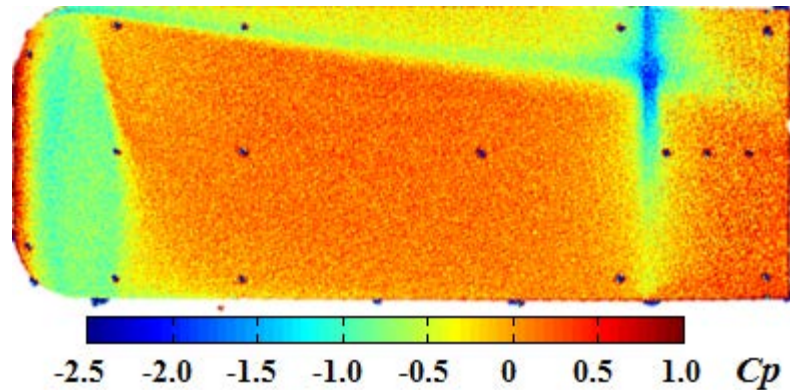


Figure 9.16 Surface pressure coefficient (C_p) field of the top surface of an Ahmed model at 20° sideslip

The skin friction line and magnitude plots for the leeward side surface of the model at 0° sideslip are shown in Figure 9.17 (a) and (b), respectively. The separation region is visualized at the leading edge curvature of the model as seen by the distinct separation line in this region and the low surface pressure region as illustrated in the surface pressure coefficient plot in Figure 9.18. A separation line is also observed along the centerline of the model side surface. Figure 9.19 (a) and (b) are the skin friction line and magnitude plots on the leeward side surface of the model at 20° sideslip, respectively. As seen in the skin friction line plot in Figure 9.19 (a), the separation region at the model leading edge is expanded compared to the case at 0° sideslip. This is confirmed by the surface pressure coefficient plot indicating a larger, lower pressure region at the leading edge of the model for the 20° sideslip case. A curved reattachment line beginning at the lower surface of the model from approximately $(x/L) = 0.2$ to $(x/L) = 0.35$ is joined with a reattachment line close to the top surface of the model indicating complex three dimensional flow separation and reattachment patterns. In all cases, the skin friction line plots have shown the complex flow phenomenon associated with the flow over an Ahmed body which is supported by surface pressure coefficient data. The complicated flows associated with the Ahmed model has been shown with measurements

of skin friction and surface pressure. These measurement techniques are powerful tools that provide an understanding of the flow associated with the Ahmed model and can assist in identifying potential flow control strategies to manage flow separation.

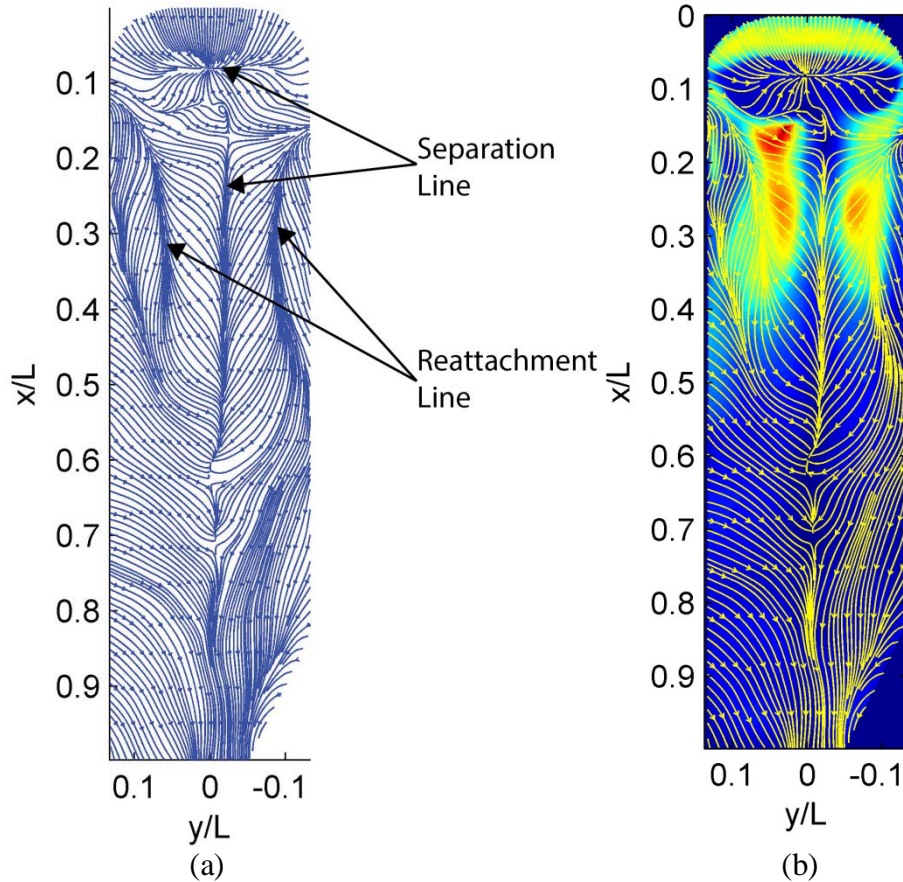


Figure 9.17 Leeward side surface of an Ahmed model at 0° sideslip, (a) skin friction line plot, and (b) skin friction magnitude plot with an overlay of skin friction lines

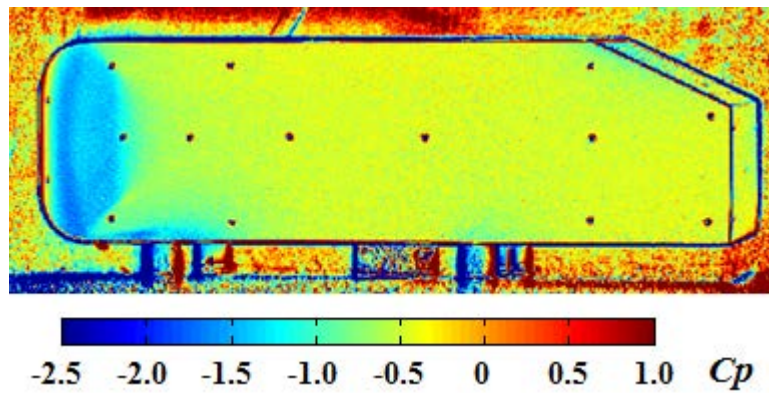


Figure 9.18 Surface pressure coefficient (C_p) field of the leeward side surface of an Ahmed model at 0° sideslip

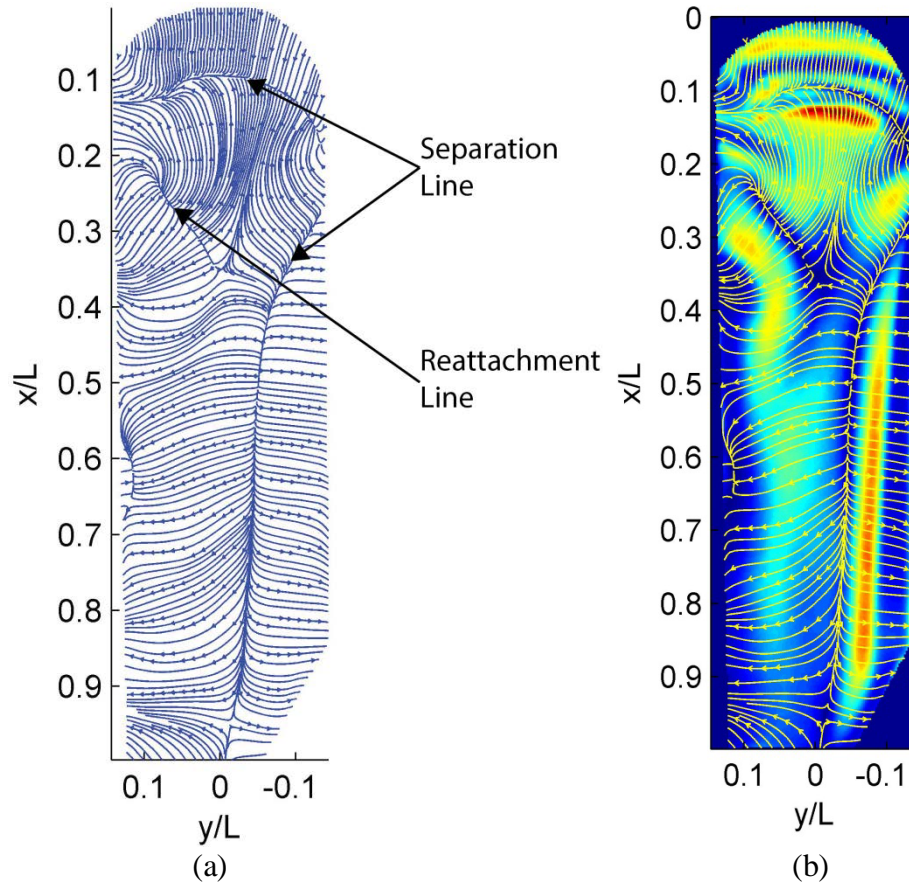


Figure 9.19 Leeward side surface of an Ahmed model at 20° sideslip, (a) skin friction line plot, and (b) skin friction magnitude plot with an overlay of skin friction lines

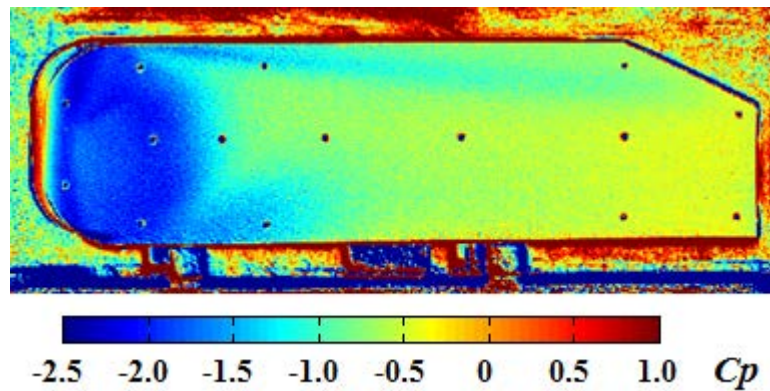


Figure 9.20 Surface pressure coefficient (C_p) field of the leeward side surface of an Ahmed model at 0° sideslip

9.4 Summary

High-resolution skin friction and surface pressure fields on the floor surface in junction flows have been measured by a combination of the global luminescent oil film

(GLOF) skin friction meter and pressure sensitive paint (PSP). The extracted skin friction vector fields reveal the detailed topological structures around a square cylinder and a diamond cylinder including the isolated singular points and separation and reattachment lines. The complex secondary separation and reattachment lines near the leading edge of the square cylinder have been extracted from high resolution images consistent with the six-vortex system. The surface pressure fields overlaid with the skin friction lines reveal the pressure signatures corresponding to the skin friction structures, particularly indicating the high pressure stagnation regions and the low pressure region behind the square and diamond cylinders demarcated by the primary reattachment line. The Poincare-Bendixson (P-B) index formula was also applied as a topological constraint to examine the conservation of the isolated singular points and the boundary switch points in the regions of interest. It was observed that the extracted skin friction fields were topologically consistent in these regions.

The skin friction and surface pressure fields on the top and leeward side surfaces of an Ahmed model at 0° and 20° sideslip were also measured. The separated flow region at the leading edge of the model was clearly visualized by the skin friction fields and supported by the surface pressure coefficient fields. The change induced by applying sideslip to the model was observed in the skin friction line and surface pressure coefficient plots highlighting the complicated flow structures that resulted from applying sideslip to the model.

From an instrumentation standpoint, since the optical instrumentation required for GLOF and PSP measurements are essentially similar, integration of these techniques provides a powerful, convenient and rapid diagnostic tool for complex flows.

CHAPTER 10

GLOBAL SKIN FRICTION DIAGNOSTICS BASED ON SURFACE TEMPERATURE MEASUREMENTS

The preceding chapters of this work have established the GLOF technique for quantitative global skin friction diagnostics in complex separated flows using luminescent oil. The GLOF technique has been successfully applied in measurements of various complicated flows as highlighted by the earlier chapters in this work. The GLOF technique is limited to steady-state or time-averaged measurements due to the nature of the oil film development process. Shear sensitive liquid crystals and the polymer film based S3F technique hold good potential for unsteady measurements although they possess limitations as discussed in Chapter 2.

Skin friction is generally related to surface heat flux by the Reynolds analogy, which signifies that skin friction can be determined by measuring heat flux. Previously, the relationship between local skin friction and surface heat flux had been derived by Lighthill [16] for a small heated element. Liu et al. [17] and Gelderblom et al. [18] have also given a further heat transfer analysis of a heated element on a wall in a boundary layer. In light of the theoretical foundation provided by Lighthill, the flush-mounted hot-film or hot-wire skin friction sensor was developed by Liepmann and Skinner [19]. At present, hot-film skin friction sensors have evolved into a mature technique for skin friction measurements at discrete locations when appropriately calibrated. The

underlying principle of a hot-film sensor is also the foundation of microelectromechanical systems (MEMS) based hot-film or hot-wire sensors [20] for skin friction measurements. At this juncture, the next step is extending the heat transfer based approach to global skin friction measurements [143-144]. The major issue to tackle for this step is defining an explicit relationship between a heat flux field and a skin friction field as it is not well established for a general case as well as it is for a local case as described by Lighthill's analytical solution. Moreover, it is not fully recognized that mathematically, this problem should be solved as an inverse problem for a skin friction field.

The objective of this study is to develop a global skin friction diagnostics technique based on surface temperature measurements using temperature sensitive paint (TSP). This approach will be a global extension of the traditional heat transfer based skin friction sensors (e.g. a hot-film skin friction sensor). This work covers several key steps. First, the asymptotic form of the energy equation near a wall is given, describing the relationship between surface temperature, heat flux and skin friction fields. Since the mathematical form of the developed equation is similar to the physics based optical flow equation [26], an inverse solution of this equation is developed to determine a skin friction field by solving the Euler-Lagrange equations when surface temperature fields are obtained from measurements using TSP. A discussion on the uncertainty and intrinsic limitations of this method is also provided. Theoretically, this method can be used for both steady and unsteady skin friction diagnostics. A simple approach for time-averaged measurements is proposed along with an iterative scheme for improvements in skin friction calculations. This method provides a relative or normalized skin friction

field. The absolute skin friction field can be determined by in-situ calibration of known values of skin friction at several locations. The experimental implementation of this approach is detailed. Finally, the feasibility of this approach is examined by measuring skin friction fields for a flat plate with an impinging jet and is compared against hot-film sensor skin friction measurements and theoretical solutions.

10.1 Theory

In this section, a relation between skin friction, surface temperature and heat flux will be obtained. The variational solution for skin friction fields with the resulting Euler-Lagrange equations is also presented along with an uncertainty analysis. Finally, a model for time-averaged measurements is developed and discussed.

10.1.1 Asymptotic Form of the Energy Equation at a Wall

The energy equation for a flow is defined as

$$\rho c_p \frac{DT}{Dt} + p \frac{\partial u_j}{\partial X_j} = k \nabla^2 T + \mu \Phi \quad (10.1)$$

where $D/Dt = \partial/\partial t + u_j \partial/\partial X_j$ ($j = 1, 2, 3$), p is pressure, ρ is density, c_p is specific heat, μ is dynamic viscosity, k is thermal conductivity, and Φ is the dissipation function [41]. The coordinates on a surface are defined as X_1 and X_2 and X_3 is the coordinate normal to the surface. The Taylor expansions of the velocity components (u_1, u_2) along the surface and temperature (T) near a wall are

$$u_1 = \frac{\tau_1}{\mu} X_3 + \left(\frac{\partial^2 u_1}{\partial X_3^2} \right)_w \frac{X_3^2}{2} + \dots \quad (10.2)$$

$$u_2 = \frac{\tau_2}{\mu} X_3 + \left(\frac{\partial^2 u_2}{\partial X_3^2} \right)_w \frac{X_3^2}{2} + \dots, \quad (10.3)$$

$$T = T_w - q_w \frac{X_3}{k} + \dots, \quad (10.4)$$

where the subscript 'w' denotes the wall condition, and $\tau_i = \mu(\partial u_i / \partial X_3)_w$ ($i = 1, 2$).

When X_3 tends to zero, the continuity equation near the wall is approximated by the incompressible one, i.e., $\partial u_j / \partial X_j \approx 0$. Integration of the continuity equation gives the velocity normal to the surface, i.e.,

$$u_3 = -\frac{X_3^2}{2} \frac{\partial}{\partial X_i} \left(\frac{\tau_i}{\mu} \right) + \dots \quad (i = 1, 2) \quad (10.5)$$

Substituting Equations 10.2 through 10.5 into 10.1 and differentiating it with respect to the normal coordinate X_3 , a limit form of the energy equation as X_3 tends to zero is obtained, i.e.,

$$F + \tau_i \partial T_w / \partial X_i = 0 \quad (i = 1, 2) \quad (10.6)$$

where

$$F = \frac{\mu}{k} \left(-\frac{\partial q_w}{\partial t} + a \frac{\partial^2 q_w}{\partial X_i \partial X_i} \right) - \mu a \left(\frac{\partial^3 T}{\partial X_3^3} \right)_w + \frac{4\mu}{\rho c_p} \tau_i \left(\frac{\partial^2 u_i}{\partial X_3^2} \right)_w \quad (10.7)$$

and $a = k / \rho c_p$ is the diffusivity of fluid, $q_w = -k(\partial T / \partial X_3)_w$ is the heat flux at the wall that is positive heat enters the fluid from the wall. Equation 10.6 describes the relationship between the skin friction vector, heat flux and temperature at the wall. It represents a balance between the skin friction vector projected on the normal vector ∇T_w to an iso-temperature line $T_w = const.$ and the term F containing the time rate of heat flux. Alternatively, $\tau_i \partial T_w / \partial X_i$ can be interpreted as the flux of a scalar T_w transported by a skin friction field τ_i , while F is considered a source term. It can also be thought of as the differential form of the Reynolds analogy. The second and third terms in F originate

from a third-order derivative term of Equation 10.4 in the thermal diffusion and the viscous dissipation terms, respectively. It will be discussed that Equation 10.6 can be utilized as a foundation to determine a skin friction field as an inverse problem when surface temperature fields are measured using TSP.

10.1.2 Variational Solution for Skin Friction Fields

Similar to the GLOF technique, for image based temperature measurements, Equation 10.6 should be projected onto the image plane of a camera. Figure 10.1 illustrates a special object-space coordinate system $(\bar{X}_1, \bar{X}_2, \bar{X}_3)$,

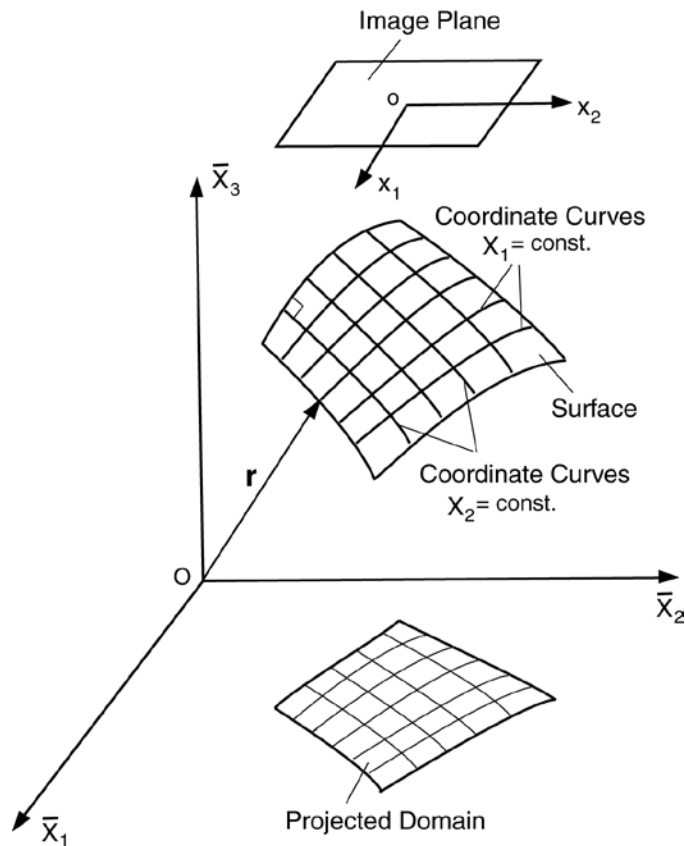


Figure 10.1 Surface, object space and image coordinates

in which the plane (\bar{X}_1, \bar{X}_2) is parallel to the image plane (x_1, x_2) . Therefore, a relationship between (\bar{X}_1, \bar{X}_2) and (x_1, x_2) is defined as $\partial / \partial \bar{X}_i = \lambda \partial / \partial x_i$, where λ is

a scaling constant. An image on a camera is the scaled projection of the surface onto the plane (\bar{X}_1, \bar{X}_2) . If the transformation between (\bar{X}_1, \bar{X}_2) and (X_1, X_2) is given by $\bar{X}_1 = F_1(X_1, X_2)$ and $\bar{X}_2 = F_2(X_1, X_2)$, then $\partial / \partial X_i = h_{ji} \partial / \partial \bar{X}_j = \lambda h_{ji} \partial / \partial x_j$ ($i, j = 1, 2$), where $h_{ji} = \partial F_j / \partial X_i$ is dependent on the geometric properties of the surface. Therefore, Equation 10.6 can be expressed in the image coordinates as,

$$F + \hat{\tau}_i \partial T_w / \partial x_i = 0, \quad (i = 1, 2) \quad (10.8)$$

where $\hat{\tau}_i = \lambda h_{ij} \tau_j$ ($i, j = 1, 2$) is the projected skin friction vector on a surface onto the image plane. The Laplace operator in F is $\partial^2 / \partial X_i \partial X_i = \lambda^2 h_{ji} h_{ji} \partial^2 / \partial x_j \partial x_j$.

Equation 10.8 is in the same form as the Horn-Schunck optical flow equation with the exception that optical flow is replaced by the projected skin friction vector $\hat{\tau}$ and the time derivative of the image intensity by the source term F [24]. In principle, if F and T_w are known, Equation 10.8 can be solved as an inverse problem for the skin friction vector, $\hat{\tau}_i$. By minimizing the functional below with the Horn-Schunck regularization term on an image domain Ω ,

$$J(\hat{\tau}) = \int_{\Omega} (F + \hat{\tau} \cdot \nabla T_w)^2 dx_1 dx_2 + \alpha \int_{\Omega} (|\nabla \hat{\tau}_1|^2 + |\nabla \hat{\tau}_2|^2) dx_1 dx_2 \quad (10.9)$$

the Euler-Lagrange equations for $\hat{\tau} = (\hat{\tau}_1, \hat{\tau}_2)$ are obtained, i.e.,

$$[F + \hat{\tau} \cdot \nabla T_w] \nabla T_w - \alpha \nabla^2 \hat{\tau} = 0 \quad (10.10)$$

where $\nabla = \partial / \partial x_i$, $\nabla^2 = \partial^2 / \partial x_i \partial x_i$, and α is the Lagrange multiplier. Given F , Equation 10.10 can be solved numerically with the Neumann condition $\partial \hat{\tau} / \partial n = 0$ imposed on the domain boundary [24, 26] from a surface temperature image. The

mathematical analysis on the uniqueness and convergence of the solution of Equation 10.10 has been given by Aubert et al. [145].

10.1.3 Uncertainty Analysis and Intrinsic Limitations

At this point, it is necessary to evaluate the sensitivity of computing skin friction to the elemental errors. The decompositions $T_w = T_{w0} + \delta T_w$, $F = F_0 + \delta F$ and $\hat{\tau} = \hat{\tau}_0 + \delta \hat{\tau}$ are introduced, where δT_w , δF and $\delta \hat{\tau}$ are errors, and T_{w0} , F_0 and $\hat{\tau}_0$ are the non-perturbed fields satisfying the Euler-Lagrange equation given by Equation 10.10. Substituting the decompositions into Equation 10.10 and neglecting the higher-order terms lead to an error propagation equation,

$$(\delta \hat{\tau} \cdot \nabla T_{w0}) \nabla T_{w0} - \alpha \nabla^2 \delta \hat{\tau} = -(\delta F + \hat{\tau}_0 \cdot \nabla \delta T_w) \nabla T_{w0} \quad (10.11)$$

where δF directly contributes to $\delta \hat{\tau}$ while δT_w contributes to $\delta \hat{\tau}$ through a gradient operator projected on the skin friction vector.

To simplify the analysis, a local region is considered where ∇T_{w0} is a constant vector (a reasonable linear approximation locally), and define $\|\nabla T_{w0}\|$ as the magnitude of ∇T_{w0} . Thus, the unit normal vector to an iso-temperature line $T_{w0} = \text{const.}$ is $N_T = \nabla T_{w0} / \|\nabla T_{w0}\|$. The error of skin friction projected on N_T is defined as $(\delta \hat{\tau})_N = \delta \hat{\tau} \cdot N_T$. Normalization of Equation 10.11 results in Equation 10.12 which describes the relative error estimate,

$$\frac{(\delta \hat{\tau})_N}{\|\hat{\tau}_0\|} = -\frac{\delta F}{\|\nabla T_{w0}\| \|\hat{\tau}_0\|} - \left(\frac{\hat{\tau}_0}{\|\hat{\tau}_0\|} \right) \cdot \delta N_T + \frac{\alpha}{\|\nabla T_{w0}\|^2} \nabla^2 \left[\frac{(\delta \hat{\tau})_N}{\|\hat{\tau}_0\|} \right] \quad (10.12)$$

where $\|\hat{\tau}_o\|$ is a characteristic value of skin friction such as the mean value. In the derivation of Equation 10.12 it is assumed that ∇ and δ can be exchanged. The first term in the right-hand side (RHS) of Equation 10.12 is the contribution from the elemental error in measurement of the time rate of heat flux (or heat flux in steady state). The second term is the contribution from the elemental error in measurement of the surface temperature gradient. The third term is the contribution from the artificial diffusion of the error $(\delta\hat{\tau})_N$ associated with the Lagrange multiplier. Equation 10.12 can be solved iteratively for $(\delta\hat{\tau})_N / \|\hat{\tau}_o\|$. The first two terms in the RHS of Equation 10.12 are used as an initial approximation of $(\delta\hat{\tau})_N / \|\hat{\tau}_o\|$, and then it is substituted into the third term to estimate the diffusion term in the first-order approximation. Repeating this process, successive approximations can be obtained.

The first and third terms in the RHS of Equation 10.12 are inversely proportional to $\|\nabla T_{wo}\|$ and its square, respectively. This indicates that the error $(\delta\hat{\tau})_N / \|\hat{\tau}_o\|$ will be large when $\|\nabla T_{wo}\|$ approaches zero. This imposes an intrinsic limitation on application of this technique in certain local regions where $\|\nabla T_{wo}\|$ is close to zero. The proportional constant in the third term is $\alpha \|\nabla T_{wo}\|^{-2}$. Therefore, the Lagrange multiplier must be appropriately small to reduce the error $(\delta\hat{\tau})_N / \|\hat{\tau}_o\|$ particularly when $\|\nabla T_{wo}\|$ is small.

10.1.4 Model for Time-Averaged Measurements

In theory, since Equation 10.10 is instantaneously valid for unsteady flow, once F and T_w are identified, an unsteady skin friction field can be determined by solving Equation 10.10. Practically, the time rate of heat flux $(\partial q_w / \partial t)$ and other terms in F are

difficult to measure on a global scale. This problem is simplified by applying a time average operator,

$$\langle \bullet \rangle_t = (t_1 - t_0)^{-1} \int_{t_0}^{t_1} \bullet d\tau \quad (10.13)$$

to Equation 10.8 over a time interval $[t_0, t_1]$ which results in,

$$\langle F \rangle_t + C_i \langle \hat{\tau}_i \rangle_t \partial \langle T_w \rangle_t / \partial x_i = 0, (i = 1, 2) \quad (10.14)$$

where C_i are the correlation coefficients defined as

$$C_i = \langle \hat{\tau}_i \partial T_w / \partial x_i \rangle_t / \langle \hat{\tau}_i \rangle_t \partial \langle T_w \rangle_t / \partial x_i \quad (\text{no summation convention is applied}).$$
 By

denoting $\hat{\tau}_{c,i} = C_i \langle \hat{\tau}_i \rangle_t$ (no summation convention is applied), the corresponding Euler-

Lagrange equations are written as

$$\left[\langle F \rangle_t + \hat{\tau}_c \cdot \nabla \langle T_w \rangle_t \right] \nabla \langle T_w \rangle_t - \alpha \nabla^2 \hat{\tau}_c = 0 \quad (10.15)$$

It is observed that Equation 10.15 has the same form as Equation 10.10. If $\langle F \rangle_t$ is known, the scaled, projected and time-averaged skin friction $\hat{\tau}_c$ can be determined by solving Equation 10.15. The skin friction field extracted by solving Equation 10.15 is a relative or normalized field, and the corresponding absolute skin friction field can be determined by in-situ calibration using a reliable point measurement approach such as oil film interferometry to obtain absolute skin friction values at several locations.

The next issue to tackle is determining $\langle F \rangle_t$. It is observed that the corresponding term to $\partial q_w / \partial t$ in F is proportional to the surface heat flux $q_w(t_1, x_1, x_2) - q_w(t_0, x_1, x_2)$ in $\langle F \rangle_t$. An empirical model, $\langle F \rangle_t = -\gamma (T_{ref} - T_w) + \varepsilon$, is introduced where γ is an empirical constant similar to the heat transfer coefficient, T_{ref} is a reference temperature selected for a specific experimental arrangement, and ε is the

contribution from all the remaining terms in Equation 10.7 that is typically unknown a priori. For the jet impingement tests in this work, T_{ref} is the base temperature of the aluminum flat plate and T_w is the wall temperature measured by TSP. The determination of the unknown term ε , in $\langle F \rangle_t$ to improve the computation of skin friction is achieved through the following iterative scheme. In the initial approximation where ε is neglected, the 0th-order estimate is $\langle F \rangle_t^{(0)} = -\gamma(T_{ref} - T_w)$ and the initial skin friction field $\hat{\tau}_{c,i}^{(0)}$ formally satisfies $\langle F \rangle_t^{(0)} + \hat{\tau}_{c,i}^{(0)} \partial \langle T_w \rangle_t / \partial x_i = 0$. Before solving the Euler-Lagrange equations for $\hat{\tau}_{c,i}^{(0)}$, a Gaussian filter with an appropriately large standard deviation (std) should be applied to surface temperature images. The effect of neglecting ε is that $\langle F \rangle_t^{(0)} = -\gamma(T_{ref} - T_w)$ may differ significantly from $-\hat{\tau}_{c,i}^{(0)} \partial \langle T_w \rangle_t / \partial x_i$ at some local locations. Therefore, the application of a Gaussian filter of an appropriately large std is performed to ensure the consistent behavior of these terms to obtain a reasonable initial estimation of the skin friction field $\hat{\tau}_{c,i}^{(0)}$ for further iterations. Additionally, the following iterative scheme is employed for successive estimates of ε and improvements to skin friction calculation, i.e.,

$$\langle F \rangle_t^{(n+1)} + \hat{\tau}_{c,i}^{(n+1)} \partial \langle T_w \rangle_t / \partial x_i = 0, \quad (n = 0, 1, 2, \dots) \quad (10.16)$$

where $\langle F \rangle_t^{(n+1)} = \langle F \rangle_t^{(0)} + \varepsilon^{(n+1)}$ and $\varepsilon^{(n+1)} = -\langle F \rangle_t^{(n)} - \hat{\tau}_{c,i}^{(n)} \partial \langle T_w \rangle_t / \partial x_i$. The corresponding Euler-Lagrange equations to Equation 10.16 are solved for $\hat{\tau}_{c,i}^{(n+1)}$. For iterative process described above, the std of the Gaussian filter is reduced by $\sigma^{(n+1)} = \sigma^{(0)} r^{n+1}$, where $\sigma^{(0)}$ is the initial std and $r < 1$. For data reduction of the TSP

images acquired in impinging jets experiments, 3 iterations are performed, where $\sigma^{(0)} = 18$ pixels and $r = 0.62$.

10.2 Measurement System

The application of the proposed method is performed using TSP for surface temperature measurements on a wind tunnel model as described by Liu and Sullivan [25]. A simple implementation is described here. A white polymer layer such as Mylar with an appropriate thickness is attached on the surface of a metal model. A TSP layer is then applied onto the polymer layer. The TSP is a thin luminescent polymer based coating that measures a surface temperature field utilizing the thermal quenching mechanism of luminescence. The luminescent molecules used in TSP are temperature sensing probes incorporated into a polymer coating on a surface. TSP is prepared by dissolving the luminescent molecule and a polymer binder in a solvent and the resulting paint is applied to a surface using a spray gun or a brush. Once the solvent evaporates, a solid polymer layer is formed on the surface in which the luminescent molecules are immobilized. When an excitation light source of a proper wavelength (e.g. ultraviolet (UV)) illuminates the coating, the luminescent molecules are excited and luminescent emission of a longer wavelength is emitted. A digital camera with a longpass or bandpass optical filter is used to detect the luminescent emission of TSP while cutting of the excitations source. Once TSP is applied on a surface and is calibrated, surface temperature fields are measurable by imaging TSP. A white polymer layer is necessary for heat flux measurements using TSP since it not only enhances the luminescent emission of TSP detected by an imaging system, but it also enhances the detectable thermal patterns on the surface. Without a base polymer layer, the spatial surface temperature difference produced by moderate heat

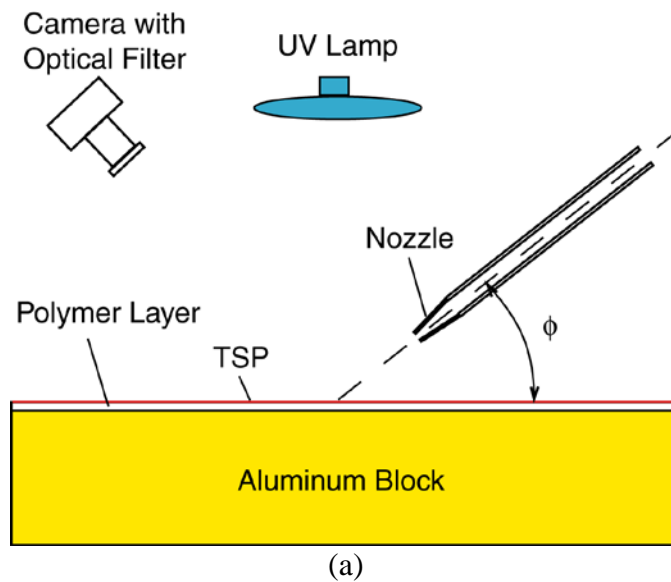
flux on a metal model with high thermal conductivity is so small that the thermal pattern is not detectable by TSP. The polymer layer plays the role of reducing lateral heat conduction that causes diffusion of the thermal patterns on the surface. For low speed, transonic and low Mach number supersonic flows, the model should be preheated to a certain temperature to allow for surface temperature change visualization by TSP. On the other hand, models in hypersonic flow do not require preheating since the model surface is naturally heated by skin friction heating. For this implementation, T_{ref} in $\langle F \rangle_t$ is the metal model temperature.

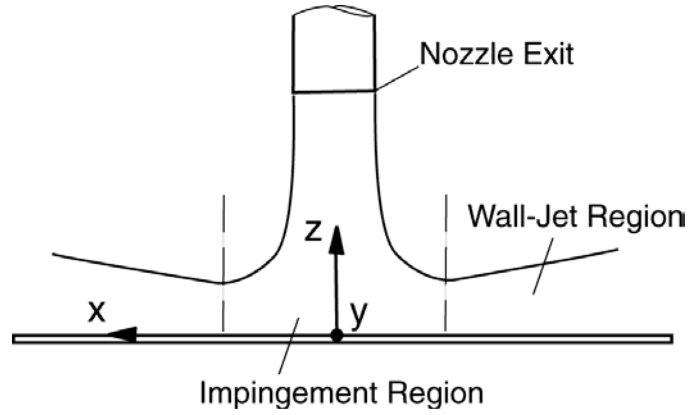
10.3 Experimental Setup

The proposed method is applied to measurements of jet impingement on a flat plate to evaluate its feasibility for global skin friction measurements. Impinging jets were selected as a flow to evaluate the proposed method since theoretical and experimental results of skin friction distributions in normal impinging jets are available for comparison. Figure 10.2 (a) illustrates the experimental setup of surface temperature measurements using TSP for an impinging jet.

The air jet was delivered from a tube with a nozzle with an exit diameter (D) of 2mm connected to a compressed air line. An aluminum plate of 203 mm, 250 mm, 30 mm width, length and thickness, respectively was used as a base. The upper surface of the aluminum plate was the surface on which the jet impinged upon. The upper surface of the plate was covered with white polymer sheet onto which the TSP was applied. TSP was prepared by dissolving europium thenoyltrifluoroacetate (EuTTA) in dope thinner and mixed with model airplane dope. The resulting mixture was brushed on the flat plate surface above the white polymer layer. A solid coating of TSP was formed after

the solvent evaporated. The thickness of the Mylar and TSP layers were $75\ \mu\text{m}$ and $30\ \mu\text{m}$, respectively. The TSP coating had an emission wavelength of about $620\ \text{nm}$ due to Stokes shift when illuminated by a UV excitation source with a peak centered around $365\ \text{nm}$. TSP images were captured at 9 frames per second by an ISG Lightwise CMOS camera with a $550\ \text{nm}$ longpass filter to cut off the emission light spectrum. The impingement angle and the distance of the jet from the flat plate were adjustable. The coordinate system in the impinging jet experiments is illustrated in Figure 10.2 (b), where x , y and z are the main streamwise coordinate, transverse coordinate, and normal coordinates to the wall. The coordinate system (x, y, z) corresponds to (X_1, X_2, X_3) as described in Section 10.1 of this chapter.





(b)

Figure 10.2 Illustrations of the (a) experimental setup for TSP measurements for an impinging jet and (b) wall jet and impingement regions and the coordinate system for the test setup

The aluminum flat plate was heated in an oven up to a base temperature of approximately 70 °C or 345 K, and placed under the jet. Image acquisition was started on the preheated base before the jet was started and continued for over one minute after the jet was turned on. Once the base surface was cooled down to ambient temperature (295 K), a reference TSP image was taken. The impingement zone was imaged without blocking the jet nozzle by viewing the surface at an oblique angle as illustrated in Figure 2 (a). Image registration was performed based on four black fiducial targets on the surface. The registered images were equivalent to viewing the impingement surface perpendicular from the top. The fiducial targets also provided a reference for metric scaling. The conversion of TSP images to temperature images was performed using a calibration relation for TSP. Over a certain temperature range, the relationship between luminescent intensity (I) of TSP and absolute temperature (T) can be expressed in the Arrhenius form given by,

$$\ln \frac{I(T)}{I(T_{amb})} = \frac{E_{nr}}{R} \left(\frac{1}{T} - \frac{1}{T_{amb}} \right) \quad (10.17)$$

where E_{nr} is the activation energy for the non-radiative process, R is the universal gas constant, and T_{amb} is the reference ambient temperature in Kelvin. For EuTTA in dope, the coefficient E_{nr}/R is 3797 (K) based on previous calibration tests [25]. In Equation 10.17, $I(T)$ is the image intensity image that is proportional to the luminescent intensity, and $I(T_{amb})$ is the reference image at the ambient temperature T_{amb} (295 K). The effects of non-uniform TSP coating thickness and illumination can be eliminated by performing image ratioing where the ratio between the flow-on image $I(T)$ and the reference image $I(T_{amb})$ is taken. Using the calibration relation given by Equation 10.17, surface temperature images of the Mylar layer were obtained.

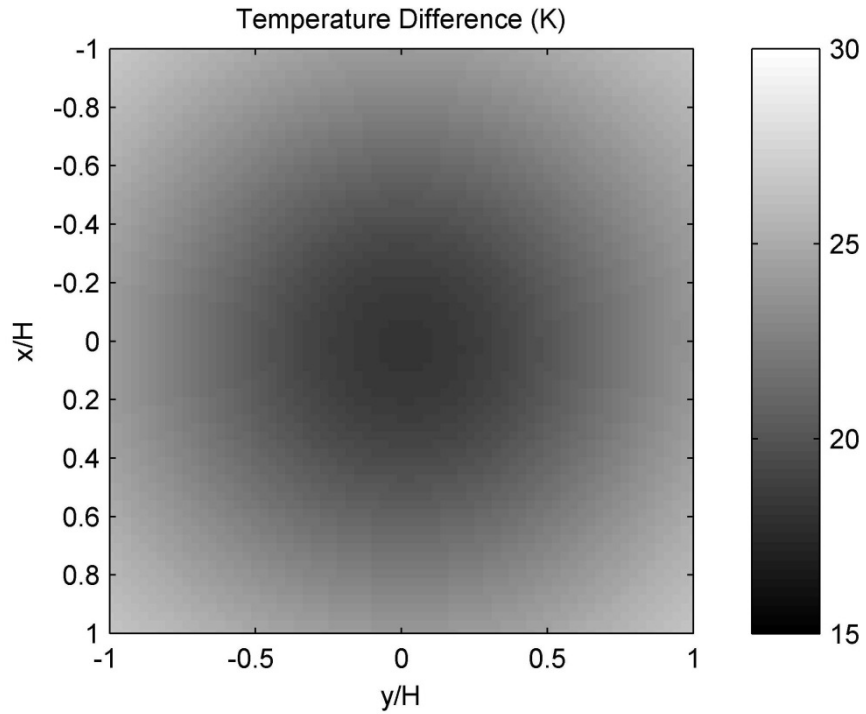
Once surface temperature was determined, $\langle F \rangle_t^{(0)} = -\gamma(T_{ref} - T_w)$ was estimated and the empirical constant γ was somewhat arbitrarily chosen (1000 in this study) to determine the relative skin friction, and T_{ref} was taken as the aluminum base temperature, T_b . The assumption was made that the aluminum base temperature did not change in the short jet run time since the thermal inertia of the base was large. It was confirmed by thermocouple measurements during a 30 second run of the jet impingement that a change in the base temperature was not detectable. In this case, T_b was replaced by T_w of the preheated base before the jet was run since natural convection is much lower than forced convection by the jet. Solving Equation 10.15 using the described iterative scheme, the scaled, projected and time-averaged skin friction $\hat{\tau}_c$ is obtained. Since the base surface was flat and the images were registered, $h_{ji} = \delta_{ij}$ where $\delta_{ij} = 1$ if $i = j$, and otherwise $\delta_{ij} = 0$, and $\hat{\tau}_c$ is considered as the scaled, time-averaged skin friction.

10.4 Measurements of Jet Impingement on a Flat Plate

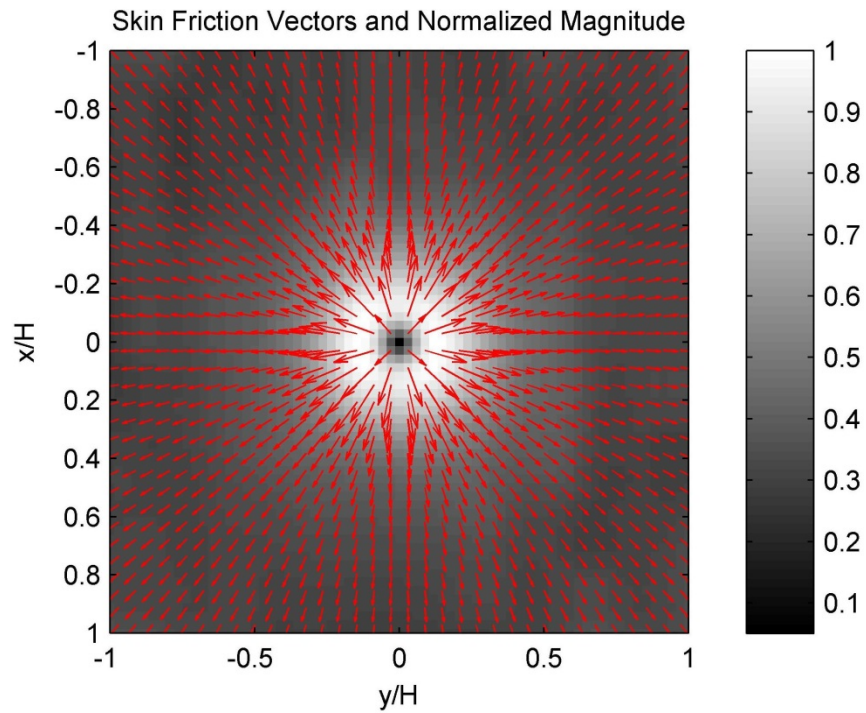
Measurements were conducted for normal and oblique impinging jets to evaluate the application of the proposed method. The results obtained from this approach were compared with existing theoretical solutions and flush mounted hot-film measurements. For all tests, jet exit velocity (U_0) was set at 50 m/s, with a corresponding Reynolds number (Re_D) based jet exit diameter of 6400 where the nozzle exit diameter (D) was 2 mm. The total temperature of the jet was 293 K, lower than the ambient temperature of 295 K. The free jet was laminar and the ratio between the nozzle to surface distance and the nozzle diameter (H/D) was 6. Measurements were also conducted for oblique impinging jets at impingement angles of 75° , 45° and 30° for H/D of 6.

10.4.1 Normal Impinging Jets

Figure 3(a) is a plot of the time averaged surface temperature difference $\langle T_w \rangle_t - T_{amb}$, where the time average is calculated over 125 images at a time step of 0.11 seconds. For the given $\langle T_w \rangle_t$ and $\langle F \rangle_t^{(0)} = -\gamma (T_{ref} - T_w)$ where γ is an arbitrarily selected positive constant (1000 in this case), the relative or normalized skin friction $\hat{\tau}_{c,j}$ was computed by solving Equation 10.16 numerically where the Lagrange multiplier (α) was set at 0.006. Three iterations were made according to the iterative scheme proposed to improve the estimate of $\langle F \rangle_t$, where $\sigma^{(0)} = 18$ pixels and $r = 0.62$. Figure 3(b) is a plot of the skin friction vector field superimposed on the magnitude field normalized by the maximum skin friction value. It is emphasized that the selection of γ does not affect the normalized skin friction field.



(a)



(b)

Figure 10.3 Plots of (a)the time averaged surface temperature field and (b)normalized skin friction vector and magnitude fields for a normal impinging jet at H/D of 6

To compare the obtained results from the proposed method, the skin friction magnitude distribution along the x-coordinate was measured by a flush mounted hot-film sensor on a Plexiglas plate under the same flow conditions. The relative skin friction magnitude was calculated using the relation $\tau = A(E^2 - E_0^2)^3$, where A is a constant to be determined, and E and E_0 are the voltages measured across the sensor with and without flow, respectively. Two measurements runs were conducted on different days. The theoretical solution given by Phares et al. [146] was also used as an additional comparison case. The theoretical solution used an analytical inviscid solution for the radial velocity along the surface and then solved the boundary layer integral equation using the Polhausen method to calculate the skin friction distributions in the impingement and wall-jet regions. Figure 10.4 is a plot of the skin friction magnitude distribution normalized by the maximum skin friction value along the x-axis for the normal impinging jet. Two peaks are observed in plot associated with the ring structure in the magnitude plot in Figure 10.3 (b). The skin friction distributions obtained using the proposed method (TSP based method) and hot-film skin friction measurements are consistent particularly in the impingement region. In the wall-jet region, the TSP based method indicates a slower decay of the skin friction magnitude. The measured surface temperature gradient in the wall-jet region is very small. This causes a large error in the computation of skin friction in that region as discussed in Section 10.1.3. Hot-film measurements indicate a small plateau around x/H of 0.4 in the skin friction distribution. In previous studies, a similar plateau has been observed in the heat flux distribution in normal impinging jets, related to local unsteady flow separation induced by organized vortices and small-scale turbulence [147]. The current method does not show this subtle

feature that may be smoothed out by the Gaussian filtering. The theoretical solution for the impingement region is in good agreement with the TSP based method and hot-film measurements although it is much higher in the wall-jet region.

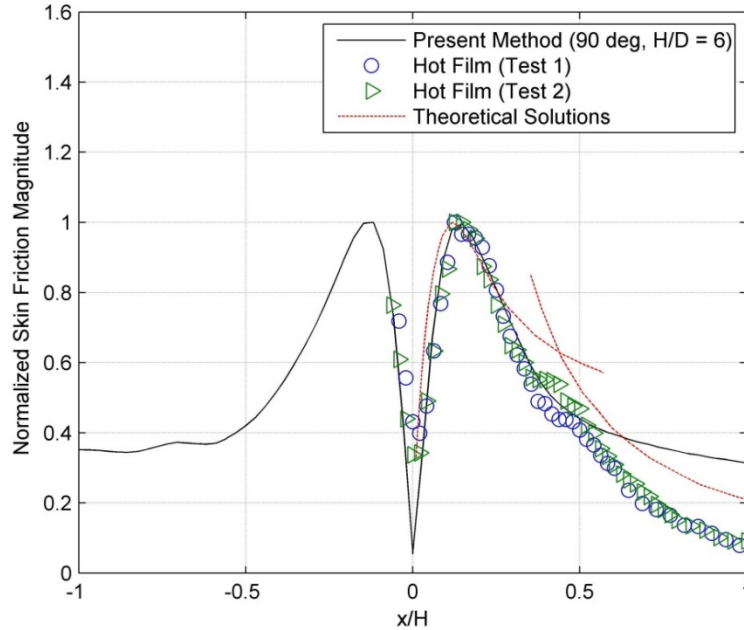
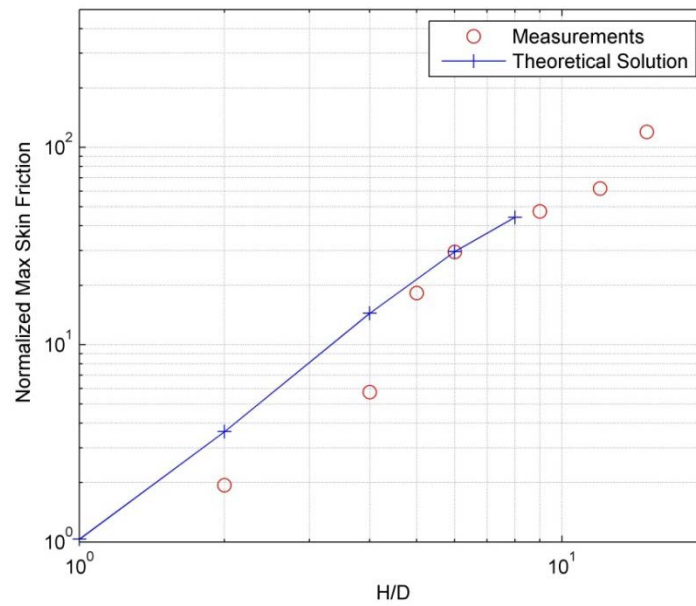


Figure 10.4 Skin friction magnitude distribution normalized by the maximum value along the x-axis for a normal impinging jet

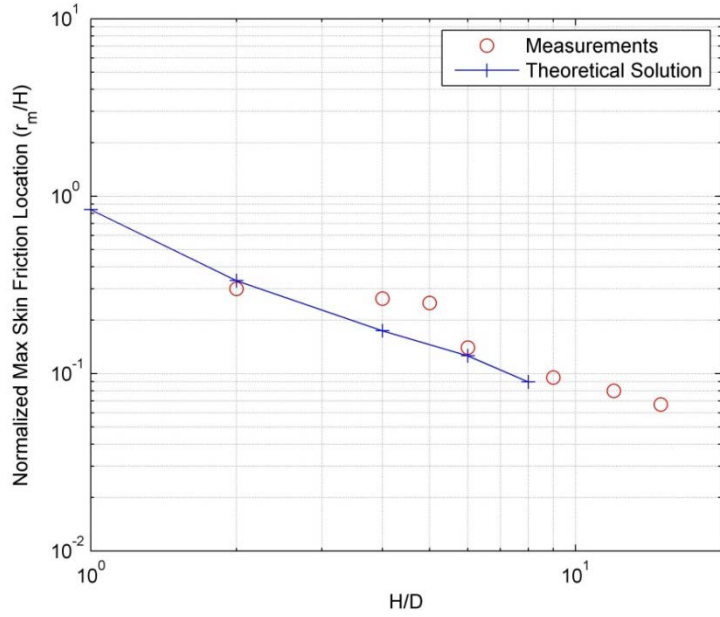
Measurements were also conducted at different values of H/D using the TSP based method. The maximum skin friction magnitude (τ_m) and the radial position of the skin friction peak (r_m) are dependent on the exit speed of the jet (U_0), jet height to diameter ratio (H/D) and Reynolds number Re_D . For comparison with the theoretical solution, the non-dimensional parameter $\tau_m Re_D^{1/2} (H/D)^2 / \rho U_o^2$ is estimated as a function of H/D . Figures 10.5 (a) and (b) are plots of the normalized maximum skin friction magnitude $\tau_m Re_D^{1/2} (H/D)^2 / \rho U_o^2$ as a function of H/D and normalized radial position r_m/H where τ_m is reached as a function of H/D .

The theoretical value of skin friction at H/D of 6 is used for in-situ calibration to determine absolute skin friction since the TSP based method only gives relative skin

friction. The trend exhibited by the results from the TSP-based method is consistent with the theoretical solution for H/D values larger than 5. It is observed that for H/D lower than 5, the measured values from the TSP based method are lower and deviate from the theoretical solution. The theoretical solution assumes that the free jet is fully developed, but at small H/D in experiments, it was not fully developed. This could lead to the variance in the measured maximum skin friction magnitude (τ_m) from the theoretical solution. Figure 10.5 (b) shows that the normalized location of maximum skin friction is consistent with the theoretical solution.



(a)



(b)

Figure 10.5 Plots of (a) normalized maximum skin friction magnitude and (b) position of the peak skin friction as a function of H/D in a normal impinging jet

10.4.2 Oblique Impinging Jets

Figures 10.6 (a) and (b) and 10.7 are plots of the time averaged surface temperature field, normalized skin friction vector and magnitude fields and skin friction magnitude distribution normalized by maximum value along the x-axis, respectively for an oblique impinging jet at an impingement angle of 75° .

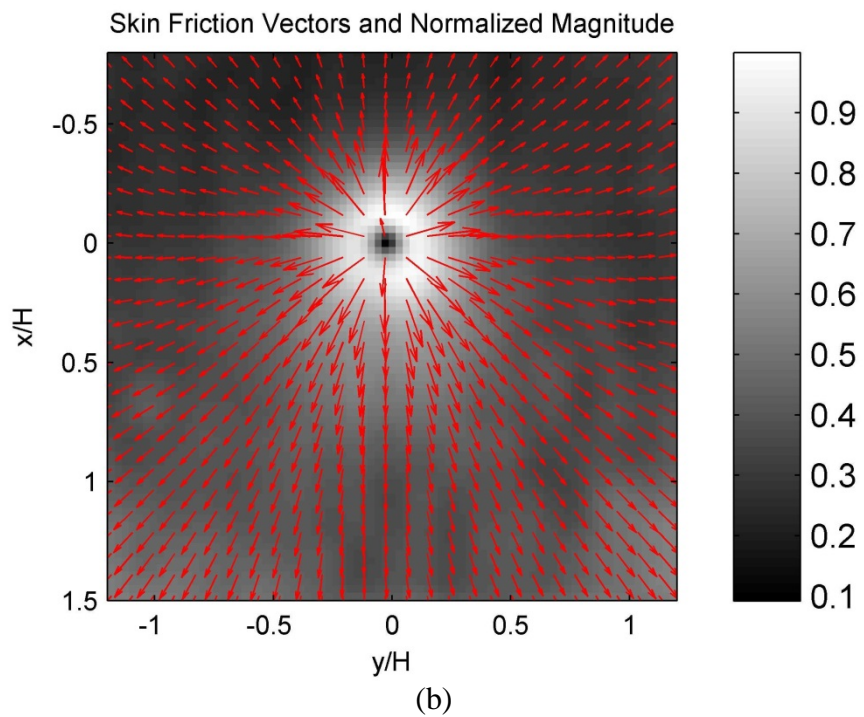
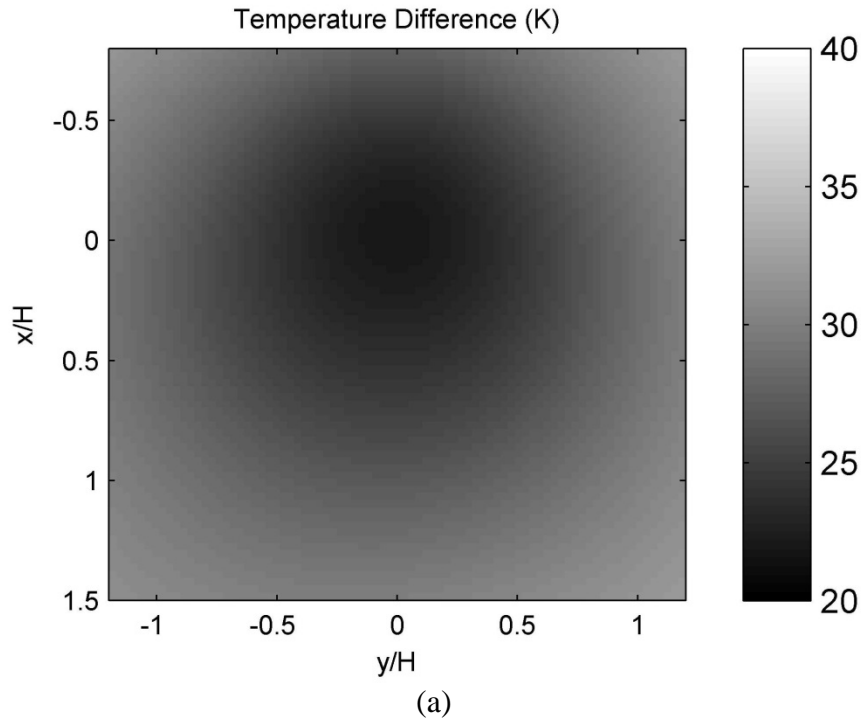


Figure 10.6 Plots of (a)time averaged surface temperature field and (b)normalized skin friction vector and magnitude fields for an oblique impinging jet at an impingement angle of 75°

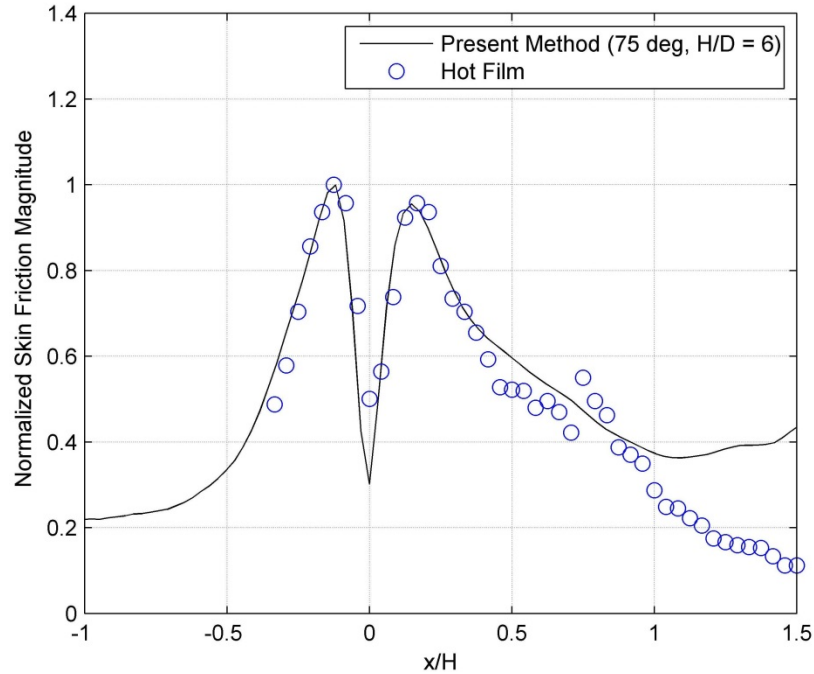
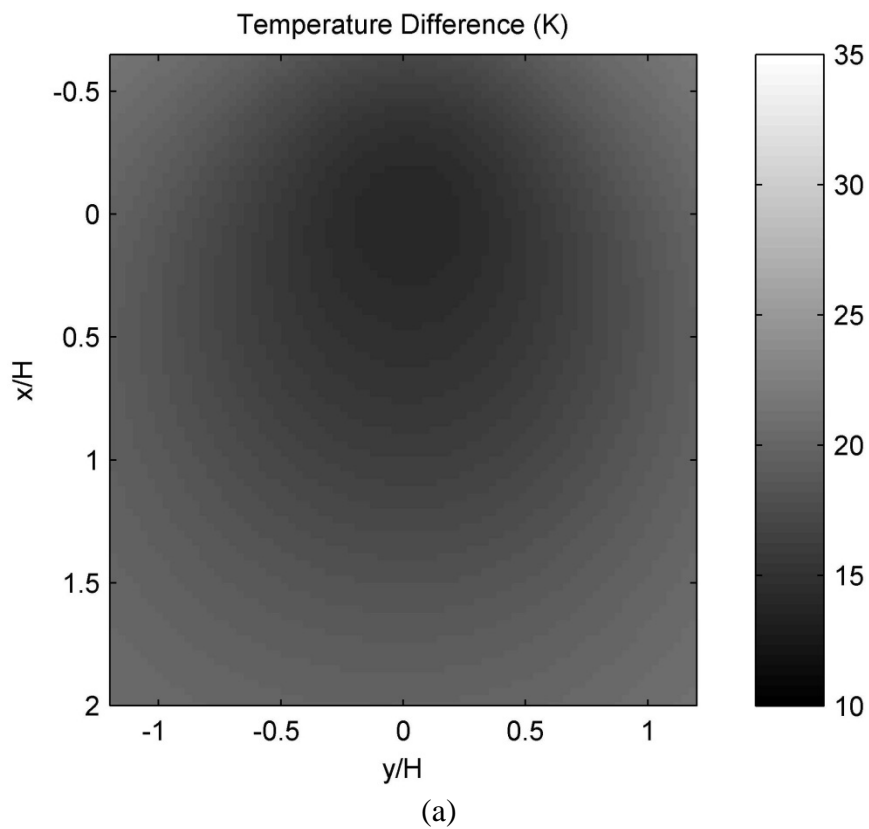


Figure 10.7 Skin friction magnitude distribution normalized by the maximum value along the x -axis in an oblique impinging jet at an impingement angle of 75°

The Lagrange multiplier (α) in the computations using the TSP based method for this case was set at 0.006. The asymmetry of the skin friction field with respect to the x -axis is observed. A plateau is also observed from x/H of 0.4 to 0.7. The results from the TSP based method agree well with hot-film measurements x/H of less than 1. Above that, the TSP-based method does not show a sufficient decay as observed with the hot-film results. This can be attributed to the small surface temperature gradient in that region contributing to large computation error. The results for impingement angles of 45° and 30° are also shown in Figures 10.8 through 10.11. The Lagrange multipliers (α) in the calculations for the 45° and 30° impingement angles were set at 0.001 and 0.002, respectively. The distributions of the skin friction magnitude are observed to be complicated, especially in the plateau region of x/H of 0.4 to 0.7. The measured surface temperature distribution for both cases also shows the plateaus or valleys in this region of x/H of 0.4 to 0.7. Since the surface temperature gradient is small or near zero locally in

this region, it could contribute to large errors in the computation of skin friction which may explain the large variations in this region. The flow structures that are responsible for the plateau in the skin friction distribution for oblique impinging jets is unknown as it is for the normal impinging jet and would be an interesting topic for further investigation. For all cases, the stagnation point is clearly identified with TSP based method. In contrast, the stagnation point location for hot-film measurements is not clearly identifiable particularly as the impingement angle is reduced. This is due to the hot-film sensor characteristic of being insensitive to the flow direction and as a result small flow oscillation in the proximity of the stagnation point could smooth out the minima of the skin friction magnitude at the stagnation point.



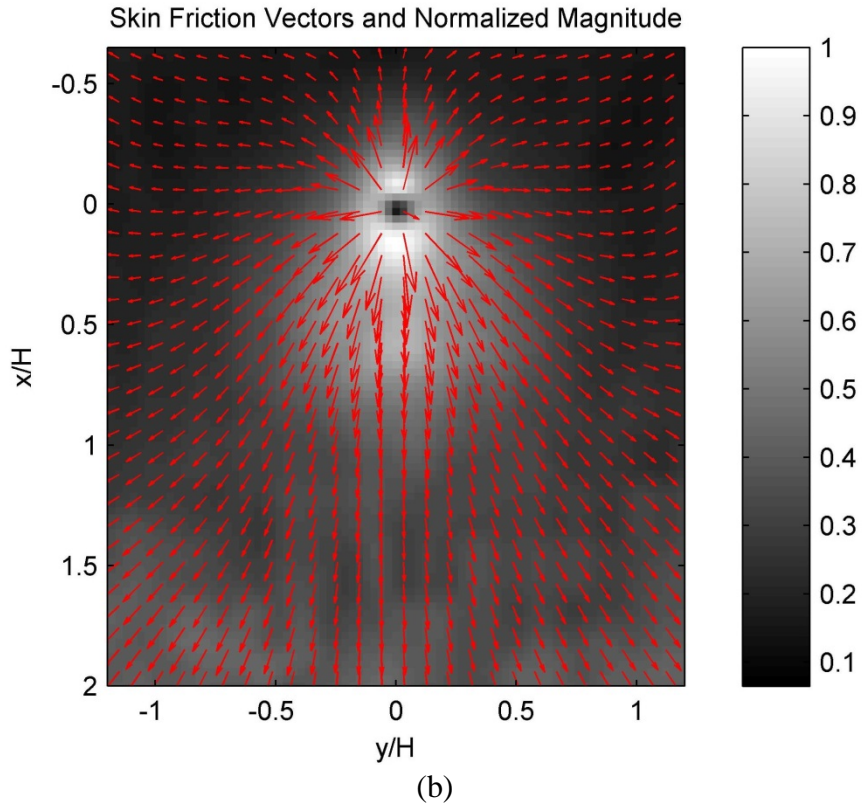


Figure 10.8 Plots of (a) time averaged surface temperature field and (b) normalized skin friction vector and magnitude fields for an oblique impinging jet at an impingement angle of 45°

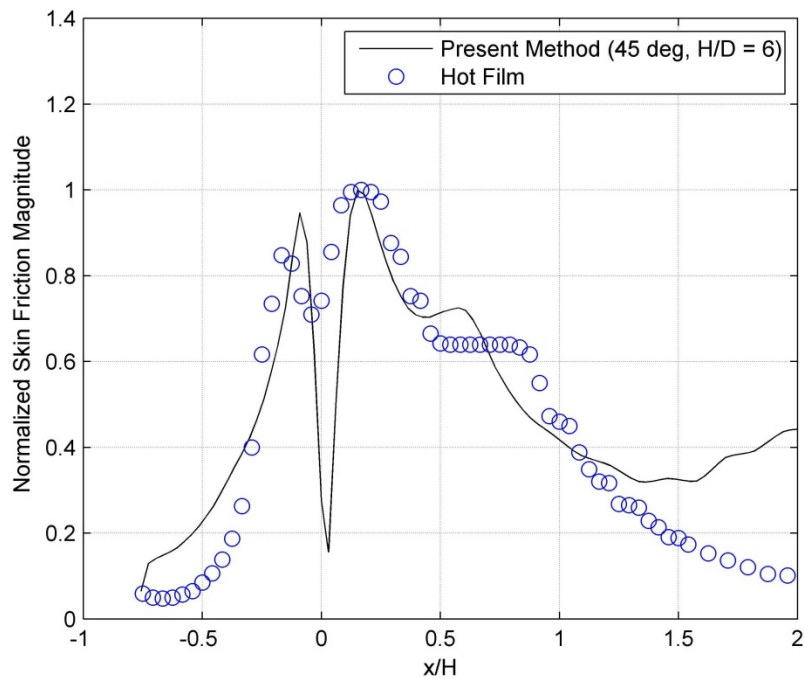


Figure 10.9 Skin friction magnitude distribution normalized by the maximum value along the x-axis in an oblique impinging jet at an impingement angle of 45°

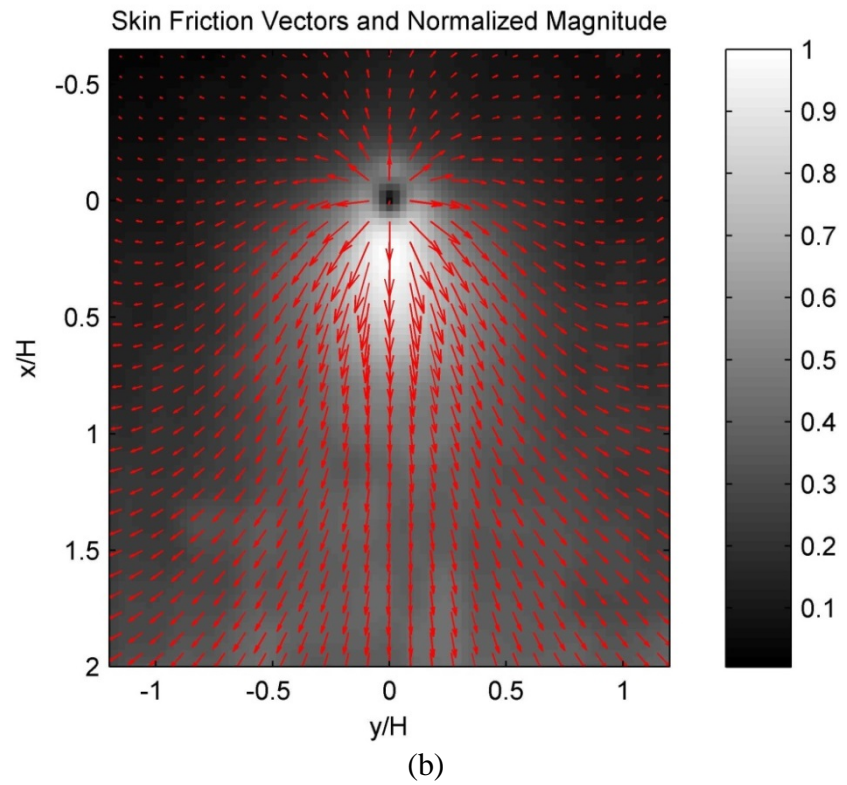
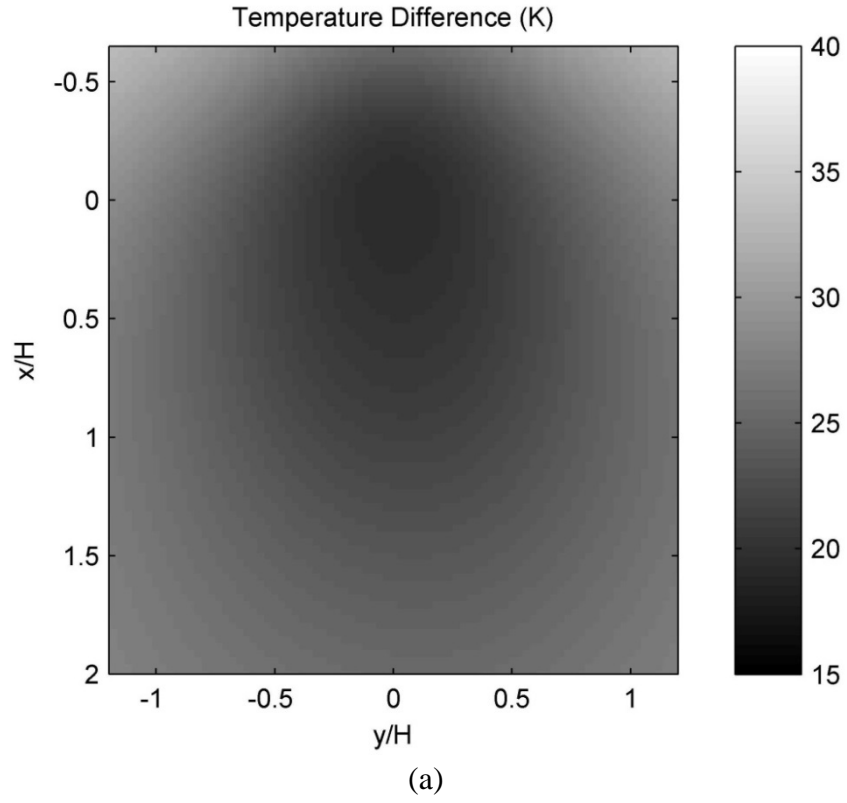


Figure 10.10 Plots of (a)time averaged surface temperature field and (b)normalized skin friction vector and magnitude fields for an oblique impinging jet at an impingement angle of 30°

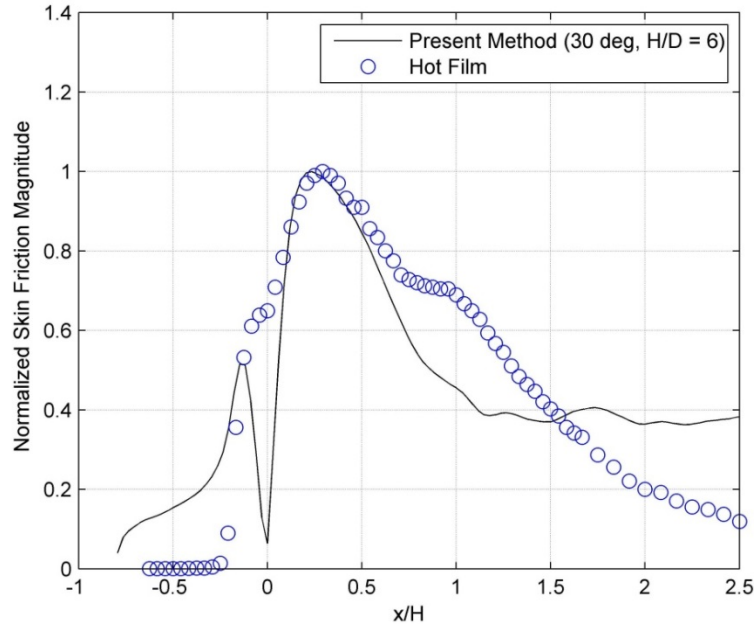


Figure 10.11 Skin friction magnitude distribution normalized by the maximum value along the x-axis in an oblique impinging jet at an impingement angle of 30°

10.5 Effects of the Lagrange Multiplier and Gaussian Filter Size

It was found that the results of solving Equation 10.15 for a skin friction field as an inverse problem for the jet impingement case is dependent on the selection of the Lagrange multiplier and the initial standard deviation (std) of the applied Gaussian filter. In contrast, the optical flow computation from flow visualization images is not sensitive to the Lagrange multiplier in a certain range as it is with the TSP based method. Typically, optical flow computation is robust because flow visualization images contain numerous distinct local features with large intensity gradients. Observing Equation 10.10 or 10.15, it is seen that the Lagrange multiplier behaves like a diffusion coefficient. Therefore, a large value of α tends to diffuse a skin friction field, whereas a small value of α tends to preserve sharp features and enhance high-frequency noise at the same time. As indicated in the uncertainty analysis in Section 10.1.3, α should be selected to be as small as possible to reduce the total uncertainty in the skin friction field computation. Conversely, if the selected Lagrange multiplier is too small, the solution could become

unstable due to the noise in the calculated surface temperature gradient. The effects of Lagrange multiplier selection are plotted in Figure 10.12(a) for the computed skin friction distribution of the normal impinging jet at H/D of 6 where the initial std of the Gaussian filter ($\sigma^{(0)}$) is 18 pixels. The diffusive effect of α on the skin friction distribution is clearly observed particularly in the wall-jet region where the surface temperature gradient is small, which is expected as discussed in the uncertainty analysis.

A rigorous theory has not been developed in selecting the Lagrange multiplier, and a trial-and-error approach is often adopted. However, simulations based on a synthetic skin friction vector field and a surface temperature image is useful to determine a suitable range of α . For the impinging jet, the time-averaged surface temperature field $\langle T_w \rangle_t$ and the normalized skin friction vector field $\hat{\tau}_{c,i}$ in Figure 10.3 are used in the simulation. The first term or source term in Equation 10.14 is estimated by $\langle F \rangle_t = -\hat{\tau}_{c,i} \partial \langle T_w \rangle_t / \partial x_i$ in the simulation. The solution of Equation 10.15 for this simulated case indicates that good recovery of the given skin friction field is achieved from the surface temperature images when α is in a range of 0.001 to 0.008.

As previously discussed, since the initial approximation $\langle F \rangle_t^{(0)} = -\gamma(T_{ref} - T_w)$ may differ from $-\hat{\tau}_{c,i}^{(0)} \partial \langle T_w \rangle_t / \partial x_i$ at some locations, a Gaussian filter with a suitably large initial std ($\sigma^{(0)}$) should be applied to TSP images to obtain a well-behaved initial field $\hat{\tau}_{c,i}^{(0)}$. The std of the Gaussian filter is then reduced by $\sigma^{(n+1)} = \sigma^{(0)} r^{n+1}$, where $r = 0.62$. The effect of the initial std ($\sigma^{(0)}$) of the Gaussian filter on the extracted skin friction distribution for α of 0.006 is plotted in Figure 12 (b).

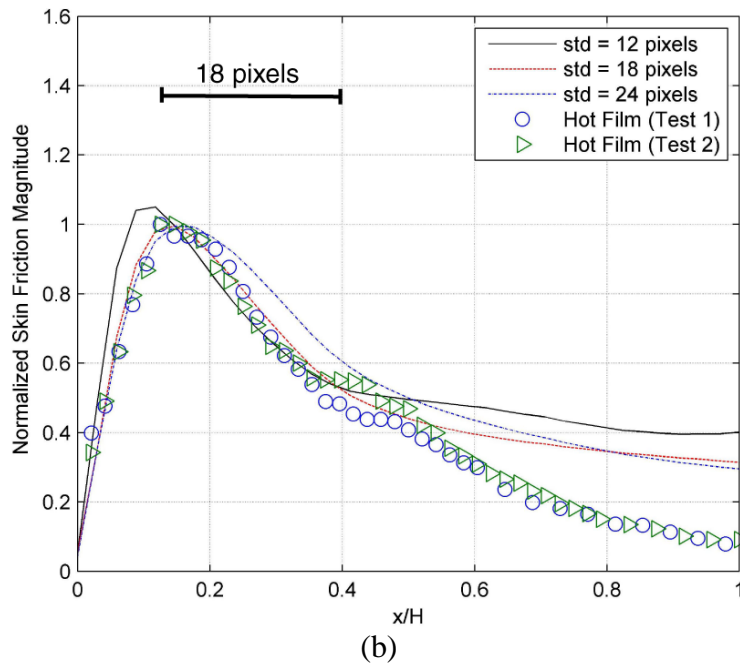
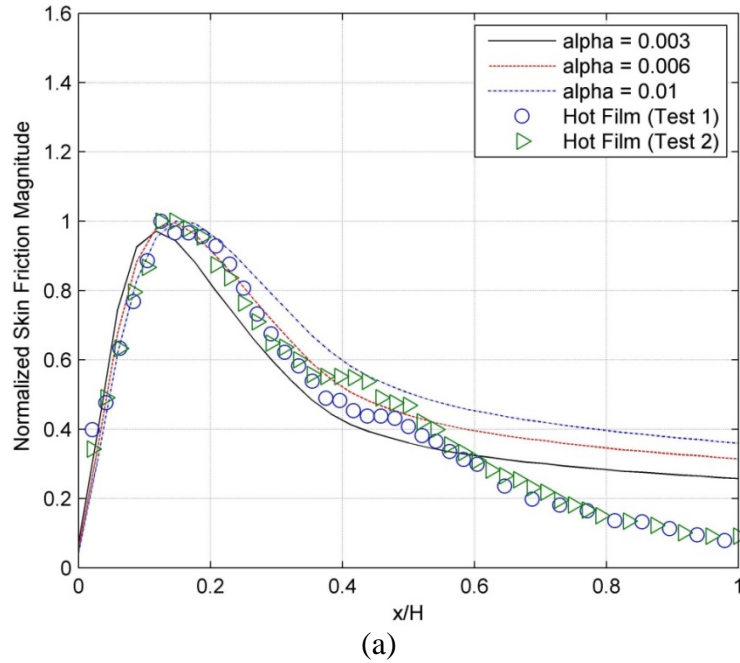


Figure 10.12 Plots of the normalized skin friction distributions along the x-axis in the normal impinging jet looking at (a)effect of the Lagrange multiplier for an initial std of 18 pixels for the Gaussian filter and (b)effect of the initial std of the Gaussian filter for α of 0.006

10.6 Summary

This study establishes the theoretical foundation for global skin friction diagnostics based on temperature sensitive paint (TSP) measurements. The asymptotic

form of the energy equation near a wall is given, which provides a relationship between the skin friction vector, heat flux and temperature at a wall. This relationship has the same form as the physics based optical flow equation which allows for extraction of a relative skin friction field from surface temperature images by solving the Euler-Lagrange equations as an inverse problem. The established formulation is further simplified for time-averaged skin friction measurements, where the source term is modeled as a linear function of the surface temperature.

An uncertainty analysis was also conducted highlighting the intrinsic limitation of this approach where the error in skin friction computation is significantly enhanced in regions where the surface temperature gradient is small. The selection of a sufficiently small Lagrange multiplier through simulations can help in reducing the error. The proposed iterative scheme is used to estimate the source term successively, during which the standard deviation of a Gaussian filter applied to surface temperature images is sequentially reduced in the iterative process.

Experimental implementation for this method is simple and essentially similar to TSP based heat flux measurements. The feasibility of this method was examined by performing TSP measurements on a flat plate for normal and oblique impinging jets and subsequently extracting high resolution normalized skin friction fields. It was observed that the TSP measured skin friction distributions are consistent with hot-film measurements and the theoretical solutions although a large error was observed in the wall-jet region where the surface temperature gradient is small. In summary, TSP based global skin friction diagnostics is feasible although limited by the requirement for a sufficiently large temperature gradient in the measurement region.

CHAPTER 11

GLOBAL SKIN FRICTION DIAGNOSTICS BASED ON SURFACE MASS TRANSFER VISUALIZATIONS

The previous chapter has described an approach for global skin friction diagnostics based on surface temperature measurements. The asymptotic energy equation at a wall is re-formed as the optical flow equation providing the relationship between surface temperature, heat flux and skin friction [147]. The variational method was used to extract a skin friction fields from surface temperature visualizations using temperature sensitive paint (TSP). This TSP based method was then validated by applying it to TSP visualizations in impinging jets.

Since a formal analogy exists between heat and mass transfer, an alternate approach to global skin friction diagnostics based on mass transfer can be investigated. The approach could potentially be based on surface mass transfer visualizations with pressure sensitive paint (PSP) as an oxygen sensor or sublimating coatings. Mass transfer sensors have previously been studied focused on local electrochemical mass transfer for skin friction measurements [1]. The crucial element for developing a global skin friction approach based on mass transfer is establishing a general relationship between skin friction, mass transfer and species on the surface and subsequently solving the inverse problem to obtain skin friction. This study aims to formulate the theoretical foundations for global skin friction diagnostics based on surface mass transfer visualizations and

develop a procedure for both steady and unsteady global skin friction measurements using PSP and sublimating coatings.

The asymptotic form of the mass transport equation at a wall is derived, and reformed in the image plane as an optical flow equation that relates the relative image intensity to skin friction for surface flow visualizations using PSP and sublimating coatings. The inverse solution is then developed for a relative skin friction field along with an uncertainty analysis discussing the intrinsic limitations of this technique. Measurements were conducted for a steady state impinging nitrogen jet and dual colliding impinging nitrogen jets. The normalized skin friction fields extracted from PSP images were compared with data obtained using a hot-film sensor across the jet for the single impinging nitrogen jet. Unsteady skin friction diagnostics was also demonstrated using PSP visualizations for an unsteady impinging nitrogen jet from a microfluidic oscillator. Visualizations were also conducted on sublimation images on the upper surface of a delta wing at low speed and on a flat plate in fin shock/boundary-layer interaction at Mach 6. Global skin friction fields were successfully extracted for both PSP and sublimating coating visualizations.

11.1 Theory

In this section, the working principle of a mass transfer based skin friction diagnostics approach is discussed and the relation between skin friction, surface mass transfer and species on the surface will be obtained. A model for time-averaged measurements using PSP as well as sublimation visualizations is developed and discussed. The variational solution for skin friction fields with the resulting Euler-Lagrange equations is also presented along with an uncertainty analysis.

11.1.1 Asymptotic Form of the Mass Transport Equation at a Wall

The binary mass diffusion equation without a source term is defined as [151]

$$\frac{D\omega_1}{Dt} = D_{12}\nabla^2\omega_1, \quad (11.1)$$

where $\omega_1 = \rho_1 / \rho$ is the relative density or concentration of species 1, $\rho = \rho_1 + \rho_2$ is the total density of the binary gas, $D/Dt = \partial/\partial t + u_j \partial/\partial X_j$ ($j = 1, 2, 3$) is the total derivative, and D_{12} is the diffusivity of a binary gas. The surface coordinates are defined as X_1 and X_2 the coordinate normal to the surface is defined as X_3 . The Taylor expansions of the velocity components (u_1, u_2) along the surface and ω_1 near a wall are

$$u_1 = \frac{\tau_1}{\mu} X_3 + \left(\frac{\partial^2 u_1}{\partial X_3^2} \right)_w \frac{X_3^2}{2} + \dots \quad (11.2)$$

$$u_2 = \frac{\tau_2}{\mu} X_3 + \left(\frac{\partial^2 u_2}{\partial X_3^2} \right)_w \frac{X_3^2}{2} + \dots, \quad (11.3)$$

$$\omega_1 = \omega_{1w} - \dot{m}_{1w} \frac{X_3}{\rho_w D_{12}} + \dots, \quad (11.4)$$

where the subscript 'w' denotes the condition at the gas-wall interface, and $\tau_i = \mu(\partial u_i / \partial X_3)_w$ ($i = 1, 2$) is the skin friction vector, μ is the dynamic viscosity of fluid, and $\dot{m}_{1w} = -D_{12}\rho_w(\partial\omega_1/\partial X_3)_w$ is the diffusive flux of species 1 at the wall. When X_3 tends to zero, the continuity equation near the wall is approximated by the incompressible one, i.e., $\partial u_j / \partial X_j \approx 0$. The velocity normal to the surface is then obtained by integrating the continuity equation, i.e.,

$$u_3 = -\frac{X_3^2}{2} \frac{\partial}{\partial X_i} \left(\frac{\tau_i}{\mu} \right) + \dots \quad (i = 1, 2) \quad (11.5)$$

Substituting Equations 11.2 through 11.5 into 11.1 and differentiating it with respect to X_3 , a limit form of Equation 11.1 is obtained as X_3 tends to zero, i.e.,

$$F + \tau_i \partial \omega_{1w} / \partial X_i = 0, \quad (i = 1, 2) \quad (11.6)$$

where

$$F = \frac{\mu}{\rho_w D_{12}} \left(-\frac{\partial \dot{m}_{1w}}{\partial t} + D_{12} \frac{\partial^2 \dot{m}_{1w}}{\partial X_i \partial X_i} \right). \quad (11.7)$$

The relationship between the skin friction vector, mass transfer flux and relative density of species 1 at the wall is described by Equation 11.6. It represents a balance between the flux of a scalar ω_{1w} transported by a vector field τ_i and the source term F containing the time rate and diffusion of the mass transfer flux at a wall.

The time derivative of the mass transfer flux in Equation 11.7 is difficult to measure on a global scale. This problem is tackled by performing time averaging of Equation 11.6. For a flow in a time interval $[t_0, t_1]$, application of the time average operator

$$\langle \bullet \rangle_t = \Delta T^{-1} \int_{t_0}^{t_1} \bullet d\tau. \quad (11.8)$$

to Equation 11.6 yields

$$\langle F \rangle_t + C_i \langle \tau_i \rangle_t \partial \langle \omega_{1w} \rangle_t / \partial X_i = 0, \quad (i = 1, 2) \quad (11.9)$$

where C_i is the correlation coefficient defined as $C_i = \langle \tau_i \partial \omega_{1w} / \partial X_i \rangle_t / \langle \tau_i \rangle_t \partial \langle \omega_{1w} \rangle_t / \partial X_i$ (no summation convention is applied here) and $\Delta T = t_1 - t_0$ is the time interval. When a snapshot of a time dependent flow is considered in an interval $[t_0, t_1]$, $\tau_i = \tau_{i,s} W(t; t_0, t_1)$, $\omega_{1w} = \omega_{1,0} + \omega_{1w,s} W(t; t_0, t_1)$ and

$\dot{m}_{1w} = \dot{m}_{1w,s} W(t; t_0, t_1)$, where $\tau_{i,s}$, $\omega_{1w,s}$ and $\dot{m}_{1w,s}$ are the steady state or frozen skin friction field, relative density and mass transfer rate of species 1 in the time interval $[t_0, t_1]$, respectively, and $\omega_{1,0}$ is a constant initial field. The window function is defined as $W(t; t_0, t_1) = H(t - t_0) - H(t - t_1)$, where the Heaviside function is defined as $H(t - t_0) = 1$ for $t - t_0 > 0$ and $H(t - t_0) = 0$ for $t - t_0 \leq 0$. Since $\tau_i = \langle \tau_i \rangle_t = \tau_{i,s}$, $\langle \omega_{1w} \rangle_t = \omega_{1,0} + \omega_{1w,s}$, $\langle \dot{m}_{1w} \rangle_t = \dot{m}_{1w,s}$ and $C_j = 1$ in the time interval $[t_0, t_1]$, Equation 11.9 becomes

$$\langle F \rangle_t + \tau_i \partial \omega_{1w,s} / \partial X_i = 0, \quad (i = 1, 2) \quad (11.10)$$

where

$$\langle F \rangle_t = \frac{\mu}{\rho_w D_{12} \Delta T} \left(-\dot{m}_{1w,s} + D_{12} \Delta T \frac{\partial^2 \dot{m}_{1w,s}}{\partial X_i \partial X_i} \right). \quad (11.11)$$

and species 1 has not been defined at this point.

11.1.2 Measurements with Pressure Sensitive Paint

Pressure sensitive paint (PSP) is an oxygen sensor that can potentially be utilized for mass transfer visualizations in low speed flows as described by Liu and Sullivan [25]. If nitrogen is added into the flow as species 1 which diffuses into the PSP layer, oxygen (defined as species 2) is purged from the layer, and the PSP coating, illuminated by an excitation source emits stronger luminescence due to reduced oxygen quenching. Conversely if oxygen is added into the flow, the luminescent emission will be weaker due to increased oxygen quenching.

11.1.2.1 Steady-State Measurements

At the interface between the gas flow and PSP layer, the mass transfer flux is defined as, $\dot{m}_{I_w} = -\rho_w D_{12} (\partial \omega_1 / \partial X_3)_w$. Based on the solution of the 1D steady-state mass transfer equation with the no-flux condition at the PSP-solid interface the mass transfer flux into a thin PSP layer at the gas-PSP interface is expressed by $\dot{m}_{I_w} = -\rho_w \gamma_m (\omega_{I_w} - \omega_{I,00})$, where ω_{I_w} and $\omega_{I,00}$ are the values of ω_1 at the gas-PSP interface and the PSP-solid interface, respectively and $\gamma_m = 2D_{1p} / h$, D_{1p} is the diffusivity of the species 1 in the polymer where h is the coating thickness.

The luminescent emission of PSP is dependent on the relative oxygen density ω_2 (species 2) in PSP due to oxygen quenching. The Stern-Volmer relation between the luminescent intensity of PSP and the relative density of oxygen is given by $I_0 / I = 1 + K\omega_2$, where I and I_0 are the intensities in the test and zero-oxygen conditions, respectively, and K is the Stern-Volmer coefficient. Since the zero-oxygen condition is not easily applied in experiments, the wind-off condition is typically used as a reference. For this approach, the Stern-Volmer relation is rewritten as $I_{ref} / I = A + B(\omega_2 / \omega_{2ref})$ or rearranged as $\omega_2 = (\omega_{2ref} / B)(I_{ref} / I) - A\omega_{2ref} / B$, where I and I_{ref} are the luminescent intensities of PSP in the wind-on and wind-off reference conditions, respectively and $A = (1 + K\omega_{2ref})^{-1}$ and $B = K\omega_{2ref} A$ are the alternate Stern-Volmer coefficients for aerodynamics applications where ω_{2ref} is the value of ω_2 at the wind-off reference condition. When nitrogen is added to the flow for surface mass-transfer visualization using PSP, using the relationship $\omega_1 = 1 - \omega_2$ for the relative density of nitrogen (species 1) in the PSP layer, Equation 11.10 becomes

$$g - \frac{I_{ref}}{I_{00}} - D_{12} \Delta T \frac{\partial^2 g}{\partial X_i \partial X_i} + \frac{D_{12} \Delta T \tau_i}{\mu \gamma_m} \frac{\partial g}{\partial X_i} = 0, \quad (11.12)$$

where $g = I_{ref} / I$ is the normalized luminescent intensity and I_{00} is the luminescent intensity of PSP corresponding to $\omega_{1,00}$ at the PSP-solid interface.

For image based measurements, Equation 11.12 must be projected onto the image plane of a camera similar to the GLOF technique and the TSP based method. Figure 11.1 illustrates a special object-space coordinate system $(\bar{X}_1, \bar{X}_2, \bar{X}_3)$,

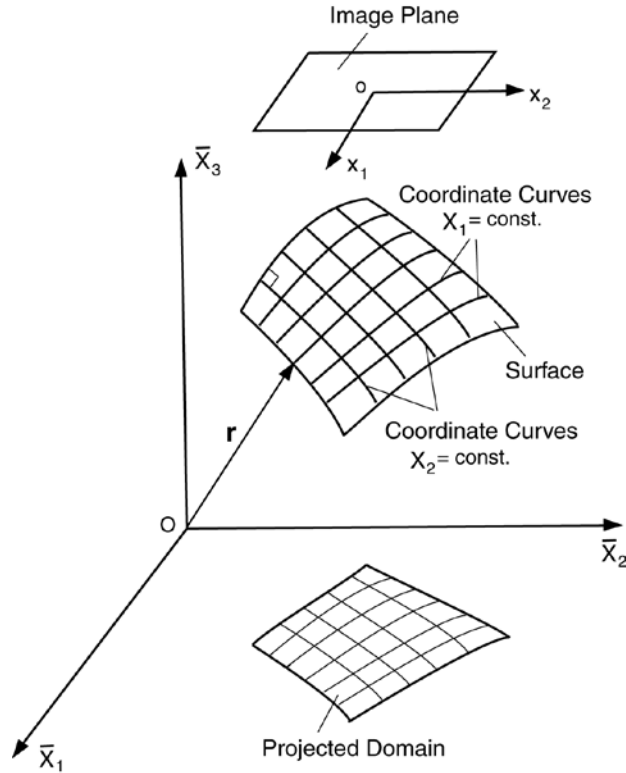


Figure 11.1 Surface, object space and image coordinates

in which the plane (\bar{X}_1, \bar{X}_2) is parallel to the image plane (x_1, x_2) . Therefore, a relationship between (\bar{X}_1, \bar{X}_2) and (x_1, x_2) is defined as $\partial / \partial \bar{X}_i = \lambda \partial / \partial x_i$, where λ is a scaling constant. An image on a camera is the scaled projection of the surface onto the plane (\bar{X}_1, \bar{X}_2) . If the transformation between (\bar{X}_1, \bar{X}_2) and (X_1, X_2) is given by

$\bar{X}_1 = F_1(X_1, X_2)$ and $\bar{X}_2 = F_2(X_1, X_2)$, then $\partial / \partial X_i = h_{ji} \partial / \partial \bar{X}_j = \lambda h_{ji} \partial / \partial x_j$ ($i, j = 1, 2$), where $h_{ji} = \partial F_j / \partial X_i$ is dependent on the geometric properties of the surface. Therefore, Equation 11.6 can be expressed in the image coordinates as,

$$G + \hat{\tau}_j \partial g / \partial x_j = 0 \quad (11.13)$$

where $g = I_{ref} / I$ is the normalized image intensity when the response function of a camera is linear and $\hat{\tau}_j = (D_{12} \Delta T / \gamma_m \mu) \lambda h_{ji} \tau_i$ ($i, j = 1, 2$) is the relative skin friction vector projected onto the image plane and G is defined as $G = g - I_{ref} / I_{00} + \varepsilon_0$ with the diffusion term defined as $\varepsilon_0 = -D_{12} \Delta T \lambda^2 h_{ji} h_{ji} \partial^2 g / \partial x_j \partial x_j$. The time interval ΔT is arbitrary and does not affect the normalized skin friction field.

The scaling constant λ in the orthographical projection is approximately the ratio between the focal length of a camera and the distance between the camera and the surface. Since λ is a parameter with a small value, $\varepsilon_0 \sim \lambda^2$ is a higher-order smaller term. For PSP in a gas flow with added nitrogen, since $I > I_{00}$, G is a negative value smaller than zero due to the smaller density of nitrogen at the PSP-solid interface. Conversely, when oxygen is added as species 1 in a gas flow, Equation 11.13 remains the same, G is a positive value larger than zero since $I < I_{00}$. In experiments, an issue is that the luminescent intensity I_{00} at the PSP-solid interface is unknown and is related directly to $\omega_{1,00}$ in the Stern-Volmer relation. Since $\omega_{1,00}$ depends on the mass transfer flux, I_{00} is typically position dependent. The term $I_{ref} / I_{00} - \varepsilon_0$ is treated as a constant, free parameter that is around one to solve this issue.

11.1.2.2 Unsteady Measurements

It is also possible to extract an unsteady skin friction field from mass transfer visualizations with PSP. For PSP visualizations in an unsteady flow with added nitrogen, using the relation $\partial \dot{m}_{I_w} / \partial t = -\rho_w \gamma_m \partial \omega_{I_w} / \partial t$ and $\omega_I = (I + A\omega_{2ref} / B) - (\omega_{2ref} / B)(I_{ref} / I)$ for the relative nitrogen density, Equation 11.6 is expressed in the image plane as

$$G + c_{ji} \tau_i \partial g / \partial x_j = 0 \quad (11.14)$$

where $g = I_{ref} / I$ is the normalized image intensity, $c_{ji} = (D_{12} / \gamma_m \mu) \lambda h_{ji}$ are the projection coefficients, $G = \partial g / \partial t + \varepsilon$ contains the effects of the time rate of g and the diffusion term $\varepsilon = -D_{12} \lambda^2 h_{ji} h_{ji} \partial^2 g / \partial x_j \partial x_j$. The time domain is decomposed into numerous small intervals $[t_k, t_{k+1}]$ ($k = 0, 1, 2, \dots$). For each interval, the decompositions $G = \langle G \rangle_t + G'$, $g = \langle g \rangle_t + g'$ and $\tau_i = \langle \tau_i \rangle_t + \tau'_i$ are introduced, where $\langle \rangle_t$ is the time average over an interval $[t_k, t_{k+1}]$ and the prime denotes the variation due to the unsteady effects in $[t_k, t_{k+1}]$. Therefore, for each interval, Equation 11.14 can be decomposed into equations for the snapshot field and the variation field, i.e.,

$$\langle G \rangle_t + c_{ji} \langle \tau_i \rangle_t \partial \langle g \rangle_t / \partial x_j = 0, \quad (11.15)$$

and

$$G' + c_{ji} \langle \tau_i \rangle_t \partial g' / \partial x_j + c_{ji} \tau'_i \partial \langle g \rangle_t / \partial x_j = 0. \quad (11.16)$$

where the smaller non-linear terms are neglected.

Additionally, an unsteady skin friction field is considered as a quasi-steady process in which a steady-state solution in a small interval is found independently by

neglecting the historical effects from the preceding interval. For this case, a continuous time sequence of g is modeled by a piecewise function described by $\sum_k [g_{00}\delta(t-t_k) + g_s W(t; t_k, t_{k+1})]$ ($k = 0, 1, 2, \dots$), where $g_{00} = I_{ref} / I_{00}$ is the initial value, I_{00} is the luminescent intensity of PSP at the PSP-solid interface, and $g_s = \langle g \rangle_t = [g(t_k) + g(t_{k+1})] / 2$ is the time averaged value in an appropriately small interval $[t_k, t_{k+1}]$. The window function is defined as $W(t; t_k, t_{k+1}) = H(t - t_k) - H(t - t_{k+1})$, where the Heaviside function is $H(t - t_k) = 1$ for $t - t_k > 0$ and $H(t - t_k) = 0$ for $t - t_k \leq 0$. The corresponding approximation for a snapshot skin friction field in $[t_k, t_{k+1}]$ is $\tau_i \approx \tau_{i,s} W(t; t_k, t_{k+1})$, where $\tau_{i,s} = \langle \tau_i \rangle_t$ is the time-averaged value in $[t_k, t_{k+1}]$. Therefore, in $[t_k, t_{k+1}]$, Equation 11.15 is defined as

$$G_I + \hat{\tau}_{j,s} \partial g_s / \partial x_j = 0 \quad (11.17)$$

where $G_I = g_s - g_{00} + \langle \varepsilon \rangle_t$, $\hat{\tau}_{j,s} = \Delta T c_{ji} \tau_{i,s}$ and $\Delta T = t_{k+1} - t_k$. Since an unsteady skin friction field in a small interval is approximated by a steady-state solution, Equation 11.17 has the same form as Equation 11.13. A snapshot skin friction field in $[t_k, t_{k+1}]$ is obtained from a single normalized PSP intensity image by solving Equation 11.17 using the variational method which will be described in Section 11.1.4. For a time sequence of unsteady PSP visualization images, solving of Equation 11.17 at sequential intervals $[t_k, t_{k+1}]$ ($k = 0, 1, 2, \dots$) results in the extraction of a quasi-steady state of an unsteady skin friction field. The quasi-steady approximation is reasonable only when the response time of PSP is smaller than the characteristic timescale of an unsteady flow.

The deviation from the quasi-steady description due to the unsteady effects is described by Equation 11.16. The variation $G' = G - \langle G \rangle_t$ in $[t_k, t_{k+1}]$ can be expressed approximately as $G' \approx (\Delta g_{k+1} - \Delta g_k) / \Delta T + \varepsilon - \langle \varepsilon \rangle_t$, where $\Delta g_{k+1} = g(t_{k+1}) - g(t_k)$ and $\Delta g_k = g(t_k) - g(t_{k-1})$. When the approximations $g' = g - \langle g \rangle_t \approx \Delta g_{k+1} / 2$ and $\varepsilon - \langle \varepsilon \rangle_t \approx 0$ in $[t_k, t_{k+1}]$ are used, Equation 11.16 is expressed as

$$G_2 + \hat{\tau}'_j \partial g_s / \partial x_j = 0, \quad (11.18)$$

where $G_2 = \Delta g_{k+1} - \Delta g_k + \hat{\tau}'_{j,s} \partial (\Delta g_{k+1} / 2) / \partial x_j$ and $\hat{\tau}'_j = \Delta T c_{ji} \tau'_i$. The unsteady effect is represented by G_2 . In a reduced case where $\Delta g_{k+1} = 0$ and $\Delta g_k = 0$, it is known that since $\hat{\tau}'_j = 0$ in $[t_k, t_{k+1}]$, the skin friction field in this interval is accurately described by the snapshot solution. Based on the described formulations, a two-step procedure is proposed for extraction of an unsteady skin friction field from a time sequence of PSP visualization images. The first step is obtaining snapshot skin friction fields ($\hat{\tau}_{j,s}$) in sequential intervals by solving Equation 11.17, which represents the quasi-steady state of the unsteady process. The variation fields ($\hat{\tau}'_j$) for the unsteady effect is subsequently obtained by solving Equation 11.18 at the corresponding intervals. A complete unsteady skin friction field then is reconstructed by superposition ($\hat{\tau}_j = \hat{\tau}_{j,s} + \hat{\tau}'_j$) in sequential intervals. An application of this procedure is described in Section 11.2.3 with an unsteady oscillating impinging nitrogen jet.

11.1.3 Measurements with Sublimating Coatings

Mass transfer visualizations can also be performed using sublimating coatings. Two types of sublimating coatings can be used. The first is a coating with varying

density where a molecule in the coating sublimates and the density change of the sublimating molecule is detectable. This approach to a sublimating coating was studied by Bouvier et al. [152] with a pyrene luminescent coating on a delta wing. In experiments, the Pyrene molecule sublimates while the thickness of the polymer coating remains unchanged. The change in Pyrene density in the coating is detected by measurements of luminescent intensity of the coating. The second type is a coating with varying thickness where the coating itself sublimates and the thickness change is measured. Since the thickness of the luminescent coating is proportional to the luminescent intensity of the excited coating, thickness change is detected by measurements of luminescent intensity. Naphthalene and acenaphthene are two sublimating chemicals that have been used for mass transfer measurements [153-156].

11.1.3.1 Coatings with Varying Density

When a flow is started suddenly at $t = t_0$, for a thin sublimating coating on a wall, the time rate of the mass of the species 1 per unit area is $\partial(\rho_{10} \omega_{1w} h) / \partial t = -\dot{m}_{1w,s} W(t; t_0, t_1)$, where $\dot{m}_{1w,s}$ is the steady-state mass diffusion flux, ρ_{10} is the density of a sublimating material in the solid state (or the saturated vapor state), and h is the coating thickness. Integration of this equation results in the relation $\dot{m}_{1w,s} = \Delta T^{-1} (\rho_{10} \omega_{1w} h)_{ref} \left[1 - \omega_{1w} h / \omega_{1w,ref} h_{ref} \right]$ in $[t_0, t_1]$, where $(\rho_{10} \omega_{1w} h)_{ref}$ is the reference value at $t = t_0$ for the wind-off reference condition and ΔT is a time interval. For an optically thin sublimating coating such as pyrene, the relative luminescent intensity of the coating is $I / I_{ref} = \omega_{1w} h / \omega_{1w,ref} h_{ref}$, where I_{ref} and $\omega_{1w,ref}$ condition, respectively. Equation 11.10 is then expressed as

$$g - I - D_{12} \Delta T \frac{\partial^2 g}{\partial X_i \partial X_i} + \frac{D_{12} \Delta T^2 \rho_w \tau_i}{\mu h_{ref} \rho_{10}} g \frac{\partial}{\partial X_i} \left(\frac{h_{ref}}{h} \right) + \frac{D_{12} \Delta T^2 \rho_w \tau_i}{\mu h \rho_{10}} \frac{\partial g}{\partial X_i} = 0 \quad (11.19)$$

where $g = I/I_{ref}$ is the normalized luminescent intensity. Equation 11.19 can be expressed in the image plane as

$$G + \hat{\tau}_j \partial g / \partial x_j = 0 \quad (11.20)$$

where $\hat{\tau}_j = (D_{12} \Delta T^2 \rho_w / h \mu \rho_{10}) \lambda h_{ji} \tau_i$ is the relative skin friction vector projected

onto the image plane with $G = g - I + \varepsilon_1 + \varepsilon_2$, where

$$\varepsilon_1 = -D_{12} \Delta T \lambda^2 h_{ji} h_{ji} \partial^2 g / \partial x_j \partial x_j \quad \text{and}$$

$$\varepsilon_2 = (D_{12} \Delta T^2 \rho_w / h_{ref} \mu \rho_{10}) g \tau_i \lambda h_{ji} \partial (h_{ref} / h) / \partial x_j. \quad \text{Since } \lambda \text{ is typically much}$$

smaller than 1, the higher order terms $\varepsilon_1 \sim \lambda^2$ and $\varepsilon_2 \sim \lambda^2$ can be neglected for a first-order approximation.

11.1.3.2 Coatings with Varying Thickness

For a thin sublimating layer on a wall, the time rate of the layer thickness h is $d(\rho_{10} h) / dt = -\dot{m}_{Iw,s} H(t - t_0)$, where ρ_{10} is the density of a sublimating material in the solid or saturated vapor state. Integration of this equation results in $\dot{m}_{Iw,s} = \rho_{10} (\Delta h / \Delta t)$, where $\Delta T = t_1 - t_0$, $\Delta h = h_{ref} - h$, and h and h_{ref} are the layer thicknesses at $t = t_1$ and $t = t_0$, respectively. The mass transfer coefficient is subsequently defined as

$$c_{Im} = \frac{\dot{m}_{Iw,s}}{\rho_w (\omega_{Iw,s} - \omega_{I\infty})} = \frac{\dot{m}_{Iw,s}}{\rho_w \omega_{Iw,s}} \quad (11.21)$$

where $\omega_{I_\infty} = 0$ for a vapor-free mainstream. Integrating the equation for the thickness and using the boundary condition $\rho_w = \rho_{I0}$, $\omega_{Iw,s} = c_{Im}^{-1} (\Delta h / \Delta t)$ is obtained.

Substitution of these relationships into Equation 11.10 leads to

$$-\Delta\bar{h} + \frac{D_{12}\tau_i}{\mu c_{Im}} \frac{\partial\Delta\bar{h}}{\partial X_i} + \frac{D_{12}}{h_0} \frac{\partial^2(h_0\Delta\bar{h})}{\partial X_i\partial X_i} + \frac{D_{12}\tau_i}{\mu c_{Im}} \frac{\Delta\bar{h}}{h_0} \frac{\partial h_0}{\partial X_i} + \frac{\tau_i}{\Delta t} \frac{\partial c_{Im}^{-1}}{\partial X_i} = 0 \quad (11.22)$$

where $\Delta\bar{h} = \Delta h / h_{ref} = 1 - h / h_{ref}$ represents the normalized thickness change. For image based measurements, the sublimating coating thickness is proportional to the radiance scattered from the coating, i.e., $h / h_{ref} = I / I_{ref}$. Equation 11.22 can then be expressed in the image coordinates, i.e.,

$$G + \hat{\tau}_j \partial g / \partial x_j = 0 \quad (11.23)$$

where $g = I / I_{ref}$ is the normalized image intensity, $\hat{\tau}_j = (D_{12} / \mu c_{Im}) \lambda h_{ji} \tau_i$ is the projected skin friction vector, $G = -g + I + \varepsilon_3$, and

$$\varepsilon_3 = -\frac{D_{12}\lambda^2 h_{ji} h_{ji}}{h_{ref}} \frac{\partial^2(h_{ref}\Delta\bar{h})}{\partial x_j\partial x_j} - \hat{\tau}_j \frac{\Delta\bar{h}}{h_{ref}} \frac{\partial h_{ref}}{\partial x_j} - \frac{\tau_i h_{ji} \lambda}{\Delta T} \frac{\partial c_{Im}^{-1}}{\partial x_j} \quad (11.24)$$

Since ε_3 is proportional to λ^2 and is usually significantly less than 1, ε_3 can be neglected for a first-order approximation.

11.1.4 Variational Solution for Skin Friction Fields

Equations 11.13, 11.17, 11.18, 11.20 and 11.23 can be expressed in a generic form given by

$$G + \hat{\tau}_j \partial g / \partial x_j = 0 \quad (11.25)$$

where G and $\hat{\tau}_j$ are defined before depending on the specific case of visualization and g is the normalized intensity (either $g = I_{ref} / I$ for PSP or $g = I / I_{ref}$ for sublimating coatings). Equation 11.25 has a similar form to the Horn-Schunck optical flow equation [24, 26]. Theoretically, if G and g are known from measurements, Equation 11.20 can be solved as an inverse problem for the skin friction vector $\hat{\tau}_j$. The following functional is minimized with the smoothness regularization term on an image domain Ω ,

$$J(\hat{\tau}) = \int_{\Omega} (G + \hat{\tau} \cdot \nabla g)^2 dx_1 dx_2 + \alpha \int_{\Omega} (|\nabla \hat{\tau}_1|^2 + |\nabla \hat{\tau}_2|^2) dx_1 dx_2 \quad (11.26)$$

which results in the Euler-Lagrange equations for $\hat{\tau} = (\hat{\tau}_1, \hat{\tau}_2)$, i.e.,

$$[G + \hat{\tau} \cdot \nabla g] \nabla g - \alpha \nabla^2 \hat{\tau} = 0 \quad (11.27)$$

where $\nabla = \partial / \partial x_i$, $\nabla^2 = \partial^2 / \partial x_i \partial x_i$, and α is the Lagrange multiplier. Once G is obtained from an image ratio field g , Equation 11.27 can be solved numerically imposing the Neumann condition $\partial \hat{\tau} / \partial n = 0$ on the image domain boundary. The mathematical analysis on the uniqueness and convergence of the solution of Equation 11.27 is given by Aubert et al. [145]. This approach allows for the extraction of a relative or normalized skin friction. The corresponding absolute skin friction field can be determined by in-situ calibration based on values obtained at several locations using a reliable point based technique such as the interferometric oil-film skin friction meter [20].

11.1.5 Uncertainty Analysis and Intrinsic Limitations

At this point it is necessary to evaluate the sensitivity of computing skin friction to the elemental errors. The decompositions $g = g_0 + \delta g$, $G = G_0 + \delta G$ and $\hat{\tau} = \hat{\tau}_0 + \delta \hat{\tau}$ are introduced, where δg , δG and $\delta \hat{\tau}$ are errors, and g_0 , G_0 , and $\hat{\tau}_0$ are

the non-perturbed fields that satisfy the Euler-Lagrange equations given by Equation 11.27. Substituting the decompositions described above into Equation 11.27 and neglecting the higher-order smaller terms, results in the error propagation equation

$$(\delta\hat{\boldsymbol{\tau}} \cdot \nabla g_0) \nabla g_0 - \alpha \nabla^2 \delta\hat{\boldsymbol{\tau}} = -(\delta G + \hat{\boldsymbol{\tau}}_0 \cdot \nabla \delta g) \nabla g_0 \quad (11.28)$$

where δG directly contributes to $\delta\hat{\boldsymbol{\tau}}$ while δg contributes to $\delta\hat{\boldsymbol{\tau}}$ through a gradient operator projected on the skin friction vector.

The analysis is simplified by considering a local region where ∇g_0 is a constant vector in a local linear approximation, and $\|\nabla g_0\|$ is the magnitude of ∇g_0 . The unit normal vector to an iso-value line $g_0 = \text{const.}$ is defined as $\mathbf{N}_T = \nabla g_0 / \|\nabla g_0\|$. The error of skin friction projected on \mathbf{N}_T is defined as $(\delta\hat{\boldsymbol{\tau}})_N = \delta\hat{\boldsymbol{\tau}} \cdot \mathbf{N}_T$. The relative error estimate is obtained by normalizing Equation 11.28 yielding

$$\frac{(\delta\hat{\boldsymbol{\tau}})_N}{\|\hat{\boldsymbol{\tau}}_0\|} = -\frac{\delta G}{\|\nabla g_0\| \|\hat{\boldsymbol{\tau}}_0\|} - \left(\frac{\hat{\boldsymbol{\tau}}_0}{\|\hat{\boldsymbol{\tau}}_0\|} \right) \cdot \delta \mathbf{N}_T + \frac{\alpha}{\|\nabla g_0\|^2} \nabla^2 \left[\frac{(\delta\hat{\boldsymbol{\tau}})_N}{\|\hat{\boldsymbol{\tau}}_0\|} \right] \quad (11.29)$$

where $\|\hat{\boldsymbol{\tau}}_0\|$ is a characteristic value of skin friction such as the mean value. In the derivation of Equation 11.29 it is assumed that ∇ and δ can be exchanged. The first term in the right-hand side (RHS) of Equation 11.29 is the contribution from the elemental error in measurement of the term G . The second term is the contribution from the elemental error in measurement of the surface gradient of the relative intensity. The third term is the contribution from the artificial diffusion of the error $(\delta\hat{\boldsymbol{\tau}})_N$ associated with the Lagrange multiplier. Equation 11.29 can be solved iteratively for the relative error $(\delta\hat{\boldsymbol{\tau}})_N / \|\hat{\boldsymbol{\tau}}_0\|$. The first two terms on the RHS of Equation 11.29 are used as an initial

approximation of $(\delta\hat{\tau})_N / \|\hat{\tau}_o\|$, and then it is substituted into the third term to estimate the diffusion term in the first-order approximation. Repeating this process, successive approximations can be obtained.

The first and third terms in the RHS of Equation 11.29 are proportional to $\|\nabla g_o\|^{-1}$ and $\|\nabla g_o\|^{-2}$, respectively. This indicates that the relative error $(\delta\hat{\tau})_N / \|\hat{\tau}_o\|$ will be large when $\|\nabla g_o\|$ approaches zero. This imposes an intrinsic limitation on application of this technique in certain regions where $\|\nabla g_o\|$ is close to zero. The proportional constant in the third term is $\alpha\|\nabla g_o\|^{-2}$. Therefore, the Lagrange multiplier α must be appropriately small to reduce the error $(\delta\hat{\tau})_N / \|\hat{\tau}_o\|$ particularly when $\|\nabla g_o\|$ is small in some regions. This requirement poses a dilemma since the error of the variational solution of Equation 11.26 increases as the Lagrange multiplier tends to zero in the fashion of $\delta / \sqrt{\alpha}$, where δ is a bound of the measurement error [157-158]. The convergence of the variational solution is ensured if the condition $\delta^2 / \alpha(\delta) \rightarrow 0$ is satisfied, indicating that the measurement error must be reduced as α decreases. For images with low signal to noise ratio, a Gaussian filter with a suitably large standard deviation is used to reduce random noise and ensure convergence of the solution.

11.2 Measurements with Pressure Sensitive Paint

The proposed mass-transfer method was applied to PSP visualizations in impinging nitrogen jets and colliding impinging nitrogen jets for steady-state measurements as well as an oscillating impinging nitrogen jet for unsteady measurements to evaluate its feasibility for global skin friction diagnostics.

11.2.1 Impinging Nitrogen Jets

Figure 11.2 is a schematic of the experimental setup for PSP visualizations for the impinging nitrogen jet. The nitrogen jet was delivered from a tube with a nozzle with an exit diameter (D) of 2 mm connected to a compressed nitrogen tank. The impingement base surface was a rectangular aluminum block with a flat upper surface onto which the jet impinged upon. The impingement surface was covered with a thin white Mylar adhesive sheet and coated with a PSP layer of approximately 20 μm thickness. PSP was prepared by mixing the pressure sensitive molecule, Bathophen Ruthenium Chloride ($\text{Ru}(\text{bpy})$) in GE RTV118 silicone. $\text{Ru}(\text{bpy})$ has an emission wavelength centered around 590 nm when excited by UV lamps [25]. PSP images were acquired using an ISG Lightwise CMOS camera with a 550 nm longpass filter to cut out the excitation source. The impingement zone was imaged without blocking the jet nozzle by viewing the surface at an oblique angle as illustrated in Figure 11.2.

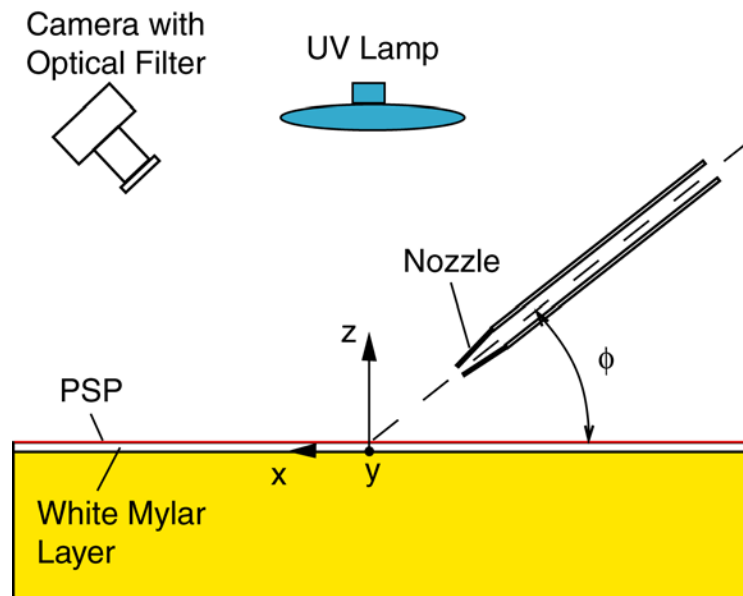


Figure 11.2 Experimental setup schematic for PSP visualizations for an impinging nitrogen jet

Image registration was performed based on four black fiduciary targets on the surface. The registered images were equivalent to viewing the impingement surface perpendicular from the top. The fiduciary targets also provided a reference for metric scaling. The impingement angle was adjustable and the ratio between the nozzle to surface distance and the nozzle diameter was fixed at H/D of 6, where H is the nozzle to surface distance and D is the nozzle exit diameter. The coordinate system in the impinging jet experiments is assigned such that x is the main streamwise coordinate, y is the transverse coordinate, and z is the normal coordinate to the wall. The exit jet velocity (U_0) was set at 50 m/s, and the corresponding Reynolds number based on the nozzle exit diameter (Re_D) was 6400. The free jet was laminar at the exit.

Measurements were conducted for a normal impinging jet and an oblique impinging jet. Figures 11.3 (a) and (b) are a typical luminescent intensity ratio image I / I_{ref} for PSP for the normal impinging jet and the extracted skin friction vector and magnitude fields normalized by the maximum skin friction value, respectively. The Lagrange multiplier, Gaussian filter and $I_{ref} / I_{00} - \varepsilon_0$ in G from Equation 11.13 were set at 0.00005, 9 pixels and 0.95, respectively. As discussed earlier, since I_{00} is position dependent setting $I_{ref} / I_{00} - \varepsilon_0$ as a constant is an approximation. Figure 11.4 is a plot of the skin friction magnitude distributions normalized by the maximum skin friction value along the x-axis for the normal impinging jet. Hot-film measurements obtained from the previous study of TSP based method were used for comparison together with the theoretical solutions given by Phares et al. [146] as plotted in Figure 11.4. The distributions obtained by the mass transfer method and hot-film measurements are consistent especially in the impingement region.

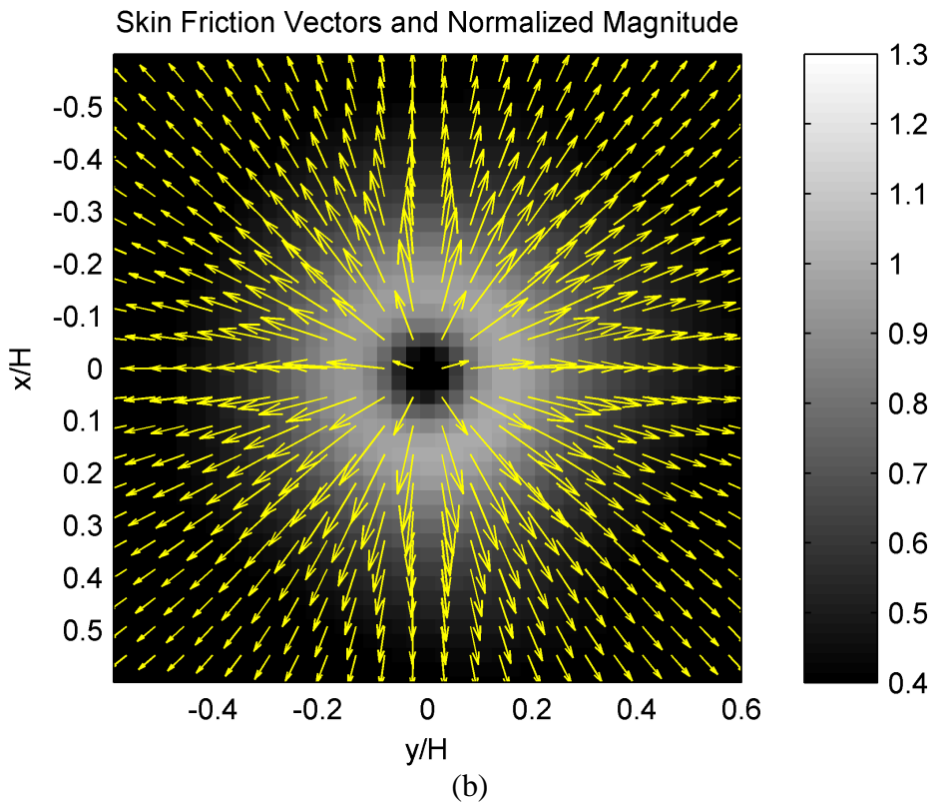
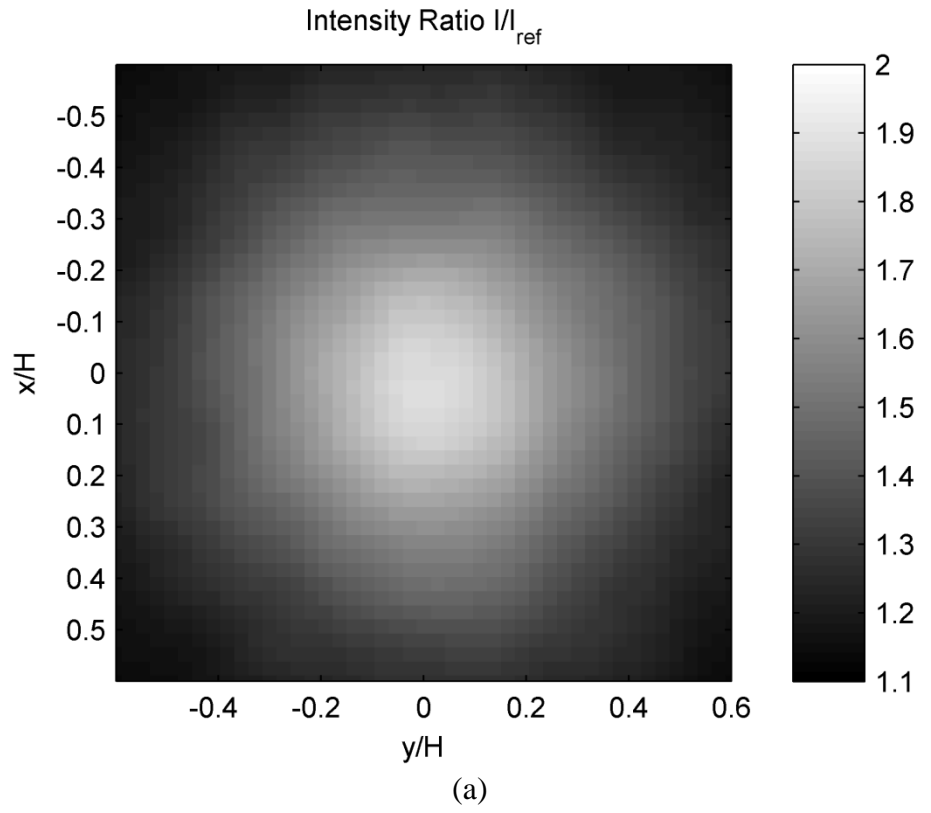


Figure 11.3 Plots of (a)PSP intensity ratio and (b)normalized skin friction vector and magnitude fields for a normal impinging jet

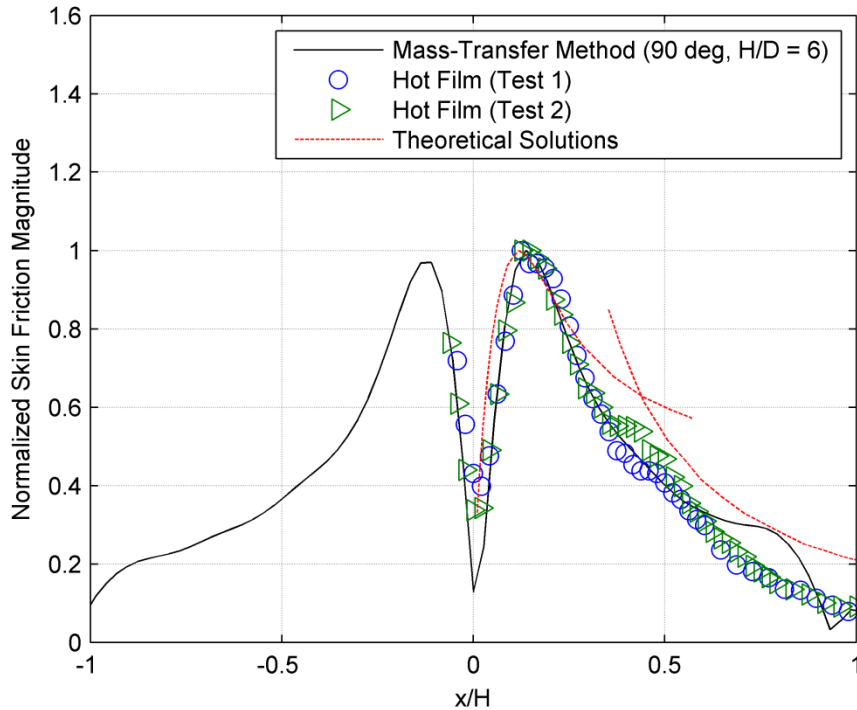


Figure 11.4 Skin friction magnitude distribution normalized by the maximum value along the x-axis for a normal impinging jet

Figures 11.5 and 11.6 are plots of the effect of the Lagrange multiplier on the extracted skin friction magnitude distribution. The root mean square (RMS) values between the results from the mass transfer method and the hot-film data are computed and normalized by the maximum value as a function of the Lagrange multiplier as shown in Figure 11.6. In interpreting Figure 11.6, there is an optimum value of the Lagrange multiplier at which the differences are at a minimum. The RMS values representing the difference between the results from the mass transfer method and hot-film data is shown to be sensitive to the Lagrange multiplier since its value is very small and the minimum difference range is narrow in this case. These observations are consistent with the uncertainty analysis.

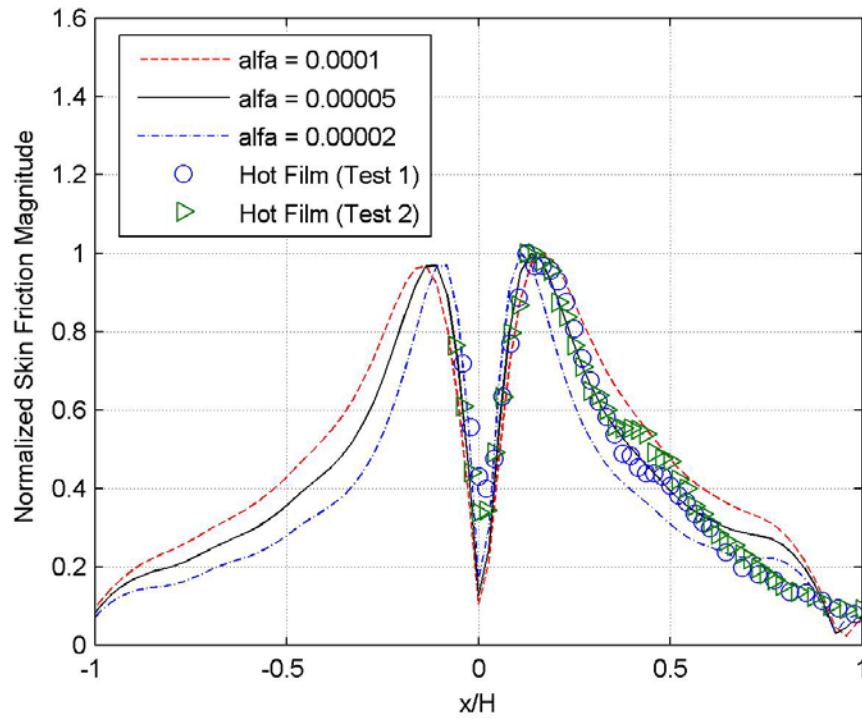


Figure 11.5 Effect of the Lagrange multiplier on the extracted skin friction magnitude distribution for a normal impinging jet

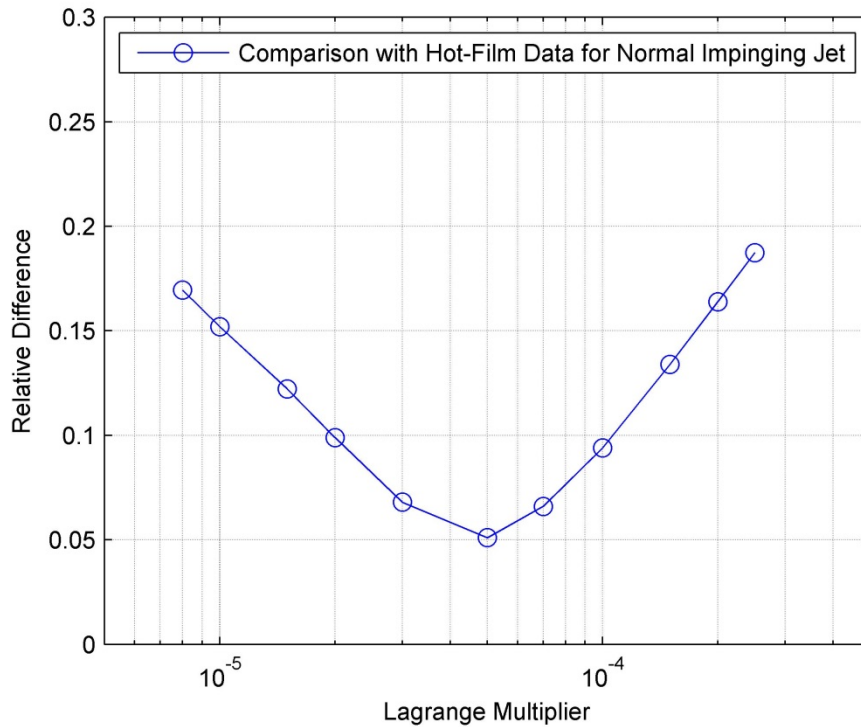
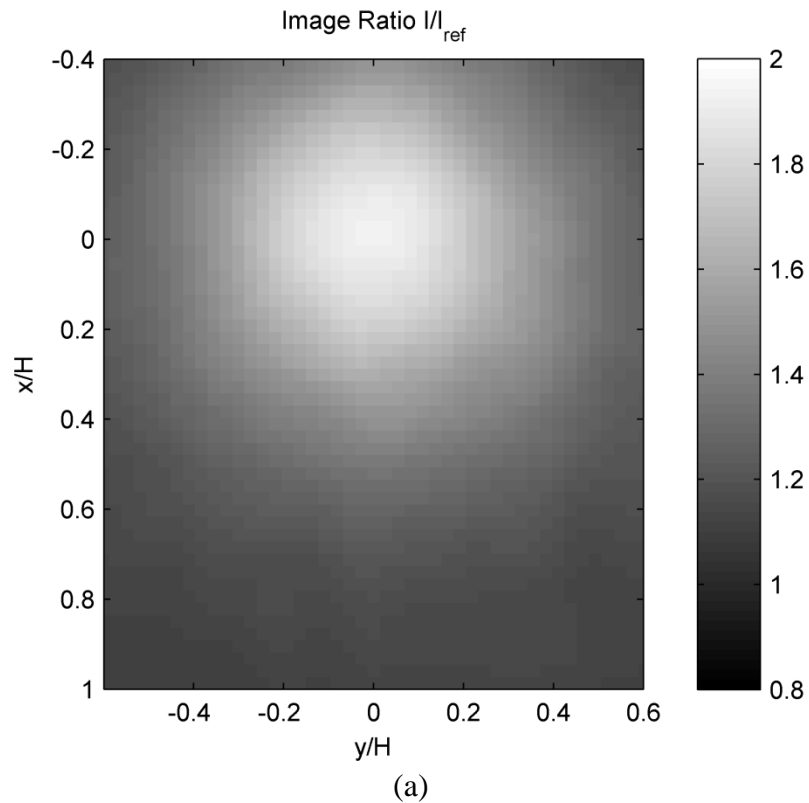


Figure 11.6 Relative difference between the extracted skin friction value and hot-film data as a function of the Lagrange multiplier for a normal impinging jet

Figures 11.7 (a) and (b) and 11.8 are plots of the PSP image intensity ratio, normalized skin friction vector and magnitude fields and skin friction magnitude distribution normalized by the maximum value along the x -axis for an oblique impinging jet at an impingement angle of 75° and height to surface and diameter ratio (H/D) of 6. The asymmetry of the skin friction field with respect to the x -axis is obvious. As observed in measurements using the TSP based method, a similar plateau between x/H of 0.4 to 0.7 that is associated with unsteady secondary separation induced by large vortical structures [30] is visible as highlighted in Figure 11.8. Figure 11.8 also shows that the skin friction distribution extracted using the mass transfer based method compares well with hot-film measurements in the impingement region of x/H between -0.5 and 0.5.



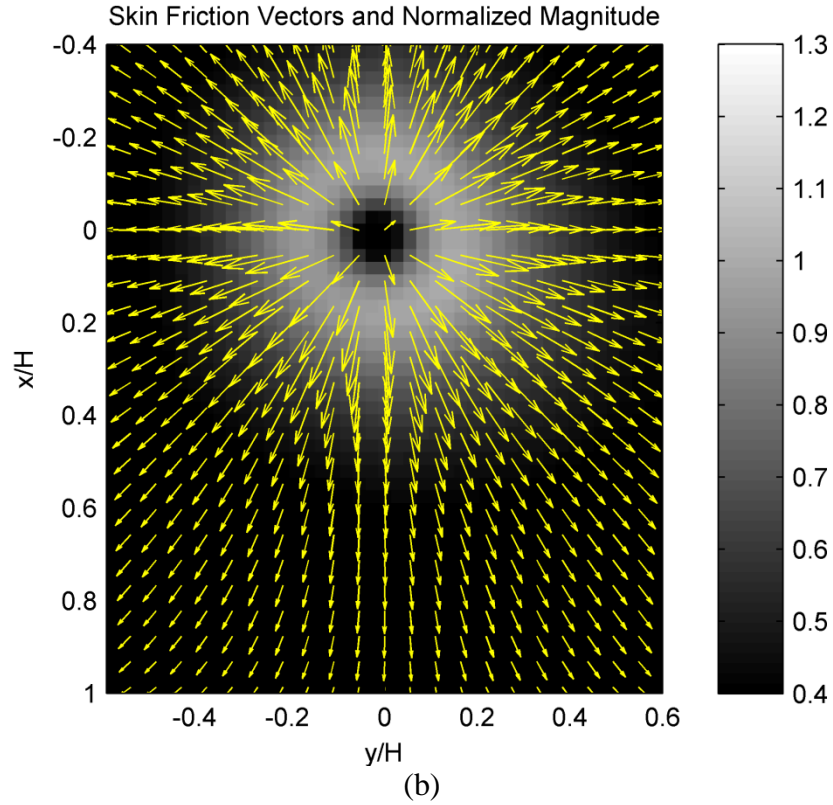


Figure 11.7 Plots of (a)PSP intensity ratio and (b)normalized skin friction vector and magnitude fields for an oblique impinging jet at an impingement angle of 75°

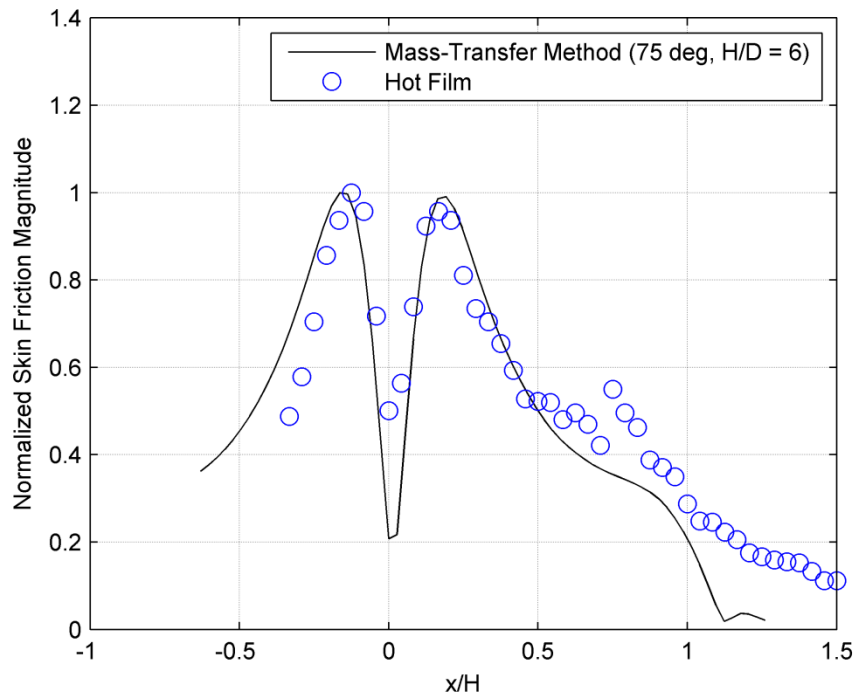


Figure 11.8 Skin friction magnitude distribution normalized by the maximum value along the x-axis in an oblique impinging jet at the impingement angle of 75°

11.2.2 Colliding Impinging Nitrogen Jets

The capability of the mass transfer method in extracting skin friction fields in more complex flows is evaluated by investigating dual colliding impinging jets using PSP visualizations. Figure 11.9 is a schematic of the experimental setup for the dual colliding impinging jets. Two nitrogen jets impinged upon the wall against each other from two tubes with an inner diameter (D) at an impingement angle of 30° . The nozzle to surface distance (H) was set at 29.5 mm and the distance between the exit centers of the two tubes along the x-axis was 80 mm. The offset between the two tubes along the y-axis was varied to generate different flow patterns. The nitrogen jet exit velocity was set at 4.14 m/s. The Lagrange multiplier, standard deviation of the Gaussian filter and $I_{ref} / I_{00} - \varepsilon_0$ were set at the same values as that for the single impinging jet.

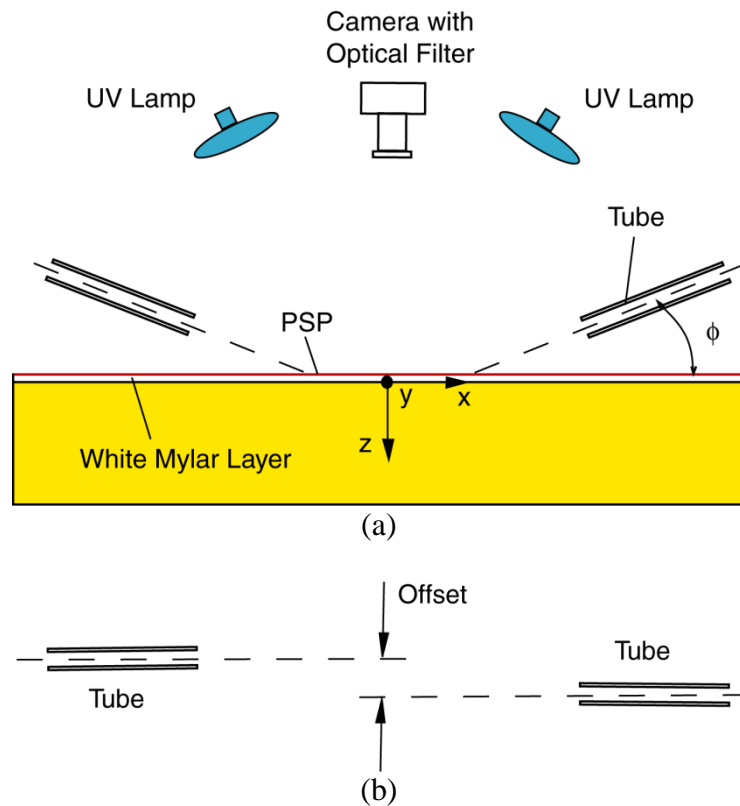


Figure 11.9 Experimental setup schematic for dual colliding impinging jets (a) side view and (b) top view

Figures 11.10, 11.11 and 11.12, (a), (b), (c) and (d) are images of the PSP intensity ratio (I/I_{ref}), skin friction vector and magnitude plots and skin friction line plots for the dual colliding impinging jets with offsets of 0 mm, 4 mm, 7.5 mm, and 11.5 mm, respectively.

For the head on impinging jets with 0 mm offset, the two wall-jets generated by the two impinging jets are deflected in the opposite directions along the y-axis around the x-coordinate of 0 as a result of the collision between the two impinging jets. This flow behavior is confirmed by the extracted skin friction vector and the magnitude fields in Figure 11.11 (a). The skin friction line plot in Figure 12 (a) confirms this observation. It is also observed that the impingement regions of the two jets are merged where only one node near x/H of 0.15 is observed in the proximity of right side jet.

The wall jets resulting from the impinging jets offset at 4mm are deflected at an angle of 25° relative to the y-axis as illustrated by Figure 11.10 (b). The extracted skin friction vector and line plots in Figures 11.11 (b) and 11.12 (b), respectively, indicate that the two nodes associated with the stagnation point in the impingement region are distinctly separated and a saddle is present between them. A saddle-node combination represents the typical closed flow separation as described by Surana et al. [42] and Tobak et al. [44]. As the offset is increased to 7.5 and 11.5 mm, the distance between the two nodes is increased while the saddle remains at the center between them as illustrated in Figures 11.12 (c) and 11.12 (d).

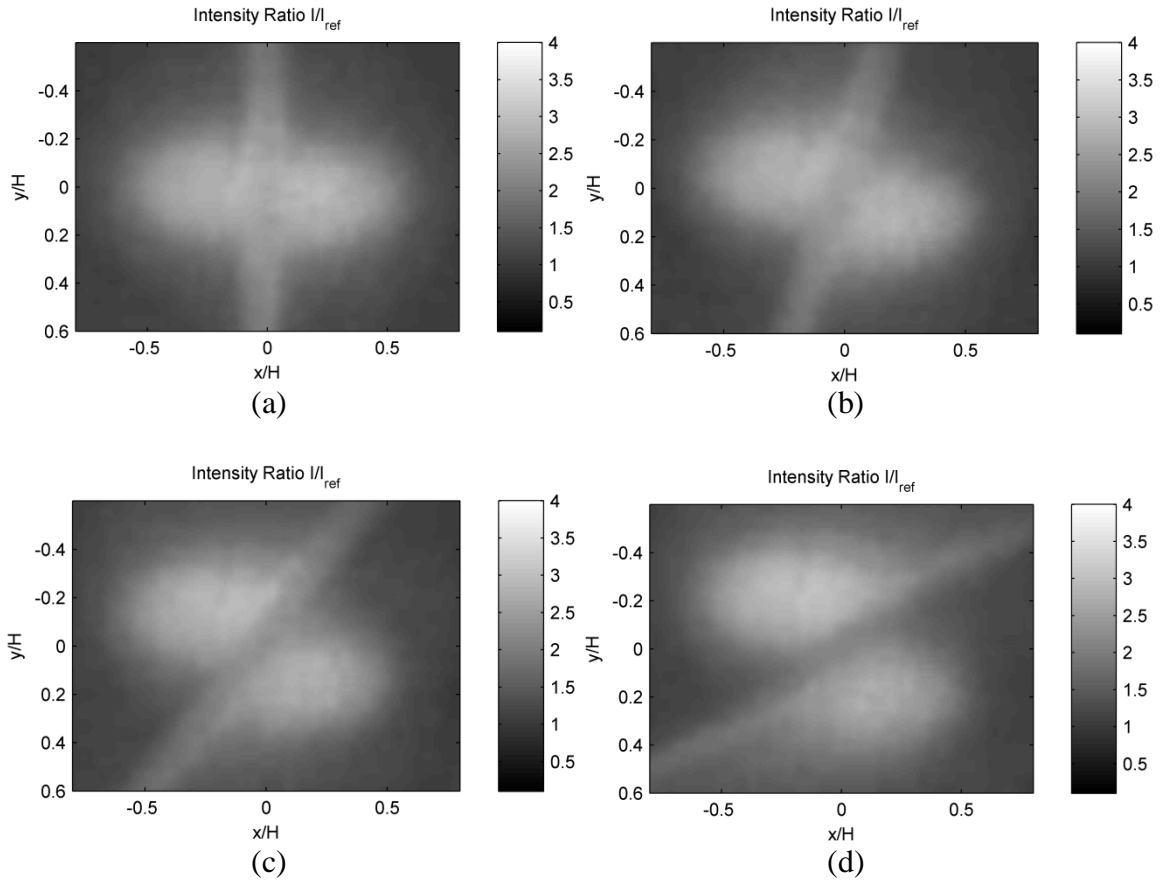


Figure 11.10 PSP intensity ratio images for dual colliding impinging jets at offsets of (a)0 mm, (b)4 mm, (c)7.5 mm and (d)11.5 mm

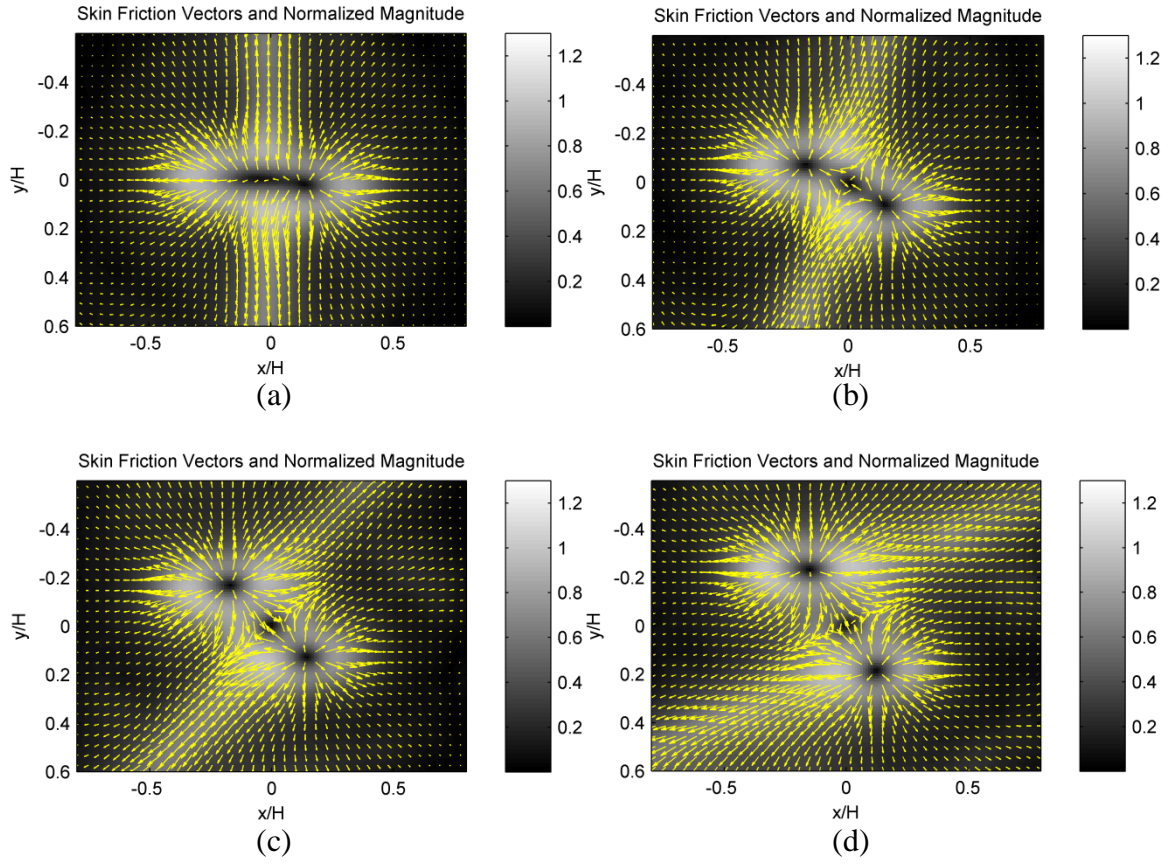


Figure 11.11 Plots of skin friction vectors and normalized magnitude fields for dual colliding impinging jets at offsets of (a)0 mm, (b)4 mm, (c)7.5 mm and (d)11.5 mm

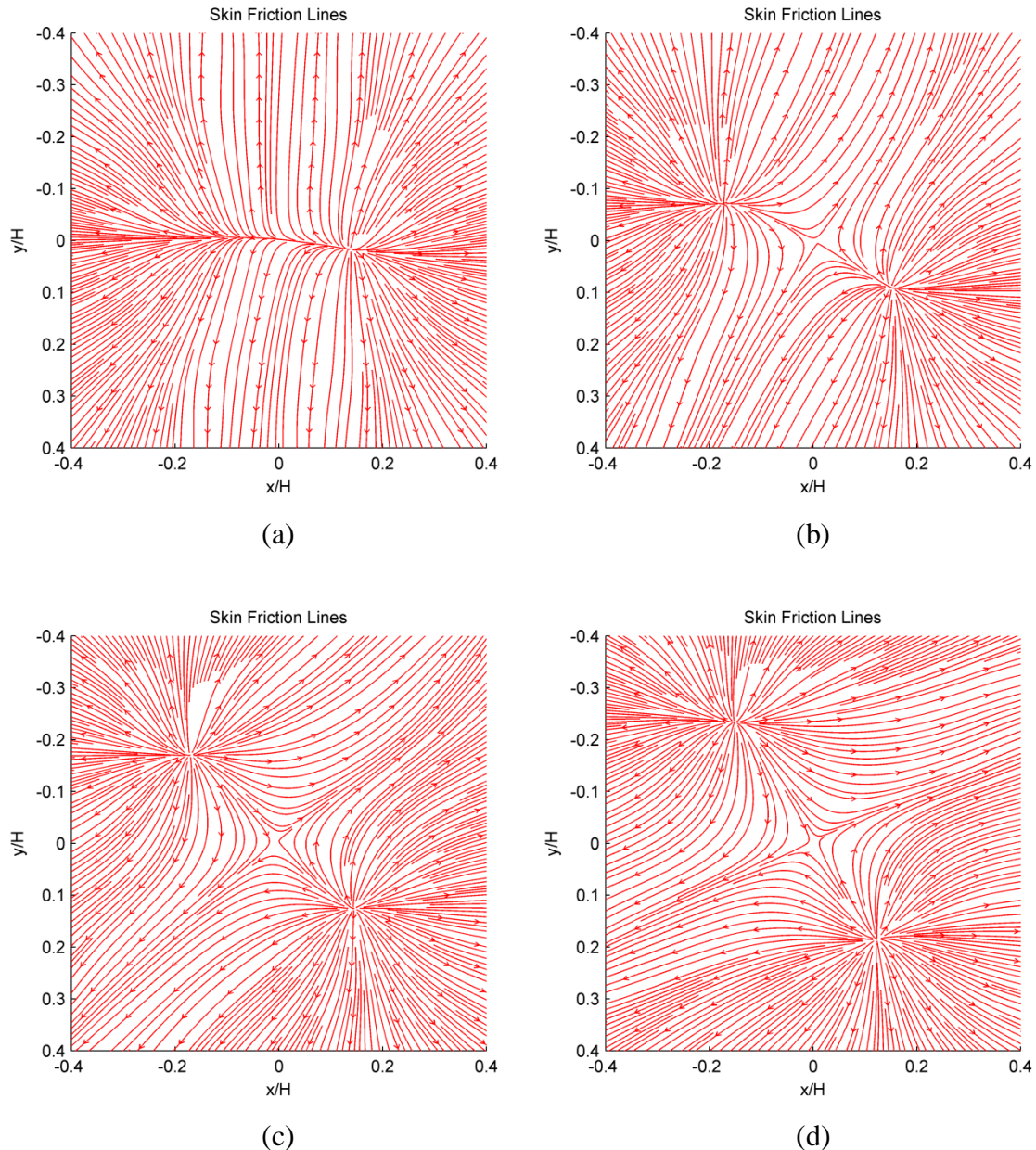


Figure 11.12 Plots of skin friction lines for dual colliding impinging jets at offsets of (a)0 mm, (b)4 mm, (c)7.5 mm and (d)11.5 mm

11.2.3 Oscillating Impinging Nitrogen Jet

The application of the mass transfer based approach to unsteady global skin friction diagnostics is evaluated using the two-step procedure for reconstruction of an unsteady skin friction field using a time-sequence of phase-averaged PSP images in a 9.4-kHz oscillating jet from a microfluidic oscillator. Anodized aluminum PSP was used for

time-resolved measurements due to its fast response time. Although the nozzle of the jet was set nominally parallel to the flat plate, it is believed that there was a small impingement angle since it was difficult to align a device on that scale to the flat plate. The description of the experiments is given by Gregory et al. [159]. The flow rate was set at 550 ml/min corresponding to a gauge pressure of 6.69 kPa. A total number of 42 flow-on phase-averaged images were processed at a time interval of 5 μs using the optical flow algorithm with the same parametric values used for the nitrogen jet impingement experiments in Sections 11.2.1 and 11.2.2. Figures 11.13 (a), (b) and (c) are the intensity ratio images of PSP at 0 μs , 20 μs and 40 μs .

Utilizing the procedure described in Section 11.1.2.2, a snapshot field ($\hat{\tau}_{j,s}$) is first obtained by solving Equation 11.17, and the variation field ($\hat{\tau}'_j$) is subsequently determined by solving Equation 11.18. Figure 11.14 are skin friction vector and normalized magnitude for the snapshot and variation fields at 0 μs , respectively. The mean magnitude of the variation field is approximately 7% of the snapshot field. The complete unsteady skin friction field is reconstructed by superposition of the snapshot and variation fields described by $\hat{\tau}_j = \hat{\tau}_{j,s} + \hat{\tau}'_j$. Figures 11.15 (a), (b) and (c) show the reconstructed skin friction vector and normalized magnitude fields at instances of 0 μs , 20 μs and 40 μs , respectively. In some instances, the oscillating impinging jet exhibits complex skin friction topological structures such as local instantaneous flow separation and reattachment as illustrated in Figure 11.15 (c).

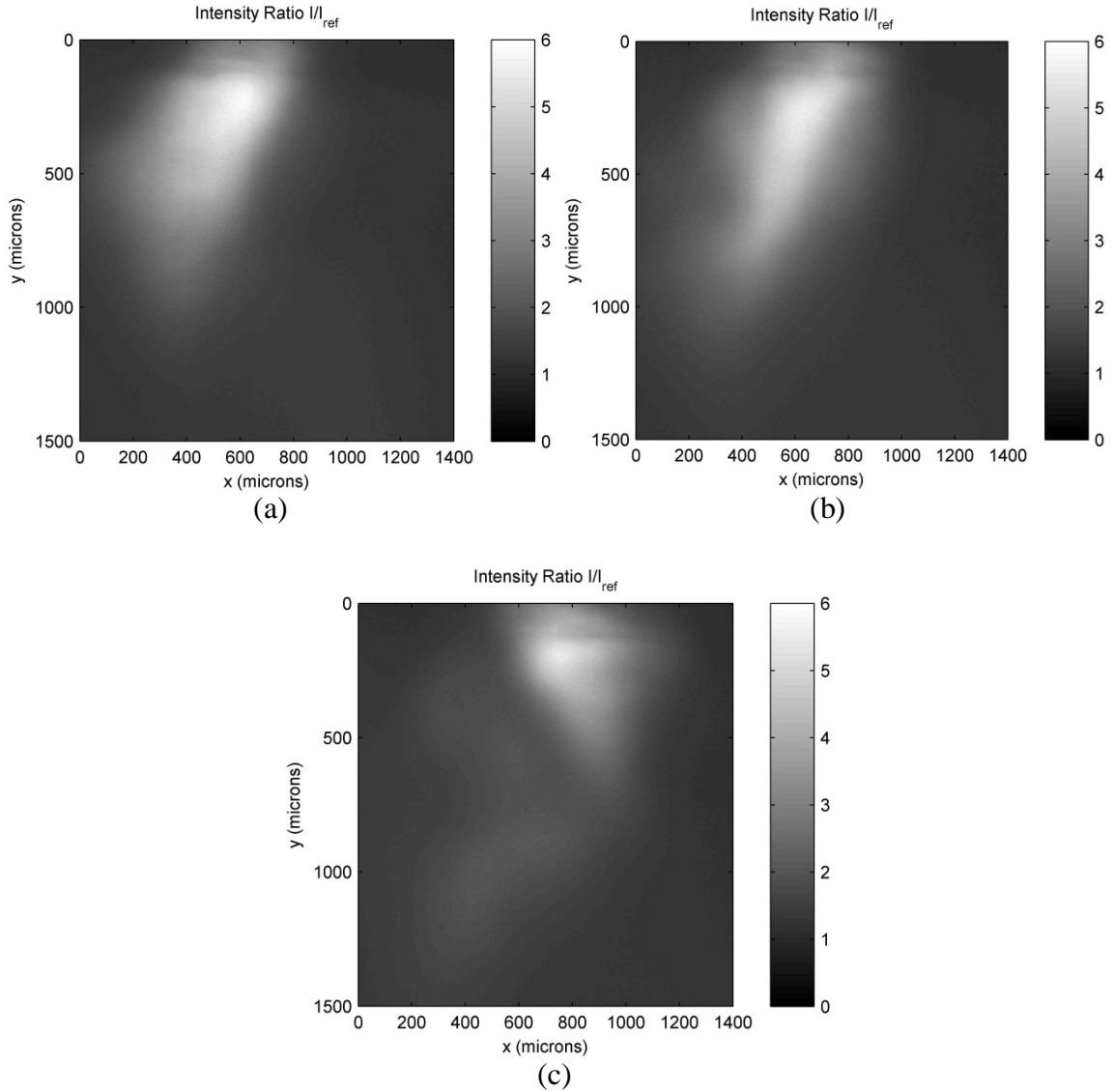


Figure 11.13 Normalized PSP intensity images for a 9.4-kHz oscillating impinging jet from a microfluidic oscillator at (a) $0 \mu\text{s}$, (b) $20 \mu\text{s}$ and (c) $40 \mu\text{s}$ [159]

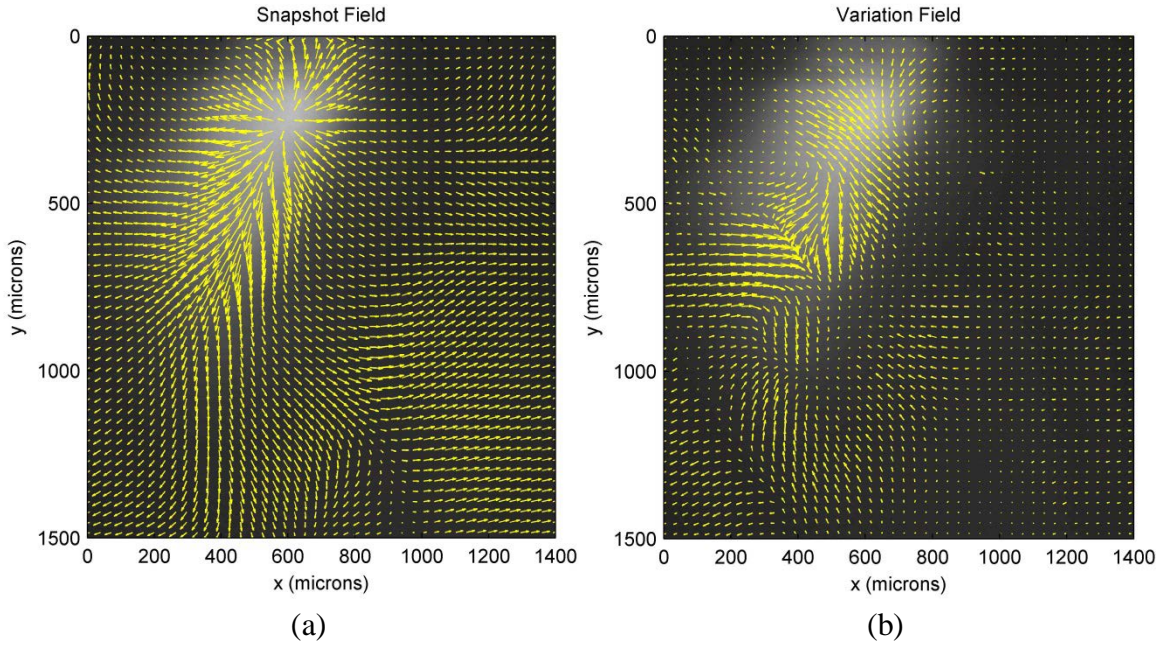
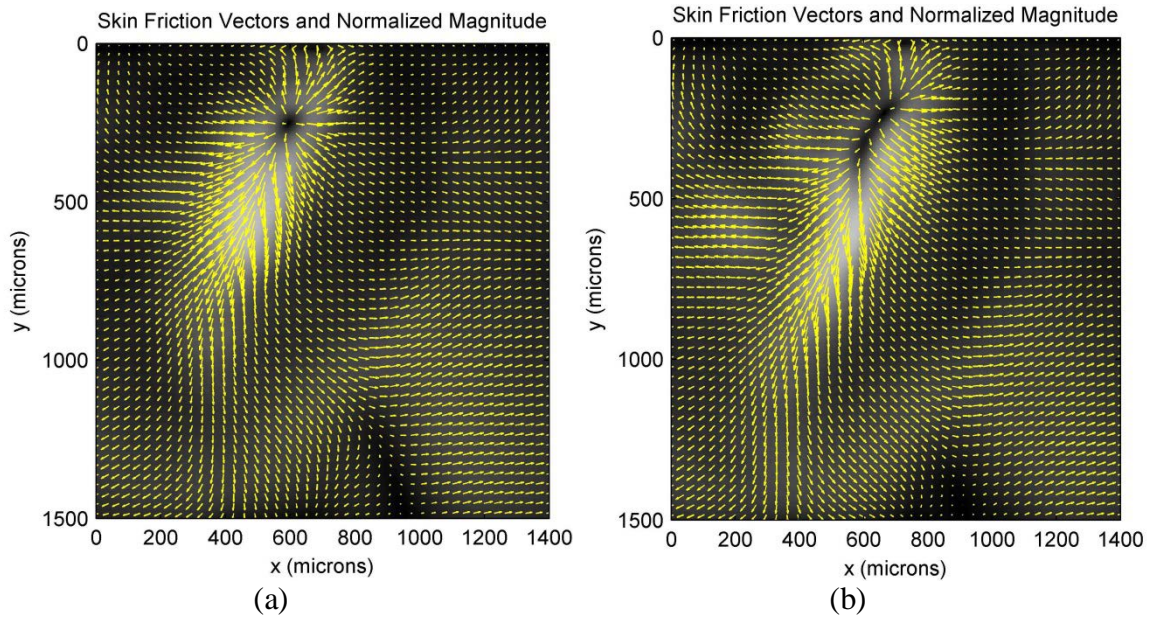


Figure 11.14 Solutions for (a)the snapshot field and (b)variation field in a 9.4-kHz oscillating impinging jet from a microfluidic oscillator at 0 μ s.



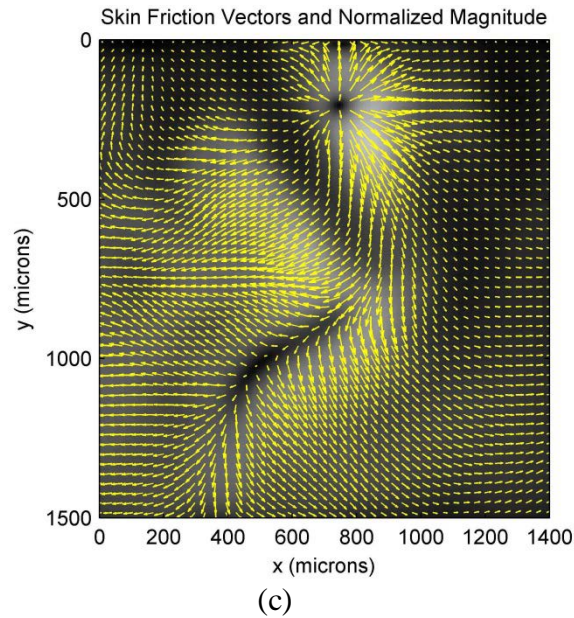


Figure 11.15 Plots of extracted skin friction vector and normalized magnitude fields in a 9.4-kHz oscillating impinging jet from a microfluidic oscillator at (a)0 μs , (b)20 μs and (c)40 μs

11.3 Measurements with Sublimating Coatings

Sublimating coatings have previously been used for mass transfer measurements in complex flows. Bouvier et al. [152] have performed sublimating coating visualizations for the upper surface of a 75° delta wing. Carbonaro et al. [160] have also performed sublimating coating visualizations for a shock/boundary layer interaction for a triangular fin on a flat plate. The images obtained from the visualizations performed Bouvier and Carbonaro will be used for the application of the varying density and varying thickness sublimating coating approaches, respectively.

11.3.1 Delta Wing

Sublimation visualization image obtained by Bouvier et al. [152] using Pyrene in GE RTV 118 on the upper surface of a 75° delta wing will be processed to extract a relative skin friction field using the varying density sublimating coating approach described in Section 11.1.3.1. The experimental setup was initially used to conduct

surface pressure measurements on the upper surface of the delta wing. The drawback of using Pyrene as an oxygen sensor is that it has a tendency to evaporate. From the perspective of this study, this characteristic of Pyrene is advantageous for mass transfer visualizations. Bouvier's tests were performed on a 75° delta wing with a root chord of 0.5 m at 25 m/s in a low speed wind tunnel. Figure 11.16 (a) shows a Pyrene sublimation mass transfer visualization image on the upper surface of the delta wing at an angle of attack of 32° , where the coordinates are normalized by the wing span (b). Observing Figure 11.16 (a) closely, the flow appears to be tripped by a roughness spot forming a curved turbulent wedge near the centerline at the chordwise normalized position (x/b) of -0.5.

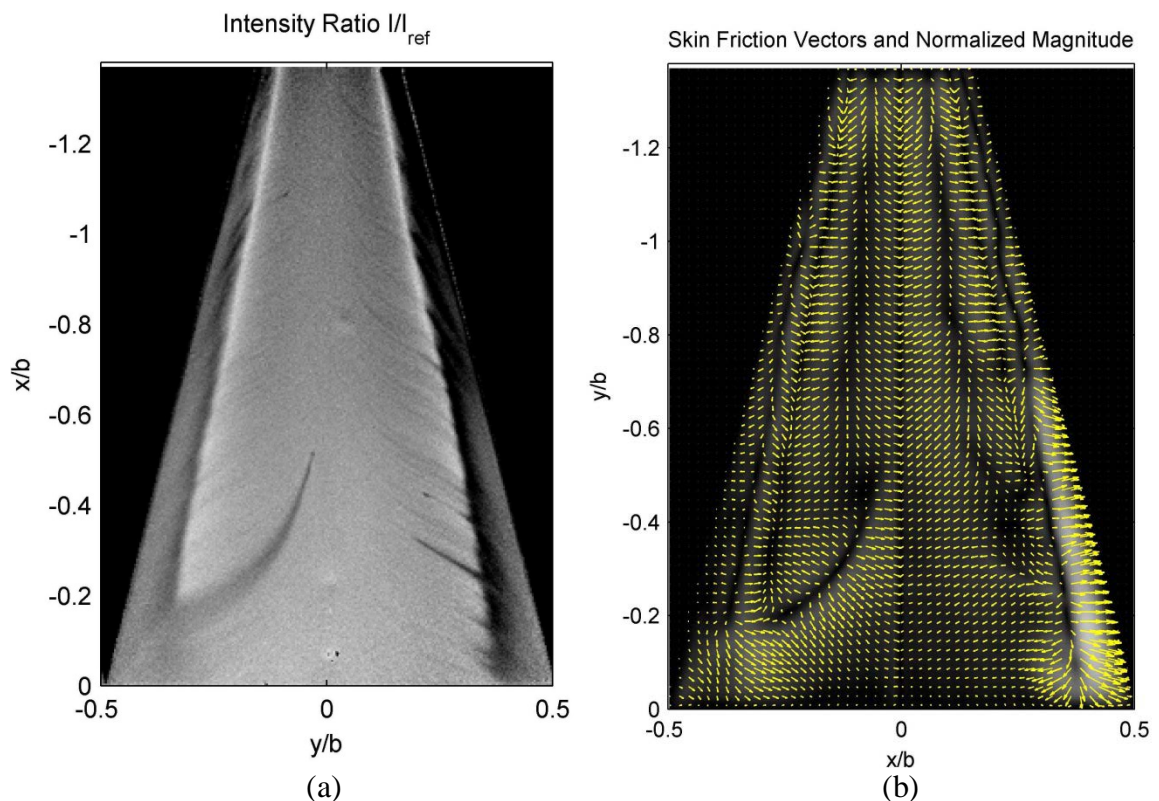


Figure 11.16 Plots of (a) sublimation image and (b) extracted skin friction vector and magnitude fields on the upper surface of a 75° delta wing at an angle of attack of 32° [152]

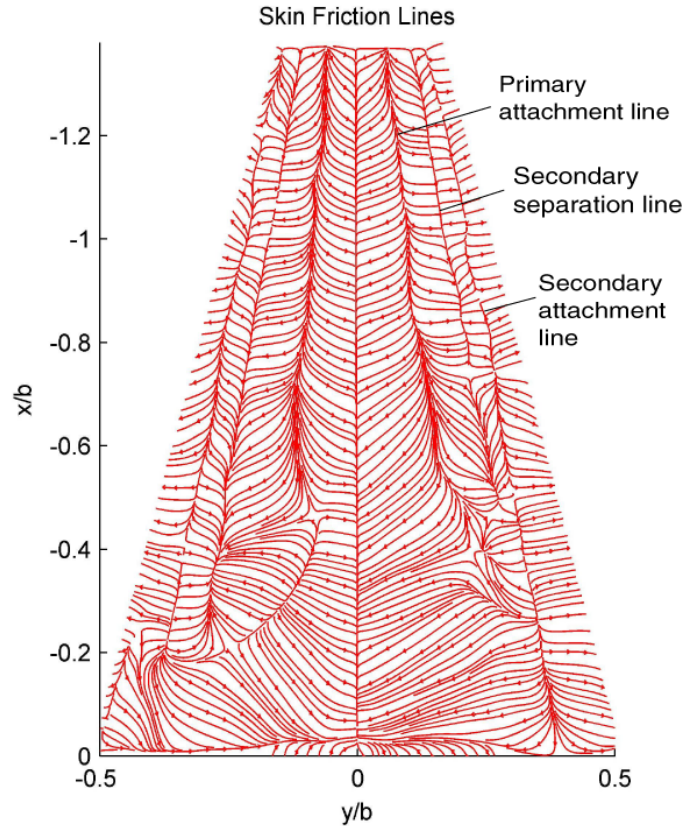


Figure 11.17 Skin friction line plot of the upper surface of a 75° delta wing at an angle of attack of 32° [152]

For these tests, the thickness of the Pyrene PSP coating remains constant while the Pyrene density is reduced. For optical flow computations, $G = g - I$ is used from Equation 11.20 where the terms ε_1 and ε_2 were neglected. The Lagrange multiplier was set at 0.001. It is observed from Figure 11.16 (a) that the image intensity gradient $\|\nabla g_0\|$ in the large area of the middle section of the wing in Figure 11.16 (a) is small and affects optical flow computation that is sensitive to noise in that region as described by the uncertainty analysis. As a direct result when the complete image was processed, the extracted primary reattachment lines near the centerline of the wing were not as well defined as the secondary separation and reattachment lines near the wing leading edges where the intensity gradient was large. A practical solution is processing the left and

right halves of the wing independently and subsequently fusing them together afterwards. This solution imposes a certain axis-symmetrical constraint on the skin friction field at a cost of generating a small discontinuity at the centerline. Figure 11.16 (b) illustrates the skin friction vector and normalized magnitude fields. The skin friction line plot shown in Figure 11.17 highlights the detailed topological structures associated with the leading edge vortex and the associated secondary vortices as visualized by the primary and secondary reattachment lines and secondary separation lines. The primary reattachment lines on both the left and right sides of the wing terminate at the chordwise location (x/b) of -0.5 which indicates breakdown of the leading edge vortices. The topological structures observed in the skin friction line plot is similar to that on a 65° delta wing extracted using the GLOF technique [85]. An interesting observation is that the transition wedge generated by the roughness spot is mistakenly identified as a reattachment line where the skin friction magnitude is small. Based only on the spatial intensity change without suitable constraints, this method is not able to automatically distinguish between a transition line and a separation or reattachment line which is a shortcoming of this method.

11.3.2 Shock/Boundary-Layer Interaction

Sublimation visualization images obtained by Carbonaro et al. [160] using a mixture of acenaphthene and diethylether will be processed to extract a relative skin friction field using the varying thickness sublimating coating approach described in Section 11.1.3.2 for experiments on a flat plate in shock/boundary-layer interaction over a vertically-mounted triangular fin with a leading edge sweep angle of 70° at an angle of attack of 40° and flow speed of Mach 6 [160-162]. The thickness of the sublimating

coating is reduced due to mass transfer. For optical flow computations, $G = -g + I$ is used from Equation 11.23 where the term ε_3 was neglected, and the Lagrange multiplier was set at 0.001.

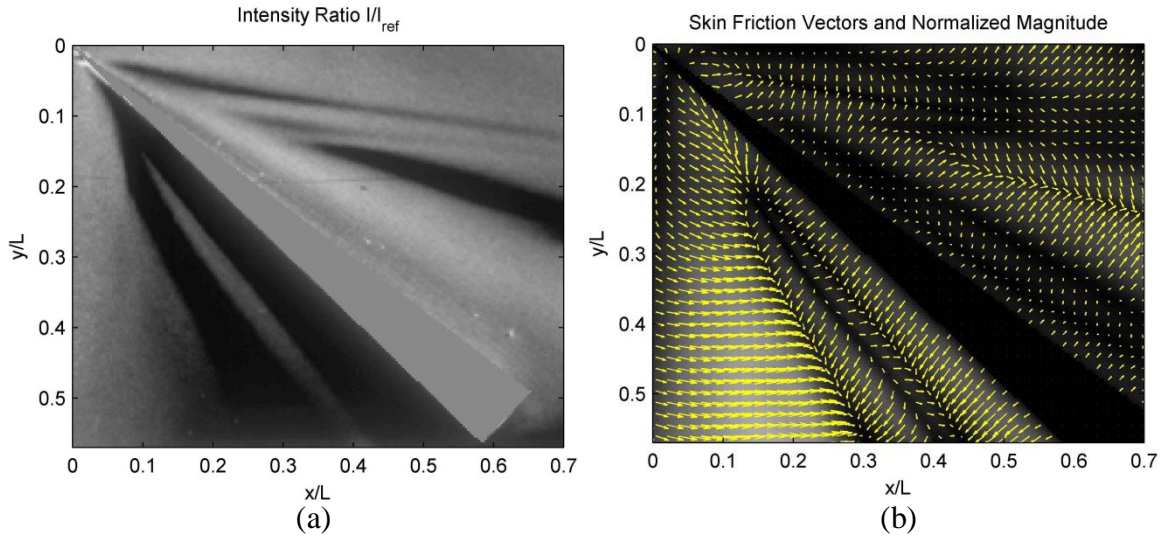


Figure 11.18 Plots of (a) sublimation image and (b) extracted skin friction vector and magnitude fields on a flat plate in shock/boundary-layer interaction over a vertically-mounted triangular fin at an angle of attack of 40° at Mach 6 (flow from left to right) [160]

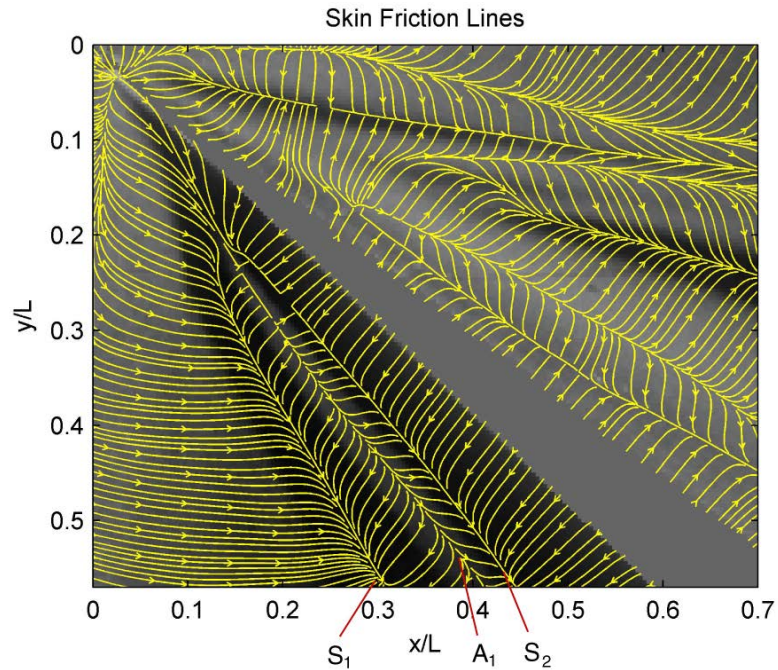


Figure 11.19 Skin friction lines extracted from the sublimation image on a flat plate in shock/boundary-layer interaction over a vertically-mounted triangular fin at an angle of attack of 40° at Mach 6 (flow from left to right) [160]

The skin friction topology is clearly illustrated by the skin friction line plot in Figure 11.19. On the pressure side of the fin where strong shock/boundary-layer interaction occurs, the primary and secondary separation lines (S_1 and S_2) and reattachment line (A_1) between them are distinctly identified. These topological structures are similar to observations in CFD simulations and surface oil streak visualizations at an angle of attack of 30.6° and flow speed of Mach 4 [125]. On the leeward side, the boundary layer interacts with the expansion waves and separated flow from the leading edge of the triangular fin. These complex interactions are clearly visualized in the skin friction line plot by the multiple separation and reattachment lines.

11.4 Summary

The development of a method for global skin friction diagnostics using surface mass transfer visualization images is established from the asymptotic form of the mass transport equation at a wall. The generalized optical flow equation relating a relative skin friction vector with the image intensity is derived for surface mass transfer visualizations with PSP and sublimating coatings. Solving the optical flow equation as an inverse problem via the variational method, a steady-state skin friction field can be extracted from a single normalized intensity image in both PSP and sublimation visualizations. Additionally, an unsteady skin friction field from a time sequence of PSP visualization images can be reconstructed. This is done by solving for a snapshot or steady-state solution in a small interval under the quasi-steady approximation, and then solving for a variation field in the same interval. An unsteady skin friction field can subsequently be reconstructed by superposition of the snapshot and the variation solutions in sequential intervals. The uncertainty analysis of the method indicates that the relative error in

optical flow computation can be significant when the image intensity gradient is small. This imposes an intrinsic limitation on the application of this method in regions where the image intensity gradient is close to zero.

The method was validated by applying it to PSP visualizations for an impinging nitrogen jet, where the steady-state skin friction fields were extracted. The normalized skin friction distributions along the transverse line across the jet were consistent with data obtained by using a hot-film sensor. The capability of the method was also tested by successful extraction of skin friction fields in a more complex impinging jet case of dual colliding impinging nitrogen jets. The capability of the developed approach was also tested for unsteady skin friction diagnostics demonstrated in PSP visualizations for an oscillating impinging nitrogen jet.

The application of the method to sublimation visualizations on the upper surface of a 75° delta wing at an angle of attack of 32° in a low speed flow is investigated. The extracted skin friction field clearly shows the primary and secondary reattachment lines and secondary separation lines associated with the leading edge vortices. Additionally, the skin friction field is extracted from sublimation visualization image on a flat plate in shock/boundary-layer interaction over a vertically-mounted triangular fin with a leading edge sweep angle of 70° at an angle of attack of 40° and flow speed of Mach 6. The primary and secondary separation lines and reattachment line on the pressure side of the fin are identified, and is qualitatively consistent with the observations from the previous CFD simulations and oil streak visualizations in similar cases. This method is advantageous from the perspective of its rigorous theoretical foundation and simplicity in application to images obtained in conventional surface mass transfer visualizations.

CHAPTER 12

CONCLUSIONS

This work can be broadly classified into three sections. The first is the discussion on background of skin friction measurements, topological studies and development and of the global luminescent oil film skin friction meter (GLOF) technique. The second and third sections are measurements of complex separated flows and the development of new global skin friction diagnostics approaches, respectively.

It has been established in the introductory material that the ability to quantitatively measure skin friction on a global scale (infinite number of points limited by optical resolution) is a highly desirable capability which will enable the characterization and understanding of near surface flow topology for complex separated flows. This capability will aid in understanding classical separated flows as well as aid in design applications focused on flow control. The GLOF technique was introduced as a global skin friction diagnostics approach. The detailed derivation of the technique was described along with an uncertainty analysis. It was found that the intensity gradient was a critical parameter which contributed to large error propagation if it was sufficiently small. The effect of a thin oil film on a model surface to the flow characteristics was also evaluated analytically. It was found that between subsonic to low supersonic speeds the presence of the oil film would not cause any adverse effects to the flow characteristics although at higher flow speeds in the high supersonic to hypersonic range, the presence

of an oil film might cause the separation location to change in a small acceptable range for flow visualizations. The measurement system for the GLOF technique was also described for applications in wind tunnel testing detailing luminescent oil preparation and application to a model surface, image acquisition setup and the data reduction procedure to extract global skin friction fields. Once the skin friction fields were extracted using the GLOF technique, topological analysis was conducted to verify the consistency of extracted skin friction fields and also for identification of critical points and features such as separation and reattachment lines which contribute towards understanding flow separation. Topological constraint analysis was performed using the Poincare-Bendixson index formula which describes the conservation of isolated singular points and boundary switch points.

A refinement was also carried out for several components of the GLOF technique i.e., data reduction, luminescent oil, UV excitation and oil film application. A complete set of MATLAB programs were developed for processing raw images of oil film development to extract skin friction fields along with a post processing program to generate plots of the extracted data. A number of luminescent dyes were also evaluated and the best candidate was identified based on the ease of preparation as well as the emission spectrum characteristics. Two excitation sources were also evaluated – UV blacklight lamps and a UV LED array and it was found that each source was appropriate for different test cases. The application of the luminescent oil onto the model surface was studied for three different methods, application by a bristle brush, foam brush and automotive paint spray gun. It was found that for smaller model surfaces, the brush was sufficient to ensure uniform oil film application but for larger model surfaces, the spray

gun approach was required to ensure uniform oil film application. A parametric analysis of data reduction variables was conducted to characterize the sensitivity of the GLOF technique to associated data reduction variables. It was found that time step and spatial resolution are sensitive parameters that have to be selected with care to ensure that appropriate results are obtained from the data reduction routine. Application of a Gaussian filter to the raw luminescent oil images also affects the calculated skin friction values and image file format and Lagrange multiplier selection appear to be the least sensitive parameters in the GLOF technique.

Global skin friction measurements were conducted for five complex separated flows – a low aspect ratio wing, delta wings, wing-body junction flow, cylindrical junction flows and an Ahmed model. For the low aspect ratio wing, the evolution of the skin friction fields as the angle of attack was varied was studied. The complex three dimensional separated flows were visualized from the global skin friction fields extracted using the GLOF technique. The consistency of the extracted skin friction fields was also validated using the Poincare-Bendixson (P-B) index formula. For the investigation of delta wings, GLOF measurements were performed on a 65° delta wing and a $76/40^\circ$ double delta wing with juncture fillets for different yaw and roll angles. The complex skin friction fields related to the generation of the leading edge vortex along with the complex vortex interactions originating from the juncture fillets and asymmetric vortex breakdown due to yaw and roll were captured. Topology constraint analysis was also performed using the P-B index formula and the consistency of the extracted skin friction fields was validated. Skin friction fields were also extracted for a wing-body junction flow along with the development of a 3D mapping approach to map skin friction vectors

from the image plane to a 3D model surface in the object space. The complex skin friction vector fields for the wing-body junction flows were successfully extracted and mapped onto the 3D model of the wing-body junction. The complex flows associated with the horseshoe vortex formed on the base surface of the model along with the wing tip vortex formed due to the pressure differences on the suction and pressure sides of the wing were clearly visualized in the extracted skin friction fields. The final measurement case using the GLOF technique was a combined global skin friction and surface pressure measurement study for a square and diamond cylinder junction flows and an Ahmed body. The study revealed the complex separated flow structures through the extracted skin friction fields and surface pressure measurements using pressure sensitive paint which revealed the stagnation, separation and reattachment regions.

Two approaches for global skin friction diagnostics were also developed. The first was a global skin friction diagnostics approach based on surface temperature measurements developed from the asymptotic form of the energy equation at a wall providing a relationship between the skin friction vector, heat flux and temperature at a wall. The resulting equation had the same form as the physics based optical flow equation and was solved using the variational method. This approach was shown to be feasible for global skin friction diagnostics through measurements of impinging jets compared with hot-film measurements and theoretical solutions. The second approach was based on surface mass transfer visualizations. The theoretical foundation of the approach was based on the asymptotic mass transport equation at a wall expressing the relationship between the skin friction vector, mass transfer flux and relative density of a particular species at a wall. The resulting equation had the same form as the physics

based optical flow equation and was solved using the variational method. Similar to the surface temperature based approach, the mass transfer based approach was shown to be feasible for global skin friction diagnostics through measurements of impinging jets compared with hot-film measurements and theoretical solutions.

In summary, this study has introduced a global skin friction diagnostic technique known as the global luminescent oil film skin friction meter. The complete derivation of the technique, uncertainty analysis and measurement system description was provided. A complete set of MATLAB data reduction routines were developed and a systematic study was conducted on selection of appropriate luminescent dyes, UV excitation sources and oil film application techniques. The technique was successfully used to performed measurements of global skin friction fields in complex separated flows. An approach to map the skin friction vectors from the image plane to a 3D model surface in the object space was developed and successfully applied. The topological analysis of the skin friction fields was carried out to understand the associated separated flow topology through examination of topological features such as separation and reattachment lines as well as isolated singular points. The consistency of the extracted skin friction vector fields was also confirmed through application of a topological constraint given by the P-B index formula. Finally, two new approaches to global skin friction diagnostics based on surface temperature measurements and mass transfer visualizations were developed and successfully tested.

CHAPTER 13

FUTURE WORK

Three areas have been identified for further development. The first is the development of a toolbox for the GLOF technique. The toolbox will be comprised of documentation on the theoretical foundation of the technique along with experimental implementation and the relevant data reduction algorithms. The purpose of this toolbox is to enable the dissemination of the technique to be used by researchers in the area of fluid mechanics and aerodynamics for reliable global skin friction diagnostics.

Next, further studies using the surface temperature and mass transfer based methods will be conducted. The study will focus on identifying new applications and discovering any potential issues in application of the methods to global skin friction diagnostics. Currently, a method for global skin friction measurements for water tunnel experiments is being evaluated using the mass transfer approach. Similar to the GLOF technique, a toolbox will also be compiled for these two methods.

Finally, unified measurements of skin friction, surface pressure and near wall velocity will be performed for a 65° delta wing. Surface pressure measurements and near wall velocity fields will be conducted using pressure sensitive paint (PSP) and particle image velocimetry (PIV). Global skin friction fields will be extracted using the GLOF technique. The goal of this study is to measure and relate the various flow quantities to understand and map out the separated flow structures over a delta wing.

REFERENCES

- [1] Goldstein R. J., "Fluid Mechanics Measurements", Taylor & Francis, 1996
- [2] Anderson J. D., "Fundamentals of Aerodynamics", McGraw-Hill, 2011
- [3] Winter K. G., "An Outline of the Techniques Available for Measurement of Skin Friction in Turbulent Boundary Layer", Progress in Aerospace Sciences", Vol. 18, 1977, pp. 1-57
- [4] Settles G. S., "Recent Skin-Friction Techniques for Compressible Flows", AIAA Paper 86-1099, 1986
- [5] Plesniak M., Peterson S., "Wall Shear Stress Measurements for Conventional Applications and Biomedical Flows", AIAA Paper-2004-2301, 2004
- [6] Reda D. C., Wilder M. C., Farina D. J., Ziliac G., "New Methodology for the Measurement of Surface Shear Stress Vector Distributions", AIAA Journal, Vol. 35, No. 4, 1997, pp. 608-614
- [7] Reda D. C., Wilder M. C., Mehta R. D., Ziliac G., "Measurement of Continuous Pressure and Shear Distributions Using Coating and Imaging Techniques", AIAA Journal, Vol. 36, No. 6, 1998, pp. 895-899
- [8] Reda D. C., Wilder M. C., "Shear-Sensitive Liquid Crystal Coating Method Applied Through Transparent Test Surfaces", AIAA Journal, Vol. 39, No. 1, 2001, pp. 195-197
- [9] Fonov S. D., Jones G., Crafton J., Fonov V., Goss L., "The Development of Optical Technique for the Measurement of Pressure and Skin Friction", Measurement Science & Technology, Vol. 17, 2006, pp. 1261-1268
- [10] McQuilling M., Wolff M., Fonov S. D., Crafton J., Sondergaard R., "An Experimental Investigation of a Low-Pressure Turbine Blade Suction Surface Using a Shear and Stress Sensitive Film", Experiments in Fluids, Vol. 4, No. 1, 2008, pp. 73-88
- [11] Tanner L. H., Blows L. G., "A Study of the Motion of Oil Films on Surfaces in Air Flow with Application to the Measurement of Skin Friction", Journal of Physics E: Scientific Instruments, Vol. 9, 1976, pp. 194-202
- [12] Monson D. J., Higuchi H., "Skin Friction Measurements by a Dual-Laser-Beam Interferometer Technique", AIAA Journal, Vol. 19, No. 6, 1981, pp. 739-744
- [13] Monson D. J., Mateer G. G., Menter F. R., "Boundary-Layer and Global Skin Friction Measurement with an Oil-Fringe Imaging Technique", SAE Paper No. 932550, 1993
- [14] Kim K. S., Settles G. S., "Skin Friction Measurements by Laser Interferometry in Swept Shock/Boundary-Layer Interactions", AIAA Journal, Vol. 28, No. 1, 1990, pp. 133-139
- [15] Naughton J. W., Brown J. L., "Surface Interferometric Skin-Friction Measurement Technique", AIAA Paper 96-2183, 1996

- [16] Lighthill M. J., "Contributions to the Theory of Heat Transfer Through a Laminar Boundary Layer", Proceedings of the Royal Society A, Vol. 202, No. 1070, 1950, pp. 359-377
- [17] Liu T., Campbell B., Sullivan J., "Surface Temperature of a Hot Film on a Wall in Shear Flow", International Journal of Heat and Mass Transfer, Vol. 37, No. 17, 1994, pp. 2809-2814
- [18] Gelderblom H., Van Der Horst A., Haartsen J. R., Rutten M. C. M., Van De ven A. A. F., Van De Vosse F. N., "Analytical and Experimental Characterization of a Miniature Calorimetric Sensor in a Pulsatile Flow", Journal of Fluid Mechanics, Vol. 666, 2011, pp. 428-444
- [19] Liepmann, H. W. Skinner, G. T., "Shearing-Stress Measurements by Use of a Heated Element", NACA Technical Note 3268, 1954
- [20] Naughton J. W., Sheplak M., "Modern Developments in Shear-Stress Measurement", Progress in Aerospace Sciences, Vol. 38, 2002, pp. 515-570
- [21] Brown J. L., Naughton J. W., "The Thin Oil Film Equation", NASA/TM 1999-208767, 1999
- [22] Liu T., Sullivan J. P., "Luminescent Oil-Film Skin Friction Meter", AIAA Journal, Vol. 36, No. 8, 1998, pp. 1460-1465
- [23] Liu T., "Geometric and Kinematic Aspects of Image-Based Measurements of Deformable Bodies", AIAA Journal, Vol. 42, No. 9, 2004, pp. 1910-1920
- [24] Horn B. K., Schunck B. G., "Determining Optical Flow", Artificial Intelligence, Vol. 17, No. 1, 1981, pp. 185-204
- [25] Liu T., Sullivan J. P., "Pressure and Temperature Sensitive Paints", Springer, Berlin, 2005
- [26] Liu T., Shen L., "Fluid Flow and Optical Flow", Journal of Fluid Mechanics, Vol. 614, No. 11, 2008, pp. 253-291
- [27] Liu T., Montefort J., Woodiga S., Merati P., Shen L., "Global Luminescent Oil-Film Skin Friction Meter, AIAA Journal, Vol. 46, No. 2, 2008, pp. 476-485
- [28] Liu T., Woodiga S., Montefort J., Conn K. J., Shen L., "Global Skin Friction Diagnostics in Separated Flows Using Luminescent Oil", Journal of Flow Visualization and Image Processing, Vol. 16, No. 1, 2009, pp. 19-39
- [29] Liu T., Wang B., Woodiga S., "Physics-Based Optical Flow Method in Global Flow Diagnostics", AIAA Paper 2010-4361, 2010
- [30] Chapman G. T., Yates L. A., "Topology of Flow Separation on Three-Dimensional Bodies", Applied Mechanics Reviews, Vol. 44, No. 7, 1991, pp. 329-346
- [31] Chern S. S., "Studies in Global Geometry and Analysis", The Mathematical Association of America, 1967
- [32] Dallmann U., "Topological Structures of Three-Dimensional Vortex Flow Separation", AIAA Paper 83-1735, 1983
- [33] Délery J. M., "Physics of Vortical Flows", Journal of Aircraft, Vol. 29, No. 5, 1992, pp. 856-876
- [34] Délery J. M., Legendre R., Werle H., "Toward the Elucidation of Three-Dimensional Separation", Annual Review of Fluid Mechanics, Vol. 33, 2001, pp. 129-154

- [35] Foss J. F., "Surface Selections and Topological Constraint Evaluations for Flow Field Analyses", *Experiments in Fluids*, Vol. 37, 2004, pp. 883-897
- [36] Foss J.F., "Topological Considerations in Fluid Mechanics Measurements", *Handbook of Experimental Fluid Mechanics*, Springer, Berlin Chapter 13, 2007
- [37] Hornung H., Perry A. E., "Some Aspects of Three-Dimensional Separation. Part 1: Streamsurface Bifurcation", *Z. Flugwiss. Weltraumforsch.* Vol. 8, No. 2, 1984, pp. 77-87
- [38] Hunt J. C. R., Abell C. J., Peterka J. A., Woo H., "Kinematical Studies of the Flows Around Free or Surface-Mounted Obstacles; Applying Topology to Flow Visualization", *Journal of Fluid Mechanics*, Vol. 88, No. 1, 1978, pp. 179-200
- [39] Legendre R., "Separation de l'écoulement laminaire tridimensionnel", *La Recherche Aeronautique*, Vol. 54, 1956, pp. 3-8
- [40] Lighthill M. J., "Attachment and Separation in Three-Dimensional Flows", *Laminar Boundary Layer Theory*, Section 2.6, Oxford University Press, 1963, pp. 72-82
- [41] Schlichting H., *Boundary-Layer Theory*, 7th Edition, McGraw-Hill, New York, Chapter XVI, 1979
- [42] Surana A., Grunberg O., Haller G., "Exact Theory of Three-Dimensional Flow Separation. Part 1. Steady Separation", *Journal of Fluid Mechanics*, Vol. 564, 2006, pp. 57-103
- [43] Surana A., Jacobs G. B., Haller G., "Extraction of Separation and Attachment Surfaces from Three-Dimensional Steady Shear Flows", *AIAA Journal*, Vol. 45, No. 6, 2007, pp. 1290-1302
- [44] Tobak M., Peake D. J., "Topology of Three-Dimensional Separated Flows", *Annual Review of Fluid Mechanics*, Vol. 14, 1982, pp. 61-85
- [45] Wang K. C., "Boundary Layer Over a Blunt Body at High Incidence with an Open-Type Separation", *Proceedings of the Royal Society of London A*, Vol. 340, 1974, pp. 33-55
- [46] Chow S. N., Hale J. K., "Methods of Bifurcation Theory", Springer, Berlin, 1982, pp. 65-88
- [47] de Leeuw W. C., van Liere R., "Collapsing Flow Topology Using Area Metrics", *Proceedings IEEE Visualization*, 1999, pp. 349-354
- [48] do Carmo M. P., "Differential Geometry of Curves and Surfaces", Prentice-Hall, Upper Saddle River, Chapter 4, 1976
- [49] Firby P. A., Gardiner C. F., "Surface Topology", 3rd Edition, Horwood Publishing, Chichester, Chapter 7, 2001
- [50] Hartman P., "Ordinary differential equations", Wiley, New York, Chapter VII, 1964
- [51] Hsieh T., Wang K. C., "Three-Dimensional Separated Flow Structure Over a Cylinder with a Hemispherical Cap", *Journal of Fluid Mechanics*, Vol. 324, 1996, pp. 83-108
- [52] Izydorek M., Rybicki S., Szafaniec Z., "A note on the Poincare-Bendixson Index Theorem", *Kodai Math Journal*, Vol. 19, 1996, pp. 145-156
- [53] Kinsey L. C., "Topology of Surface", Springer, Berlin, Chapter 11, 1996

- [54] Ma T., Wang S., “A generalized Poincare-Hopf Index Formula and its Applications to 2-D Incompressible Flows, *Nonlinear Analysis: Real World Applications*, Vol. 2, 2001, pp. 467–482
- [55] Perry A. E., Chong M. S., “A Series-Expansion Study of the Navier-Stokes Equations with Application to Three-Dimensional Separation Patterns”, *Journal of Fluid Mechanics*, Vol. 173, 1986, pp. 207–223
- [56] Perry A. E., Chong M. S., “A Description of Eddying Motions and Flow Patterns Using Critical-Point Concepts”, *Annual Review of Fluid Mechanics*, Vol. 19, 1987, pp. 125–155
- [57] Liu T., Woodiga S. and Ma T., “Skin Friction Topology in a Region Enclosed by Penetrable Boundary”, *Experiments in Fluids*, Vol. 51, 2011, pp. 1549-1562
- [58] Bewley T. R. and Protas B., “Skin Friction and Pressure: The “Footprints” of Turbulence”, *Physica D*, Vol. 196, 2004, pp. 28-44
- [59] Zheng C., “Study of Experimental Technique of Oil Flow with Emphasis on Quantitative Determination of the Flow Position Parameters on the Surface”, *Acta Aerodynamica Sinica*, Vol. 5, 1987, pp. 383-389
- [60] Mueller T.J., DeLaurier J.D., “Aerodynamics of Small Vehicles”, *Annual Review of Fluid Mechanics*, Vol. 35, 2003, pp. 89-111
- [61] Mueller T.J., Batill S.M., “Experimental Studies of Separation on a Two-Dimensional Airfoil at Low Reynolds Numbers”, *AIAA Journal*, Vol. 20, No. 4, 1982, pp. 457-463
- [62] Pelletier A., Mueller T.J., “Low Reynolds Number Aerodynamics of Low-Aspect-Ratio, Thin/Flat/Cambered-Plate Wings”, *Journal of Aircraft*, Vol. 37, No. 5, 2000, pp. 825-831
- [63] Torres G.E., Mueller T.J., “Low-Aspect Ratio Wing Aerodynamics at Low Reynolds Numbers”, *AIAA Journal*, Vol. 42, No. 5, 2004, pp. 865-873
- [64] Kaplan S.M., Altman A., Ol M., “Wake Vorticity Measurements for Low Aspect Ratio Wings at Low Reynolds Number”, *Journal of Aircraft*, Vol. 44, No. 1, 2007, pp. 241-251
- [65] Ringuette M.J., Milano M., Gharib M., “Role of the Tip Vortex in the Force Generation of Low-Aspect-Ratio Normal Flat Plates”, *Journal of Fluid Mechanics*, Vol. 581, 2007, pp. 453-468
- [66] Jian T., Zhu K-Q., “Numerical and Experimental Study of Flow Structure of Low-Aspect-Ratio Wing”, *Journal of Aircraft*, Vol. 41, No. 5, 2004, pp. 1196-1201
- [67] Cosyn P., Vierendeels J., “Numerical Investigation of Low-Aspect-Ratio Wings at Low Reynolds Numbers”, *Journal of Aircraft*, Vol. 43, No. 3, 2006, pp. 713-721
- [68] Hebbar S.K., Platzer M.F., Fritzelas A.E., “Reynolds Number Effects on the Vortical-Flow Structure Generated by a Double-Delta Wing”, *Experiments in Fluids*, Vol. 28, 2000, pp. 206-216
- [69] Hebbar S.K., Platzer M.F., and Khozam A., “Investigation Into The Effects of Juncture Fillets on The Vertical Flow Over a Cropped, Double-Delta Wing”, *AIAA Paper 94-0626*, 1994
- [70] Erickson G.E., Gonzalez H.A., “Pressure-Sensitive Paint Investigation of Double-Delta Wing Vortex Flow Manipulation”, *AIAA Paper 2005-1059*, 2005
- [71] Verhaagen N.G., Jenkins L.N., Kern S.B., Washburn A.E., “A Study of The Vortex Flow Over a 76/40-deg Double-Delta Wing”, *NASA/ICASE-95-5*, 1995

- [72] Kern S.B., "Numerical Investigation of Vortex Flow-Control Through Small Geometry Modifications at The Strake/Wing Junction of a Cropped Double-Delta Wing", AIAA Paper 92-0411, 1992
- [73] Kern S.B., "Vortex Flow Control Using Fillets on a Double-Delta Wing", *Journal of Aircraft*, Vol. 30, No. 6, 1993, pp. 818-825
- [74] Narayan K.Y., Seshadri S.N., "Types of Flow on The Lee Side of Delta Wings", *Progress in Aerospace Sciences*, Vol. 33, 1997, pp. 167-257
- [75] Gursul I., "Recent Development in Delta Wing Aerodynamics", *The Aeronautical Journal*, Vol. 108, No. 1087, 2004, pp. 437-452
- [76] Huang X.Z., Hanff E.S., Jobe C.E., "Surface Flow Topology on a Delta Wing at High Incidence for a Range of Roll Angles", AIAA Paper 96-2398, 1996
- [77] Huang X.Z., Verhaagen N.G., "Vortex Flow Behavior Over Slender Delta Wing Configurations: Experimental Studies, Numerical and Analytical Solutions, Springer, Berlin, 2008
- [78] Verhaagen N.G., "Effects of Reynolds Number on Flow Over 76/40-degree Double-Delta Wings", *Journal of Aircraft*, Vol. 39, No. 6, 2002, pp. 1045-1052
- [79] Verhaagen N.G., Jobe C.E., "Wind-Tunnel Study on a 65-deg Delta Wing at Sideslip", *Journal of Aircraft*, Vol. 40, No. 2, 2003, pp. 290-296
- [80] Van Bossuyt B.C., "Experimental Investigation of The Vortex Flow Over The Apex of a Delta Wing", MS Thesis, Department of Aerospace Engineering, Delft University of Technology, 2005
- [81] Fuji K., Schiff L.B., "Numerical Simulation of Vortical Flows Over Strake-Delta Wing", *AIAA Journal*, Vol. 27, No. 9, 1989, pp. 1153-1162
- [82] Rizzi A., Miillerf B., "Large-Scale Viscous Simulation of Laminar Vortex Flow Over a Delta Wing", *AIAA Journal*, Vol. 27, No. 7, 1989, pp. 833-840
- [83] Ekaterinaris J.A., Coutley R.L., Schiff L.B., Platzer M.F., "Numerical Investigation of High Incidence Flow Over a Double-Delta Wing", *Journal of Aircraft*, Vol. 32, No. 3, 1995, pp. 457-463
- [84] Gordnier R.E., "Numerical Simulation of a 65-degree Delta-Wing Flow", *Journal of Aircraft*, Vol. 34, No. 4, 1997, pp. 492-499
- [85] Woodiga S., Liu T., "Skin Friction fields on Delta Wings", *Experiments in Fluids*, Vol. 47, 2009, pp. 897-911
- [86] Verhaagen N.G., Naarding S.H.J., "Experimental and Numerical Investigation of the Vortex Flow Over a Yawed Delta Wing", AIAA Paper 88-2563, 1988
- [87] Verhaagen N.G., Jobe C.E., "Topology of the Flow on a 65-deg Delta Wing at Sideslip", AIAA Paper 2002-0095, 2002
- [88] Verhaagen N.G., Kunst V.F., "Topology of the Flow on Delta Wings at Sideslip", AIAA Paper 2005-60, 2005
- [89] Gordnier R.E., "Computation of Delta Wing Roll Maneuvers", *Journal of Aircraft*, Vol. 32, No. 3, 1995, pp. 486-492

- [90] Grismer D., Nelson R., “Aerodynamic Effects of Sideslip on Double Delta Wings”, AIAA Paper 93-0053, 1993
- [91] Hebbar S.K., Platzer M.F., Chang W.H., “Juncture Fillets for Vortex Flow Control on Double-Delta Wings Undergoing Sideslip”, AIAA Paper 96-0663, 1996
- [92] Su W., Liu M., Liu Z., “Topological Structures of Separated Flows About a Series of Sharp-Edged Delta Wings at Angles of Attack up to 90°”, Topological Fluid Mechanics, Proceedings of the IUTAM Symposium, 1989, pp. 395-407
- [93] Yavuz M.M., Elkhoury M., Rockwell D., “Near-Surface Topology and Flow Structure on a Delta Wing”, AIAA Journal, Vol. 42, No. 2, pp. 332-340
- [94] Barker. C. J., “The Laminar Horseshoe Vortex”, Journal of Fluid Mechanics, Vol. 95, No.2, 1979, pp. 347-367
- [95] Martinuzzi R., Tropea C., “The Flow Around Surface-Mounted, Prismatic Obstacles Placed in a Fully Developed Channel Flow”, Journal of Fluids Engineering, Vol. 115, No. 1, 1993, pp. 85-92
- [96] Seal. C., Smith. C., Rockwell D., “Quantitative Characteristics of a Laminar, Unsteady Necklace Vortex System at a Rectangular Block-Flat Plate Juncture”, Journal of Fluid Mechanics, Vol. 286, 1995, pp. 117-135
- [97] Seal. C., Smith. C., Rockwell D., “Dynamics of the Vorticity Distribution in the Endwall Junctions”, AIAA Journal, Vol. 35, No. 6, 1997, pp. 1041-1047
- [98] Lin C., Chiu P., Shieh S., “Characteristics of Horseshoe Vortex System Near a Vertical Plate-base Plate Juncture”, Experimental Thermal and Fluid Science, Vol. 27, No.1, 2002, pp. 25-46
- [99] Wang J., Bi W., Wei Q., “Effects of an Upstream Inclined Rod on the Circular Cylinder-flat Plate Junction Flow”, Experiments in Fluids, Vol. 46, 2009, pp. 1093-1104
- [100] Depardon S., Lasserre J.J., Boueilh J.C., Brizzi L.E., Boree J., “Skin Friction Pattern Analysis Using Near-Wall PIV”, Experiments in Fluids, Vol. 39, 2005, pp. 805-818
- [101] Gordeyev S. Jumper E., “Fluid Dynamics and Aero-optics of Turrets”, Progress in Aerospace Science, Vol. 46, No. 8, 2010, pp. 388-400
- [102] Sattari P., Bourgeois J.A., Martinuzzi R.J., “On the Vortex Dynamics in the Wake of a Finite Surface-Mounted Square Cylinder”, Experiments in Fluids, Vol. 52, pp. 1149-1167
- [103] Devenport W., Simpson R., “Time Dependent and Time Averaged Turbulence Structure near the Nose of a Wing/Body Junction”, Journal of Fluid Mechanics, Vol. 210, 1990, pp. 23–55
- [104] Pierce F. J., Shin J. “The Development of a Turbulent Junction Vortex System”, Journal of Fluids Engineering, Vol. 114, No. 4, 1992, pp. 559-565
- [105] Fleming J., Simpson R., Cowling J., Devenport W., “An Experimental Study of a Turbulent Wing-Body Junction and Wake Flow”, Experiments in Fluids, Vol. 14, No. 5, 1993, pp. 366–378
- [106] Olcmen S., Simpson R., “An Experimental Study of a Three-Dimensional Pressure-Driven Turbulent Boundary Layer”, Journal of Fluid Mechanics, Vol. 290, 1995, pp. 255-262
- [107] Khan M., Ahmed A., Tropper R., “Dynamics of the Juncture Vortex”, AIAA Journal, Vol. 33, No. 7, 1995, pp. 1273–1278

- [108] Paik J., Escauriaza C., Sotiropoulos F., “On the Bimodal Dynamics of the Turbulent Horseshoe Vortex System in a Wing Body Type Junction”, *Physics of Fluids*, Vol. 19, 2007, pp. 045107-1-045107-20
- [109] Gand F., Brunet V., Deck S., “Numerical Investigation of a Simplified Wing Body Junction Flow”, *AIAA Paper 2009-3894*, 2009
- [110] Fu S., Xiao Z., Chen H., Zhang Y., Huang J., “Simulation of Wing-Body Junction Flows with Hybrid RANS-LES Methods”, *International Journal of Heat and Fluid Flow* Vol. 28, No. 6, 2007, pp. 1379–1390
- [111] Gand F., Deck S., Brunet V., Sagaut P. “Flow Dynamics Past a Simplified Wing Body Junction”, *Physics of Fluids*, Vol. 22, No. 11, 2010, pp. 115111-1-115111-16
- [112] Gand F., Brunet V., Deck S., “Experimental and Numerical Investigation of a Wing-Body Junction Flow”, *AIAA Journal*, Vol. 50, No. 12, 2012, pp. 2711-2719
- [113] Simpson R., “Junction Flows”, *Annual Review of Fluid Mechanics*, Vol. 33, 2001, pp. 415-439
- [114] Johnson T.A., Patel V.C., “Skin-Friction Topology Over a Surface Mounted Semi-Ellipsoidal Wing at Incidence”, *AIAA Journal*, Vol. 31, No. 10, 1993, pp. 1842-1849
- [115] Visbal M.R., “Structure of Laminar Junction Flows”, *AIAA Journal*, Vol. 29, No. 8, 1991, pp. 1273-1282
- [116] Hung C.M., Sung C.H. and Chen C.L., “Computation of Saddle Point of Attachment”, *AIAA Journal*, Vol. 30, No. 6, 1992, pp. 1561-1569
- [117] Liu T., Cattafesta L., Radezsky R., Burner A.W., “Photogrammetry Applied to Wind Tunnel Testing”, *AIAA Journal*, Vol. 38, No. 6, 2000, pp. 964-971
- [118] Liu T., “Geometric and Kinematic Aspects of Image-Based Measurements of Deformable Bodies”, *AIAA Journal*, Vol. 42, No. 9, 2004, pp. 1910-1920
- [119] Liu T., Burner A., Jones T., Barrow D., “Photogrammetric Techniques for Aerospace Applications”, *Progress in Aerospace Science*, Vol.54, 2012, pp. 1-58
- [120] Karthikeyan N., Venkatakrishnan L., “Application of Photogrammetry to Surface Flow Visualization”, *Experiments in Fluids*, Vol. 50, 2011, pp. 689-700
- [121] Zhong H.J., Lee C., Su Z., Chen S., Wu J., Zhou M., “Experimental Investigation of Freely Falling Thin Disks. Part 1. The Flow Structures and Reynolds Number Effects on the Zigzag Motion”, *Journal of Fluid Mechanics*, 2013, Vol. 716, pp. 228-250
- [122] Zhong H. J., Chen S., Lee C., “Experimental Study of Freely Falling Thin Disks: Transition from Zigzag to Spiral”, *Physics of Fluids*, Vol.23, No. 1, 2011, pp. 011702-1-011702-4
- [123] Abdel-Aziz Y.I., Karara H.M., “Direct Linear Transformation from Comparator Coordinates into Object Space Coordinates in Close-range Photogrammetry”, *Proceedings ASP/UI Symposium on Close-Range Photogrammetry*, University of Illinois at Urbana-Champaign, 1971, pp. 1–18
- [124] Liu T., Burner A.W., “Photogrammetry Toolbox Reference Manual”, *NASA Langley Research Center Contract Report*, May 2007

- [125] Knight D., Yan H., Panaras A.G., Zheltovodov A., “Advances in CFD prediction of Shock Wave Turbulent Boundary Layer Interactions”, *Progress in Aerospace Sciences*, Vol. 39, 2003, pp. 121-184.
- [126] Wu J.Z., Ma H.Y., Zhou J.Z., “Vorticity and Vortex Dynamics”, Springer, Berlin, 2005
- [127] Bewley T.R., Protas B., “Skin Friction and Pressure: The “Footprints” of Turbulence”, *Physica D: Nonlinear Phenomena*, 2004, Vol. 196, No. 1, pp. 28-44
- [128] Ahmed S.R., Ramm G., Faitin G., “Some Salient Features of the Time-Averaged Ground Vehicle Wake”, SAE-TP-840300, 1984
- [129] Liu T., Campbell B., Burns S., Sullivan J., “Temperature and Pressure-Sensitive Paints in Aerodynamics”, *Applied Mechanics Reviews*, Vol. 50, No. 4, 1997, pp. 227-246
- [130] Bell J.H., Shairer E.T., Hand L.A., Mehta R.D., “Surface Pressure Measurements Using Luminescent Coatings”, *Annual Review of Fluid Mechanics*, Vol. 33, 2001, pp. 155-206
- [131] Engler R., “Pressure-Sensitive Paint (PSP) - In Handbook of Experimental Fluid Mechanics”, Springer, Chapter 4.4, 2007
- [132] Gregory J., Asai K., Kamada M., Liu T., Sullivan J., “A Review of Pressure Sensitive Paints in Hypersonic and Unsteady Flows”, *Journal of Aerospace Engineering*, Vol. 222, No. G, 2008, pp. 249-290
- [133] Yamashita T., Sugiura H., Nagai H., Asai K., Ishida K., “Pressure-Sensitive Paint Measurement of the Flow around a Simplified Car Model”, *Journal of Visualization*, Vol. 10, No. 3, 2007, pp. 289-298
- [134] Coon M.D., Tobak M., “Experimental Study of Saddle Point of Attachment in Laminar Junction Flow”, *AIAA Journal*, Vol. 33, No. 2, 1995, pp. 2288-2292
- [135] Ozturk N.A., Akkoca A., Sahin B., “PIV Measurements of Flow Past a Confined Cylinder”, *Experiments in Fluids*, Vol. 44, 2008, pp. 1001-1014
- [136] Lakehal D., Rodi W., “Calculation of the Flow Past a Surface-Mounted Cube with Two-Layer Turbulence Models”, *Journal of Wind Engineering*, Vol. 67, 1997, pp. 65-78
- [137] Hung C.M., Sung C.H., Chen C.L., “Computation of Saddle Point of Attachment”, *AIAA Journal*, Vol. 30, No. 6, 1992, pp. 1561-1569
- [138] Hwang J.Y., Yang K.S., “Numerical Study of Vortical Structures Around a Wall-Mounted Cubic Obstacle in Channel Flow”, *Physics of Fluids*, Vol. 16, No. 7, 2004, pp. 2383-2394
- [139] Liu Y., Moser A., “Numerical Modeling of Airflow over the Ahmed Body”, *Proceedings of CFD, Canada*, 2003, pp. 507-512
- [140] Guilmineau E., “Computational Study of Flow Around a Simplified Car Body”, *Journal of Wind Engineering and Industrial Aerodynamics*, Vol. 96, 2008, pp. 1207-1217
- [141] Spohn A., Gillieron P., “Flow Separations Generated by a Simplified Geometry of an Automotive Vehicle”, *IUTAM Symposium : Unsteady Separated Flows*, 2002
- [142] Marusic I., MacKeon B.J., Monkewitz P.A., Nagib H.M., Smits A.J., “Wall-Bounded Turbulent Flows at High Reynolds Numbers”, *Physics of Fluids*, Vol. 22, 2010, pp. 065103

- [143] Baughn J.W., Byerley A.R., Gregory J.W., “An Optical Method for Measuring Low Wall Shear Stresses Using Thermal Tufts, AIAA Paper 2006-647, 2006
- [144] Reyer M., Rudolph I., Nitsche W., “Investigations into the Visualization and Quantification of Wall Shear Stress Distributions Using Infrared Thermography”, AIAA Paper 2006-3840, 2006
- [145] Aubert G., Deriche R., Kornprobst P., “Computing Optical Flow via Variational Techniques”, *Journal of Applied Mathematics*, Vol. 60, 1999, pp. 156-82
- [146] Phares D., Smedley G.T., Flagan R.C., “The Wall Shear Stress Produced by the Normal Impingement of a Jet on a Flat Plate”, *Journal of Fluid Mechanics*, Vol. 418, 2000, pp. 351-75
- [147] Liu T., Sullivan J., “Heat Transfer and Flow Structures in an Excited Circular Impinging Jet”, *International Journal of Heat & Mass Transfer*, Vol. 39, 1996, pp. 3695-3706
- [148] Brücker C., Bauer D., Chaves H., “Dynamic Response of Micro-Pillar Sensors Measuring Fluctuating Wall-Shear-Stress,” *Experiments in Fluids*, Vol. 42, 2007, pp. 737–749
- [149] Große S., Schröder W., “Mean Wall-Shear Stress Measurements Using the Micro-Pillar Shear-Stress Sensor”, *Measurement Science and Technology*, Vol. 19, 2008, pp. 015403
- [150] Liu T., Woodiga S., “Feasibility of Global Skin Friction Diagnostics using Temperature Sensitive Paint”, *Measurement Science and Technology*, Vol. 22, 2011, pp. 115402
- [151] Burmeister L.C., “Convective Heat Transfer”, Wiley, New York, 1993, Chapter 2
- [152] Bouvier F., Le Sant Y., Merienne M.C., “A New Skin Friction Technique using Pressure Sensitive Paint”, *Aerodynamic Research Conference, Londres (Grande-Bretagne)*, April 9-10, 2001
- [153] Obara C.J., “Sublimating Chemical Technique for Boundary-Layer Flow Visualization in Flight Testing”, *Journal of Aircraft*, Vol. 25, No. 6, 1988, pp. 493-498
- [154] Goldstein R.J., Cho H.H., “A Review of Mass Transfer Measurements using Naphthalene Sublimation”, *Experimental Thermal and Fluid Science*, Vol. 10, 1995, pp. 416-434
- [155] Lamar J.E., “Flow-Visualization Techniques Used at High Speed by Configuration Aerodynamics Wind-Tunnel-Test Team”, NASA TM-2001-210848, 2001
- [156] Han J.C., Rallabandi A.P., “Turbine Blade Film Cooling using PSP Technique”, *Frontiers in Heat and Mass Transfer*, Vol. 1, 2010, pp. 013001
- [157] Tikhonov A.N., Arsenin V.Y., “Solutions of Ill-Posed Problems” Wiley, New York, Chapter II, 1977
- [158] Groetsch C.W., “Inverse Problems in the Mathematical Sciences”, Vieweg Braunschweig, Chapter 5, 1993
- [159] Gregory J.W., Sullivan J.P., Raman G., Raghu S., “Characterization of the Microfluidic Oscillator”, *AIAA Journal*, Vol. 45, No. 3, 2007, pp. 568-576
- [160] Carbonaro M., “Measurement Techniques in Fluid Dynamics an Introduction,” VKI Lecture Series, Belgium, 1994
- [161] Zemsch S., “Fin-Induced Vortex Boundary-Layer Interactions in High Speed Flow”, PhD Thesis, The von Karman Institute for Fluid Dynamics, 1995

- [162] Zemsch S. and Degrez G., "Fin Induced Vortex Boundary Layer Interactions", *Aerothermodynamics and Propulsion Integration for Hypersonic Vehicles*, AGARD Report 813, 1996, pp. 2A-34-2A-40